UNIVERSITY OF CAPE TOWN
IYUNIVESITHI YASEKAPA • UNIVERSITEIT VAN KAAPSTAD

An Investigation of the Response of Different Materials to Blast Loading

Wei-Chi Lee

Supervisor

A/Prof Genevieve Langdon

October 2012

Blast Impact and Survivability Research Unit

Department of Mechanical Engineering

University of Cape Town

Declaration

I understand the meaning of plagiarism and declare that all the work in this report, except for that which is properly acknowledged, is my own.

.....

Wei-Chi Lee

Abstract

This dissertation reports on the results of an experimental and numerical investigation into the response of different materials to air-blast loading. Mild steel, armour steel (Armox 370T and 440T), Aluminium alloy 5083-H116, Twintex and Dyneema square plates were blast loaded on a horizontal pendulum at the Blast Impact and Survivability Research Unit (BISRU), University of Cape Town. The blasts were generated by detonating disc-shaped PE4 explosives of various diameters and stand-off distances. The chosen plates are of side length 500mm (4mm thick mild steel and armour steel plates) and side length of 400mm (aluminium, Twintex and Dyneema panels).

The charge mass was varied between 9g and 60g for two charge diameters, namely: 50mm and 75mm, and stand-off distances of 25mm, 38mm and 50mm. A polystyrene bridge was used to position the charges at the centre of plates, without any polystyrene between the charge and the plate in order to minimise any effects the polystyrene may have had on the plate deformation.

The transient response of the 500mm square plates (mild steel and Armox 370T) was measured with the use of Light Interference Equipment (LIE) and numerical simulations performed in ANSYS AUTODYN, with the aim of gaining greater insight into the response of the two different materials. The details of the experimental setup and method used for the LIE as well as the development of the AUTODYN computational model are presented. The air and explosive were modelled as Arbitrary Langrange-Euler (ALE) elements while the test plates were modelled as Langrangian shell elements. Since the geometry of the plates was square, the simulations had to be performed in 3D quarter-symmetry.

The transient response, permanent final displacement and maximum transient displacement of the numerical simulations were compared to the corresponding experimental results. The mild steel plates all exhibited good correlation between experimental and simulated results. However, the Armox 370T simulated results showed an under-prediction of the displacement magnitude and impulse compared to the experimental results. Experimentally, both the mild steel and armour steel exhibited a linear increase in deformation with increasing charge mass.

Blast tests were also performed on 3mm thick mild steel, aluminium, Twintex and Dyneema square plates of 400mm side length. The aim was to gain a greater understanding and compare of the response of different material types (ferrous, non-ferrous, Glass Fibre Polypropylene and Ultra High Molecular Weight Polyethylene) under blast loading. The aluminium plates performed better than the mild steel, on an equivalent mass basis, in terms of permanent displacements and failure threshold impulse. The aluminium plates were significantly thicker (10.5mm compared to 3mm) than the mild steel plates, which may have contributed to its response under blast. The Twintex panels mostly exhibited failure in the form of fibre fracture and matrix failure whereas the Dyneema panels only exhibit large inelastic deformation, although the Dyneema were clamped differently to the other panels.

Dimensionless analysis was performed on all of the materials except for Dyneema. Initially a scaling factor was used to account for the varying stand-off distances but proved to be unnecessary due to the type of confinement used (unconfined free air-blasts versus partially confined tube). Once the scaling factor was removed, the dimensionless impulse values showed relatively good linear correlation with the predicted trend.

Acknowledgements

The author would like to thank the following people for their significant contributions:

- A/Prof Genevieve Langdon for her guidance and expert knowledge of the work performed, her patience and willingness to help was never-ending. Her constant assistance in compiling this report, through proof-reading and providing suggestions for improvement is greatly appreciated. It has been a great pleasure working with you.
- Prof Gerald Nurick for his advice and assistance throughout the project.
- Carlo Geretto for his assistance in the setup of the Light Interference Equipment, countless hours spent resolving issues with the equipment and valuable advice on numerical modelling.
- Victor Balden and Erik Pickering for their guidance during critical stages in the development of the numerical models.
- Adam Ozinsky for his initial guidance into using AUTODYN, his continued advice and assistance throughout the project and being an entertaining office mate.
- Gregory Sinclair and Travis Henchie, in no particular order, for their willingness to help when needed and for being equally entertaining office mates.
- Dr. Reuben Govender for his assistance with waterjet cutting the Dyneema Panels and his advice and guidance during the manufacture of the Twintex panels.
- Richard Curry for ensuring the PC's were always running and for his assistance throughout the project.
- Dr. Steeve Chung Kim Yuen for his guidance and for ensuring a safe working environment
- Glen Newins and the rest of the workshop staff for their help and assistance with manufacturing, machining and acquisition of parts and materials throughout the project.
- The financial assistance of the National Research Foundation (NRF) and the UCT University Research Council.

Table of Contents

Declaration ..... **i**

Abstract ..... **ii**

Acknowledgements ..... **iv**

Table of Contents ..... **v**

List of Figures ..... **xi**

List of Tables ..... **xxi**

1. INTRODUCTION **1**

2. LITERATURE REVIEW **3**

2.1. Detonation of Explosives 3

2.2. Blast Loading Conditions 4

2.2.1 Uniform Loading *5*

2.2.2 Localised Loading *7*

2.3. Material Properties 8

2.4. Blast Loading of Metals 10

2.4.1. Steel Plates *10*

2.4.2. Armour Steel *11*

2.4.3. Blast Loading of Aluminium *13*

2.5. Composite Panels 15

2.6. Failure Modes 17

2.6.1. Failure Modes of Metals *17*

2.6.2. Comparison of Failure Modes between Square and Circular Plates *19*

2.6.3. Failure Modes of Composites *21*

2.6.4. The Effect of Boundary Conditions *22*

2.7. Transient Measurements during Blast Loading 24

2.7.1. Displacement-time Measurements Using Light Interference Method *24*

2.7.2. Displacement-time Measurement using Digital Image Correlation *28*

2.7.2.1. DIC Using Stereo Vision System *28*

2.7.2.2 DIC Using Single Camera System *29*

2.8. Theoretical Predictions 31

2.8.1. Jones Damage Numbers *31*

2.8.1.1. Jones Damage Number for Circular Plates *31*

2.8.1.2. Jones Damage Number for Quadrangular Plates *33*

2.8.2. Nurick and Martin Damage Numbers *34*

2.9. Numerical Modelling 39

2.10. Summary of Literature Review 42

3. EXPERIMENTAL DETAILS 43

3.1. Experimental Procedure 43

3.1.1. Configuration of Test Rig *43*

3.1.2. Material Properties and Dimensions of Explosive Loads *44*

3.1.3. Ballistic Pendulum *46*

3.1.4. Light Interference Equipment *48*

3.1.4.1. Calibration of the LIE *49*

3.1.4.2. Transient Displacement Measurement *49*

3.2. Specimens 53

3.3. Material Properties of Test Specimens 57

4. EXPERIMENTAL RESULTS: 500 X 500 PLATES 62

4.1. 4mm Thick Mild Steel Plates 64

4.1.2. Post-test Results *67*

4.2. Armour Steel Plates (Armox 370T) 69

4.2.1. Post-test Results *72*

4.3. Armour Steel Plates (Armox 440T) 73

4.3.1. Armox 440T Plate Deformation *73*

4.3.2. Post-test Results *75*

5. NUMERICAL SIMULATIONS 77

5.1. 2D Model 77

5.2. Boundary Conditions 80

5.3. Final Model 83

5.3.1. Air Mesh Size *83*

5.3.2. Plate Mesh Size *86*

5.3.3. Material Modelling *86*

5.3.4. Explosive *87*

5.3.5. Plate Materials *87*

5.3.6. Output Variable *89*

5.4. Simulation Results 92

6. EXPERIMENTAL RESULTS: 400 X 400 PLATES 97

6.1. Mild Steel 97

6.2. Aluminium Plates 106

6.3. Twintex Plates 118

6.3.1. Plate Damage Analysis *118*

6.4. Dyneema Plates 124

6.4.1. Plate Damage Analysis *125*

7. DISCUSSION 129

7.1. Comparison of 500 x 500 Equivalent Mass Plates 129

7.1.1. Permanent Displacement Profiles *129*

7.1.2. Comparison of the Transient Responses *131*

7.1.3. Comparison of Numerical and Experimental Results *134*

7.1.3.1. Mild Steel *134*

7.1.3.2. Armox 370T *138*

7.1.3.3. Summary of Numerical Results *140*

7.1.4. Effect of Grade on Armour Steel: Armox 370T vs. 440T *143*

7.2. Comparison of 400 x 400 Plates 146

7.2.1. Mild Steel vs. Aluminium *146*

7.2.2. Composite Panels *151*

7.3. Summary of Impulse Versus Charge Mass for all Blasts 152

7.4. Dimensionless Analysis 153

8. CONCLUSIONS 164

8.1. Sensitivity of the Experimental Setup 164

8.2. Effect of Varying Loading Parameters on Plate Response 164

8.3. The Influence of Material Type 165

8.3.1. Comparison of Different Materials *166*

8.3.1.1. Mild Steel vs. Armox 370T *166*

8.3.1.2. Mild Steel vs. Aluminium *166*

8.3.1.3. Armox 370T vs. Armox 440T *167*

8.3.1.4. Twintex and Dyneema *167*

8.4. Validity of Numerical Results 167

8.5. Significance of Applying Dimensionless Analysis 168

9. RECOMMENDATIONS 169

REFERENCES 170

APPENDIX A: Material Characterisation 179

APPENDIX B: Additional Numerical Simulation Details 184

B.1. Investigating the Effect of De-activating the Air Mesh 184

B.2. Effect of a Leader Charge on Profile of Blast Wave 187

B.3. Impulse Calculations from Simulations 190

APPENDIX C: Pendulum Impulse Derivation 191

APPENDIX D: Engineering Drawings 197

APPENDIX E: Light Interference Example 212

APPENDIX F: Ethics Declaration 214

List of Figures

Figure 1: Typical Pressure-time history of a Blast Wave resulting from a far-field explosion 3

Figure 2: Diagram showing Effective charge height 5

Figure 3: Concentric Annuli used on a Square Test Plate [14] 6

Figure 4: Cross-section schematic of tube arrangement used by Jacob [12] for uniform loading ... 6

Figure 5: Schematic of method proposed by Marchand and Alfawakhiri [15] for determining blast loading conditions 7

Figure 6: Schematic and photograph of experimental setup used by Neuberger *et al* [37] 12

Figure 7: Numerical model used by Neuberger *et al* and the transient response obtained numerically [37] 13

Figure 8: Schematic of experimental setup used by Veldman *et al* [38] 14

Figure 9: Photograph of Experimental rig used by Veldman *et al* [38] 14

Figure 10: Computational model showing delaminated area (top) and matrix cracking damage (bottom) [40] 15

Figure 11: Photograph of BISRU ballistic pendulum with blast tube used by Cantwell *et al* [41] .. 16

Figure 12: Failure modes as defined by Menkes and Opat [43]: (a) *Mode I* – Large inelastic deformations; (b) *Mode II* – Tensile Tearing at supports; (c) *Mode III* – Shear failure at supports.18

Figure 13: Schematic of fully clamped (a) and built-in plates (b) as described by Jacob *et al* [12] 22

Figure 14: Schematic of sharp edge boundary (a) and curved edge boundary (b) [12] 23

Figure 15: Schematic Layout of LIE test rig used by Nurick [46], [47] 25

Figure 16: Typical deflection –time curve measured by Nurick [48], showing time in msec and voltage change in mV .....**Error! Bookmark not defined.**

Figure 17: Displacement-time graphs of (a) Fully confined and (b) Unconfined Plates [49]. 27

Figure 18: Schematic Diagram and Photos of the experimental setup used by Tiwari *et al* [50] ... 29

Figure 19: Relation between out-of-plane displacement and apparent in-plane displacement [51] 30

Figure 20: Diagram of the Experimental setup used by Tay *et al* [51] 30

Figure 21: Fully clamped circular plate, radius R, subjected to uniformly distributed Impulse at velocity Vo, [52] 31

Figure 22: AUTODYN screenshots from Pickering's models showing response of sand at different burial depths [55] 40

Figure 23: Pressure contour plot from Rossiter's model of a perforated plate and target plate in a tube [54] 41

Figure 24: Exploded CAD Diagram of Ballistic Pendulum Setup 44

Figure 25: Photograph of Polystyrene Bridge 45

Figure 26: Photograph of the Polystyrene Bridge with the Explosive attached underneath 45

Figure 27: Schematic Diagram Showing Configuration of Explosive for Localised Impulsive Loading used in the current work 46

Figure 28: Photograph of Ballistic Pendulum 47

Figure 29: Photograph of the Protective Shroud Mounted onto the Test Rig 47

Figure 30: Photograph of the Light Interference system mounted to the back of the Test Plate 48

Figure 31: Calibration Curve of Displacement versus Voltage Change 50

Figure 32: Schematic of LIE system illustrating light intensity of LEDs at various positions 52

Figure 33: Graph of Displacement versus Voltage Drop % of Theoretical and Experimental Results 52

Figure 34: Drawing of the 500mm x 500mm, 4mm Thick Test Plate 54

Figure 35: 400mm x 400mm Test Plate 55

Figure 36: Dyneema test plate dimensions 56

Figure 37: Photograph showing clamping arrangement for Dyneema plates 56

Figure 38: Graph of a typical Stress-Strain Curve for 4mm thick Mild Steel..... 57

Figure 39: Graph of a typical Stress-Strain Curve for 3mm thick Mild Steel..... 58

Figure 40: Graph of a typical Stress-Strain Curve for 4mm thick Armox 370T Steel 58

Figure 41: Graph of a typical Stress-Strain Curve for 4mm thick Armox 440T Steel 59

Figure 42: Graph of a typical Stress Strain curve for 10.5mm thick Aluminium 5083 H116..... 59

Figure 43: Stress-Strain Curves of all materials..... 60

Figure 44: Summary of all Impulse versus Charge mass data for Section 4..... 62

Figure 45: Tearing and thinning on MS-P6, Subjected to a 40g, 50mm diameter charge at 25mm SOD..... 64

Figure 46: Different view of MS-P6 showing tearing and thinning..... 64

Figure 47: Deformations profiles of mild steel plate cross-sections arranged in descending order from top 65

Figure 48: Deformation Profiles of Plates blast loaded with 50mm diameter charges at 25mm sod 66

Figure 49: Deformation Profiles of Plates blast loaded with 75mm diameter charges at 25mm sod 66

Figure 50: Key of Symbols used in all Graphs..... 67

Figure 51: Graph of Displacement versus Impulse for 4mm thick Mild Steel..... 68

Figure 52: Deformations profiles of armour steel plate cross-sections arranged in descending order from top..... 69

Figure 53: Tearing and thinning on AS-P1 (back-face), subjected to a 40g, 50mm diameter charge at 25mm sod..... 70

Figure 54: Photograph of front-face (blast loaded side) of AS-P1 (40g, 50mm diameter, 25sod) . 71

Figure 55: Cross-section of AS-P1 showing signs of thinning before fracture (40g, 50mm diameter, 25sod)..... 71

Figure 56: Displacement versus Impulse for 4mm thick Armox 370T 72

Figure 57: Deformation profiles Armox 440T subjected to 25sod 74

Figure 58: Deformation profiles of Armox 440T subjected to 38sod 74

Figure 60: Graph of Displacement versus Impulse for 4.5mm thick Armox 440T 75

Figure 61: Graph of Normalized Displacement versus Impulse for Armox 370T and 440T 76

Figure 62: 2D model of explosive 78

Figure 63: 2D Detonated charge which is re-mapped into 3D model (a) and grading bias in the detonation model (b) 79

Figure 64: 3-D Model showing flow-out boundaries 80

Figure 65: Image showing the zero x-velocity boundaries replicating the clamp frame 81

Figure 66: Zero Y and Z velocity boundaries along edge of plate to simulate bolts 82

Figure 67: 3-D Model showing front and back air blocks and re-mapped explosive 84

Figure 68: Pressure-time histories of various charge masses 85

Figure 69: Final model used in numerical simulation of blast tests 89

Figure 70: Position of Gauges used in Pressure model to obtain pressure–time histories and impulse for a 16g detonation 90

Figure 71: Graph showing the difference between the pressure readings for rigid boundary (blue) and test plate (red) for a 9g charge mass at 25 SOD 91

Figure 72: Pressure-time histories of MS-C7 at different distances from mid-point showing significant points from Error! Reference source not found.-Error! Reference source not found. . 92

Figure 73: Plastic Strain Distribution and Pressure Contours from MS-C7 Numerical Model 93

Figure 74: Plastic Strain Distribution and Pressure Contours from MS-C7 Numerical Model (continued from Figure 73) 94

Figure 75: Plot of Mid-point Pressure-time and Displacement-time for MS-C7 95

Figure 76: Displacement-time histories of mild steel subjected to 9g, 16g and 20g charge masses 96

Figure 77: Ring at centre of plate showing signs of necking and capping on MS400-12, subjected to a blast load of 24g at 25sod 99

Figure 78: Cross-section of plate showing deformation profile and thinning on MS400-12, subjected to a blast load of 24g at 25sod 100

Figure 79: Photograph showing partial capping on MS400-15, subjected to a blast load of 33g at 38sod 100

Figure 80: Cross-section showing deformation profile of partially capped MS400-15, subjected to a blast load of 33g at 38sod 101

Figure 81: Photograph showing opposite cross-section deformation profile of MS400-15, subjected to a blast load of 33g at 38sod 101

Figure 82: Photograph showing ruptured MS400-11, blast loaded with 28g charge at 25sod 102

Figure 83: Failure surface of ruptured MS400-11 showing thinning and ductile fracture surface102

Figure 84: Cross-section photograph of MS400-11 showing deformation profile 102

Figure 85: Deformation profiles of 3mm Mild steel plates subjected to blasts at 25mm sod 103

Figure 86: Deformation profiles of 3mm Mild steel plats subjected to blasts at 38mm sod 104

Figure 87: Deformation profiles for 75mm diameter charge mass at 25mm sod 104

Figure 88: Graph showing displacement versus impulses for all MS400 Tests 105

Figure 89: Photograph showing a distinct melted region in the centre of AL-6 plate subjected to 33g charge at 38mm SOD..... 108

Figure 90: Photograph showing the melted region as well as a circular spray of melted material in AL-3 subjected to 28g charge at 38mm SOD..... 108

Figure 91: Diagram showing the burn and spray diameters measured from the AL plates 109

Figure 92: Graph showing spray and melt diameters of melted aluminium versus their respective impulses 110
Figure 93: Close-up of cross-section of AL-6 showing thinning and material loss due to melting 111
Figure 94: Photograph showing the front face fracture surface of AL-5 112
Figure 95: Photograph showing the back face of the fracture surface of AL-5 112
Figure 96: Cross-Section photograph of AL-5 showing fracture surfaces and displacement profiles 113
Figure 97: Close-up photograph showing brittle fracture surface and signs of melting 113
Figure 98: Close-up photograph of AL-5 showing mid-point fracture surface with pitting and melting visible 114
Figure 99: photograph showing 45 degree shear in the aluminium tensile specimens 114
Figure 100: Photograph of 45 degree shear surface of aluminium tensile test specimens..... 114
Figure 101:Cross-section of displacements arranged in descending order 115
Figure 102: Cross-section of plates subjected to blast load at 25mm stand-off distance 115
Figure 103: Cross-section of plates subjected to blast load at 38mm stand-off distance 116
Figure 104: Displacement versus Impulse for blast test on aluminium plates at 25mm and 38mm stand-off distances 117
Figure 105: Photograph of front face damage on TW-1 showing fibre fracture as well as delamination lines 119
Figure 106: Close-up photograph showing the damage on the front face of TW-1 119
Figure 107: Photograph of the front face damage sustained by TW-7 120
Figure 108: Photograph showing the back face of TW-6 where matrix cracking is visible as well as minimal fibre fracture 121
Figure 109: Photograph showing the small area of fibre fracture and matrix cracking on the back face of panel TW-1 121

Figure 110: Photograph of TW-3 showing more extensive back-face fibre fracture as the charge mass is increased 122

Figure 111: Photograph of TW-4 showing complete failure as a result of decreasing the stand-off distance 122

Figure 112: Displacement versus impulse for Twintex composite panels 123

Figure 113: Photograph showing front-face damage and pull-in of DYN-4 125

Figure 114: Photograph showing back-face deformation and Pull-in of DYN-4, subjected to a blast load of 53g at 50mm sod 126

Figure 115: Photograph showing close-up of front-face of DYN-4, with melting and destroyed layers clearly visible 126

Figure 116: Photograph showing area of damage on front-face of DYN-4 127

Figure 117: Photograph of DYN-5 subjected to blast load of 23g at 50mm sod, showing significantly less pull-in 127

Figure 118: Photograph showing front-face damage on DYN-5, subjected to blast load of 23g at 50mm sod 128

Figure 119: Graph of Displacement versus Impulse for Dyneema Panels 128

Figure 120: Photographs showing the cross-section profiles for three different charge mass configurations between mild steel(TOP) and Armox 370T (BOTTOM) 130

Figure 121: Displacement-time histories of mild steel and Armox 370T 131

Figure 122: Displacement-time histories of steel and Armox 370T 132

Figure 123: Displacement-time histories of steel and Armox 370T 132

Figure 124: Graph to show the measured and simulated disp-time histories for mild steel (16g charge, 50mm diameter, 25mm sod) 135

Figure 125: Graph to show the measured and simulated disp-time histories for mild steel (20g charge, 50mm diameter, 25mm sod) 135

Figure 126: Graph to show the measured and simulated disp-time histories for mild steel (33g charge, 50mm diameter, 25mm sod)..... 136

Figure 127: Graph to show the measured and simulated disp-time histories for mild steel (40g charge, 50mm diameter, 25mm sod)..... 136

Figure 128: Graph to show the measured and simulated disp-time histories for mild steel (50g charge, 50mm diameter, 38mm sod)..... 137

Figure 129: Graph to show the measured and simulated disp-time histories for Armox 370T (40g charge, 500m diameter, 25mm sod)..... 138

Figure 130: Graph to show the measured and simulated disp-time histories for Armox 370T (33g charge, 50mm diameter, 25mm sod)..... 139

Figure 131: Graph to show the measured and simulated disp-time histories for Armox 370T (50g charge, 50mm diameter, 38mm sod)..... 139

Figure 132: Plot of Maximum transient displacement of AUTODYN vs. Experimental Results 141

Figure 133: Plot of Permanent transient displacement of AUTODYN vs. Experimental Results .. 141

Figure 134: Plot of Impulse for AUTODYN vs. Experimental tests 142

Figure 135: Photographs showing the deformation profiles for three different charge mass configurations for Armox370T (TOP) and Armox 440T (BOTTOM)..... 143

Figure 136: Graph of displacement/thickness ratio versus impulse for Armox 370T and 440T... 144

Figure 137: Photograph showing deformation profiles for AL-1 (BOTTOM) vs. MS400-14(TOP) 146

Figure 138: Photograph showing deformation profiles for AL-2 (BOTTOM) vs. MS400-8(TOP) .. 146

Figure 139: Photograph showing deformation profiles for AL-3 (BOTTOM) vs. MS400-13(TOP) 147

Figure 140: Photograph showing deformation profiles for AL-4 (BOTTOM) vs. MS400-11(TOP) 147

Figure 141: Photograph showing deformation profiles for AL-6 (BOTTOM) vs. MS400-15(TOP) 147

Figure 142: Graph of Displacement versus Impulse for aluminium and Mild Steel 149

Figure 143: Plot of Impulse versus charge mass for all blast tests performed 152

Figure 144: Graph of Displacement/thickness Ratios versus Dimensionless Impulse for all Tests 155

Figure 146: Schematic of set-up used by Jacob showing the tube used [12] 157

Figure 147: Highly Simplified Illustration Showing Blast Propagation in a Tube 158

Figure 148: Displacement/Thickness ratio versus Dimensionless Impulse Plots with corrected 38mm stand-off..... 160

Figure 149: Graph of Displacement/thickness ratio versus Dimensionless impulse of highlighted section from Figure 147 161

Figure 150: Graph of Failure Thresholds for each Material plotted against % Elongation 163

Figure A. 1: Photograph of typical tensile test specimen..... 179

Figure A. 2: Engineering Stress-Strain curves at varying crosshead speeds for 4mm thick Mild Steel 180

Figure A. 3: Engineering Stress-Strain curves at varying crosshead speeds for 3mm thick Mild Steel 180

Figure A. 4: Engineering Stress-Strain curves at varying crosshead speeds for Aluminium 5083-H116 181

Figure A. 5: Engineering Stress-Strain curves at varying crosshead speeds for Armox 440T 181

Figure A. 6: Graph showing best fit between true stress strain and power law hardening curves for 4mm mild steel 183

Figure B. 1: Displacement-time history for 16g charge at 25mm sod 185

Figure B. 2: Displacement-time history for 20g charge at 25mm sod 186

Figure B. 3: Displacement-time history for 33g charge at 25mm sod 186

Figure B. 4: Explosive charge without leader showing point of detonation as red line..... 187

Figure B. 5: Pressure contours showing the difference between blast wave propagation at various times..... 188

Figure B. 6: Graph of Pressure-time histories of a 33g detonation with a 1g leader and without the leader 189

Figure C. 1: Schematic of ballistic pendulum showing required variables..... 191

List of Tables

Table 1: Summary of modes of failure for steel plates subjected to Uniform and Localised Loading [12] 20

Table 2: Failure Modes of Composite panels for uniform and localised loading [5] [44] 21

Table 3: Matrix of Test Parameters and Plate Dimensions 53

Table 4: Table of Material Properties 60

Table 5: Summary of Test Parameters and Results for Section 4 63

Table 6: Material properties used for air in the computational model 86

Table 7: Material Properties used for C4, from AUTODYN Material Library [59] 87

Table 8: A, B and n values obtained for materials used in computational models 88

Table 9: Table of blast testing parameters and results for 3mm thick mild steel 98

Table 10: Table of blast testing parameters and results for Al 5083-H116 aluminium 106

Table 11: Table of Burn Diameters and Spray Diameter of Aluminium Test Plates 110

Table 12: Table of blast testing parameters and results for Twintex composite panels 118

Table 13: Table of Results for Dyneema Blast Tests 124

Table 14: Table of test results for Armox 370T vs. Armox 440T listed in same order as photographs 145

Table 15: Table of test results for 3mm thick Mild Steel vs. Aluminium 150

Table 16: Table of Test Results with updated Dimensionless Impulse for 38mm SOD 162

1. INTRODUCTION

The ever-increasing threat of terrorism and the need for protection against explosions and explosive devices have resulted in research to understand the effects these explosives have on vehicles, aircraft, buildings and various structures. War has contributed greatly to the need for blast protection, especially for military personnel being transported in vehicles. Military vehicles transporting personnel through war-stricken areas are especially susceptible to landmine explosions or attacks from local militia armed with grenades and improvised explosive devices (IEDs).

Research has been performed into the development of protective measures for vehicles and structures against close-proximity blast loading in the past for example, the work performed by Nurick [1] and Jones and Baeder [2]. This research has been predominantly experimental in nature and concentrated on the post mortem effects of the blast on a structure. Work has mainly examined steels, although lightweight materials are also being explored. Computational modelling has also been performed, greatly improving numerical codes and computational capabilities in the field of blast loading definition and structural response to dynamic and impulsive loads.

In this current work, experiments were performed to investigate the response of plates comprised of various materials when subjected to free air blasts at close proximity. Armour steel, mild steel, aluminium alloy, glass-fibre reinforced polypropylene (GFPP) and ultra-high molecular weight polyethylene (UHMWPE) were investigated. Plastic explosive (PE4) was used to generate the blast loading on the test plates. Numerical simulations of the armour steel and mild steel

responses were performed using ANSYS AUTODYN, and validated against experimentally obtained results. Light interference equipment was also used to measure the transient displacement response of the materials during blast loading.

The objectives of this work were to:

1. Understand the influence material type on the structural response of clamped square plates to localised blast loading.
2. Determine the failure mechanism for each material subjected to blast loading.
3. Develop a transient response measurement system, to enable insight into the response of the blast loaded plates.
4. Use numerical simulations to further insight into the differences in response of the armour steel and mild steel plates.
5. Draw conclusions and recommendations based on the outcome of the results.

This dissertation is based on information from experiments undertaken at the Blast Impact and Survivability Research Unit (BISRU), University of Cape Town.

Chapter 2 reports on the results of the literature review, which covers blast loading and the response of structures to blast loading. The experimental procedures as well as the material properties of the various materials used in the experiments are described in Chapter 3.

The results of the 500mm armour steel and mild steel square plates are presented in Chapter 4 followed by the results of the numerical simulations of their responses in Chapter 5. The results of the 400mm square plates of various materials are presented in Chapter 6 followed by a discussion of all of the results in Chapter 7.

Conclusions are drawn in Chapter 8 and recommendations based on the findings are made in Chapter 9.

2. LITERATURE REVIEW

2.1. Detonation of Explosives

An explosive is a substance which goes through a rapid chemical reaction, usually in the form of a detonation, whereby a large amount of energy is produced (in the form of gases and heat). During an explosion, a pressure wave is generated by the rapid release of energy caused by the detonation of the explosive material [3]. The rapid energy accumulation is dissipated in the form of a blast wave.

The magnitude of the blast wave may be quantified as an impulse, which is represented by the area underneath the pressure-time history of the blast wave. A typical pressure-time history from a far-field explosion is shown in Figure 1. The pressure rises sharply from ambient pressure (P_a) immediately as the blast wave impinges until it reaches the maximum positive pressure P_a+P, known as the overpressure. The pressure then decays until it is slightly below ambient pressure, known as the under-pressure, before returning to ambient (Baker [3]).

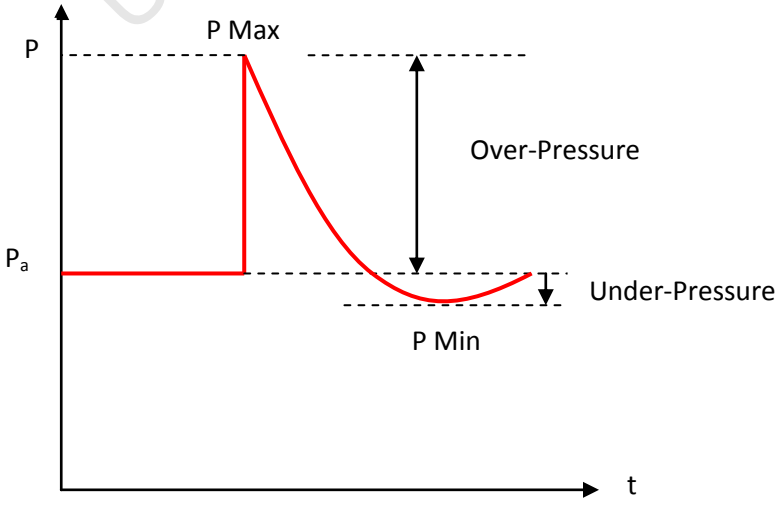

Figure 1: Typical Pressure-time history of a Blast Wave resulting from a far-field explosion

The impulse imparted by the pressure wave can be calculated as follows:

$$I = A_i \times \int P(t) d\,t \qquad \text{(eq. 1)}$$

Where A_i is the initial area over which the impulsive load is acting, P(t) = t is the time (running variable).

2.2. Blast Loading Conditions

The blast loading in the current work was generated from the detonation of the plastic explosive, PE 4, which is composed of Lithium grease and RDX with a ratio of 12 percent to 88 percent respectively. PE4 has a density of 1.6 g/cm^3 and a detonation velocity of 8200m/s, which is similar to that of C4: a plastic explosive which is commonly used by military and terrorist forces all over the world [4]. Weckert and Anderson [4] compared TNT and PE4 using plate tests for plate deformations and peak overpressures and reported that 1kg of PE4 was equivalent to 1.37kg of TNT. However, a mass range of 1.09 - 1.21kg, was required to match the plate accelerations equivalent to 1kg of PE4 [4].

One advantage of using PE4 is that it is stable and can only be detonated by an extreme shock such as one provided by a detonator pin. Another advantage is that plastic explosives can be shaped into various different geometrical shapes depending on the desired loading condition, such as concentric annuli for uniform loading or circular discs for localized loading.

The impulse during a blast test is controlled by the mass of the explosive used. There have been many studies in the past where a disc-shaped charge mass were used [5-9]. Kennedy [5] investigated the impulse imparted to metal through the detonation of an explosive charge disc. Kennedy [5] showed that, for a given charge diameter, there exists a charge mass above which a further increase in charge mass will not significantly increase the impulse generated by the

explosion. The shaded area of the triangle in Figure 2 describes the charge mass contributes significantly to the impulse in the blast test, with the effective charge height defined as:

$$h_{eff} = \frac{d_c}{2} \tan 60^0$$

Where d_c – charge diameter, h_c – height of triangle

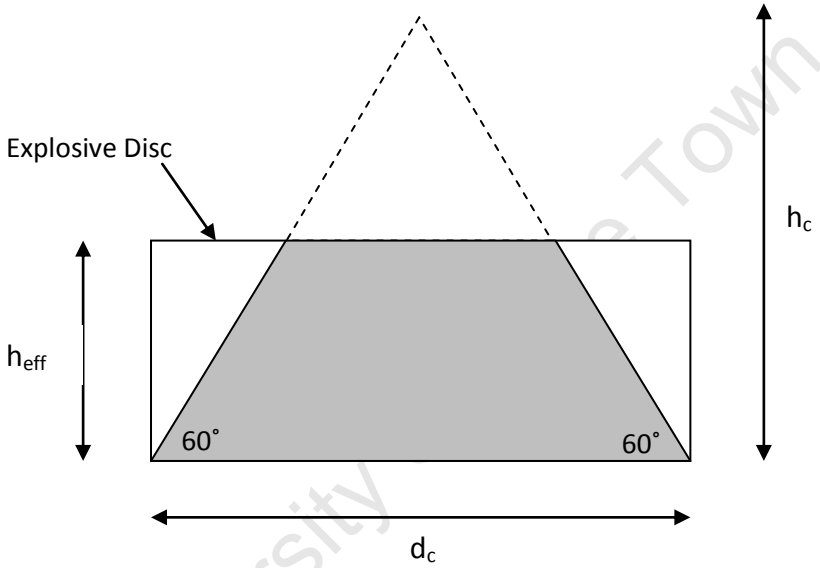

Figure 2: Diagram showing Effective charge height

2.2.1 Uniform Loading

Two methods have been employed by Nurick and co-workers [6], [7] to generate near-uniform blast loading conditions. In order to achieve uniform impulsive loading over the entire exposed area of the target plate the plastic explosive must be moulded into concentric annuli which correspond to the shape of the plate. An example of this is shown for a square plate in Figure 3. Using concentric annuli ensures that the minimum thickness of 2mm needed for the explosive to detonate is achieved, as stated by Nurick and Martin [6]. Another way to achieve uniform loading is to increase the distance between the explosive and the plate (SOD). Jacob *et al* [8] made use of

a tube test rig in order to create the required distance between the explosive and test plate, as shown in Figure 4. Langdon *et al* [9] used a similar method for square plates.

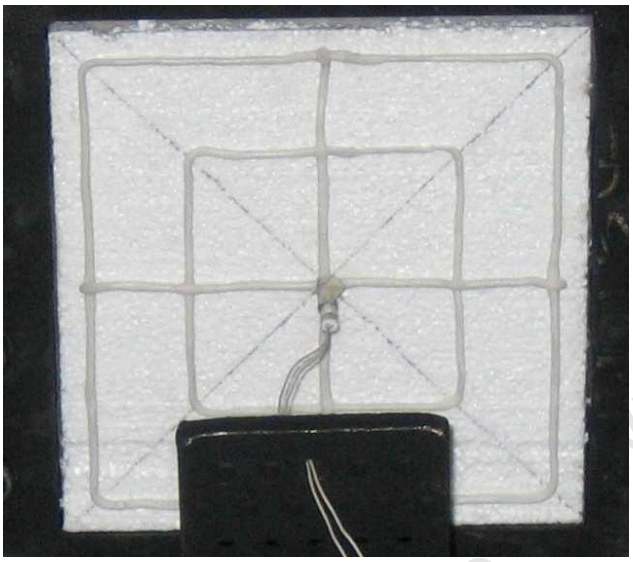

Figure 3: Concentric Annuli used on a Square Test Plate [10]

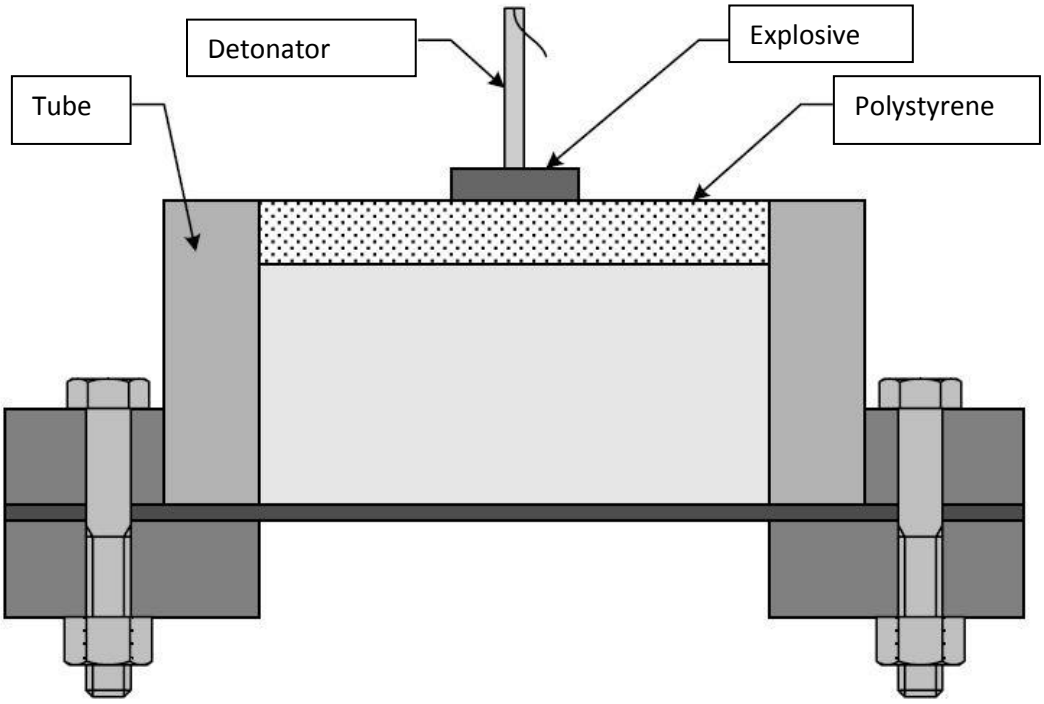

Figure 4: Cross-section schematic of tube arrangement used by Jacob [7] for uniform loading

Marchand and Alfawakhiri [11] proposed a method for determining the loading condition for a disc-shaped charge at a distance *S* from a plate of dimension *D*. The method shown schematically

in Figure 5 states that for charge stand-off distances which are less than half the large plate dimension *D*, the loading is classified as localised.

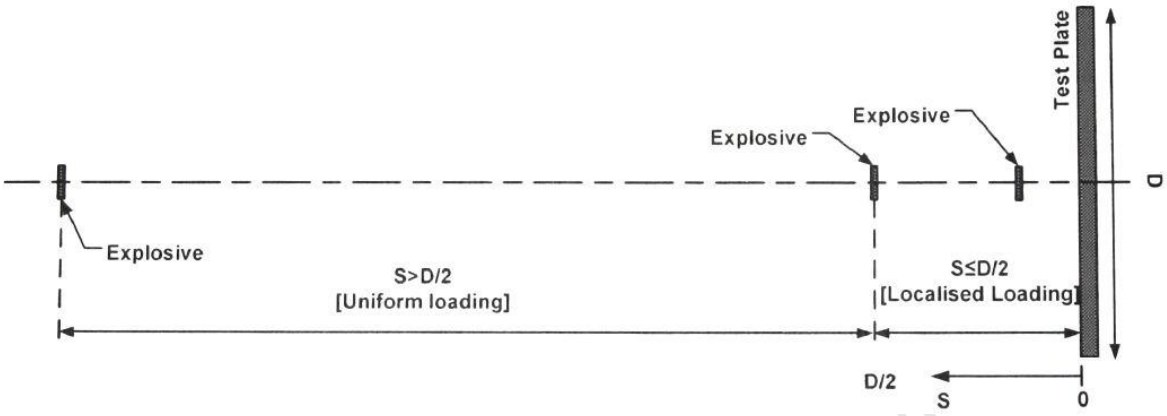

Figure 5: Schematic of method proposed by Marchand and Alfawakhiri [11] for determining blast loading conditions

2.2.2 Localised Loading

Localised impulsive loading of a plate is achieved by decreasing the stand-off distance to less than half the maximum planar dimensions of the plate [12], [13]. Typically, the plastic explosive is moulded into a disk of specific diameter while varying the charge height to acquire different charge masses. The disc is usually attached to a polystyrene pad to position the explosive. Ozinsky [14] used a polystyrene 'bridge' to remove the polystyrene between the explosive and the plate, as well as creating the desired stand-off distance between the plate and explosive. When the explosive was detonated, it acts over a small central area of the plate rather than over the entire plate [14]. Alternatively, the explosive disk was placed onto a polystyrene panel which would be in direct contact with the test plate as reported by Nurick *et al* [1], [12], [13], [15].

2.3. Material Properties

Mild steel has been widely tested; its material properties are well understood and serve as a good benchmark for comparing other materials. Mild steel has been used at the Blast Impact and Survivability Research Unit in many studies and its properties are well characterized [7], [16], [17]. Typically, the mild steel sourced locally is a low-carbon steel (0.05 – 0.15% carbon) and has high ductility.

The armour steel types tested in the current work are Armox 370T and Armox 440T. Armox 370T and 440T are classified as grain –refined medium carbon steel (with 0.32% and 0.21% carbon respectively) [18]. Both materials contain high levels of Manganese (1.2%), Chromium (1%) and Nickel (1.8-2.5%) which give the material its high Brinell hardness values (380-480) compared to mild steel (100-130) [18]. Armox 370T is a traditional Rolled Homogenous Armour (RHA) steel and used in vehicle protection for bullets and blasts [18]. Armox 440T is a more recent development and intended to be particularly effect against blasts [18].

Aluminium alloys are metals in which the predominant metal, aluminium, has been alloyed with other elements. Typical alloying elements are copper, chromium, magnesium, manganese, silicon and zinc [19], [20]. Aluminium alloys have good corrosion resistance compared to steel. Aluminium alloys are divided into seven major classes designated according to their principle alloying elements. The AL 5083-H116 class aluminium chosen for the current work has an aluminium composition of 92-96% and is alloyed with Chromium, Copper, Magnesium, Manganese, Silicon, Titanium and Zinc with the major alloy being Magnesium (4 - 4.9%) [19]. AL 5083-H116 was chosen because it is among the strongest aluminium alloys available. The AL 5083-H116 alloy is predominantly used in naval structures as ballistic protection [21], which makes it an ideal candidate for blast testing.

Composites are a combination of two individual materials which results in a material with superior properties than that of each material individually. They consist of a reinforcement held in a matrix to carry the load and improve strength and stiffness. Glass Fibre Reinforced Polymers (GFRP) are composite materials comprising a woven glass fabric held in some form of polymeric resin matrix to form a structure. One type of GFRP is Glass-Fibre Reinforced Polypropylene (GFPP), known as Twintex. [22]. Twintex comes in a variety of forms, including twill weave cloth. The Twintex, prior to consolidation, comprises co-mingled glass fibre and polypropylene strands. The cloths are stacked in a mould and heated to cause the polypropylene to flow. Subsequently, the Twintex is cooled, the polypropylene solidifies to produce a laminated Twintex panel. Consolidated Twintex panels have similar tensile strengths to mild steel (350MPa) but with a higher stiffness to weight ratio [23].

Ultra-High Molecular Weight Polyethylene (UHMWPE) is a woven synthetic fibre. The fibres are aligned and bonded into sheets, which are combined to form panels of various geometries [24]. An example of such a composite is Dyneema, a gel spun synthetic fibre composite which has high toughness and impact strength [25]. Dyneema is finding applications in personnel and vehicle protection due to its good ballistic properties [24]. Typically, Dyneema has a tensile strength of up to 3000 MPa [26].

2.4. Blast Loading of Metals

Early studies on the blast response of plates focused on underwater explosive loading [28-30]. Taylor [27] tested large steel plates (1.83 x 1.22m) and measured the volume of water displaced. Studies on effect of underwater explosive forming on fully clamped circular discs of various thicknesses and materials were performed by Johnson *et al* [28] and Travis *et al* [29]. In these experiments only the permanent displacement of the plate was measured.

Witmer [30], Humphreys [31] and Jones *et al* [2], [32] reported the results of experiments where the loading generated by the detonation of spherical charges, creates pressure waves. The air-blast loading caused permanent deformations of up to 16 plate thicknesses [30]. A ballistic pendulum is often used to determine the impulse applied to the rigidly clamped test specimen [6], [31], for example Jones *et al* [32] tested fully clamped rectangular plates where the impulse was measured using a ballistic pendulum. Jones and Baeder [2] performed further experiments on fully clamped plates of varying length and breadth ratios. Only the final plate deflections were reported [2], [32].

2.4.1. Steel Plates

Nurick and co-workers [1], [13], [15], [6], [33], [34] investigated the large deformations of thin steel plates subjected to blast loading and reported a linear relationship between the impulse measured and the mass of the explosive used. Nurick and Martin [33] proposed an empirical equation to predict the damage on the plate with good correlation. The dimensionless analysis used by Nurick and Martin [33] was able to compare quantitatively compare specimens tested under different loading conditions by correcting for differences in geometry, thickness, yield and material density. Nurick *et al* [35] investigated the tearing and shearing failure modes (Modes II and III respectively) for clamped and fully built-in square plates. Nurick *et al* [34], [35] further

investigated the tearing mechanisms of thin square plates .The clamping or fixing conditions at the boundary of the plate affected the tearing mechanisms [35]. Sharp edge clamped conditions casued premature failure of the clamped boundary edges [35]. Bonorchis and Nurick [15] later performed experimental and numerical investigations on the influence of boundary conditions on the loading of rectangular plates subjected to localised blast loading and found that the geometry of the clamp affected the amount of impulse recorded, meaning that all of the impulse recorded by the pendulum was not necessarily causing plate deformation.

2.4.2. Armour Steel

There is little available literature on the blast loading of armour steel, with the exception of work done by Neuberger *et al* [36] investigating the springback effect of clamped circular armour steel plates subjected to spherical air-blasts, both experimentally and numerically using LS-DYNA. Neuberger *et al* [36] tested RHA steel plates of 1m in diameter with thicknesses varying from 10mm to 25mm, subjected to charge masses of up to 15kg of TNT at different stand-off distances. The experimental setup used by Neuberger *et al* [36] is shown in Figure 6.

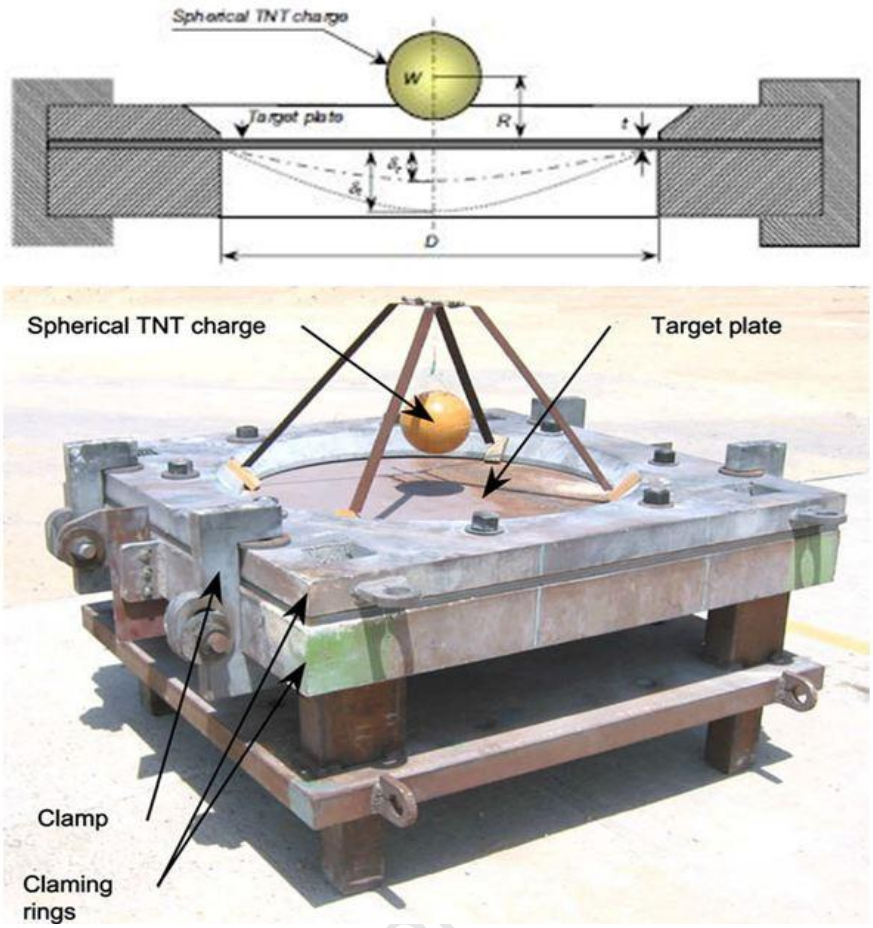

Figure 6: Schematic and photograph of experimental setup used by Neuberger *et al* [36]

Neuberger *et al* [36] found that the relationship between the transient and residual non-dimensional deflections as function of the non-dimensional stand-off distance exhibits a point of inflexion, where the critical point separates the stand-off distance into two characteristic categories; namely before the inflexion point where the increase in deflection with decreasing stand-off distance has a positive gradient, and past the point of inflexion where the increase in deflection with a decrease in stand-off distance increases with a negative gradient. When the stand-off distance is larger than the critical inflexion point, the response of the plate deflection shows a reduced sensitivity to the stand-off distance, while for closer stand-offs the response is more sensitive to distance from the charge. Figure 8 shows the numerical model for an 8.75kg TNT charge detonated at 0.2m from the plate at a time of 1.3 ms and the corresponding displacement-time history.

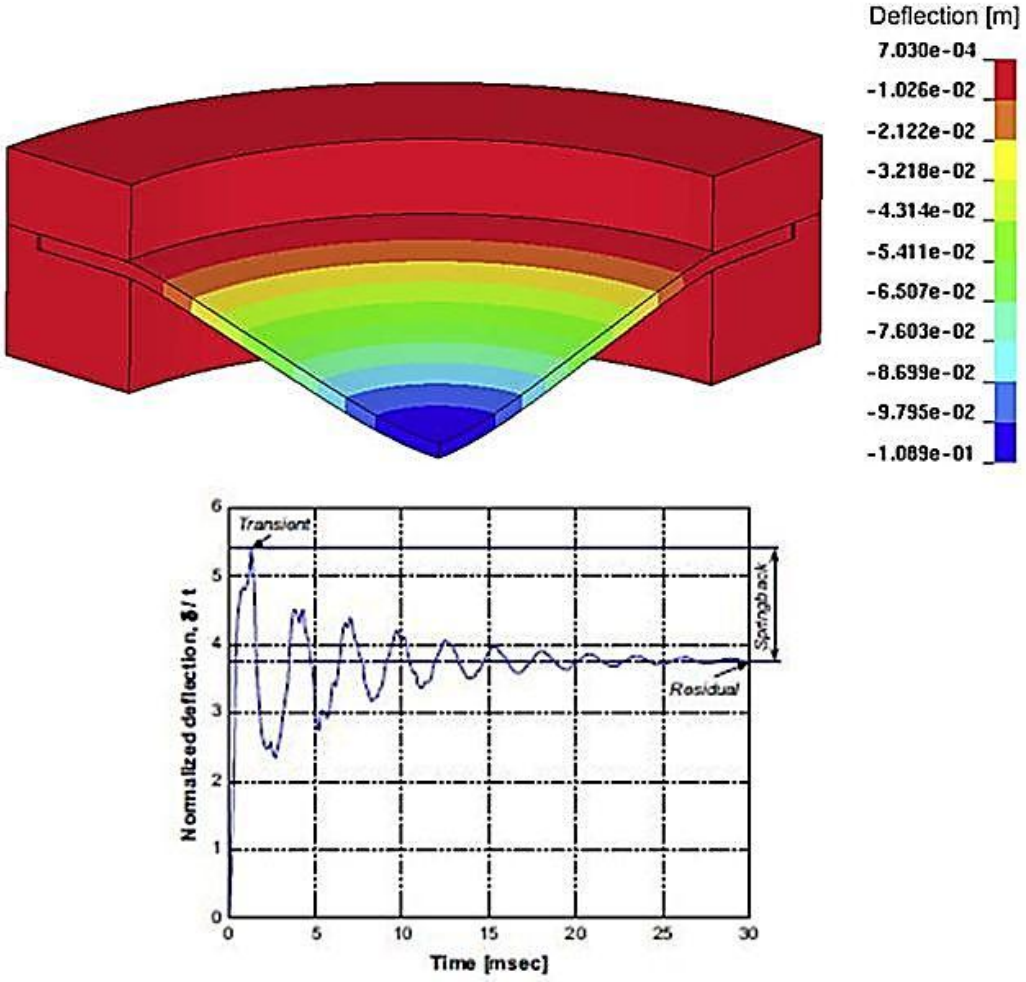

Figure 7: Numerical model used by Neuberger *et al* and the transient response obtained numerically [36]

2.4.3. Blast Loading of Aluminium

Veldman *et al* [37] investigated the effects of pre-pressurisation on the blast response of clamped aluminium plates experimentally and numerically. The purpose of the investigation was to determine the effect that a pressurised aircraft cabin would have on aluminium when subjected to blast loading. Veldman *et al* used a static pre-pressurisation in the range of 0-62.1 KPa to represent in-flight loads experienced by the outer skin of an aircraft applied by a vacuum seal shown in Figure 8 and Figure 9. Finite element analysis was performed to obtain numerical predictions of the dynamic plate response. Veldman *et al* concluded that for the case of clamped

aluminium plates subjected to blast loads, there was no significant increase in plate deflection or damage as static pressure increased from 0 to 62.1 KPa.

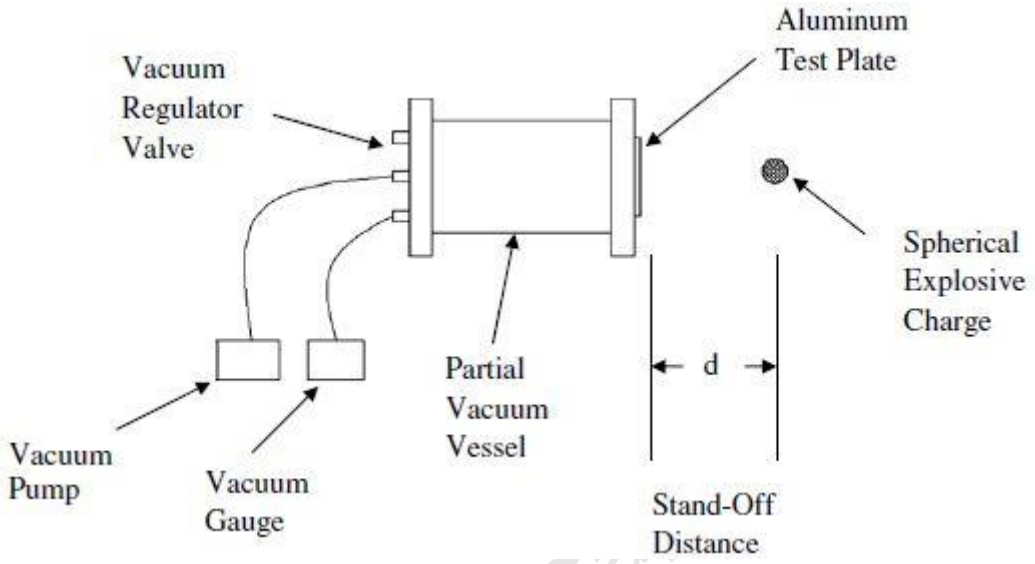

Figure 8: Schematic of experimental setup used by Veldman *et al* [37]

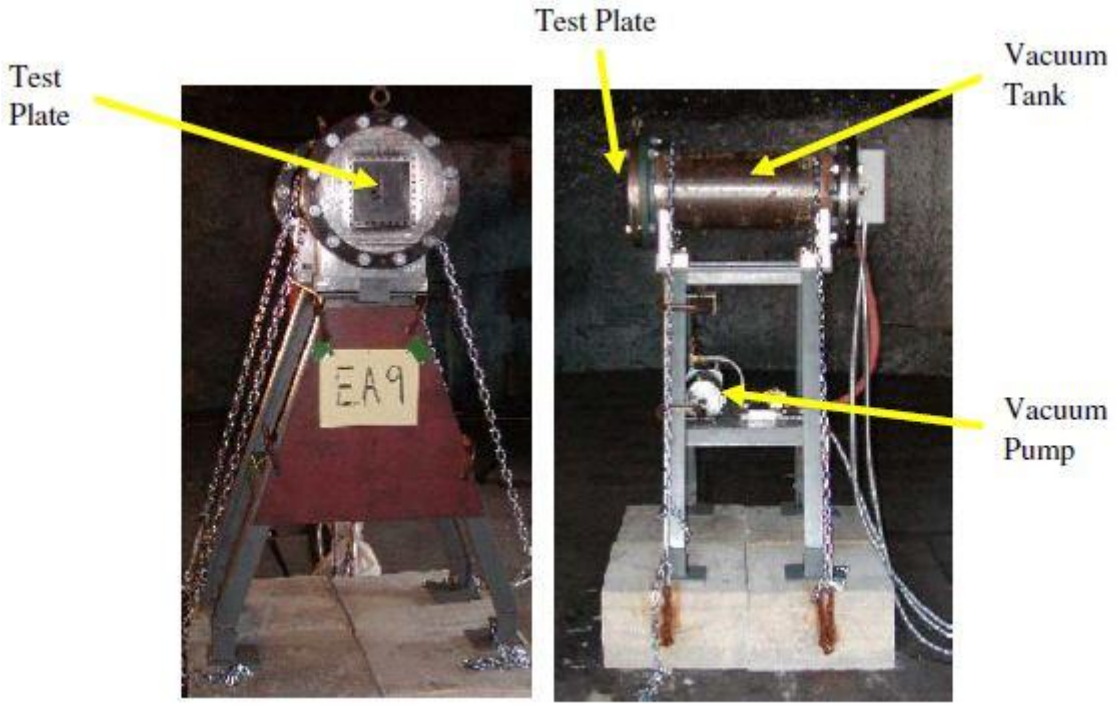

Figure 9: Photograph of Experimental rig used by Veldman *et al* [37]

2.5. Composite Panels

Blast testing of E-glass vinyl fibre composites manufactured using the Vacuum Assisted Resin Transfer Moulding (VARTM) process was performed by Tekalur *et al* [38]. It was observed that the composite panels exhibited continuous damage progression and various failure modes such as permanent deformation, fibre breakage and delamination [38].

Batra and Hassan [39] investigated the blast response of uni-directional fibre reinforced composites through a finite element method and reported that the fibre orientation influences the failure modes and direction of propagation. Batra and Hassan [39] also found that the matrix cracking damage which occurs during blast loading initiates at the center of the back surface where the highest tensile stresses developed and propagates faster along the fibres than in the transverse direction. The delaminated area and matrix cracking damage exhibited by the composite panel is shown in Figure 10.

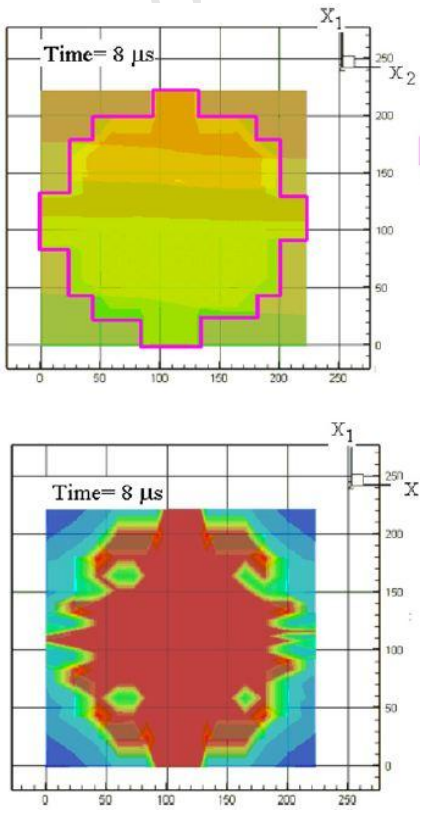

Figure 10: Computational model showing delaminated area (top) and matrix cracking damage (bottom) [39]

Cantwell *et al* [40] investigated the blast resistance of carbon-fibre reinforced epoxy (CFRE) panels subjected to blast loading. The ballistic pendulum at the Blast Impact and Survivability Research Unit (BISRU) with a 90mm diameter blast tube, shown in Figure 11, was used to measure impulse. Square panels of 150mm side length with 8, 18 and 32 plies were compression moulded with nominal thicknesses of 2.2, 4.5 and 8.4 mm respectively [40]. Cantwell *et al* [40] reported a number of various failure mechanisms including delamination, top surface fibre buckling, fibre fracture and shear failure along the edges of the panels. It was also found that the impulses associated with the onset of fibre fracture until complete failure increased linearly [40].

Similar fibre fracture modes were observed by Langdon and Rowe [41] for blast tests performed on glass-fibre reinforced polypropylene (GFPP) composite panels.

A summary of the failure modes for composites discussed in this section are presented in Section 2.6.3.

Figure 11: Photograph of BISRU ballistic pendulum with blast tube used by Cantwell *et al* [40]

2.6. Failure Modes

2.6.1. Failure Modes of Metals

Menkes and Opat [42] were the first to classify the various failure modes of structures subjected to impulsive loading. They distinguished three modes of failure for a blast loaded clamped beams namely: *Mode I* – Large inelastic deformation; *Mode II* – Large inelastic deformation with tensile tearing at the boundary; and *Mode III* – Transverse shear failure. The latter two modes resulted in the beam rupturing at the clamped boundaries. Figure 12 shows the failure modes defined by Menkes and Opat [42].

Nurick *et al* [13] and Nurick and Shave [34] defined similar modes of failure for fully clamped circular plates and fully clamped square plates respectively. *Mode II* failure was divided further into three more phases: *Mode II** - Partial tearing; *Mode IIa* - Complete tearing with increasing mid-point deformation; and *Mode IIb* – Complete tearing with decreasing mid-point deformation [34].

Jacob *et al* [8] further elaborated on the various modes of failure by including several previously undefined intermediate failure modes. A summary of the classifications of the failure modes used by Jacob *et al* [8] is shown in Table 1.

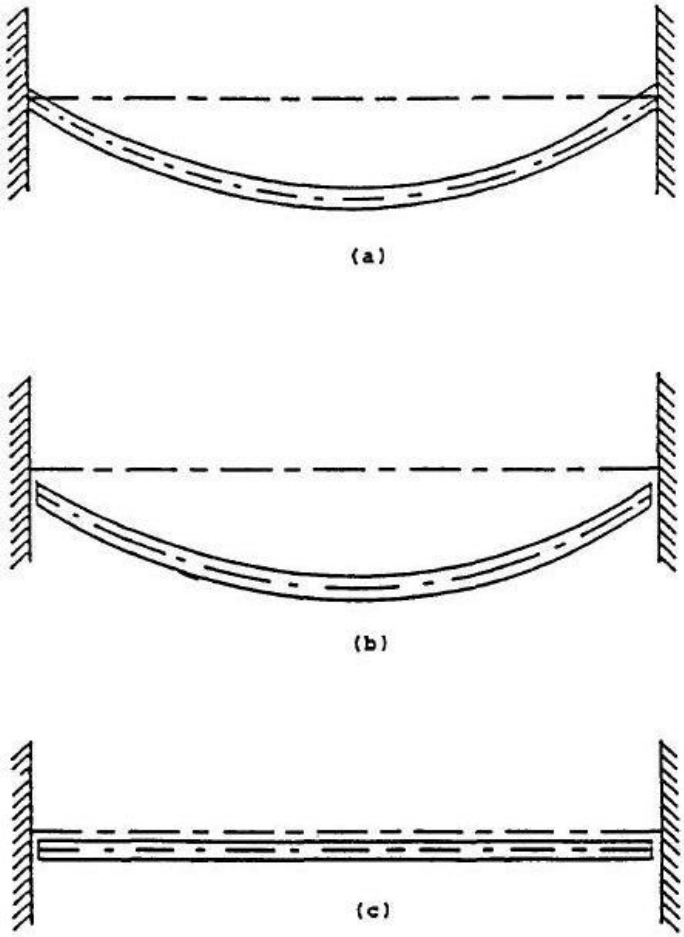

Figure 12: Failure modes as defined by Menkes and Opat [42]: (a) *Mode I* – Large inelastic deformations; (b) *Mode II* – Tensile Tearing at supports; (c) *Mode III* – Shear failure at supports.

2.6.2. Comparison of Failure Modes between Square and Circular Plates

Nurick and Shave [34] demonstrated that for plates of different geometry but equal thickness and area with similar impulses, similar mid-point deflections were obtained for *Mode I* failure. In cases where the onset of tearing has occurred, circular plates exhibit *Mode IIb* failure whereas square plates exhibit *Mode IIa* failure mode. Nurick and Shave [34] also observed that for *Mode III* failure modes, even though the masses of the square and circular discs are similar, their velocities differ due to their different geometries.

Table 1: Summary of modes of failure for steel plates subjected to Uniform and Localised Loading [7]

Modes of Failure	Description	Localised Loading	Uniform Loading
Mode I	Large inelastic deformation	X	X
Mode Ia	Large inelastic deformation and partial necking in boundary region		X
Mode Ib	Large inelastic deformation and necking in entire boundary region	X	X
Mode Itc	Large inelastic deformation and thinning in central region	X	
Mode II*	Large inelastic deformation and partial tearing in boundary region		X
Mode II*c	Large inelastic deformation and partial tearing in central region	X	
Mode II	Tensile tearing in boundary region	X	X
Mode IIa	Increasing mid-point deflection with increasing impulse with complete tearing at the boundary		X
Mode IIb	Decreasing mid-point deflection with increasing impulse with complete tearing at the boundary		X
Mode IIIc	Complete tearing in the central area due to capping	X	
Mode III	Transverse shear failure at boundary		X
Mode IIIp	Complete tearing in central area due to petalling	X	

2.6.3. Failure Modes of Composites

Failure modes for fibre metal laminates includes those observed for steel plates have been made by Langdon *et al* [12] for locally blast loaded FML panels, where *Mode I* and *Mode II* failure were observed. Due to the different material composition and properties of FML panels compared to steel plates, Langdon *et al* [43] observed the following modes of failure for composites: large inelastic deformation of the back face of the panel, tearing of the back face of the panel and the transition between the two modes. Based on the failure modes for composite panels reported by Langdon *et al* [43], Tekalur *et al* [38], Batra and Hassan [39] and Cantwell *et al* [40] in Section 2.5 , the following failure modes have been defined for composite panels: large inelastic deformation, matrix failure, front face fibre rupture, back face fibre rupture, delamination of composite layers and complete fibre rupture. The failure modes for composites are listed in Table 2.

Table 2: Failure Modes of Composite panels for uniform and localised loading [12] [43]

Description of Modes of Failure	Localised Loading	Uniform Loading
Large inelastic deformation of back face of panel	X	X
Matrix Failure	X	X
Delamination	X	X
Front Face Fibre Rupture	X	X
Back Face Fibre Rupture	X	X
Complete Fibre Rupture	X	X

2.6.4. The Effect of Boundary Conditions

For most experiments on the large inelastic deformation response of thin metal plates subjected to blast loads, measurements and predictions have only considered simply supported, fully built-in or fully clamped plates at the boundary [15], [35].

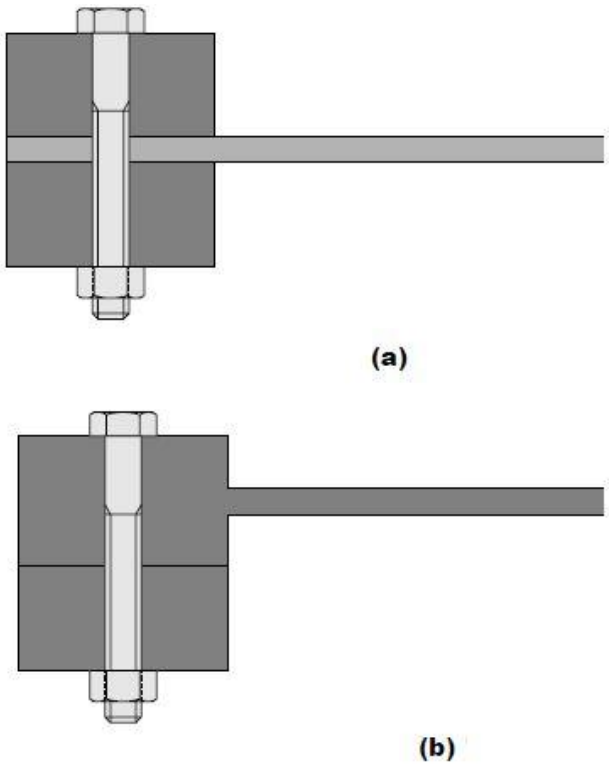

Figure 13: Schematic of fully clamped (a) and built-in plates (b) as described by Jacob *et al* [7]

Thomas and Nurick [44] have reported that the large inelastic mid-point deformation response was similar for fully clamped and built-in plates. However, according to Nurick *et al* [35], the boundary conditions are critical in the assessment of the tearing mechanisms which occur when a blast load is large enough to cause partial or complete tearing along the plate boundaries. Nurick *et al* [35] also reported that thinning and rupture were influenced by the boundary conditions, and the radius of the clamped edge in particular. Sharp edged clamps, shown in Figure 14(a) produced tearing failures at lower impulses than plates clamped with a fillet.

For sharp edged boundary conditions, shown in Figure 14, necking initially takes the form of a sharp indentation due to the sharp edge of the clamp, thereafter stretching and thinning occurs [35]. Curved edge boundaries displayed stretching and thinning conditions that resembled those in a uniaxial tensile test. Impulses for the different modes of failure increased linearly with an increasing clamp/fillet radius [35]. The results showed that, for example, for a 3,2mm radius boundary, a 15% increase in impulse and a 25% increase in mid-point deflection were required before tearing occurred (when compared to sharp edged boundary conditions).

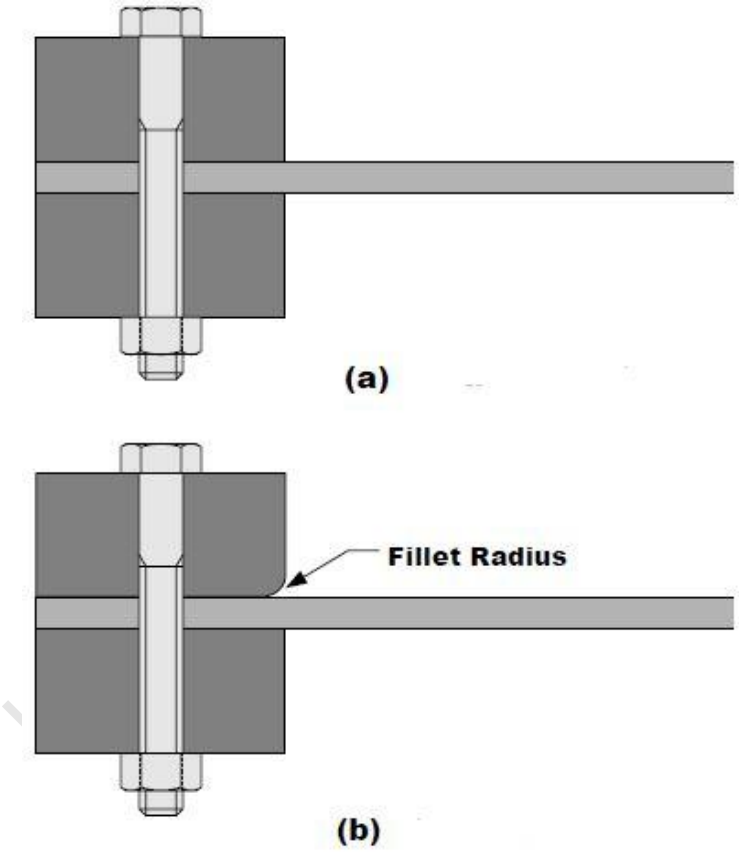

Figure 14: Schematic of sharp edge boundary (a) and curved edge boundary (b) [7]

2.7. Transient Measurements during Blast Loading

It is considered desirable to capture the dynamic response of blast loaded structures. One such measurement would be the transient deflection-time history of the structure at a point of interest, such as the mid-point of a plate. Other transient measurements could include pressure measurements, although the intensity of the explosive event makes pressure measurement difficult to perform and analyse afterwards.

2.7.1. Displacement-time Measurements Using Light Interference Method

Measurement of the dynamic response of a structure as it is deforming under a blast load can be obtained by recording the deflection-time history of the structure. Nurick [45], [46] repeated experiments including the impulse and deflection–time history measurements using a ballistic pendulum and photo-voltaic diodes respectively. The Light Interference Equipment (LIE) used by Nurick [45] - [46] comprised a light sensitive cell, silicon photo voltaic diodes, which produced an electrical output dependant on the light intensity over the area of the cell supplied by a 24 V dc light bulb. The light from the source was deflected by a 45˚ prism across the back surface of the test plate onto the diodes. Any movement of the plate interferes with the light ray which causes a voltage change on the photovoltaic diodes which was remotely recorded by a digital storage oscilloscope. The schematic of the LIE used by Nurick [45], [46], is shown in Figure 15.

According to Nurick [47] the specifications for the design of the LIE require that it should have the ability to:

i. Record the deflection of a localised region of the plate as opposed to the average deflection over a larger area
ii. Record deflections up to 20 mm
iii. Record the peak deflections, occurring some 100-200μs after detonation, and the final deflections after a few milliseconds.
iv. Operate on a ballistic pendulum behind the specimen.

It was further reported by Nurick [45] of the usefulness, reliability and cost-effectiveness of using LIE as compared to other forms of measurements such as a laser light configuration.

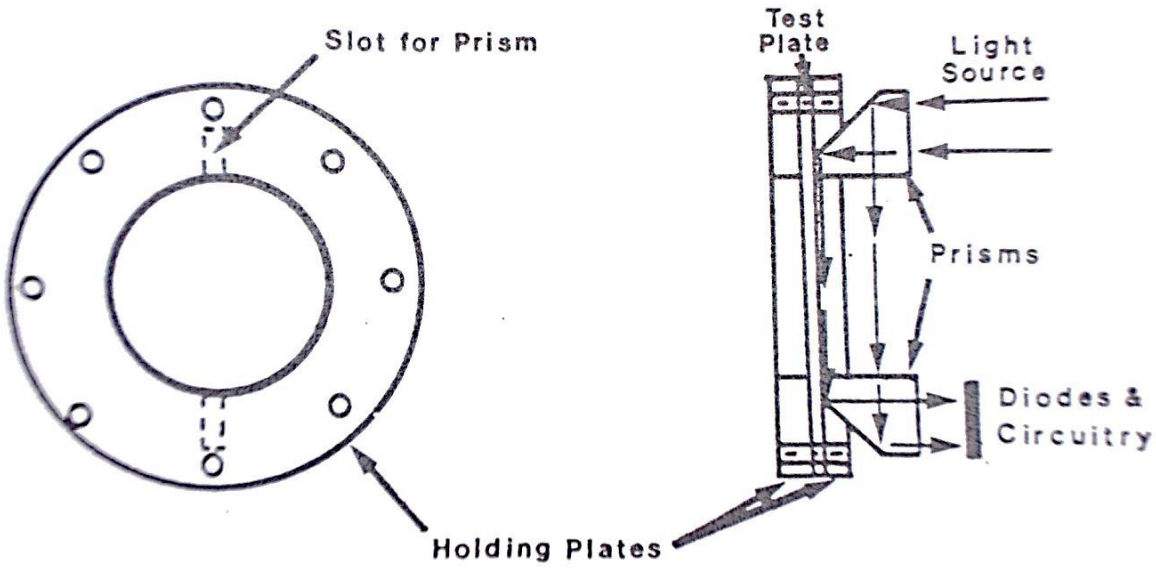

Figure 15: Schematic Layout of LIE test rig used by Nurick [45], [46]

More recently Geretto [48] used light interference equipment to measure the deflection-time histories of various blast loaded plates. Geretto [48] made use of Infrared LED diode emitters and UV Photodiode receivers mounted on specially designed aluminium frames and mounted onto the back face of the test plate. Tests involving confined and unconfined blasts were performed on clamped square plates. Typical displacement-time histories recorded by Geretto [48] are shown in Figure 16.

The un-deformed plate did not impede any of the light emitted by the emitter and the receiver outputs a certain voltage. During the blast, as the surface of the deforming plate interrupted the signal between the receivers and emitters, a voltage drop occurred and was recorded. The equipment was calibrated beforehand using plates of known displacements in order to correlate the voltage drop to the plate deflection.

The electronic circuit, the emitters and receivers were designed to accommodate for a maximum deflection of 40 mm and recorded displacement measurements for time periods of between 5 and 50 ms. The distance between the LEDs and photodiode arrangement used by Geretto [48] was 282mm for a 200mm x 200mm exposed plate area.

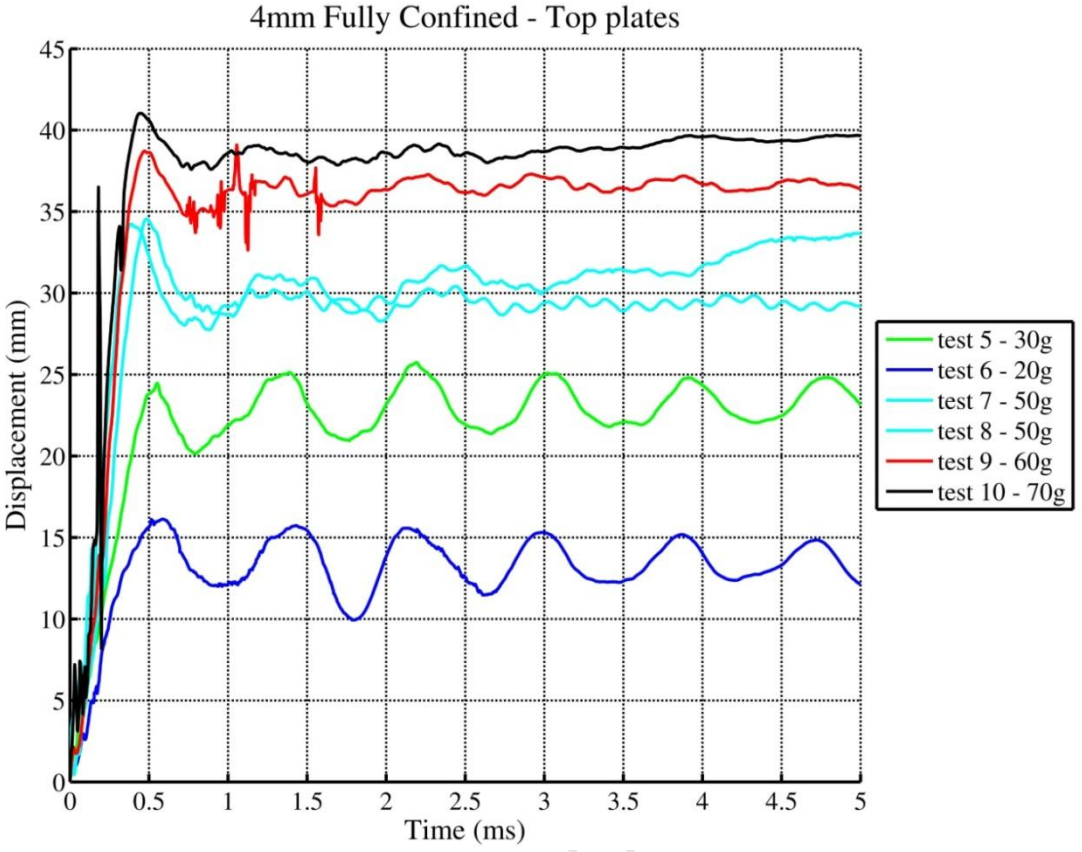

(a)

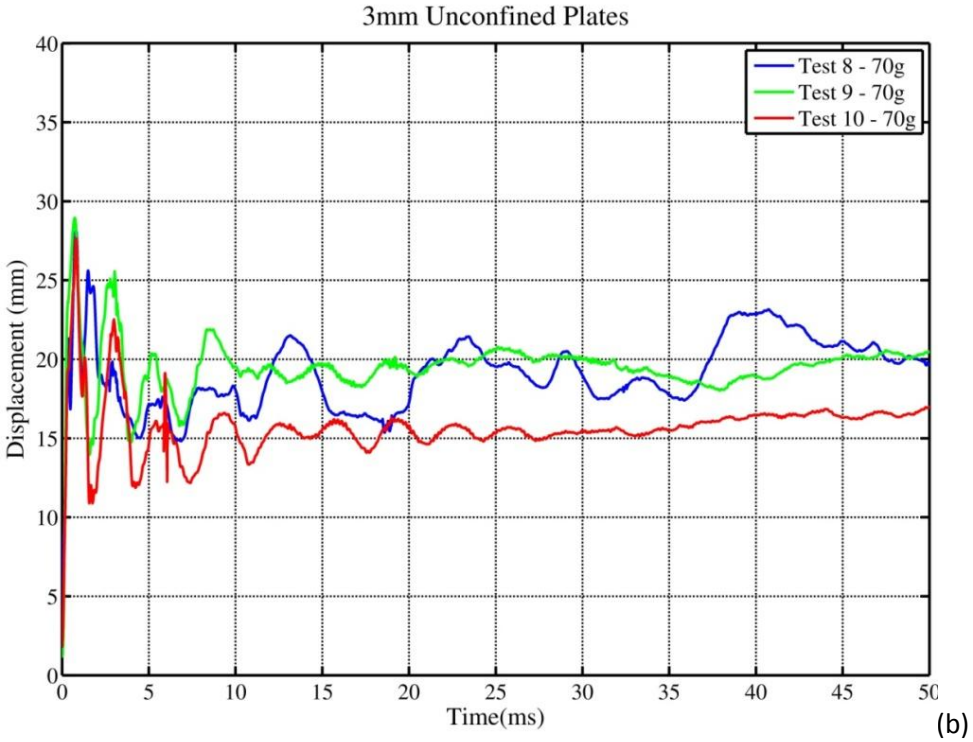

(b)

Figure 16: Displacement-time graphs of (a) Fully confined and (b) Unconfined Plates [48].

2.7.2. Displacement-time Measurement using Digital Image Correlation

Digital Image Correlation (DIC) is an optical method used for displacement and strain measurement often employing single or multiple high speed cameras to capture and correlate images of objects during deformation. Usually, a surface speckle pattern is required as information carriers which also cross correlates images taken from the various cameras before during and after deformation in order to obtain whole field displacements of objects. Transient displacements are obtained during post-processing of the images.

2.7.2.1. DIC Using Stereo Vision System

Tiwari *et al* [49] made use of a high speed stereo vision system consisting of an arrangement of two high speed cameras which used 3D image correlation to obtain synchronized, patterned stereo vision images and deformation measurements of plates subjected to buried charges. Figure 17 shows the experimental arrangement of the high speed cameras used by Tiwari *et al* [49]. The stand-off distance used by Tiwari *et al* [49] was 28.7mm at a depth of burial of 7.6mm and 25.4mm. since the explosion were buried in sand, the problem of saturating the camera sensors during the light flash that occurs during the detonation of explosives is avoided.

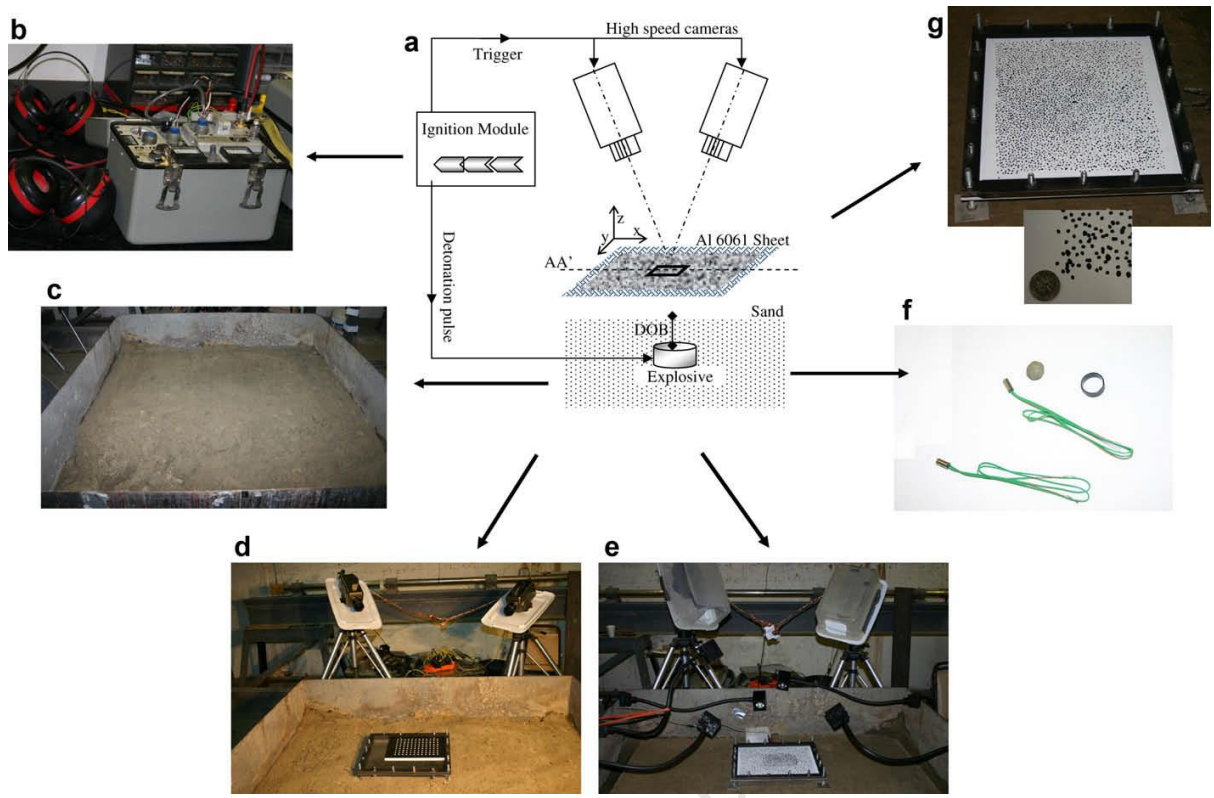

Figure 17: Schematic Diagram and Photos of the experimental setup used by Tiwari *et al* [49]

2.7.2.2 DIC Using Single Camera System

Traditionally, single camera systems are used only for in-plane displacement and strain measurements. Tay *et al* [50] developed a system to measure whole field out of plane displacements using only a single camera. Tay *et al* [50] used digital image correlation to determine the out-of plane displacement due to the change in magnification of the in-plane displacement as shown in Figure 18. Experiments were accurately performed on plates, cantilevers and surfaces with height variations, although only at low speeds.

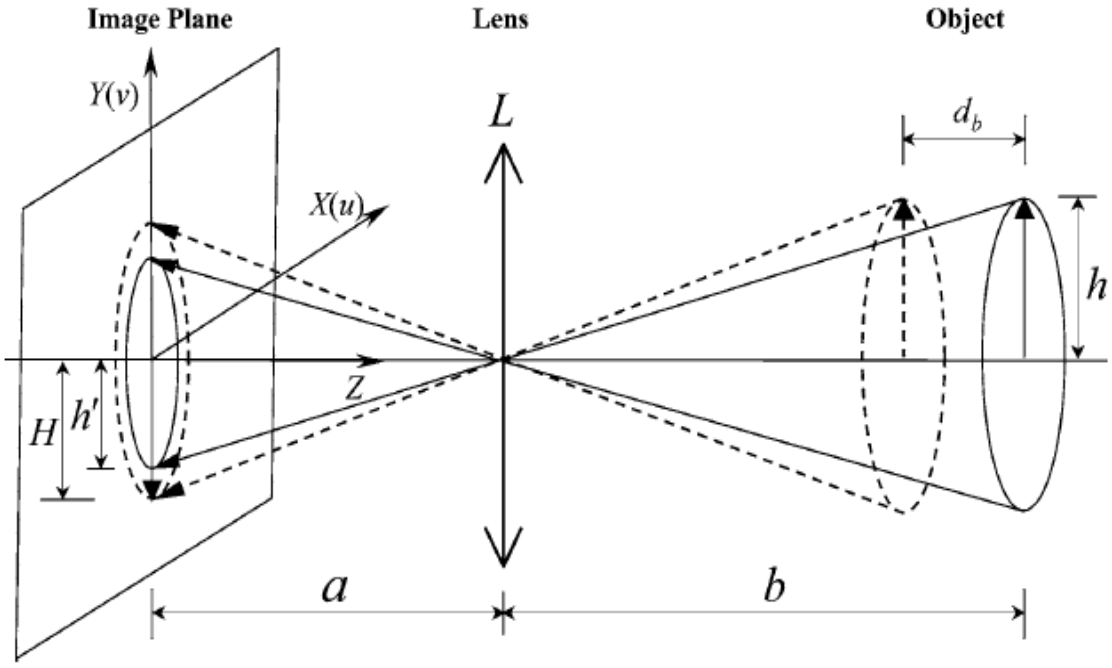

Figure 18: Relation between out-of-plane displacement and apparent in-plane displacement [50]

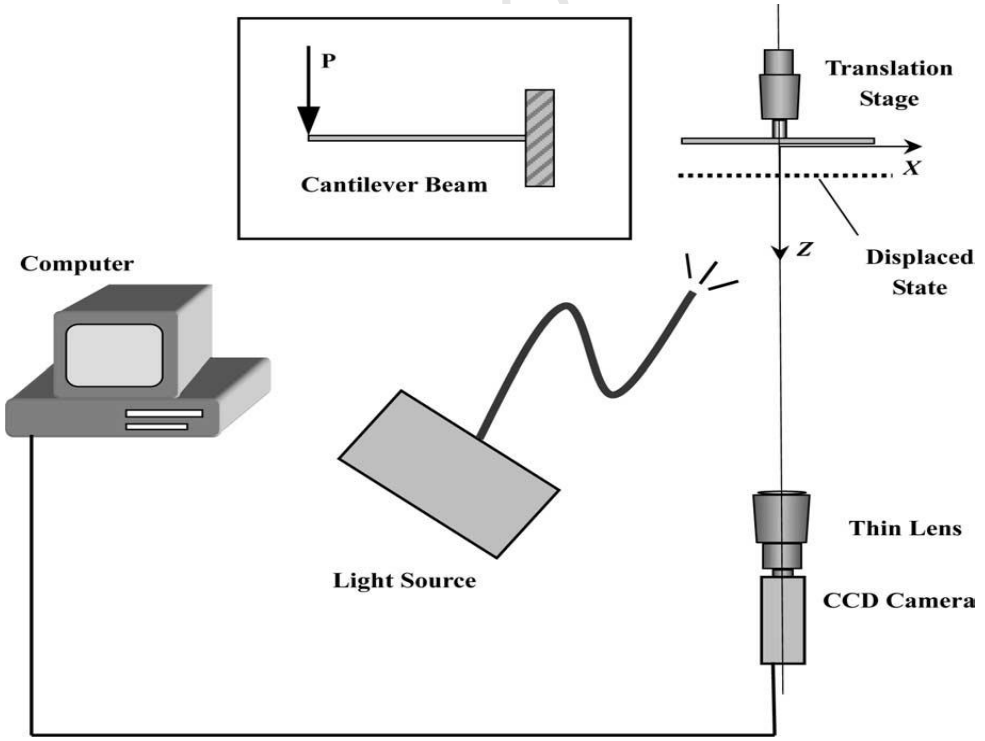

Figure 19: Diagram of the Experimental setup used by Tay *et al* [50]

2.8. Theoretical Predictions

Theoretical predications for plates subjected to impulsive loading have previously been reported by Jones [51] and Nurick and Martin [52], with the formulation of damage numbers in order to predict the inelastic deformation of plates of various geometries.

2.8.1. Jones Damage Numbers

Jones [51] formulated damage numbers for fully clamped rigid circular plates as well as for quadrangular plates.

2.8.1.1. Jones Damage Number for Circular Plates

In order to predict the large inelastic deformation experienced by fully clamped circular plates when impulsively loaded by a uniformly distributed impulsive load of velocity V_0, shown in Figure 20, Jones [51] proposed the use of a damage number λ.

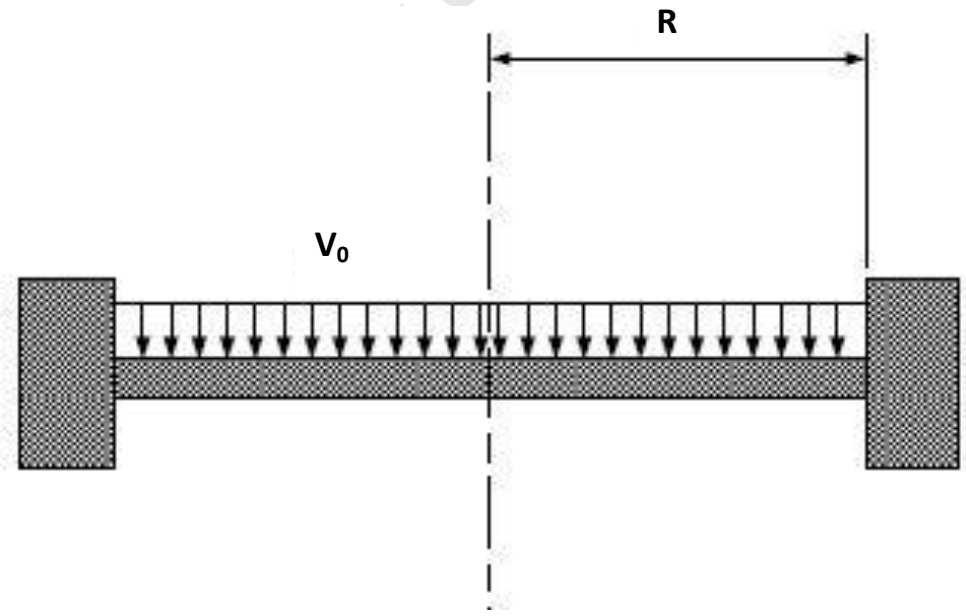

Figure 20: Fully clamped circular plate, radius R, subjected to uniformly distributed Impulse at velocity Vo, [51]

The damage number λ, is a dimensionless initial kinetic energy term:

$$\lambda = \frac{\mu V_0^2 R^2}{M_0 H} \qquad \text{(eq. 2)}$$

Where V_0 – Initial velocity, μ - Mass per unit area(ρH), M_0 – $\sigma H^2/4$, R – Plate radius, H – Plate thickness.

Equation 2 can be written in terms of impulse through substitution, where:

Substituting for equations M_0 and μ, λ becomes

$$\lambda = \frac{\mu V_0^2 R^2}{M_0 H} = \frac{(\rho H) V_0^2 R^2}{\left(\frac{\sigma_0 H^2}{4}\right) H} = \frac{\rho V_0^2 R^2}{\sigma_0 H^2} \qquad \text{(eq. 3)}$$

Impulse is given as,

$$I = mV_0 \qquad \text{and re-written as:} \qquad V_0 = \frac{I}{m} \qquad \text{(eq. 4)}$$

Where m – mass of the plate, which can be calculated from the volume and density (ρ) of the plate and velocity becomes:

$$V_0 = \frac{I}{\pi R^2 H \rho} \qquad \text{(eq. 5)}$$

Substituting (eq. 5) into (eq. 3) gives:

$$\lambda = \frac{\rho\left(\frac{I}{\pi R^2 H \rho}\right)^2 R^2}{\sigma_0 H^2} \qquad \text{which is then simplified to:}$$

$$\lambda = \frac{4I^2}{\pi^2 R^2 H^4 \rho \sigma_0} \qquad \text{(eq. 6)}$$

Where ρ - plate density and σ – static yield stress

The mid-point permanent displacement of the plate is given by:

$$\frac{\delta}{H} = \frac{\left(1+\frac{2\lambda}{3}\right)^{\frac{1}{2}}-1}{2} \qquad \text{(eq. 7)}$$

Where δ – permanent mid-point displacement of plate

2.8.1.2. Jones Damage Number for Quadrangular Plates

The Jones damage number for quadrangular plates is as follows:

$$\lambda = \frac{\mu V_0^2 L^2}{M_0 H} \qquad \text{(eq. 8)}$$

When Written in terms of impulse becomes:

$$\lambda = \frac{4I^2L^2}{A_0^2\rho\sigma_0 H^4} \qquad \text{(eq. 9)}$$

Where L – plate half length, A_0 – loaded area

The mid-point permanent displacement of the plate is given by:

$$\frac{\delta}{H} = \frac{(3-\xi_0)\left\{\left[1+\frac{1}{6}\lambda\xi_0^2\left(1-\xi_0+\frac{1}{2-\xi_0}\right)\right]^{\frac{1}{2}}-1\right\}}{\{2[1+(\xi_0-1)(\xi_0-2)]\}} \qquad \text{(eq. 10)}$$

Where B – plate half width, $\xi_0 = \frac{B}{L}$ tanφ and tanφ = $-\frac{B}{L} + \left[3+\left(\frac{B}{L}\right)^2\right]^{\frac{1}{2}}$

2.8.2. Nurick and Martin Damage Numbers

Nurick and Martin [52] proposed modified damage numbers for quadrangular and circular plates loaded impulsively based on Johnson's damage number α, shown in equation 11. This number incorporated the material density (ρ), impact velocity (υ) and damage stress (σ_d):

$$\alpha = \frac{\rho v^2}{\sigma_d} \qquad \text{(eq. 11)}$$

Johnson's damage number did not consider the method of impact, the target dimensions and geometry or the boundary conditions.

Johnson's damage number can be written in terms of impulse:

$$I = mv \qquad \text{(eq. 12)}$$

Where, m – mass of plate, I – impulse imparted on the plate.

$$v = \frac{I}{m} = \frac{I}{A_0 H \rho} \qquad \text{(eq. 13)}$$

Where, A_0 - load area, H – plate thickness

Substituting (eq. 13) into (eq. 11) gives:

$$\alpha = \frac{I^2}{A_0^2 H^2 \rho \sigma_d} = \frac{I_0^2}{H^2 \rho \sigma_d} \qquad \text{(eq. 14)}$$

Where I_0 is impulse per area (I/A_0)

Nurick and Martin introduced a damage number (Ψ), given by:

$$\Psi = \frac{I}{AH(\rho\sigma_d)^{\frac{1}{2}}} \quad \text{(eq. 15)}$$

Where A – plate area

A relationship between the distance from the plate centre to the closest boundary and the thickness of the plate was established. This relationship is known as the aspect ratio λ

For circular plates is given as:

$$\lambda = \frac{R}{H} \quad \text{(eq. 16)}$$

Where R – plate radius, H – Plate thickness

For quadrangular plates a similar parameter is given as:

$$\lambda = \frac{b}{2H} \quad \text{(eq. 17)}$$

A loading parameter for the consideration of the loaded area with regard to the total plate area was introduced for circular plates and is given as the relationship [52]:

$$\zeta = 1 + ln\left(\frac{R}{R_0}\right) \quad \text{(eq. 18)}$$

Where, R_0 is the radius of the loaded area.

This relationship controls the loading parameter for circular plates, as R_0 tends to R, so ζ tends to 1. This indicates that the plate is uniformly loaded over the entire plate area.

Nurick and Martin [52] combined equations 15-18 in order to obtain a modified damage number that incorporates both the plate dimensions and the loading conditions.

$$\phi = \Psi\lambda\zeta \quad \text{(eq. 19)}$$

For uniformly loaded circular plate

$$\phi_c = \frac{I}{\pi R H^2 (\rho\sigma_0)^{\frac{1}{2}}} \quad \text{(eq. 20)}$$

For locally loaded circular plate

$$\phi_c = \frac{I\left(1+ln\frac{R}{R_0}\right)}{\pi R H^2 (\rho\sigma_0)^{\frac{1}{2}}} \quad \text{(eq. 21)}$$

Where R – plate radius, R_0 – radius of loaded area

For quadrangular plate under uniform loading

$$\phi_q = \frac{I}{2H^2 (bl\rho\sigma_0)^{\frac{1}{2}}} \quad \text{(eq. 22)}$$

Where *b* – plate width, *l* – plate length

Quadrangular plates under localised loading

Jacob *et al* [7] reported a modification to the damage number in order to account for quadrangular plates subjected to localised loading. A loading parameter (which is a function of the charge area and the plate area) is incorporated into eq. 10, and the modified damage number then becomes:

$$\phi_{ql} = \frac{I\left(1+ln\left(\frac{lb}{\pi R_0^2}\right)\right)}{2H^2(bl\rho\sigma_0)^{\frac{1}{2}}} \qquad \text{(eq. 23)}$$

The loading parameter for circular (eq. 21) and quadrangular plates (eq. 23) are similar because the charge shape plate shape and charge shape are geometrically similar when using disc shaped explosive charges. For the quadrangular plate which is subjected to blast loading from disc shaped charges, this geometrical similarity does not exist and hence the ratio of plate area and charge area are incorporated.

Jacob *et al* [7] also further introduced a loading factor into (eq. 23) in order to account for the effect of the stand-off distance on the response of the plate. The parameter is a function of the stand-off distance and charge radius, written as:

$$\zeta_s = \left(1 + ln\left(\frac{S}{R_0}\right)\right) \qquad \text{(eq. 24)}$$

This is used for circular plates subjected to blast loading when the blast wave propagates along a tube.

The new parameter is then incorporated into the dimensionless impulse equation for localised loading (eq. 23):

$$\phi_{ql} = \frac{I\left(1+ln\left(\frac{lb}{\pi R_0^2}\right)\right)}{2H^2(bl\rho\sigma_0)^{\frac{1}{2}}} \times \frac{1}{\zeta_s} \qquad \text{(eq. 25)}$$

Nurick and Martin [52] also developed empirical relationships between the permanent mid-point displacement/thickness ratio and damage number for circular and quadrangular plates, reported as:

For circular plates

$$\frac{\delta}{H} = 0.425\phi_c \qquad \text{(eq. 26)}$$

For quadrangular plates

$$\frac{\delta}{H} = 0.48\phi_q \qquad \text{(eq. 27)}$$

Equations 26 – 27 are based on results from hundreds of blast tests on fully clamped thin steel plates [1], [52].

2.9. Numerical Modelling

Numerical modelling of the dynamic loading of structures can be achieved by constructing a model using a hydrocode designed for non-linear dynamic analysis. Hydrocodes usually incorporate Lagrangian, Arbitrary Lagrange Euler (ALE) and Euler mesh solvers. One of the most widely used hydrocodes for blast simulations is ANSYS AUTODYN. The multiphysics simulation package LS-DYNA has also been used to model blast simulations [48].

When approaching a blast modelling problem, a common first step is to construct a detonation model and determine the detonation mesh size, which could affect on the detonation pressure, as investigated for example, by Ozinsky [53] and Rossiter [54]. When modelling explosions using AUTODYN Ozinsky [53] and Rossiter [54] both determined, for detonations in rigid walled tubes with a 106mm inner diameter, that a coarser mesh (such as a 10mm mesh) caused lower CJ pressures than a finer mesh. The CJ pressure for C4 explosive as given in the AUTODYN material library is approximately 28 GPa. Thus the mesh size chosen should cause the development of maximum pressures in the order of the CJ pressure while also being coarse enough not to have significantly long run times. As the CJ pressure is obtained experimentally in highly confined explosive detonations, the pressure should always be lower than 28 GPa in simulations.

AUTODYN was used to model the response of plates to buried charges by Pickering [55] where a three-dimensional quarter-symmetry model was used to simulate blast loading from charges at different burial depths, shown in Figure 21. The geometrical relationship between the charge (disc shaped) and the plate (quadrangular) dictated that the model had to be constructed three-dimensionally. The disadvantage of a three-dimensional model is that it requires significantly longer processing times and is not necessarily more accurate due to the computational limits restricting the mesh size and resolution of the model.

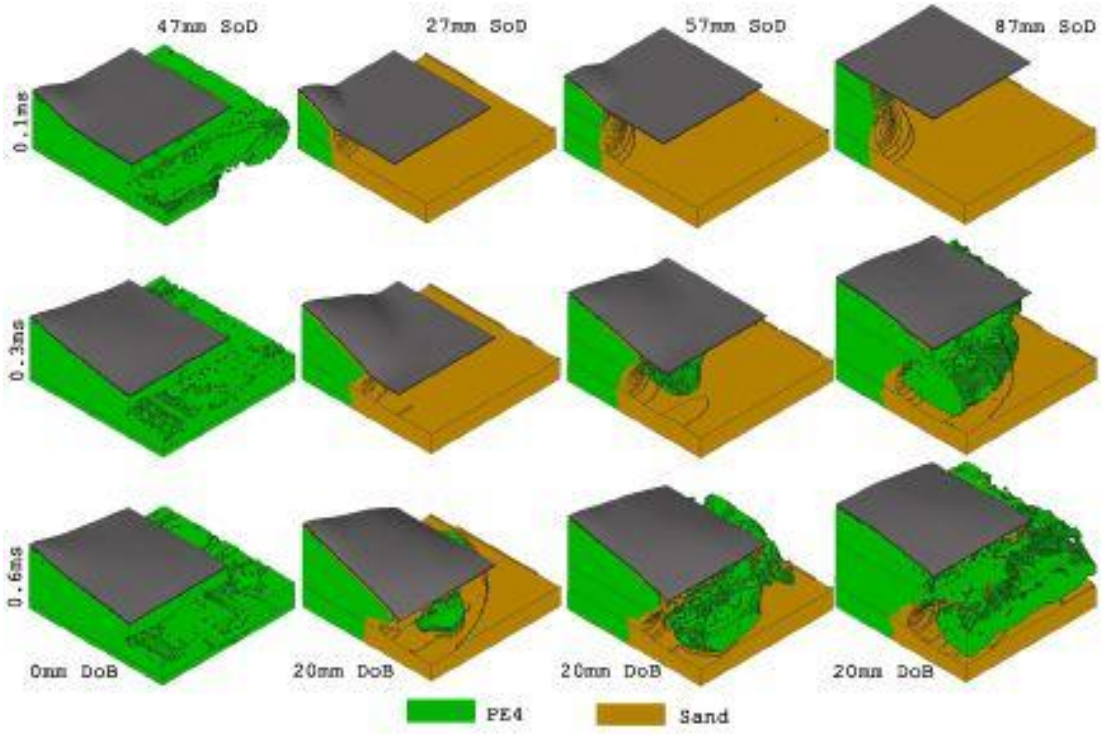

Figure 21: AUTODYN screenshots from Pickering's models showing response of sand at different burial depths [55]

Pickering [55] obtained relatively accurate results from his models with respect to permanent mid-point displacements and plate deformation profiles.

Rossiter [54] also used numerical simulations to investigate the effects of geometric parameters on the performance of perforated plates as a blast mitigation technique. Rossiter [54] modelled the effect of perforated plates on the behaviour of a target plate subjected to blast loading in a tube [54]. The model was axi-symmetric (two-dimensional), shown in Figure 22, as the geometry of the charge and tubes were both circular. The 3D model was reconstructed by revolving it. Running axi-symmetric models is less time consuming and can be more accurate due to larger mesh sizes and finer mesh resolutions being computable.

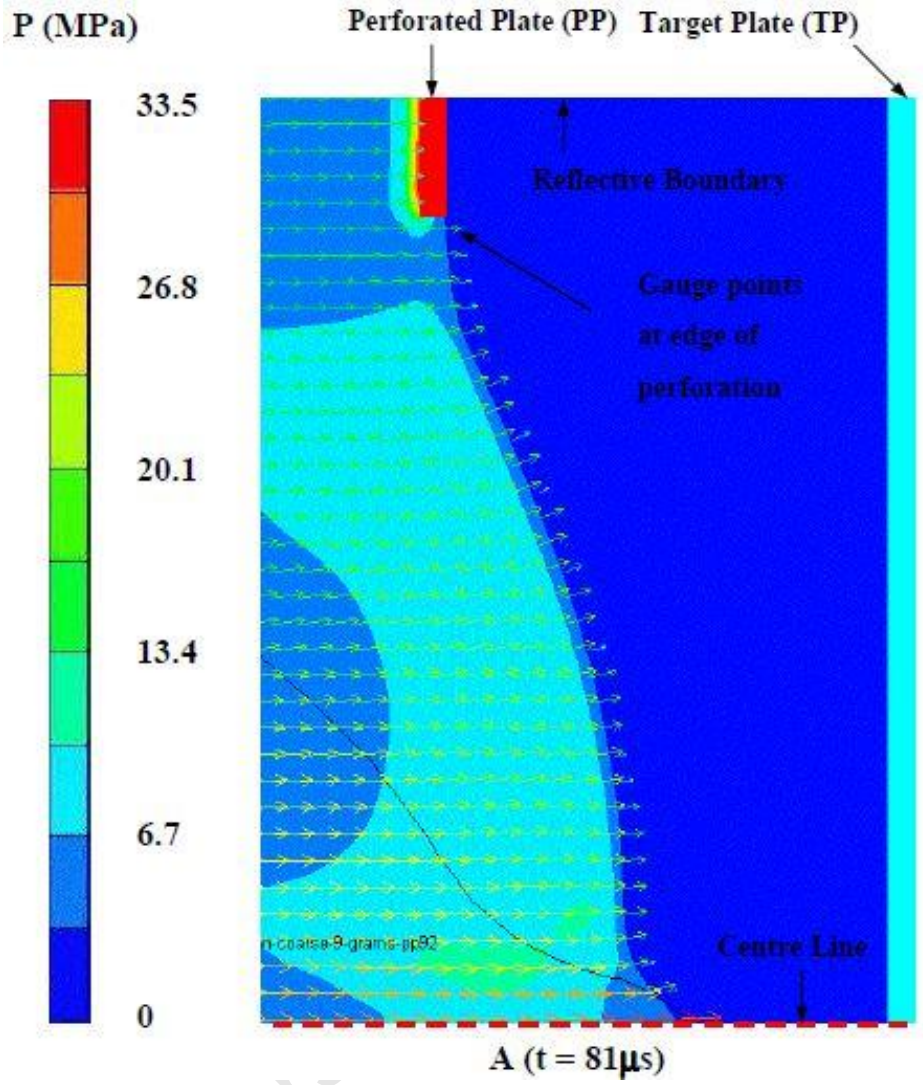

Figure 22: Pressure contour plot from Rossiter's model of a perforated plate and target plate in a tube [54]

2.10. Summary of Literature Review

- The detonation of PE4 explosive is a safe, reliable way to generate blast loading and has been used to investigate the response of plates of different materials ([1] , [21], [56]), geometries ([13], [7]), boundary conditions [35] and with different spatial loading distributions.
- Metal plates, such as steel, exhibit large inelastic deformation failures, followed by tearing and shearing at higher charge masses. The locations of tearing and rupture are dependent on the load distribution, boundary conditions and geometry of the plates.
- Composite panels exhibit many additional failure types including delamination, matrix failure and fibre ruptures.
- Transient measurement of structural response during blast load testing are difficult to make, but light interference techniques have been successfully employed by others ([45], [48]).
- Dimensionless analysis has been used to normalize for loading, material properties and geometric differences in metal plates, but not yet for composites.
- Numerical modelling packages such as AUTODYN have been used to successfully model the response of steel plates to explosive detonations in air ([53], [16]) and sand [55]. Due to computational and time constraints, 3D models can have meshes which are not of the ideal resolution.

3. EXPERIMENTAL DETAILS

The details of the blast loading experiments which were performed on various plates in the BISRU Laboratory at the University of Cape Town are provided in this chapter.

3.1. Experimental Procedure

3.1.1. Configuration of Test Rig

The blast test rig consisted of two clamp frames. The back clamp frame had two slots in opposing corners for mounting the light interference system. Four spacer bars were used to attach the back clamp frame to the mounting plate at the front of the pendulum. This provides the space required at the back of the test plate for the light interference system and the protective (and light-blocking) shroud shown in Figure 23. The test plate was clamped between the two clamp frames and secured by bolts fastened around the sides of the clamp frames. The explosive, which was attached to a polystyrene bridge (Figure 24), was mounted onto the front centre of the test plate using double-sided tape.

The stand-off distance is the distance between the explosive charge and the test plate. Typically, more localised blast loads develop when the explosive charge is placed nearer to the target plate. Stand-off distances of 25 mm and 38 mm were used for various tests, which will be discussed in more detail in Chapter 4 and Chapter 6.

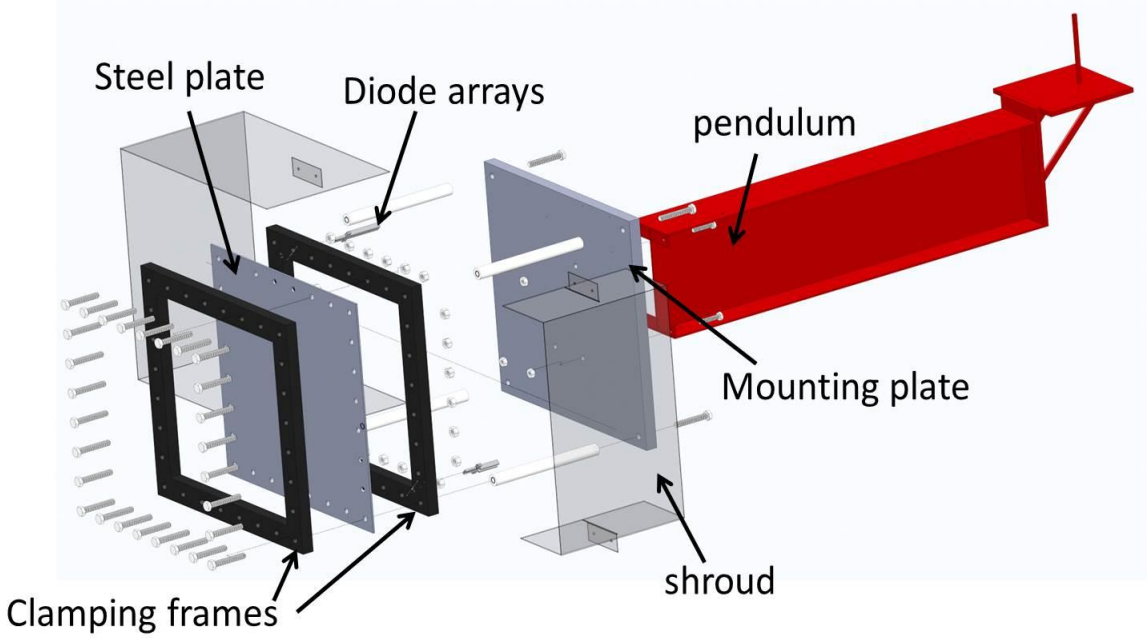

Figure 23: Exploded CAD Diagram of Ballistic Pendulum Setup

3.1.2. Material Properties and Dimensions of Explosive Loads

Air blast loading was created by electronically detonating cylindrical plastic explosive PE4. Three different charge diameters and various charge masses were used, as shown in Table 3.

The explosive was detonated by means of an electronic detonator pin, shown in Figure 24. The detonator was joined to the main explosive charge by means of a leader made up of 1g of PE4. The detonator was inserted through a hole at the back of the polystyrene bridge. A photograph of the polystyrene bridge is shown attached to the test plate in Figure 24.

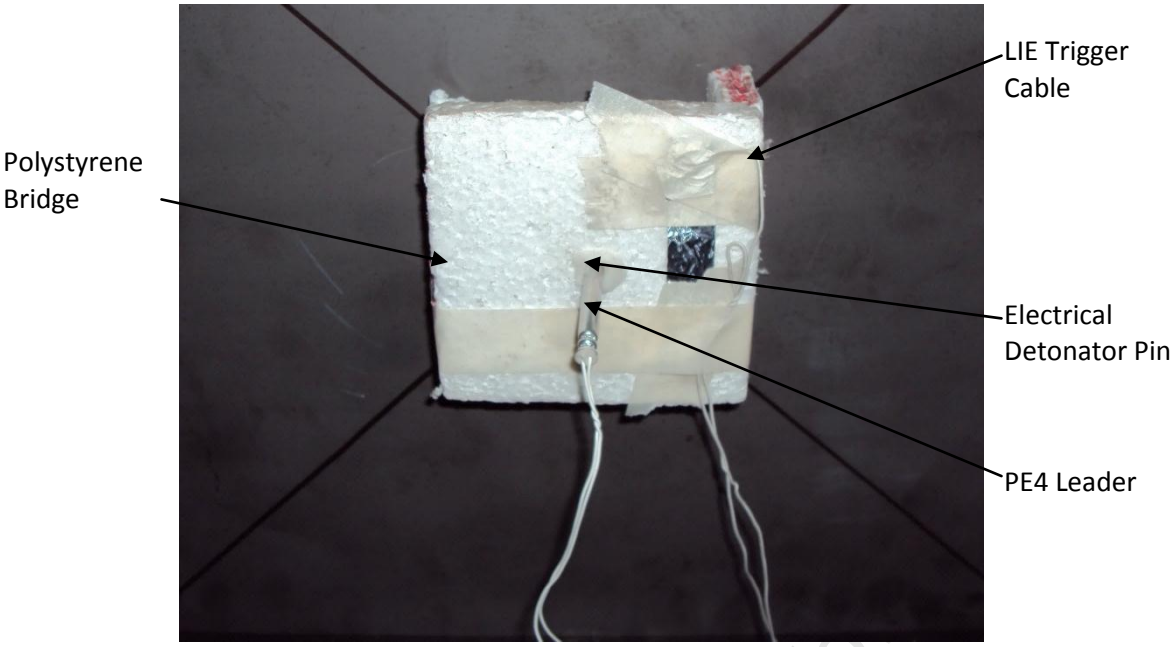

Figure 24: Photograph of Polystyrene Bridge

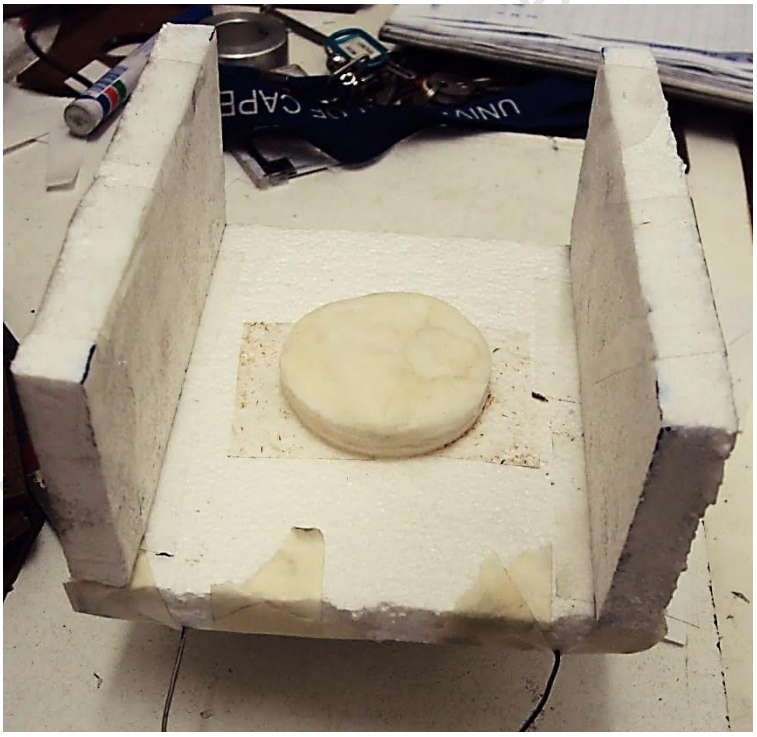

Figure 25: Photograph of the Polystyrene Bridge with the Explosive attached underneath

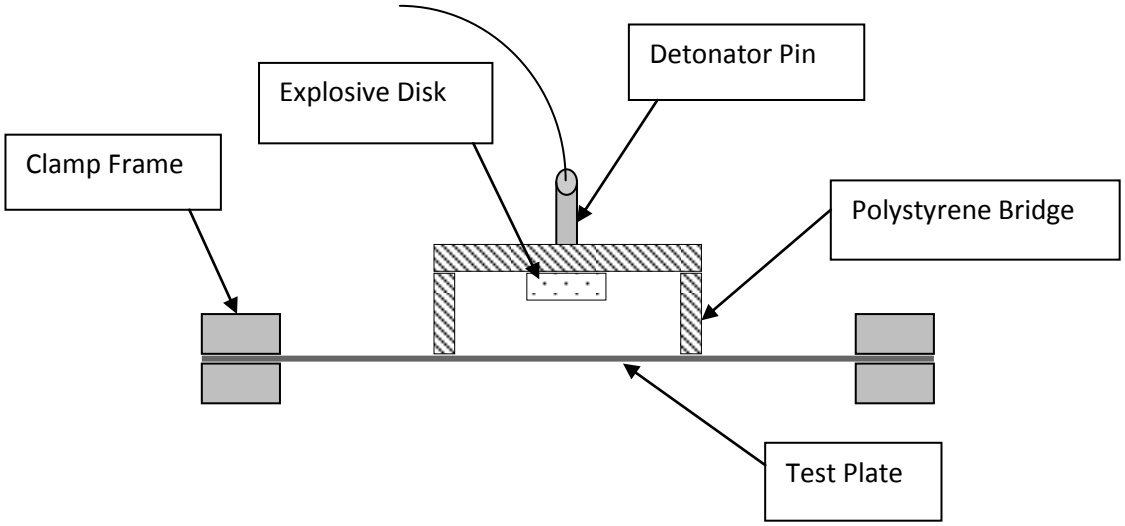

Figure 26: Schematic Diagram Showing Configuration of Explosive for Localised Impulsive Loading used in the current work

3.1.3. Ballistic Pendulum

The impulse imparted by the blast load was calculated using the swing from the ballistic pendulum. The pendulum consists of four spring steel cables which suspend a steel I-beam and are attached by four independently adjustable screws. The method used to calculate the impulse is shown in Appendix C. The experimental arrangement of the ballistic pendulum is shown in Figure 27 and Figure 28. The weight of the test plate and clamp frames attached to the front of the pendulum is balanced by counterweights loaded onto the rear, as shown in Figure 27. The counterweights are used to ensure that the tension in each of the four cables is evenly distributed. During the blast the oscillation of the pendulum is directly related to the impulse imparted to the test by using single degree of freedom modeling as described in Appendix C. The oscillation amplitude is measured on a piece of tracing paper by a marker pen attached to the bottom rear of the pendulum.

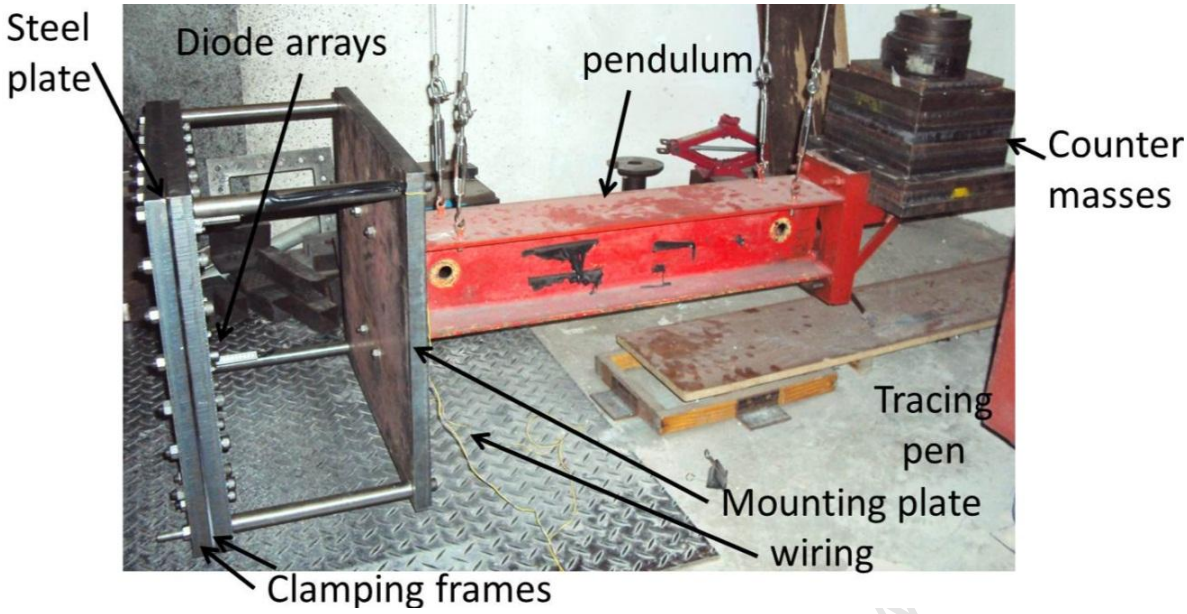

Figure 27: Photograph of Ballistic Pendulum

Figure 28: Photograph of the Protective Shroud Mounted onto the Test Rig

3.1.4. Light Interference Equipment

In an attempt to obtain the transient deformation response of the steel plates, light interference equipment was developed. This required LEDs to transmit light across a larger separation distance than used in previous studies [45], [48]. The Light Interference Equipment (LIE) was mounted onto the back clamp frame. The configuration, shown in Figure 29, consisted of one row of infrared Light Emitting Diodes (LEDs) mounted into the slot in one corner of the clamp frame directly facing the Photodiode receivers in the opposite corner. The infrared LEDs and photodiodes were wired in series and in parallel respectively. The maximum measurable displacement of the system was 65mm.

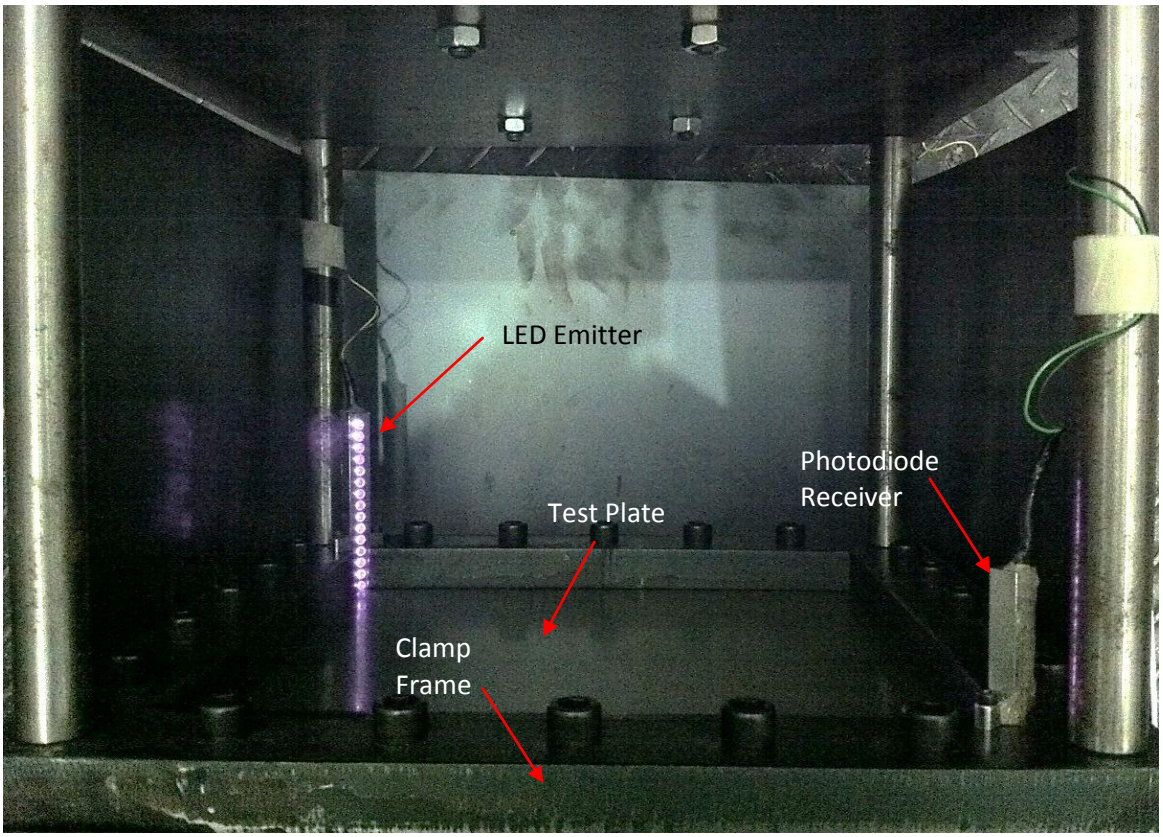

Figure 29: Photograph of the Light Interference system mounted to the back of the Test Plate

3.1.4.1. Calibration of the LIE

The calibration of the light interference equipment is achieved by measuring pre-deformed plates of known displacement and correlating these displacements which the corresponding voltage changes. A curve plotted through the displacement against voltage change points is used as the calibration curve, Figure 30.

3.1.4.2. Transient Displacement Measurement

As the light interference equipment was sensitive to light, the diodes and the measurable deformation area at the back of the test plate must be sealed to prevent the explosive flash from interrupting the measurement system. This was achieved by using the protective shroud shown in Figure 28. Movement of the test plate during blocked the infrared light- emitted by the LEDs, decreasing the intensity of the light received by the photodiodes which caused a corresponding voltage drop across the photodiodes. This voltage drop was recorded and compared to a calibration voltage measured at ambient conditions using pre-deformed plates of known displacements, which can be used to obtain a displacement-time history.

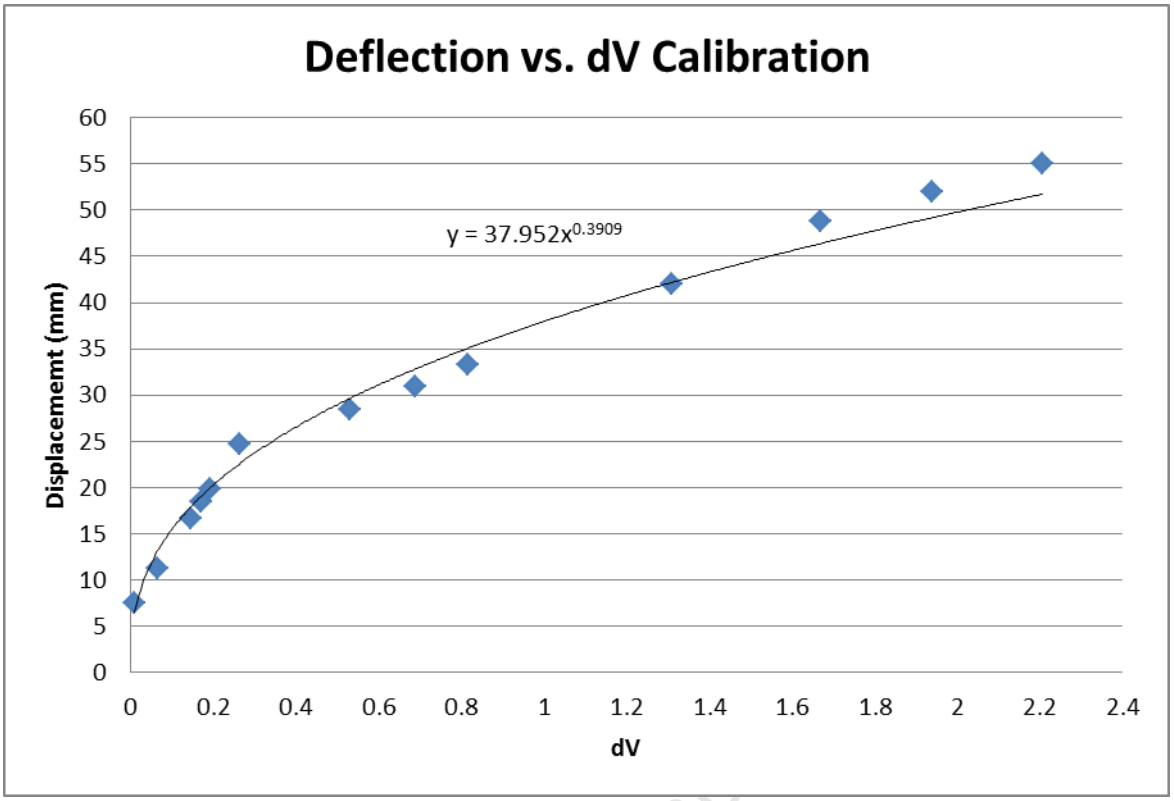

Figure 30: Calibration Curve of Displacement versus Voltage Change

It can be observed from Figure 30 that the calibration points do not form a linear trend. A power law curve was fitted to the data points and showed good correlation. The power law equation obtained from the calibration points was thus used to convert the voltage change from the experimental transient results into displacement-time histories.

An investigation into the non-linearity of the calibration data was performed through theoretical calculations done to predict the percentage of voltage change against the displacement. Theoretically, the intensity of the light emitted onto the receiving diode by each light individually can be calculated for various plate displacement heights. The amount of light from each LED that covers the diode can be expressed as a percentage of the length of the diode able to receive light. The average of the sum of the light intensity from each LED gives the total percentage of light intensity received by the photodiodes for a specific displacement. The method for determining the light intensity emitted from a specific LED is as follows:

If the height of the LED is less than the height of the plate displacement, then the light intensity is calculated by:

$$LI = \left\{\frac{[Hr-\delta-(\delta-He)]}{Hr}\right\} \times 100 \qquad \text{(eq. 28)}$$

Where LI = light intensity%, Hr = height of receiver, δ = plate displacement and He = height of LED

Based on simple geometry, it can be observed that if the height of the LED emitter is greater than or equal to twice the height of the plate displacement then the light intensity will be at 100%.

If however, the height of the LED is greater than the height of the plate displacement but less than twice the height of the same plate displacement, then the light intensity is calculated by:

$$LI = \left\{\frac{[Hr-\delta+(He-\delta)]}{Hr}\right\} \times 100 \qquad \text{(eq. 29)}$$

For the light intensity calculations, the distance between the emitter and receiver has no effect as the plate displacement is considered to be exactly half-way between them. A diagram of the LIE system is shown in Figure 32, illustrating the method for calculating the light intensity for each LED. The case where the use of equation 28 is required is indicated by the dark blue line, where the height of the emitter He1 is less than the height of the plate displacement δ. The light intensity percentage would then be calculated by dividing the amount of light received by the photodiodes, hL1, by the total height of the photodiodes, Hr, and multiplying the result by 100.

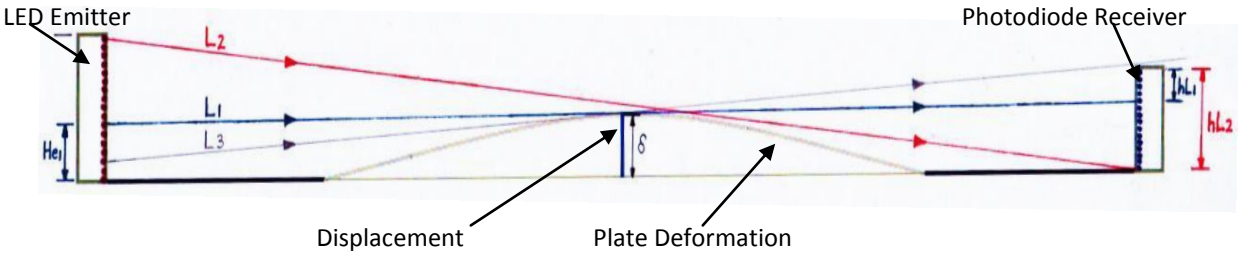

Figure 31: Schematic of LIE system illustrating light intensity of LEDs at various positions

Figure 32 shows that the decrease in light intensity due to increasing back-face displacement is non-linear, which corresponds to the shape of the experimental results. The use of power law equation of the line trend through the curve used to calculate and plot the displacement-time histories of the actual blasts tests was thus sufficiently justified.

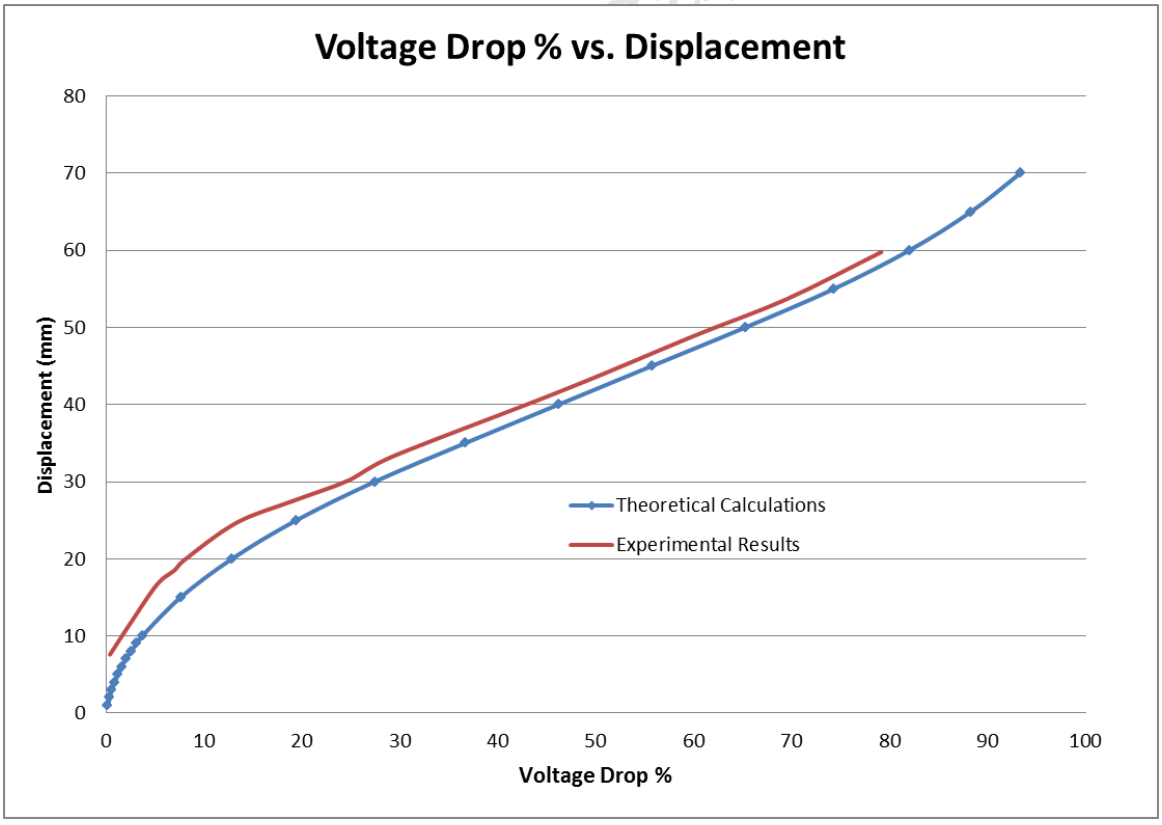

Figure 32: Graph of Displacement versus Voltage Drop % of Theoretical and Experimental Results

3.2. Specimens

Tests were performed on plates manufactured from the following materials namely: mild steel; armour steel (Armox 370T and Armox 440T), aluminium 5083-H116, UHMWPE Dyneema and Twintex GFPP composite panels. Due to availability of materials, some tests were performed on plates with different exposed areas. A matrix of tests showing the geometry and material information is presented in Table 3. Engineering drawings of the two different test plate sizes are provided in Figure 33 and Figure 34. The thickness of the aluminium, GFPP and Dyneema panels were chosen to closely match the areal density of the steel plates.

Table 3: Matrix of Test Parameters and Plate Dimensions

Material	Charge Mass Range (g)	Charge Diameter Range (mm)	Stand-off Distances (mm)	Exposed Area Planar Dimensions (mm)	Nominal Thickness (mm)	Boundary Conditions	Density (g/m^3)
Mild Steel 3mm	7-33	50, 75	25, 38	300 x 300	3	Clamped, Bolted	7850
Mild Steel 4mm	9-40	50, 75	25, 38	400 x 400	4	Clamped, Bolted	7850
Armour Steel-Armox 370T	33-50	40, 50, 75	25, 38	400 x 400	4	Clamped, Bolted	7850
Armour Steel-Armox 440T	24-40	50	25, 38	400 x 400	4.5	Clamped, Bolted	7850
Aluminium 5083-H116	12-33	50	25, 38	300 x 300	10.5	Clamped, Bolted	2680
Twintex	12-24	50	25, 38	300 x 300	11.5	Clamped, Bolted	1500
Dyneema	15-60	50	50	300 x 300	25	Clamped	970

The results of the 500mm armour steel and mild steel square plates are presented in Chapter 4 followed by the results of the numerical simulations of their responses in Chapter 5. The results of the 400mm square plates of various materials are presented in Chapter 6 followed by a discussion of all of the results in Chapter 7. Conclusions are drawn in Chapter 8 and recommendations based on the findings are made in Chapter 9.

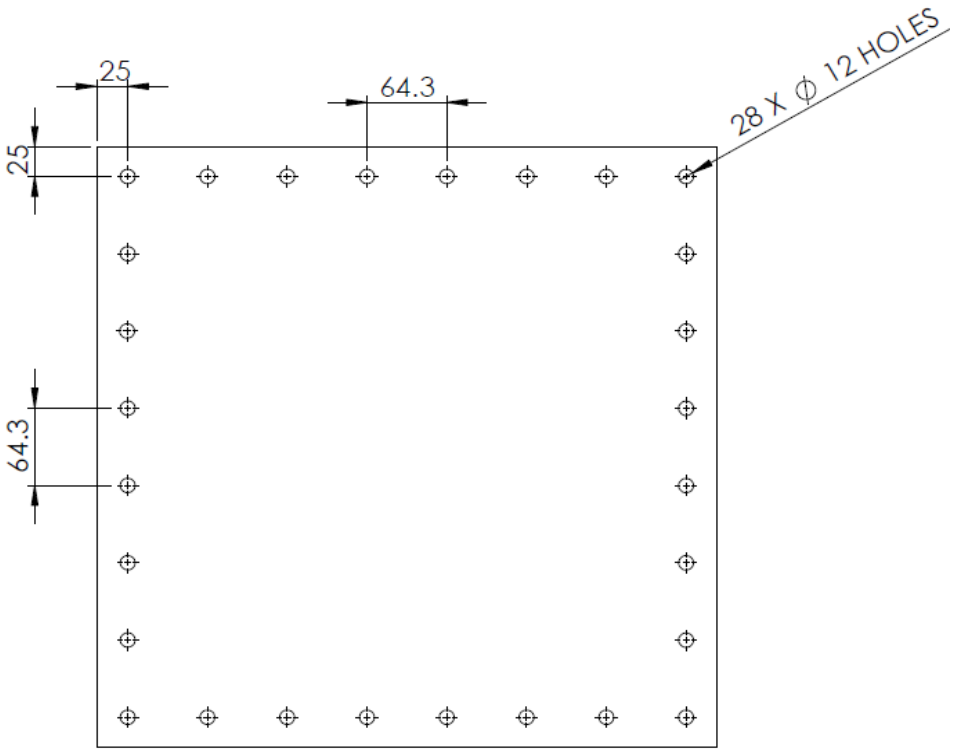

Figure 33: Drawing of the 500mm x 500mm, 4mm Thick Test Plate

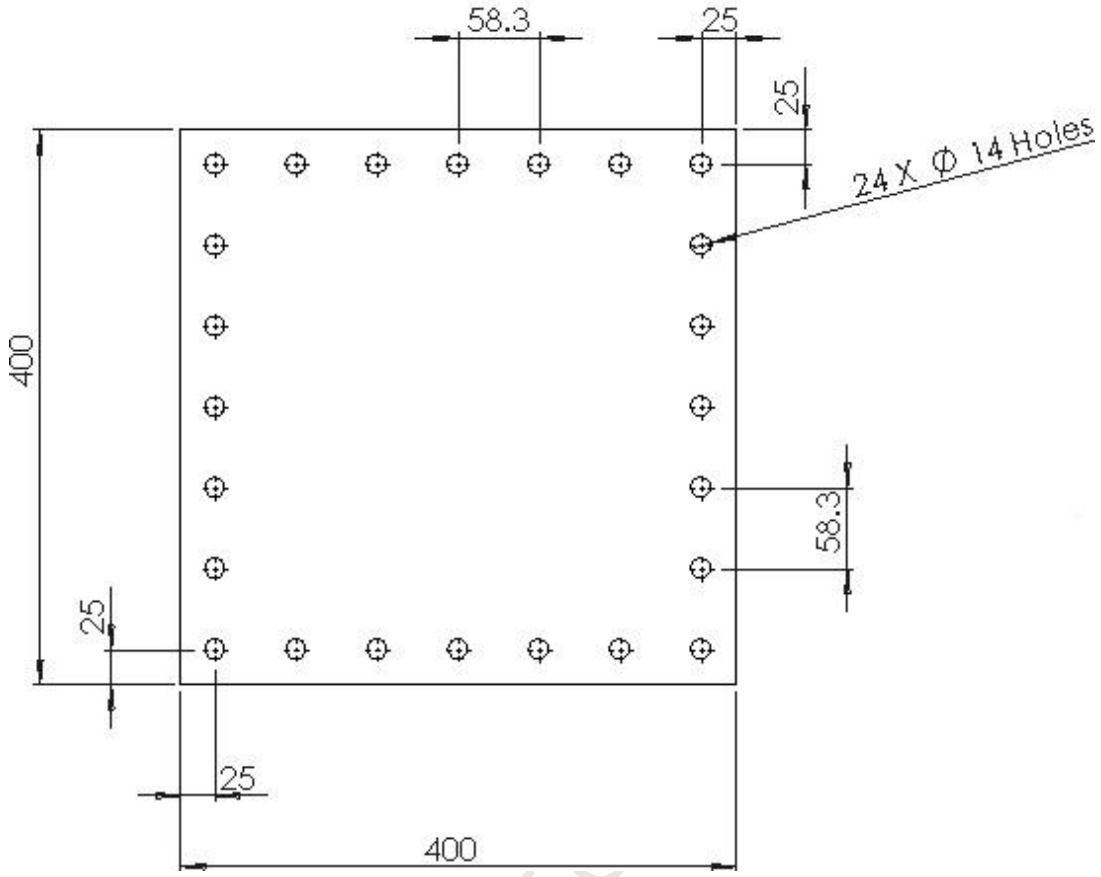

Figure 34: Drawing of the 400mm x 400mm, 3mm Thick Test Plate

It should be noted that the Dyneema panels were mounted differently to the other plates due to difficulties in machining. An engineering drawing of the Dyneema test plates is shown in Figure 35. The Dyneema panels had to be water jet cut to the required geometry as other attempts to cut the panels were unsuccessful. The panels were held between two clamp frames. Spacers, matching the Dyneema plate thickness, were used in the corners to mount the plates to the spacer bars (shown in Figure 36).

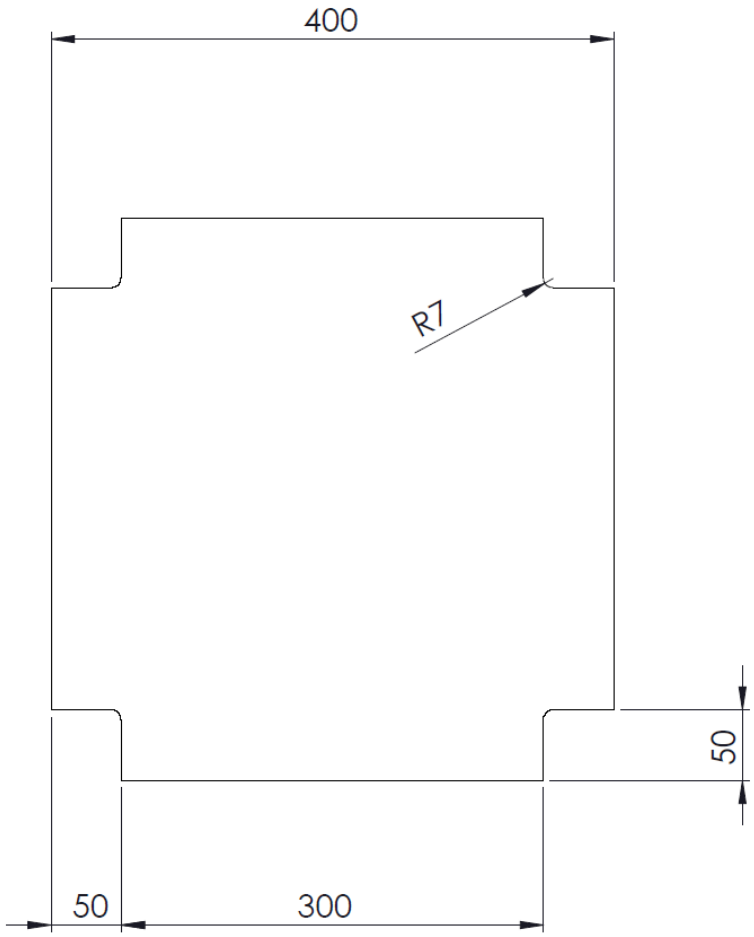

Figure 35: Drawing of the Dyneema test plate dimensions

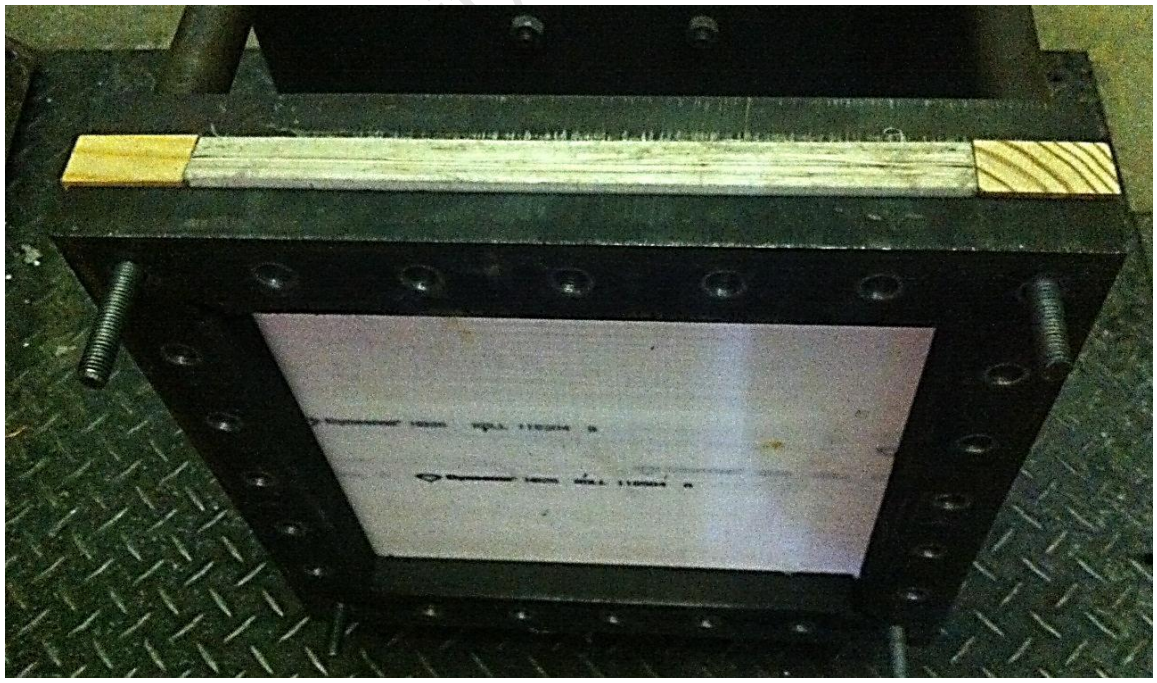

Figure 36: Photograph showing clamping arrangement for Dyneema plates

3.3. Material Properties of Test Specimens

The material properties of the metal specimens were obtained from tensile test results from specimens cut from the material to be blast loaded. The dimensions of the tensile test specimens conformed to ASTM Standard E8/E8M-11 for tensile specimens. Tests on mild steel, Armox 440T and aluminium were performed on the Zwick machine in the Centre for Materials Engineering at the University of Cape Town. Engineering stress-strain curves, true stress-true strain curves, yield stress and ultimate tensile stress for mild steel were all obtained from the tensile tests. Tensile tests for the Armox 370T were performed by Imperial College in London [57], with some results reported here. Refer to Appendix A for additional material characterization results.

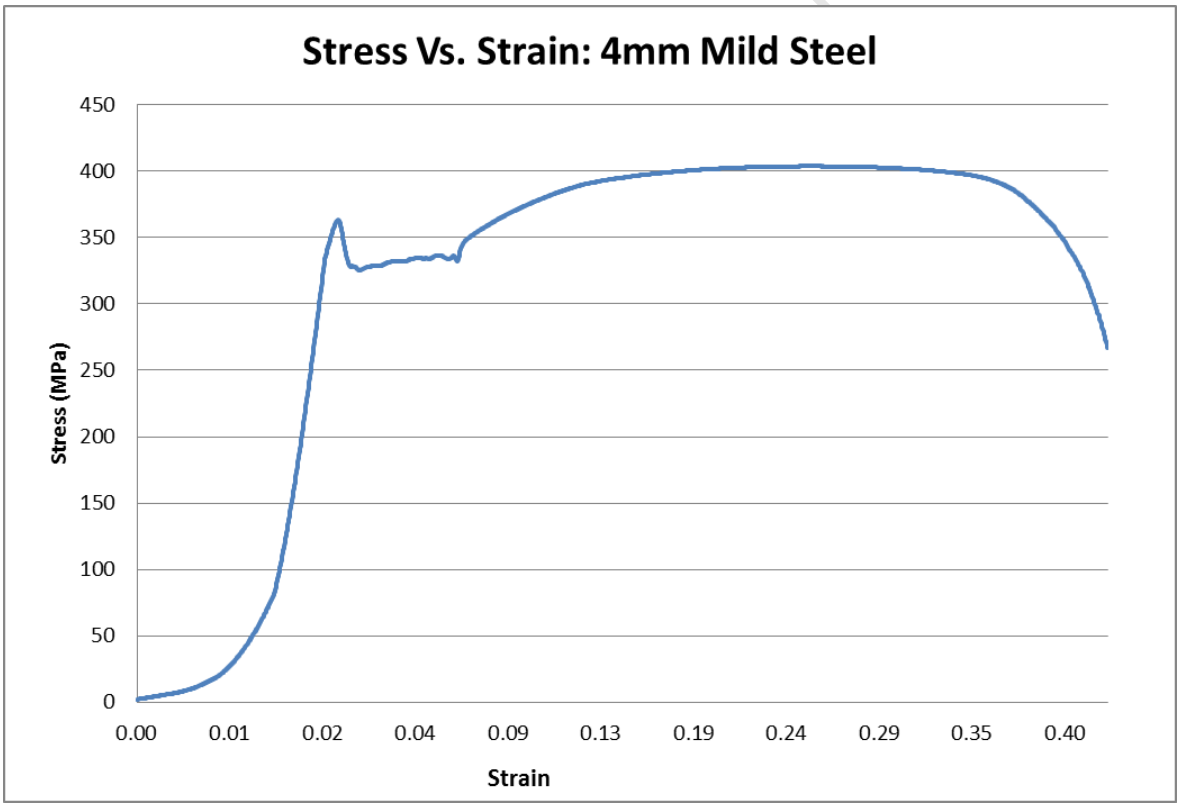

Figure 37: Graph of a typical Stress-Strain Curve for 4mm thick Mild Steel

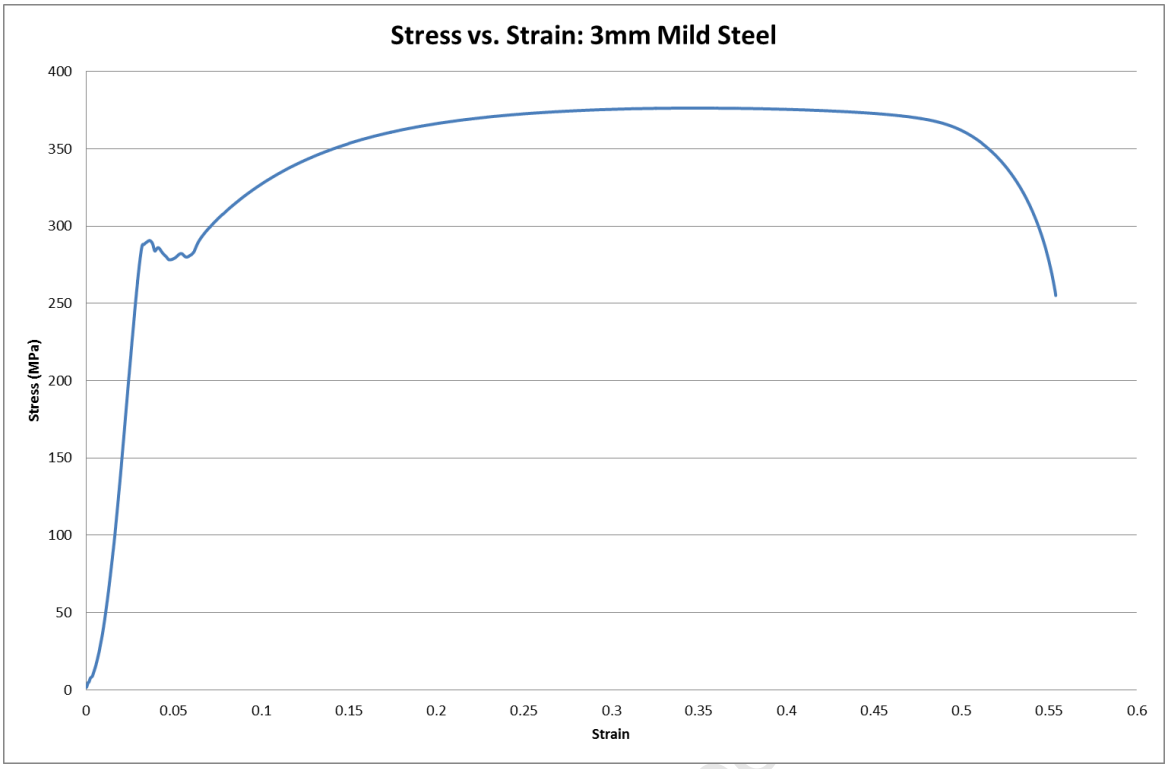

Figure 38: Graph of a typical Stress-Strain Curve for 3mm thick Mild Steel

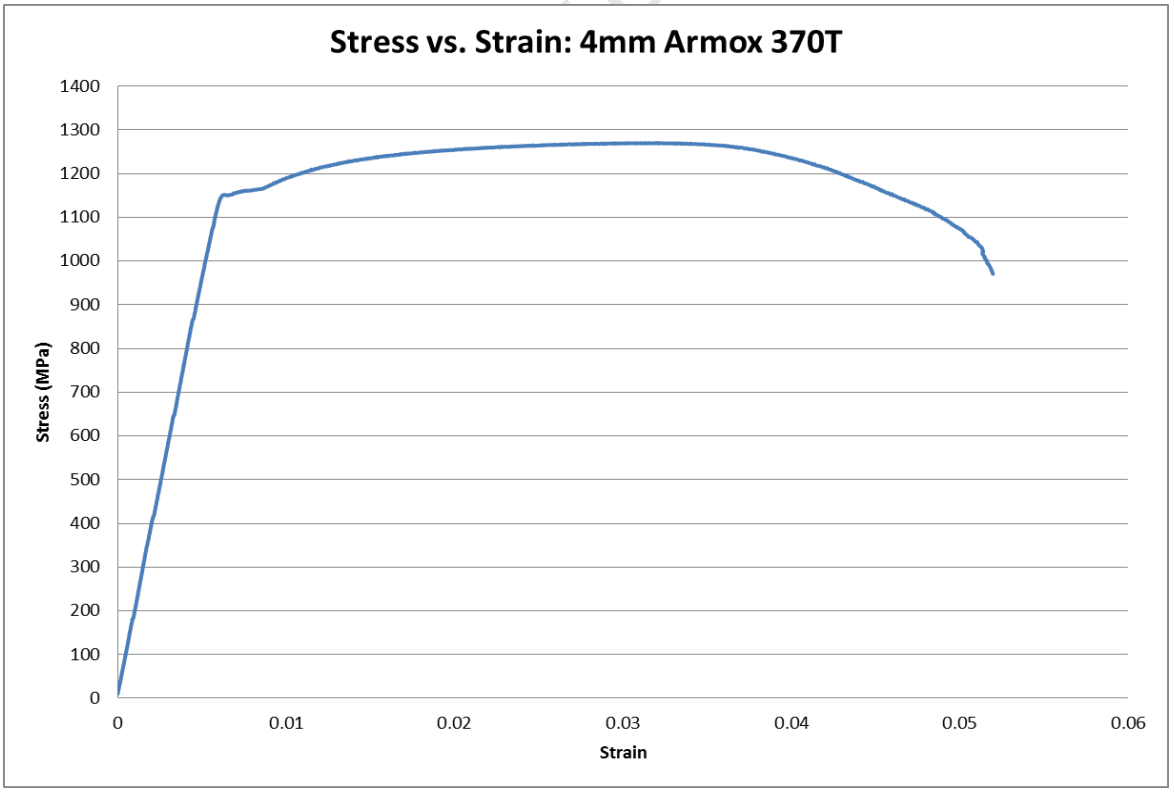

Figure 39: Graph of a typical Stress-Strain Curve for 4mm thick Armox 370T Steel

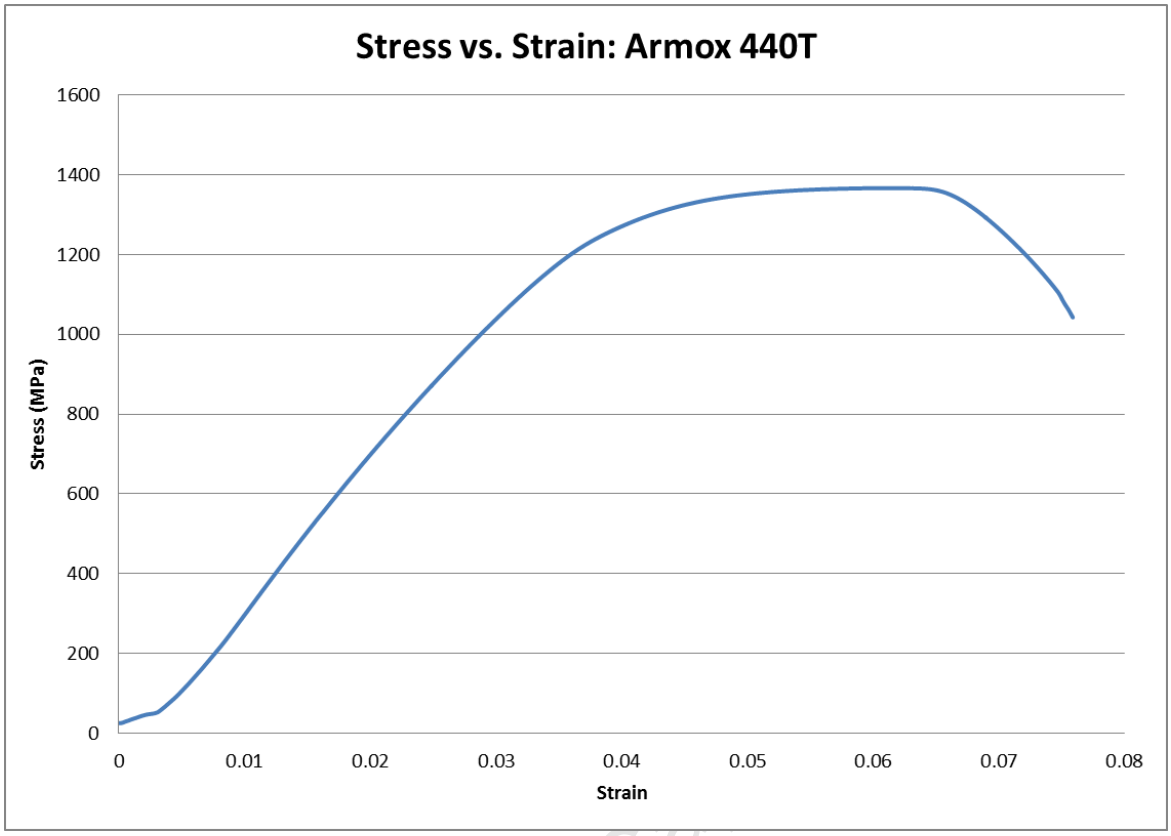

Figure 40: Graph of a typical Stress-Strain Curve for 4mm thick Armox 440T Steel

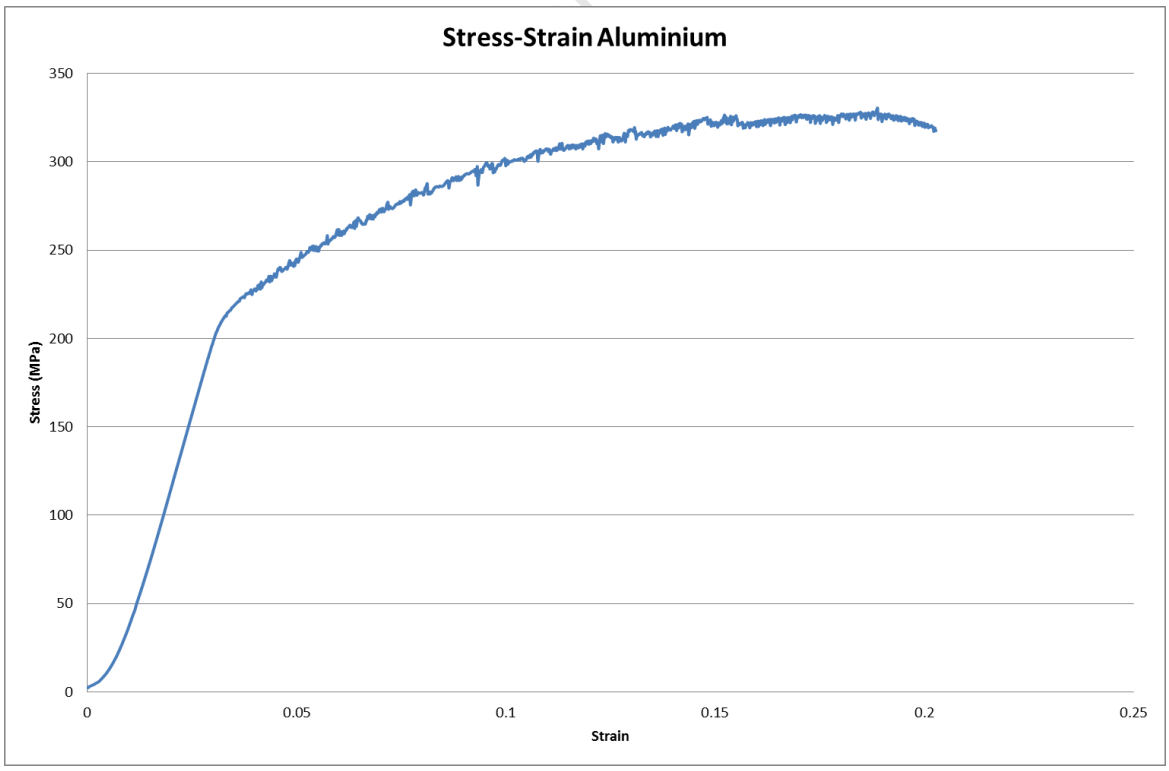

Figure 41: Graph of a typical Stress Strain curve for 10.5mm thick Aluminium 5083 H116

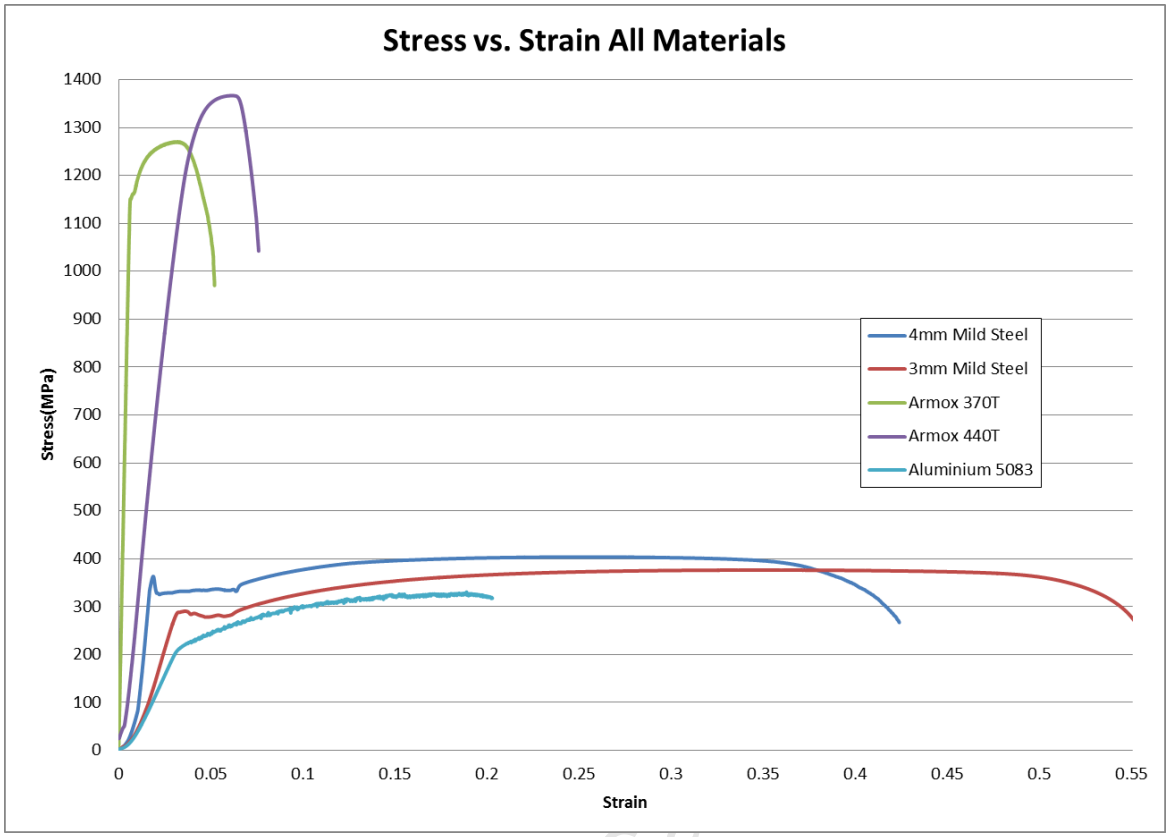

Figure 42: Stress-Strain Curves of all materials

Material	Mean Average Yield Strength	Mean Average UTS
4 mm Mild Steel	350MPa	404MPa
3 mm Mild Steel	250MPa	372MPa
4 mm Armox 370T	1150MPa	1271MPa
4.5 mm Armox 440T	1200MPa	1360MPa
10 mm Aluminium 5083	200MPa	331MPa
Twintex [23]	300MPa	315MPa
Dyneema [57]	650MPa	700MPa

Table 4: Table of Material Properties

It is evident from Figure 42 that the Armox 307T and 440T armour steel are significantly stronger than the other materials, whereas the 4mm and 3mm mild steel and aluminium plates have

similar strengths. The armour steel is far less ductile than the metals. Mild steel is the most ductile.

4. EXPERIMENTAL RESULTS: 500 X 500 PLATES

This chapter describes the results of the blast tests which were performed on the mild steel, Armox 370T and Armox 440T plates with a side length of 500mm. Thirty one blast tests were performed in total, which included variations of explosive charge dimensions, charge mass, stand-off distance and test plates of different materials. A summary of the results obtained are shown in Figure 43 and Table 5. Note that the results for Armox 440 are shown in green in Table 5.

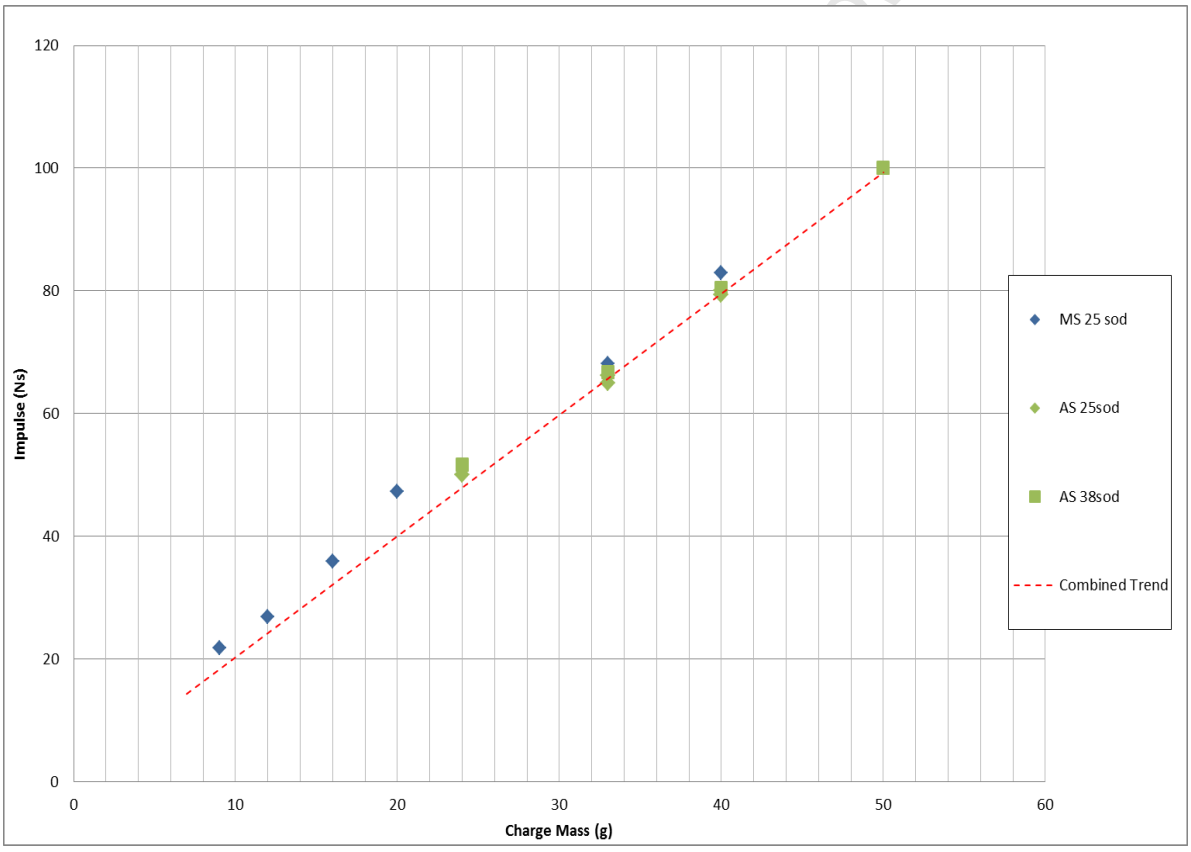

Figure 43: Summary of all Impulse versus Charge mass data for Section 4

Table 5: Summary of Test Parameters and Results for Section 4

Plate Number	Charge Mass (g)	SOD (mm)	Charge Diameter (mm)	Permanent Mid-Point Displacement (mm)	Impulse (Ns)	Dimensionless Impulse	d/H
AS-P2	33	25	50	21.86	66.15	10.29	5.75
AS-P1	40	25	50	29.50	80.02	12.45	N/A
AS-P12	24	25	50	13.54	50.33	5.68	3.56
AS-P10	33	25	50	16.57	64.94	7.38	4.36
AS-P14	40	25	50	19.07	79.31	9.01	5.02
AS-P5	40	38	50	21.27	80.47	8.82	5.60
AS-P7	40	38	40	17.62	82.20	9.76	4.64
AS-P6	50	38	50	27.07	100.06	10.97	7.12
AS-P8	50	38	40	18.62	91.01	10.81	4.90
AS-P11	24	38	50	10.10	51.61	4.13	2.66
AS-P9	33	38	50	12.44	66.71	5.34	3.27
AS-P13	40	38	50	13.78	83.2	6.65	3.63
AS-P3	40	50	50	14.38	82.21	12.79	3.78
AS-P4	70	60	50	25.61	143.21	22.28	6.74
MS-C5	9	25	50	11.26	21.70	6.09	2.96
MS-C6	12	25	50	16.64	26.87	7.54	4.38
MS-C7	16	25	50	19.94	35.94	10.08	5.25
MS-C8	20	25	50	27.58	47.28	13.26	7.26
MS-P8	33	25	50	42.01	68.17	19.12	11.06
MS-P6	40	25	50	53.72	82.93	23.26	N/A
MS-C1	12	25	75	7.48	20.27	4.83	1.97
MS-C2	17	25	75	18.58	34.64	8.26	4.89
MS-C3	21	25	75	24.51	44.49	10.60	6.45
MS-P4	25	25	75	28.80	55.83	13.31	7.58
MS-P1	25	25	75	30.16	56.37	13.43	7.94
MS-P2	40	25	75	48.86	88.60	21.12	12.86
MS-P5	40	25	75	48.88	82.90	19.76	12.86
MS-P3	50	25	75	59.78	116.84	27.84	15.73
MS-P9	25	13	75	34.10	53.55	12.76	8.97
MS-P10	50	38	50	41.58	87.66	17.33	10.94

4.1. 4mm Thick Mild Steel Plates

Plastic deformation which is typical of the Mode I failure type described in section 2 was observed in all the mild steel test plates during a post-test inspection (Figure 46). One plate exhibited failure in the form of tearing in the centre of the deformed bulge, shown in Figure 44 and Figure 45. The deformation profiles of the test plates resembled the expected profiles created by localized blast loading. The profile variations, shown in Figure 46, are attributed to the different charge diameters and stand-off distances.

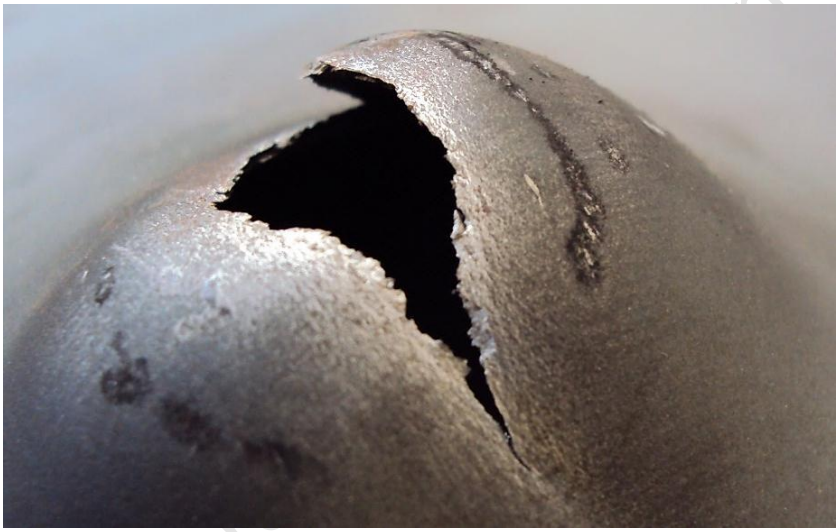

Figure 44: Photograph showing tearing and thinning on MS-P6, Subjected to a 40g, 50mm diameter charge at 25mm SOD

Figure 45: Photograph showing different view of MS-P6 showing tearing and thinning

Figure 46 shows a photograph of the sectioned plates, comparing the deformation profiles of all the 4mm thick square mild steel plates, arranged in descending magnitude of deformation. MS-P3 has a higher final back face displacement than MS-P6 but it has not failed by fracture. The MS-P3 plate was tested with a charge mass of 50g (10g higher than MS-P6) but a larger charge diameter was used (75mm compared to 50mm). Due to its smaller charge diameter, MS-P6 was subjected to a more localised blast load than MS-P3, which resulted in rupture of the plate. The variation in deformation profiles visible in Figure 46 is due to the different explosive charge configurations.

Figure 46: Photograph of deformations profiles of mild steel plate cross-sections arranged in descending order from top

The profiles, separated according to stand-off distance and charge diameter, are shown in the photographs in Figure 47 and Figure 48. The plates which were blast loaded with the 50mm diameter charges exhibit a steeper, more narrow profile compared to the plates subjected to the more uniform blast load provided by the 75mm diameter charge.

Figure 47: Photograph showing deformation Profiles of plates blast loaded with 50mm diameter charges at 25mm sod

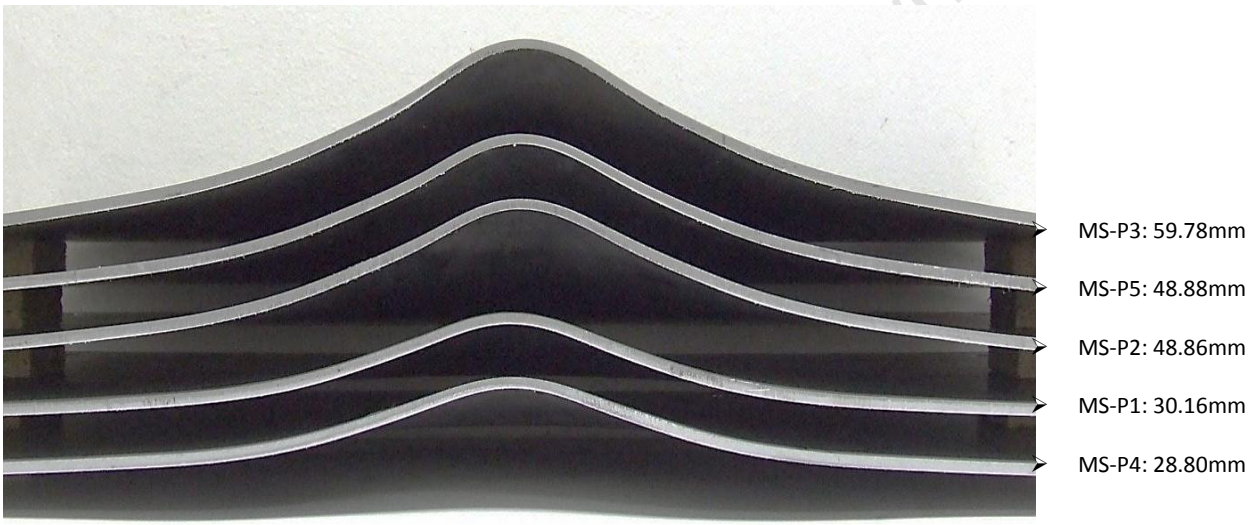

Figure 48: Photograph showing deformation profiles of plates blast loaded with 75mm diameter charges at 25mm sod

4.1.2. Post-test Results

All of materials and their respective charge configurations shown in the graphs in this report are classified by the key shown in Figure 49.

Figure 49: Key of Symbols used in all Graphs

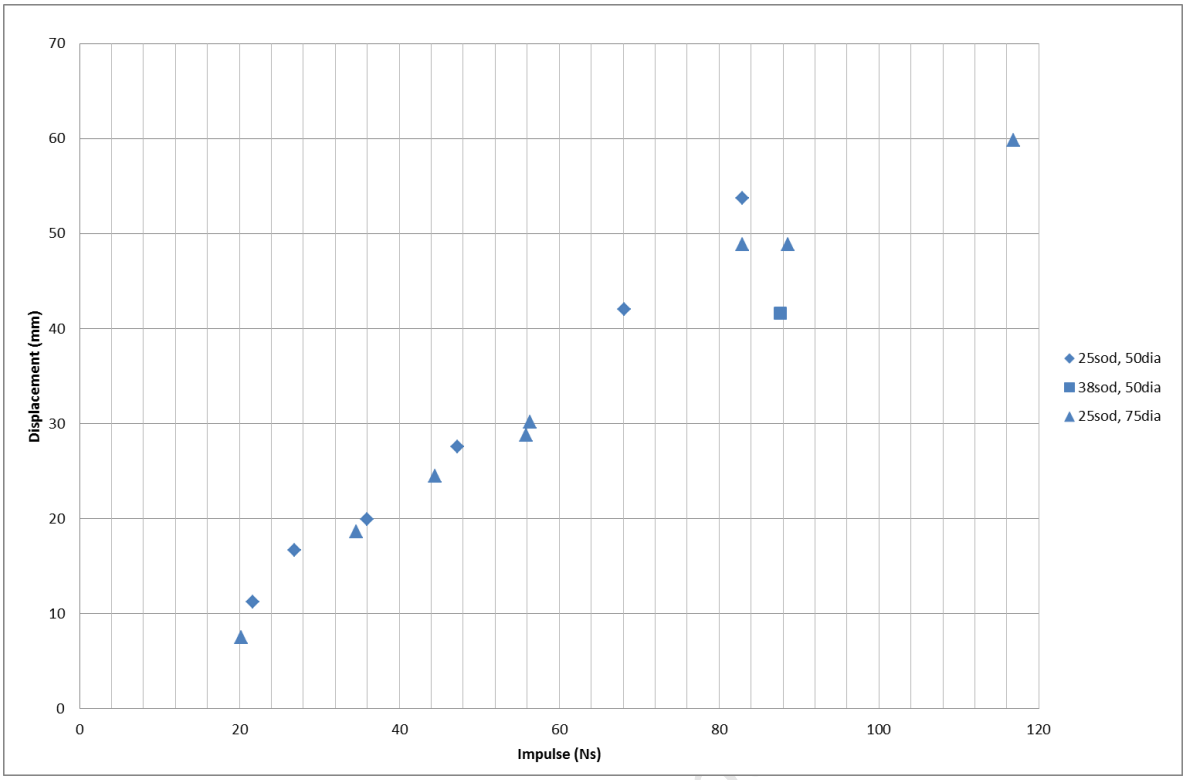

Figure 50: Graph of Displacement versus Impulse for 4mm thick Mild Steel

It is observed from the displacement versus impulse graph in Figure 50 that the 4mm mild steel plates exhibit linear correlation for each combination of stand-off distance and charge diameter. The plates subjected to the 75mm diameter charge blasts at 25mm stand-off exhibit slightly lower displacements, as expected due to the more uniform load distribution.

4.2. Armour Steel Plates (Armox 370T)

The final deformation profiles of the armour steel plates, shown in Figure 51, after blast loading showed similar profiles to that of the mild steel (Figure 46), but with smaller magnitudes of deformation. This result was expected as the armour steel has a significantly higher yield stress and UTS than mild steel. One of the armour steel test plates cracked during a 40g charge mass explosion (50mm diameter charge at a stand-off distance of 25mm).

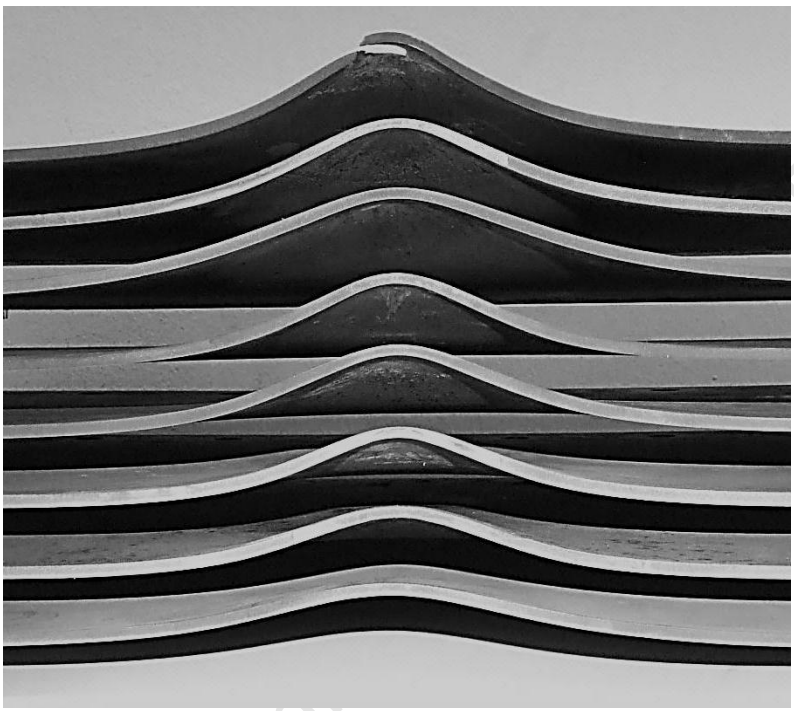

- AS-P1: 29.5mm, Dia: 50mm, sod: 25mm
- AS-P6: 27.1mm, Dia: 50mm, sod: 38mm
- AS-P4: 25.6mm, DIa: 50mm, sod: 60mm
- AS-P2: 21.9mm, Dia: 50mm, sod: 25mm
- AS-P5: 21.3mm, Dia: 50mm, sod: 38mm
- AS-P8: 18.6mm, Dia: 40mm, sod: 38mm
- AS-P7: 17.6mm, Dia: 40mm, sod: 38mm
- AS-P3: 14.4mm, Dia: 50mm, sod: 50mm

Figure 51: Photograph of deformation profiles of armour steel plate cross-sections arranged in descending order from top

Photographs of the crack in the Armox plate are shown in Figure 52 and Figure 53. The cracking in the armour steel plate shows brittle characteristics, indicated by the sharp angular nature of the fracture surface. It can also be observed that the circular nature of the crack indicates the initiation of capping failure.

Figure 52: Photograph of tearing and thinning on AS-P1 (back-face), subjected to a 40g, 50mm diameter charge at 25mm sod

Figure 53: Photograph of front-face (blast loaded side) of AS-P1 (40g, 50mm diameter, 25sod)

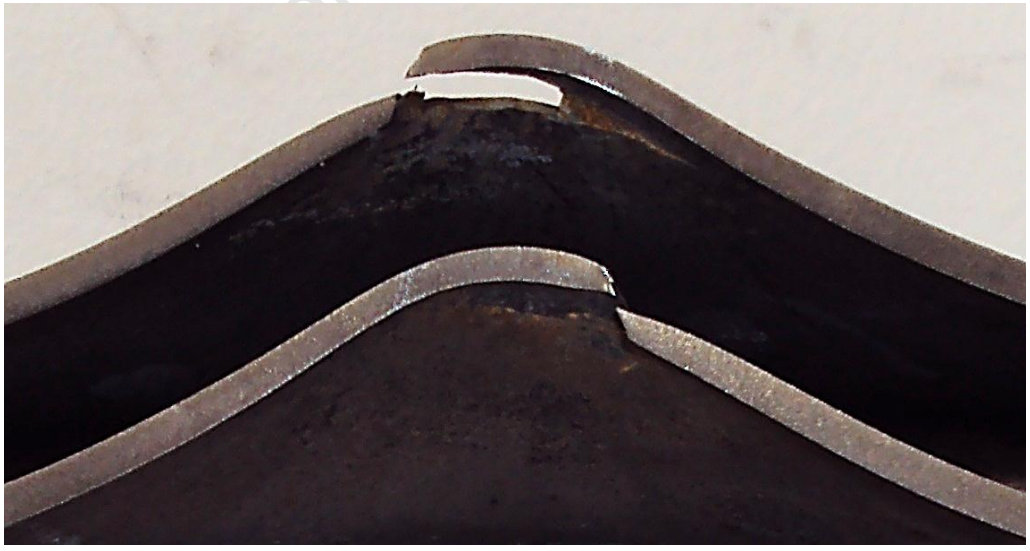

Figure 54: Photograph of cross-section of AS-P1 showing signs of thinning before fracture (40g, 50mm diameter, 25sod)

4.2.1. Post-test Results

Another notable result from the Armox 370T tests are the comparison between the 40mm diameter and 50mm diameter charges for the 38mm stand-off distance tests. Although the 40mm diameter charge produced a more concentrated localised loading condition than the 50mm diameter charge, it produced lower displacements as shown in Figure 55.

A possible reason for the lower displacements of the 40mm diameter charge could be due to the material strength and more brittle nature as compared to mild steel. The ability of the material to greatly withstand the highly localised nature of projectile penetration, such as bullet fire, could be a contributing factor to the lower displacements seen in the 40mm diameter tests. This phenomenon could not be further investigated due to availability of the material.

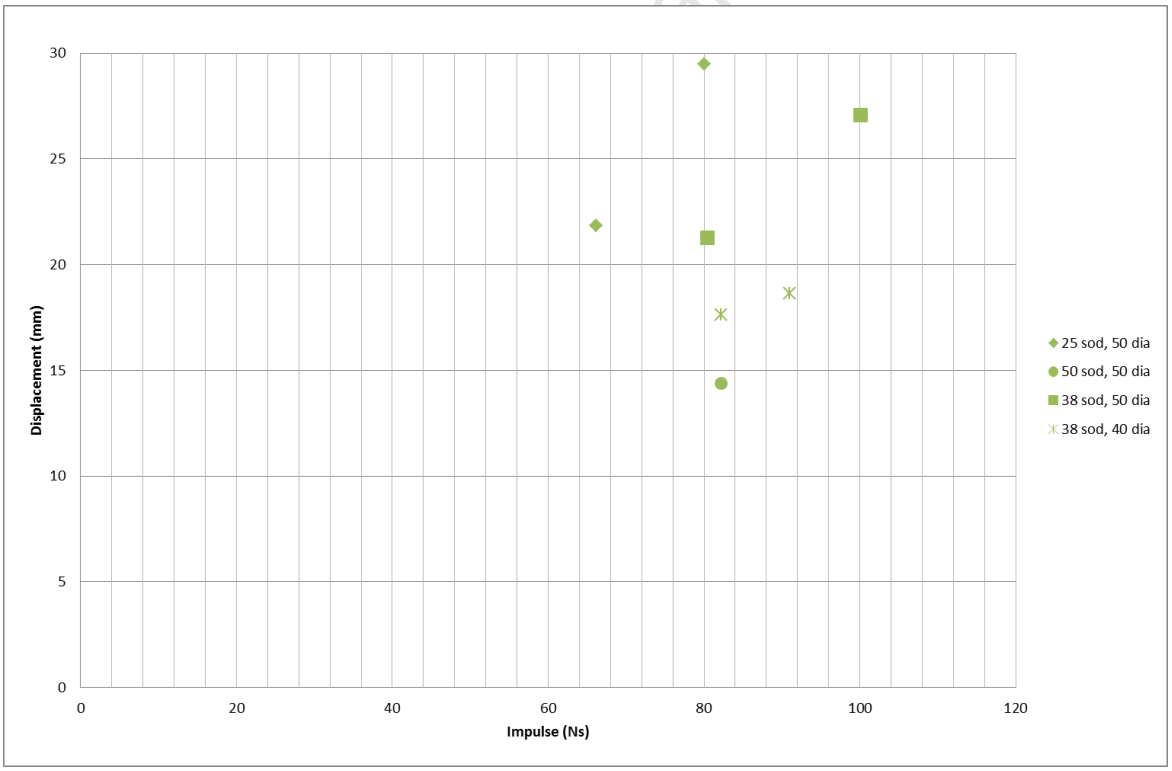

Figure 55: Displacement versus Impulse for 4mm thick Armox 370T

4.3. Armour Steel Plates (Armox 440T)

The second set of stronger armour steel plates, Armox 440T, was also tested using similar blast loading conditions to the Armox 370T as tabulated in Table 5. As the stronger of the two materials, the Armox 440T exhibited significantly lower displacements (up to 35%) compared to Armox 370T.

4.3.1. Armox 440T Plate Deformation

Stand-off distances of 25mm and 38mm were used for Armox 440T (larger stand-off distances would not produce the desired displacements). As there was limited availability of the material, it was decided that the most beneficial method of investigating its response was to test the same charge masses at two different stand-off distances in order to obtain a good range of data for dimensionless analysis.

The deformation profiles for the 25mm stand-off distance and 38mm stand-off distance tests are shown separately in Figure 56 and Figure 57 respectively.

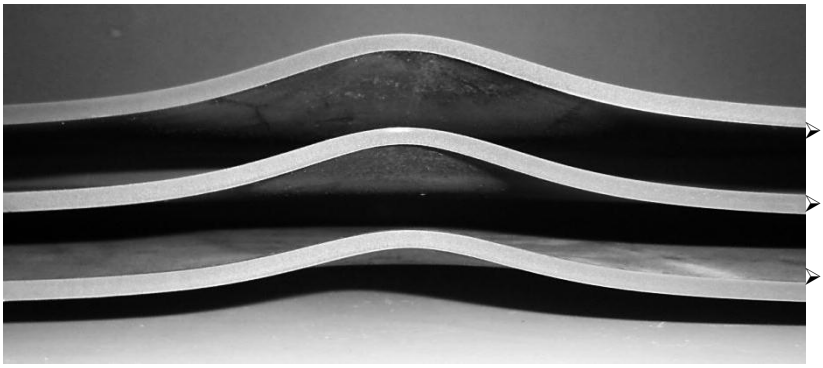

Figure 56: Photograph of deformation profiles Armox 440T subjected to 25sod blast

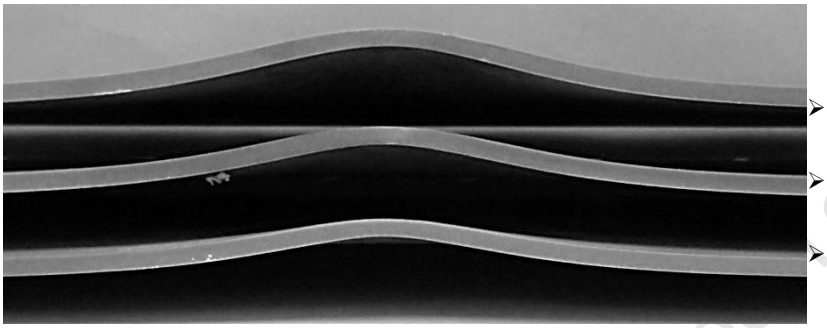

Figure 57: Photograph of deformation profiles of Armox 440T subjected to 38sod blast

Due to the higher strength and lower displacements of the Armox 440T, the difference in the deformation profiles for two stand-off distances is less discernable. It is likely that the Armox 440T could have withstood higher blast loads, but this was not investigated due to lack of availability of the material. The Armox 440T plates were also nominally 0.5mm thicker than the Armox 370T plates, which also contributed towards the lower displacements exhibited. Dimensionless analysis of the test plates, discussed in Section 7.4, will take account of this.

4.3.2. Post-test Results

It can be observed from the displacement versus impulse graph shown in Figure 58 that the 25mm stand-off distance blasts exhibited higher displacements at similar impulses compared to the 38mm stand-off distance blasts. This response was as expected, as a blast of the same charge mass at a closer proximity is known to cause more damage [58]. The displacements of the Armox 440T plates were normalized, with respect to plate thickness and yield strength, and plotted together with the Armox 370T plates in Figure 59. It is observed that the displacements of the Armox 440T plates are still lower than the 370T plates. The difference in displacement can thus be attributed to a difference in material composition as a result of the different treatment processes of the two materials.

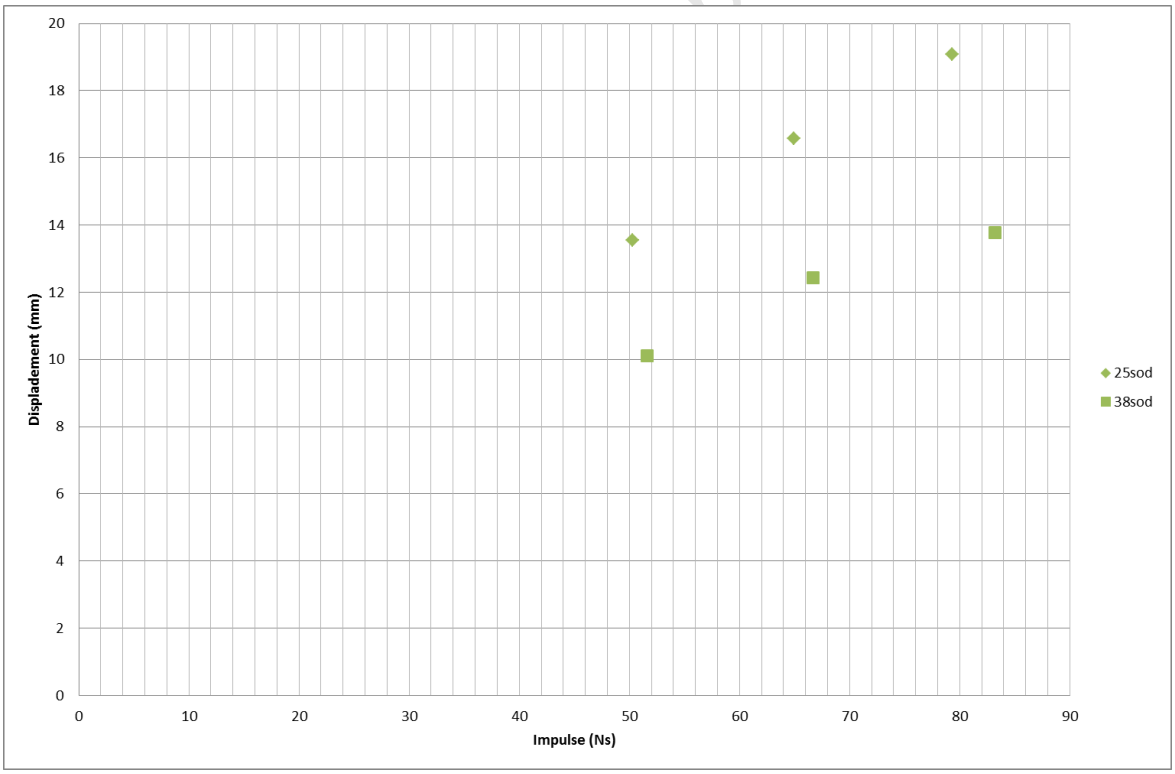

Figure 58: Graph of Displacement versus Impulse for 4.5mm thick Armox 440T

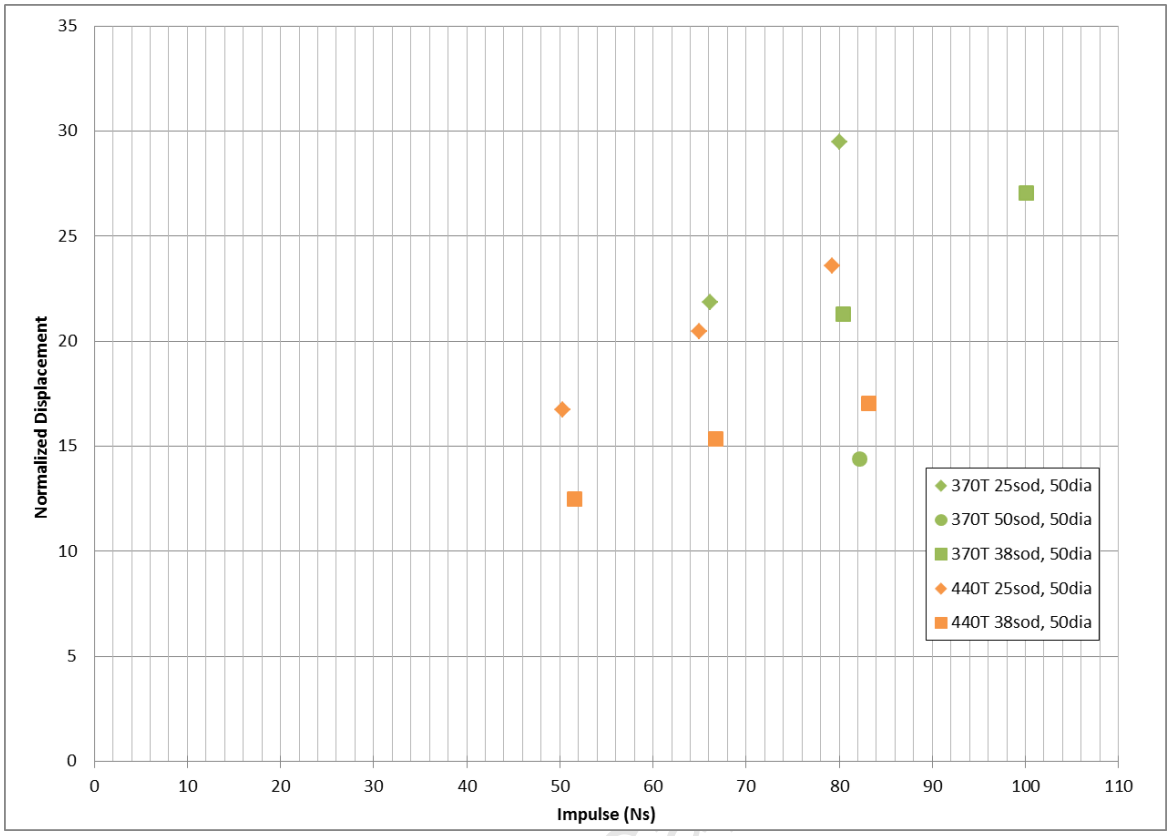

Figure 59: Graph of Normalized Displacement versus Impulse for Armox 370T and 440T at charge diameter of 50mm

5. NUMERICAL SIMULATIONS

Numerical simulations were performed in order to analyze the behaviour of the mild steel and armour steel plates. The simulation allowed additional insights into loading and response which are difficult to measure directly from the blast tests. The numerical simulations were performed using AUTODYN, an engineering hydrocode software which was designed for solving non-linear dynamic problems using Lagrangian, Eulerian and ALE solvers [59].

5.1. 2D Model

The detonation for all of the various charge configurations were modeled in 2D, and then re-mapped into the final 3D model once detonation has occurred. A 3D model was required to model the plate behaviour as the test plates were square and so a quarter-symmetry model was constructed. Detonation is modelled using a 2D axi-symmetric model to allow for a small mesh size and acceptable run time. The charge geometry, shown in Figure 60, was detonated and run until one cycle before the pressure wave reached the rigid reflective boundary (which will be the position of the plate in the 3D model) and then re-mapped. The purpose of this process was to retain the maximum amount of pressure from the detonation model before it is re-mapped into the coarser 3D air mesh. Thus, at the point of remapping the optimal pressure is still present just before contact with the test plate is made, and the pressure will only start to reduce once it is reflected away from the test plate.

The detonation mesh size, which could have some effect on the detonation pressure, was investigated by Ozinsky [53] and Rossiter [54]. Ozinsky [53] and Rossiter [54] both determined that a coarser mesh (such as a 10mm mesh) gives lower pressures than a finer mesh for a blast tube configuration simulated in AUTODYN. The CJ pressure for C4 explosive as given in the

AUTODYN material library is approximately 28GPa [59]. Thus the mesh size chosen should produce similar pressures while also being coarse enough not to have significantly long run times.

Initially a 0.5 x 0.5mm mesh size was used which gave a CJ pressure of 19 GPa, which is 30 % below CJ pressure. A much finer 0.2 x 0.2mm mesh size was then used with a resulting pressure of 22 GPa, which differs from the theoretical CJ pressure by less than 20%. It is noted that the CJ pressure is determined experimentally for confined detonations, and therefore it would not be possible to reach this in an unconfined detonation. It was thus decided that the 0.2mm mesh would be used and that the 20% deviation from the CJ pressure was acceptable.

An air block with a 1mm mesh size was constructed. The air block was partially filled with explosive of a specific geometry as required for different charge masses and diameters (see Figure 60 for example). Initially the detonation model was made up of an ungraded air mesh, whereas the final detonation was modelled with a graded air mesh of 0.2mm biased in the region where the pressure wave first interacts with the test plate. Due to computational limitations with running 3D graded air meshes in AUTODYN, the 2D detonation model was graded instead. Figure 61 shows the detonation model at the time it is re-mapped into the 3D model in (a) and the grading bias of 25mm in the x and y direction from the plate boundary (b).

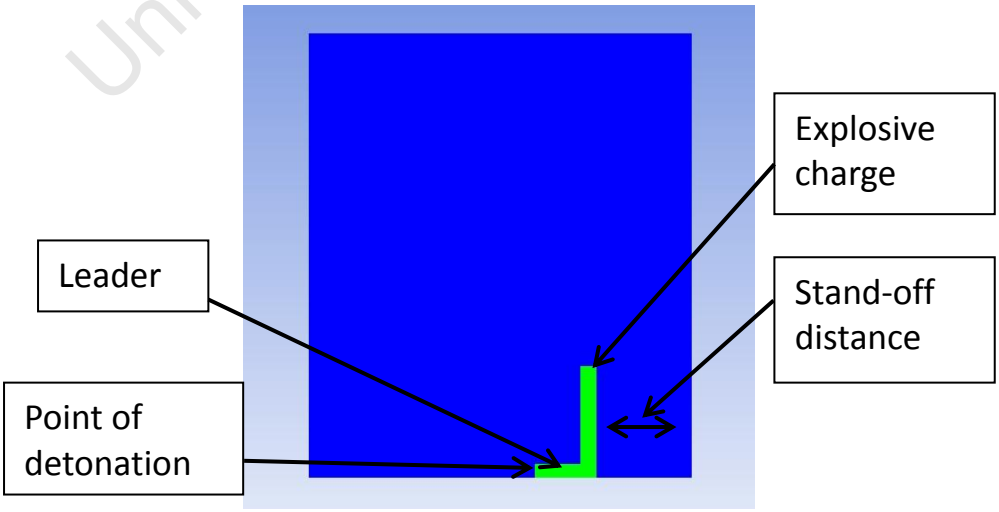

Figure 60: 2D model of explosive

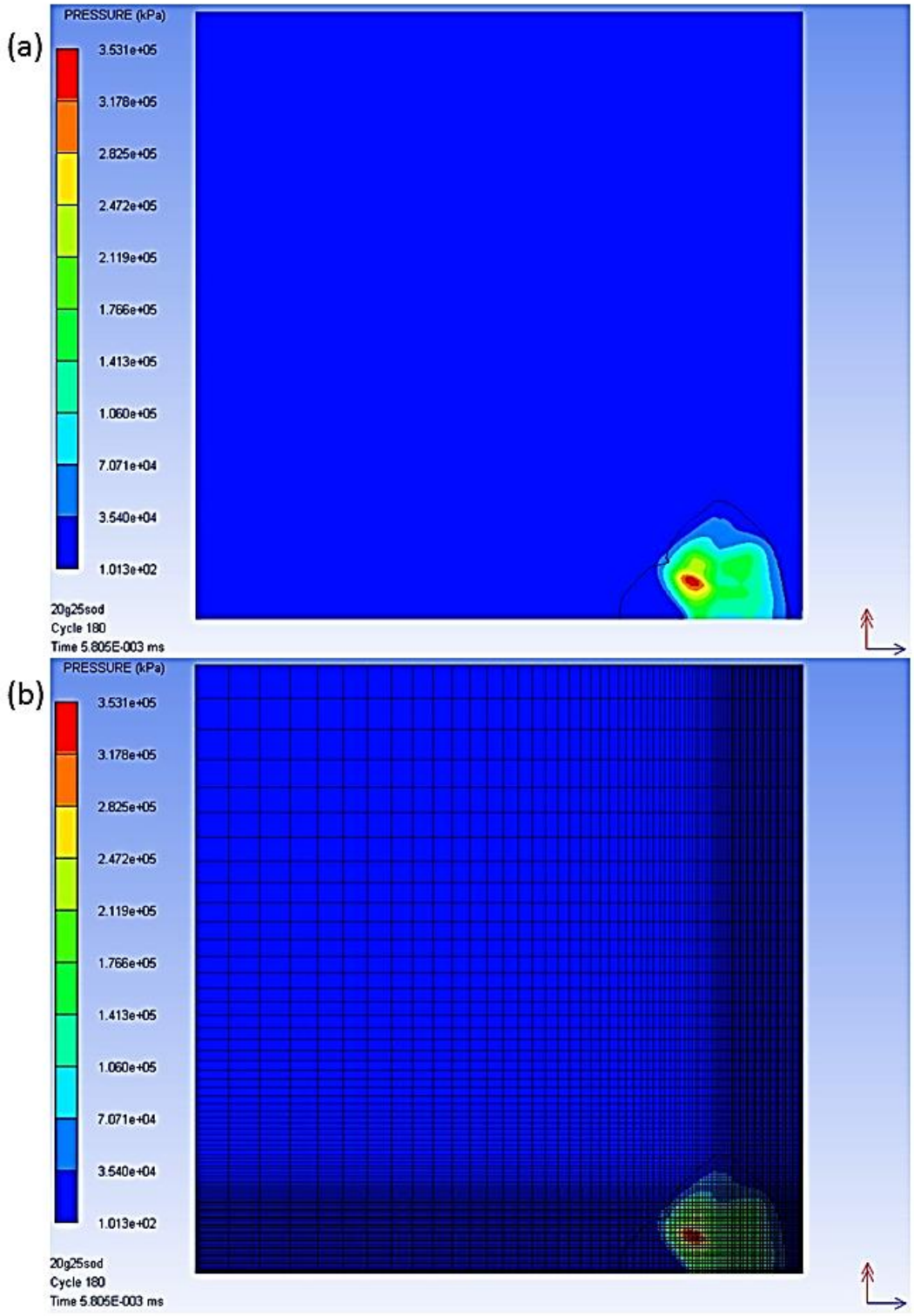

Figure 61: 2D Detonated charge which is re-mapped into 3D model (a) and grading bias in the detonation model (b)

5.2. Boundary Conditions

During the blast, the back of the plate is covered with a shroud in order to prevent the flash from the explosion from interfering with the light interference equipment. By covering the area behind the test plate the shroud also prevents any pressure from flowing around and behind the plate during the blast. This achieved in the 3D model by applying a flow out boundary condition to the block of air at the front of the plate. Thus any pressure flowing over the plate during the blast will flow out from the boundary of the front air block and is prevented from flowing into the back air block. In Figure 62 the flow-out boundaries are labelled on the air block faces, as appropriate.

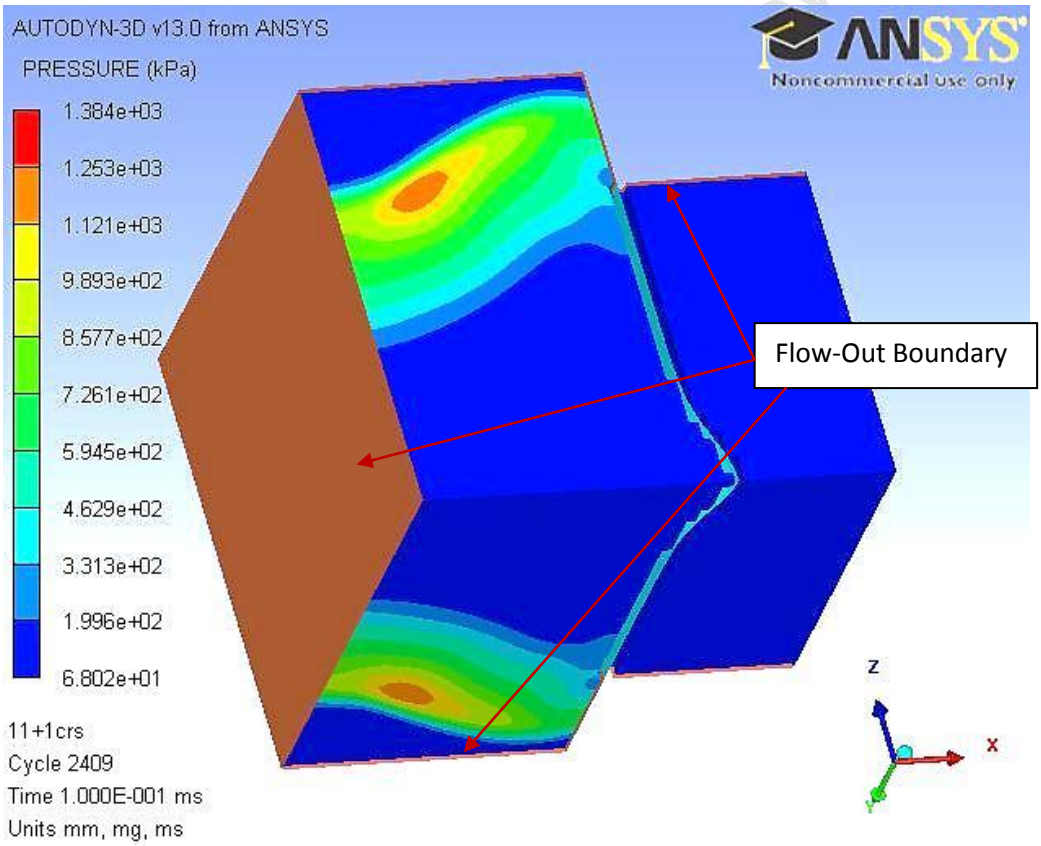

Figure 62: 3-D Model showing flow-out boundaries

The test plate is modelled as a shell with the same thickness and material characteristics as the plates used in the experiments. In order to replicate the clamping conditions of the experimental tests as accurately as possible zero velocity boundaries are used in different configurations. Firstly, a zero x-velocity boundary is used to simulate the effect of the clamp frame. This boundary only inhibits movement of the plate along the direction of the x-axis (along the direction of blast) and is created to be the same dimensions as the clamp frame (Figure 63).

Figure 64 shows the zero y-velocity boundaries which prohibits movement of the plate along the y-axis of the model. The boundaries are placed separately in intervals along the edge of the plate in order to simulate the effects of the bolts in the experimental set up. The same boundary conditions are placed along the adjacent side to simulate the bolts acting on the z-axis.

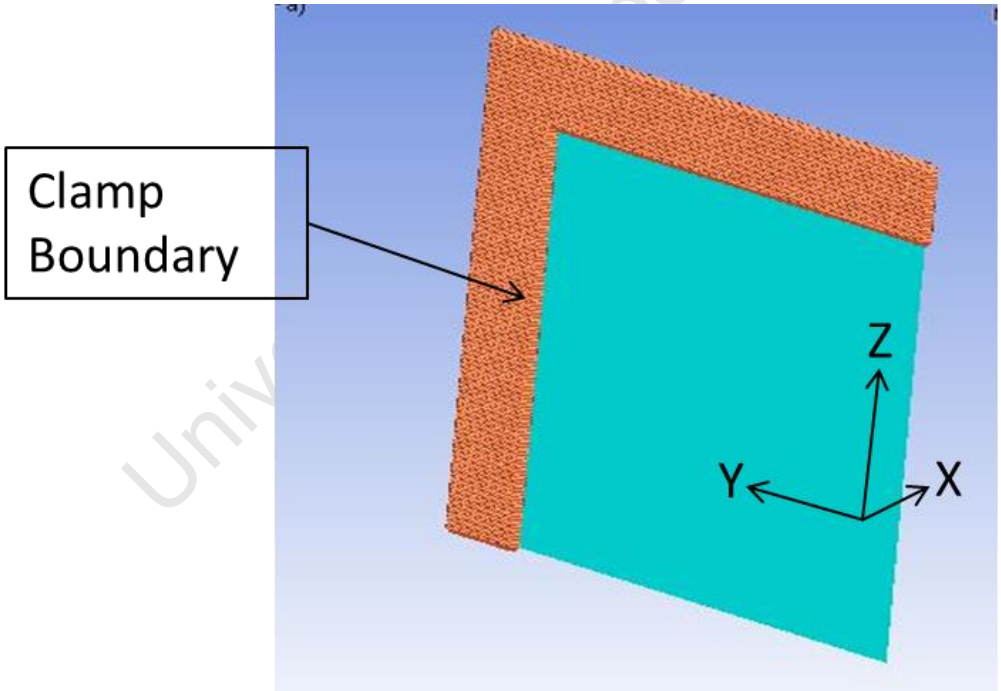

Figure 63: Image showing the zero x-velocity boundaries replicating the clamp frame

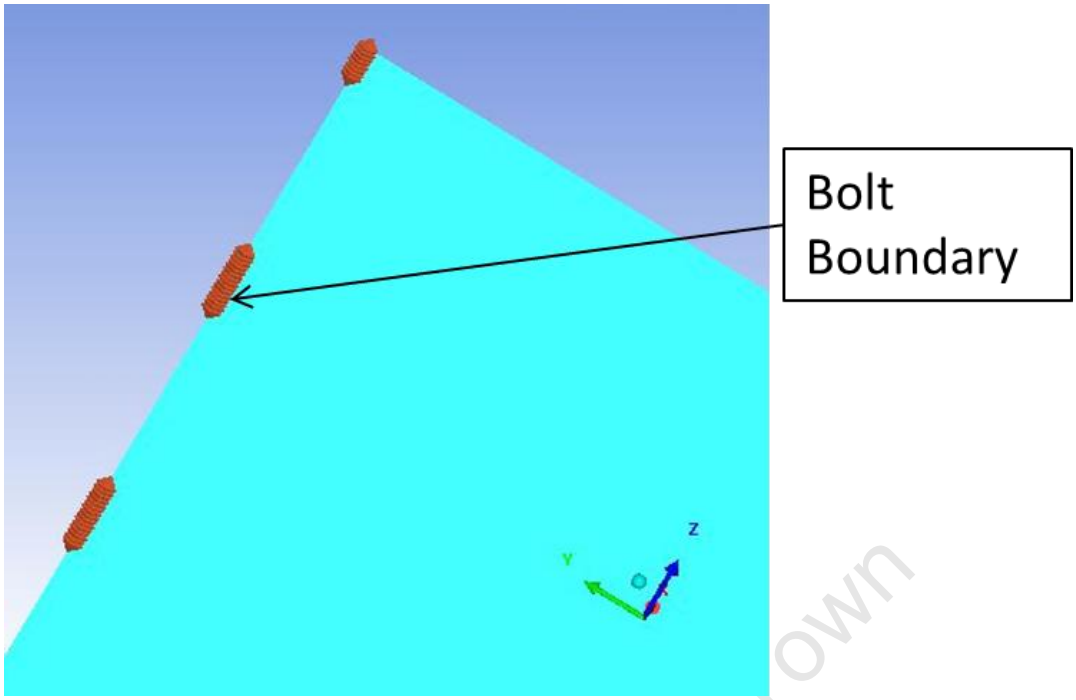

Figure 64: Zero Y and Z velocity boundaries along edge of plate to simulate bolts

5.3. Final Model

The final model used in the computational analysis of the experiments is similar to the preliminary model in design, but with differences in mesh sizes and in the re-mapped detonation model. The air blocks are built up of an air mesh with a resolution of 5mm, which is subject to the computational limits of AUTODYN, and the computing hardware available.

5.3.1. Air Mesh Size

The geometry of the 3-D model must replicate the experimental conditions as closely as possible in order to ensure accurate results. The air domain is comprised of two blocks of air of different sizes joined together. The larger air block is on the front face of the plate and is where the detonation model is re-mapped into. The second smaller block of air is at the back face of the plate and covers the same surface area of the plate. The larger block of air in front of the plate will be referred to as the front air block and the smaller block of air behind the plate will be referred to as the back air block, shown in Figure 65.

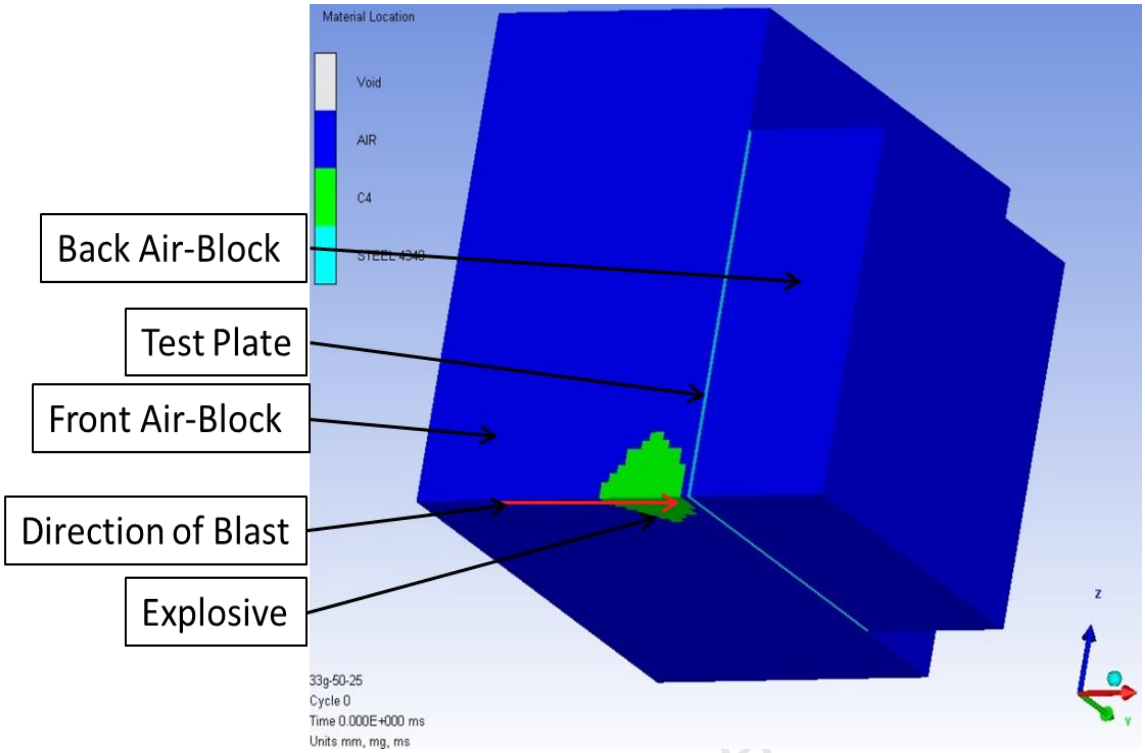

Figure 65: 3-D Model showing front and back air blocks and re-mapped explosive

The decision on the size and resolution to be used for the air mesh used was mainly dictated by the computational limits of AUTODYN as well as the available hardware. Due to the relatively large size of the test plates, the size of the front air mesh used was 200mm in the x-direction and 240mm in the y and z-directions, for a 3 dimensional quarter symmetric model. The size of the back air mesh was made to be the same size as the test plate. The reason the front air mesh was made to be larger than the test plate was to allow for the blast pressure to flow past the plate in the x direction, instead of directly out of the air mesh in the y and z directions if the air mesh was the same size as the plate in order to match the experimental conditions as closely as possible. The purpose of the back air mesh being the same size as the plate, as well as not being joined to the front air mesh, is to simulate the effect of the shroud used in the experimental setup which prevents the pressure wave from flowing behind the plate.

The resolution of the air mesh that was used was also dictated by computational limits as the model was too large and the test conditions were too extreme to allow for a finer air mesh

resolution. The resolution for the air mesh used was 5mm, meaning the each block of air that comprised the entire air mesh was 5mm x 5mm. The finely graded 2D model was then re-mapped into the coarse 3D model.

The final modification to the air mesh was the deactivation time, changing to 0.3ms from 1.2ms from the preliminary model. The reason for de-activating the air mesh earlier is due to the fact that the pressure loading the plate has already subsided completely before 0.3ms and keeping the air mesh active until 1.2ms would increase the run-time unnecessarily. By 0.1ms, the pressure loading the plate has already dissipated and the plate is deforming due to inertia from the impulse. Figure 66 shows the pressure-time histories of the various charge masses tested, which clearly shows that the pressure on the plate surface has completely dissipated before reaching 0.1ms. Thus by de-activating both the front and back air meshes a significant amount of unnecessary computational is eliminated, which decreases the total run-time by two to three days to between 25-35 hours.

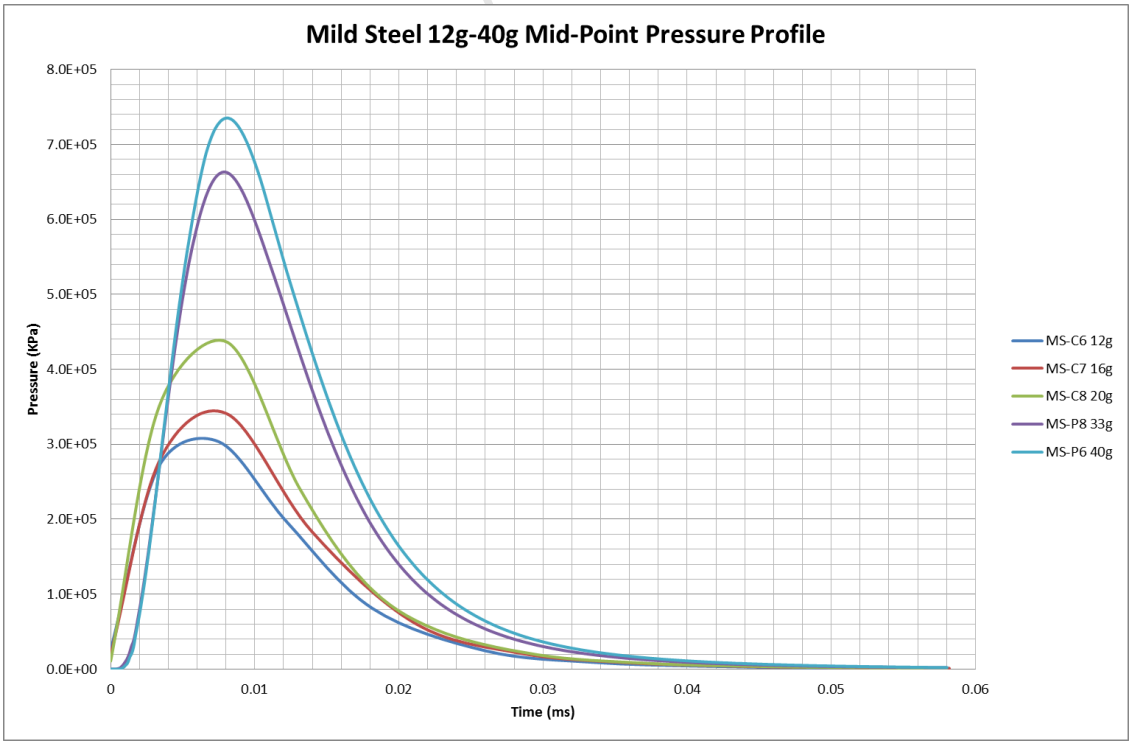

Figure 66: Pressure-time histories of various charge masses

5.3.2. Plate Mesh Size

The plate was modelled as a shell element rather than solid continuum elements to avoid material leakage through the plate. Shell elements only have one element through the entire thickness of the plate. The plate element size should ideally be at most half that of the air mesh size, a 2mm element size was used.

5.3.3. Material Modelling

The air was modelled as an ideal gas, with the ideal gas equation of state being:

$$PV = nR_gT \qquad \text{(eq. 30)}$$

An alternative expressed may be used:

$$P = \rho_a(\gamma - 1)E_0 \qquad \text{(eq. 31)}$$

Where ρ_a – air density, γ – ratio of specific heats C_p/C_v, E_0 – Specific internal energy as given by:

$$E_0 = C_vT \qquad \text{(eq. 32)}$$

Where T – temperature

The material properties of air are obtain from the AUTODYN material library [59], and are given in Table 6.

Table 6: Material properties used for air in the computational model

ρa (g/cm³)	T (K)	Cp (kJ/kgK)	Cv (kJ/kgK)	γ	Eo (kJ/kg)
1.225 x 10^{-3}	288.2	1.005	0.718	1.4	206.8

5.3.4. Explosive

The Jones-Wilkens-Lee (JWL) equation of state is used to model the rapid expansion of detonated high explosive products. The explosive initiation is idealised as a line of detonation moving through each cell of the explosive and the expanding gas pressure is given as:

$$p = A\left(1 - \frac{\omega\rho_p}{R_1\rho_e}\right)exp\left(-R_1\frac{\rho_e}{\rho_p}\right) + B\left(1 - \frac{\omega\rho_p}{R_2\rho_e}\right)exp\left(-R_2\frac{\rho_e}{\rho_p}\right) + \omega\rho E_0 \quad \text{(eq. 33)}$$

Where ρ_e – density of explosive, ρ_p – density of explosive products, E_0 – specific internal energy and A, B, R_1, R_2 – empirically derived constants.

The AUTODYN material library has C4 as the closest equivalent to the PE4 used in the experimental tests. AUTODYN reverted back to the ideal gas equation of state for the remaining calculations once all the explosive material had been completely consumed, leaving behind high temperature and pressure gases.

Table 7: Material Properties used for C4, from AUTODYN Material Library [59]

ρ (g/cm^3)	A (GPa)	B (GPa)	R 1	R 2	ω	CJ Detonation Velocity (m/s)	CJ Energy/Volume (kJ/m^3)	CJ Pressure (GPa)
1.601	609.8	12.96	4.5	1.4	0.25	8193	9.0E+06	28

5.3.5. Plate Materials

The effects of the strain rate on the different materials were modelled using the Cowper-Symonds material model (eq. 34) and the strain hardening effects were modelled using power law hardening. The true stress-strain data obtained from the quasi static tensile test results (reported in Section 3) were used to obtain the required parameters. A least squares fit between the power law hardening curve and the true stress-strain curve was used to obtain A, B and n. The values for D and q used for mild steel were obtained from the materials library in AUTODYN

[59]. Due to the strain rate insensitive nature of armour steel (for highly work-hardened materials) [51], the D and q values were ignored (left as zero). The temperature effects were also neglected.

$$\sigma = (A + B\varepsilon^{n})\left(1 + \left(\frac{\dot{\varepsilon}}{D}\right)^{\frac{1}{q}}\right) \qquad \text{(eq. 34)}$$

Where ε̇ - plastic strain rate

The values obtained for the Cowper-Symonds material model for each of the materials used is shown in Table 8.

Table 8: A, B and n values obtained for materials used in computational models

Material	A (MPa)	B (MPa)	n	D	q
Mild Steel	259.95	491.46	0.567	3117	2.226
Armox 370T	1142.94	1447.66	0.560	0	0

5.3.6. Output Variable

Transient displacement-time histories for the plate were obtained by placing gauges on the test plates. Simulated plate movement was recorded by the gauges and exported to Microsoft Excel, where a displacement-time graph was plotted. Figure 67 shows the position of the gauges used to obtain displacement.

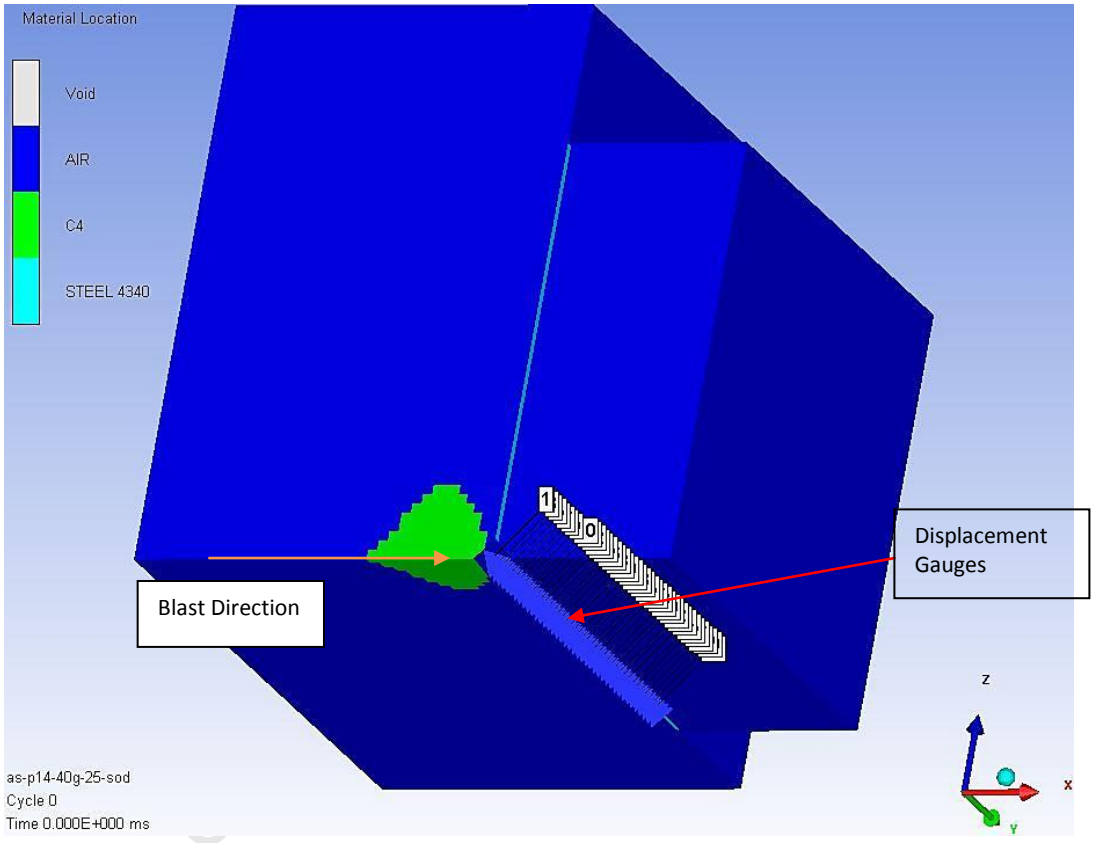

Figure 67: Final model used in numerical simulation of blast tests

To obtain pressure-time histories from the simulations, the test plate was replaced by a rigid reflective boundary on which the gauges are placed, represented in Figure 68. The reason for this modification is because the gauges are incapable of recording any pressure readings while the plate is occupying the same node, and gauges placed on the plate are only able to record displacement. In addition, as the blast wave deformed the test plate, a space was created behind the gauges and caused a slight pressure drop once the plate started to move. In order to

determine whether this modification has a significant effect on the pressure readings, gauges are placed at fixed locations in both the rigid boundary model as well as the test plate model. The pressure reading from the two different models are compared in Figure 69. Overall, the pressure behaviour in the models is well compared, although the reflective boundary model does predict a higher peak pressure and increased residual pressures at the gauge location of interest which can be attributed to the pressure drop created by movement of the plate.

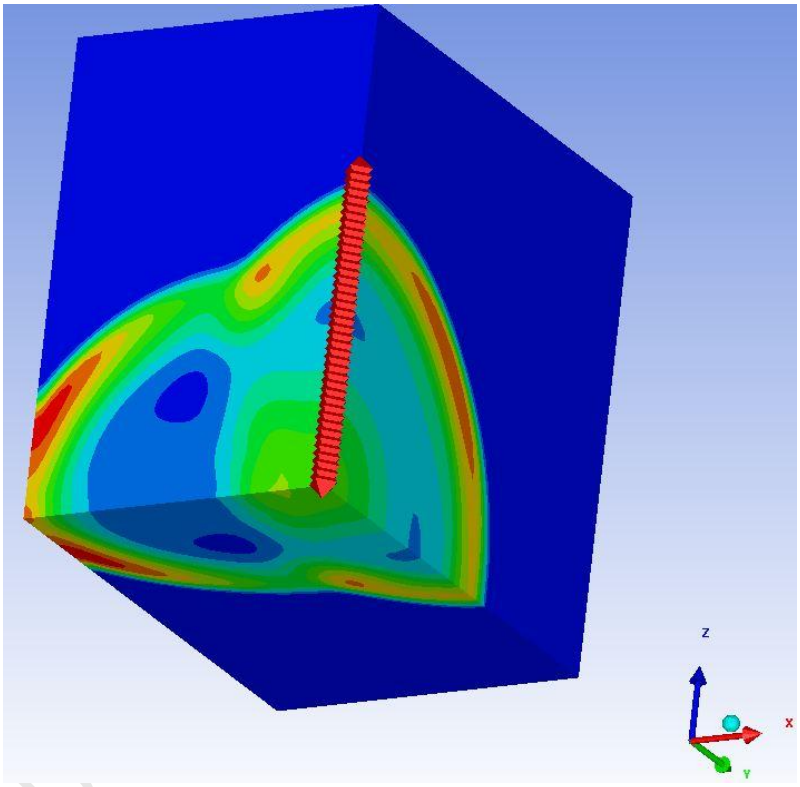

Figure 68: Position of Gauges used in Pressure model to obtain pressure–time histories and impulse for a 16g detonation

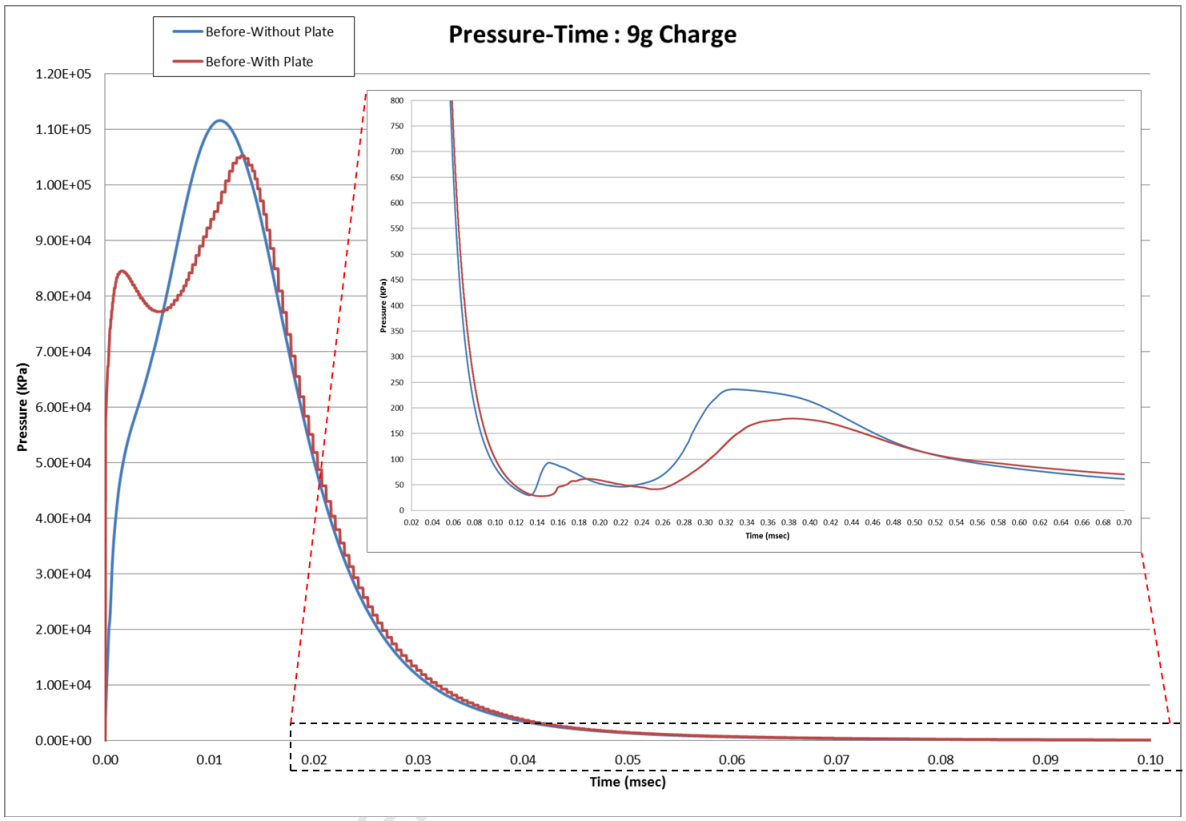

Figure 69: Graph showing the difference between the pressure readings for rigid boundary (blue) and test plate (red) for a 9g charge mass at 25 SOD

5.4. Simulation Results

Some of the transient results obtained from the numerical models are briefly discussed in this section. Most of the numerical results are compared to the experimental transient measurements and discussed in greater detail in Section 7.

Pressure-time histories at different distances from the mid-point are shown in Figure 70. As expected, pressure decreased as the distance from the mid-point increased. Figure 71 and Figure 72 shows the distribution of the plastic strain in the test plate on the right side and the accompanying pressure contour on the left side for MS-C7, subjected to a blast load of 16g (50mm diameter charge at a stand-off distance of 25mm), at various times from the peak pressure (A) until the pressure wave has subsided at (F), as shown in Figure 70.

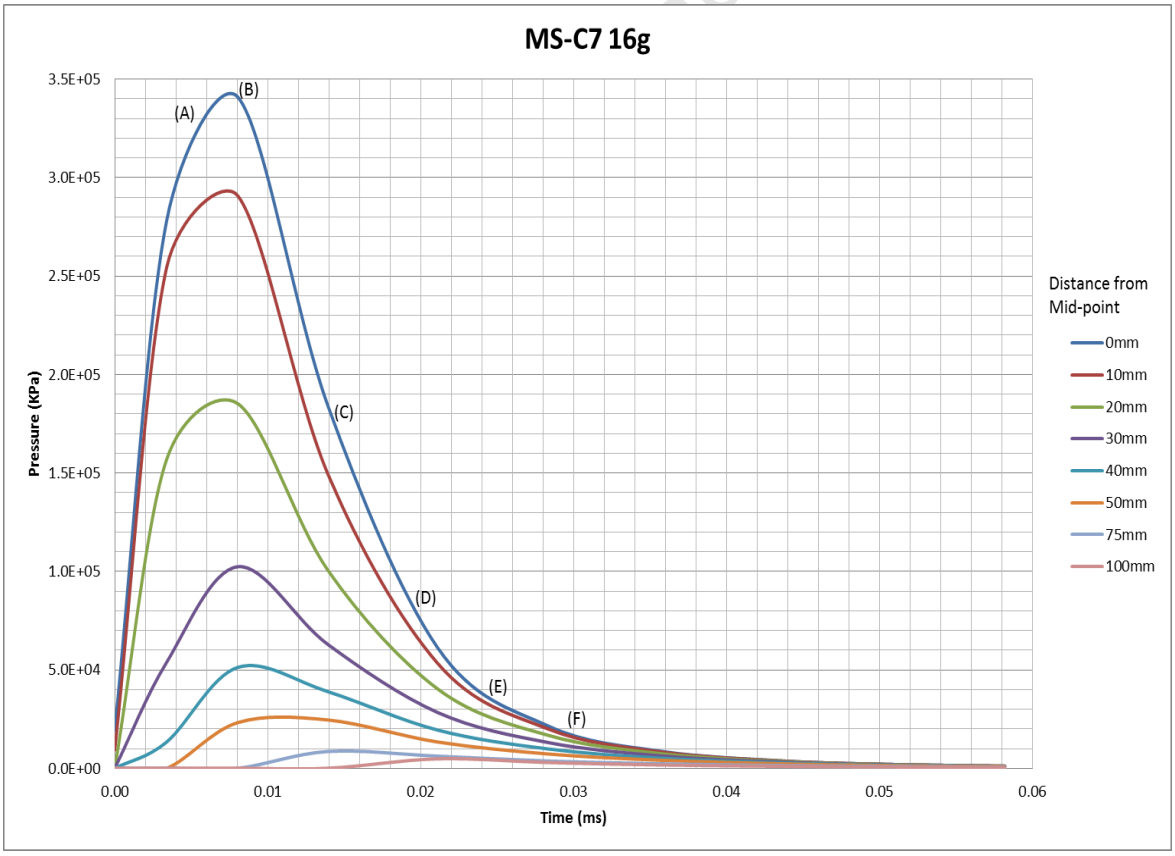

Figure 70: Pressure-time histories of MS-C7 at different distances from mid-point showing significant points from

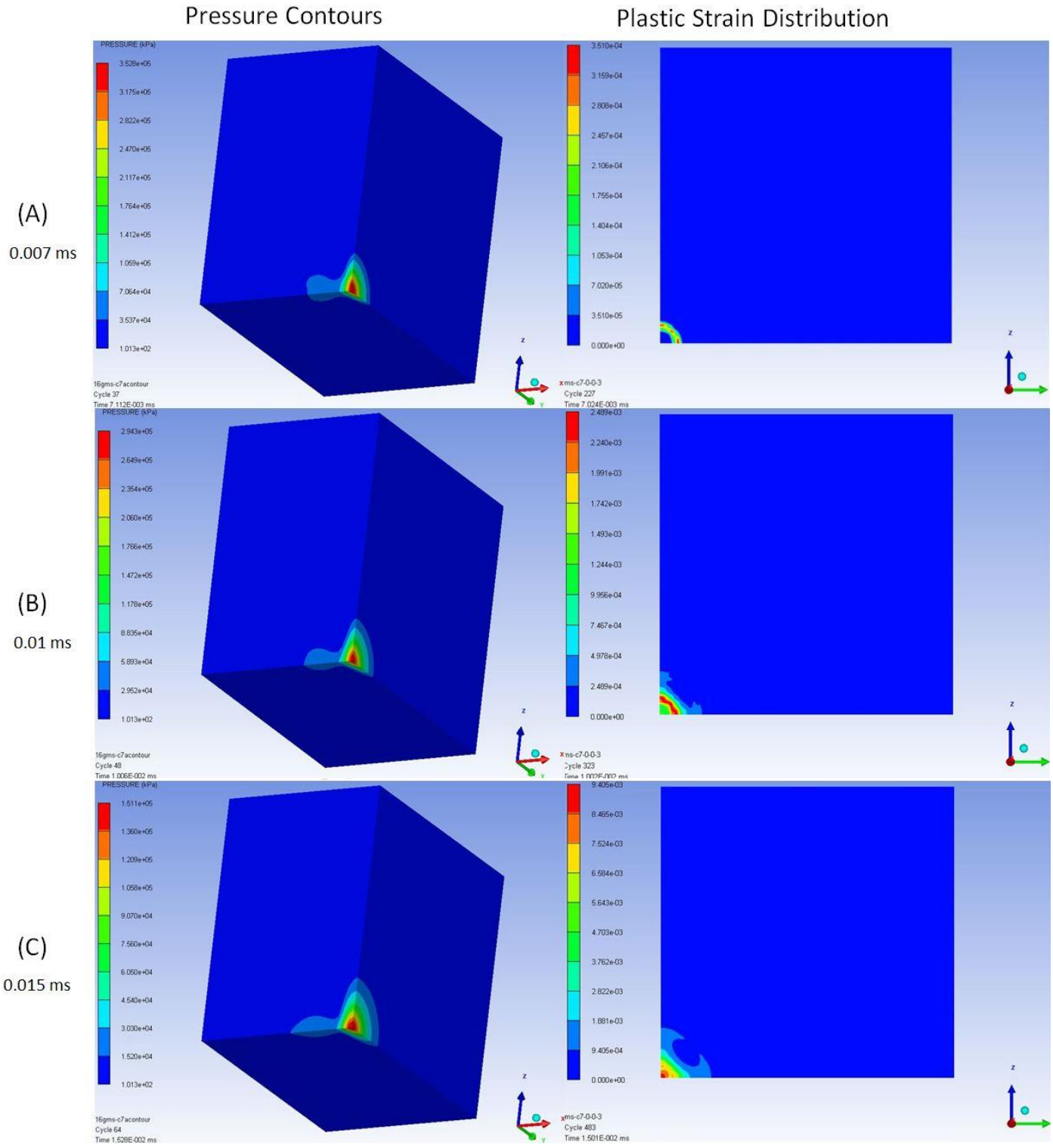

Figure 71: Plastic Strain Distribution and Pressure Contours from MS-C7 Numerical Model

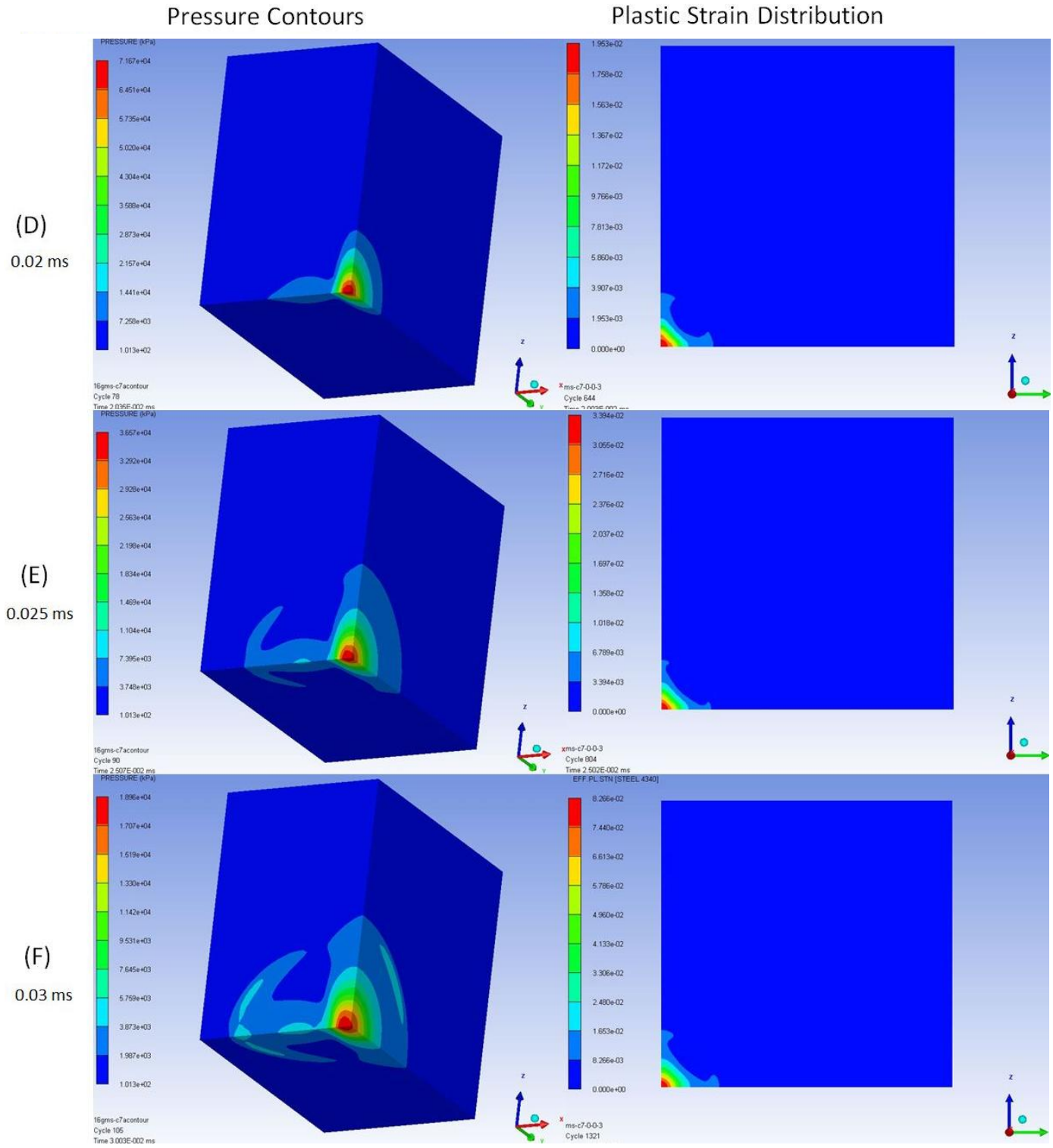

Figure 72: Plastic Strain Distribution and Pressure Contours from MS-C7 Numerical Model (continued from Figure 71)

From the contour plots in Figure 71 and Figure 72, it was observed that initial signs of plastic strain were evident between 7µs and 30µs were small, and that the plate deformation is not significant. As can be seen at 30µs (time F) in Figure 72 the pressure wave had not yet expanded fully, although the peak pressure has decreased significantly. The test plate only started to respond plastically at 7µs, once the pressure was almost at its peak, as shown in Figure 73. This could be due to the inertia of the material. It can be observed that the plastic strain experienced by the test plate was mostly concentrated around the mid-point of the plate, which was expected due to the localised nature of the blast load. The mid-point displacement of the plate continued to increase until it reached its peak at 1.2ms, 0.9ms after the air mesh was de-activated, as shown in Figure 74.

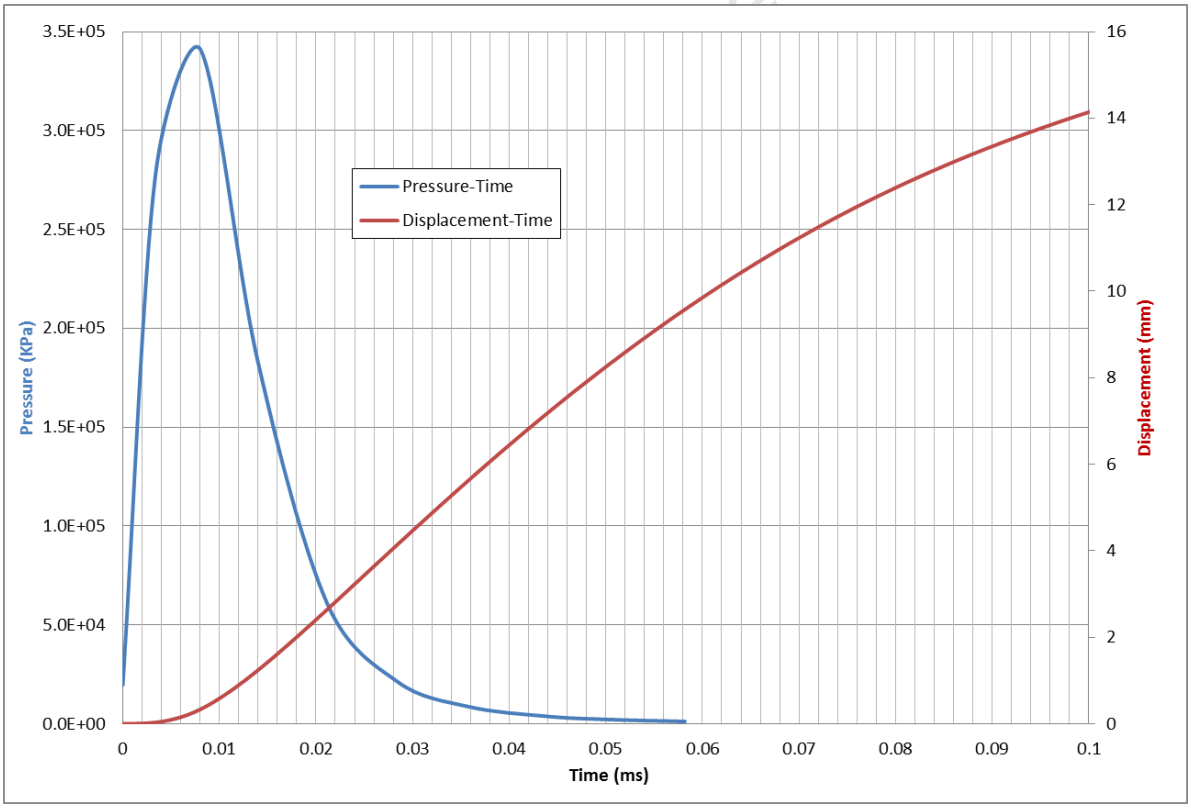

Figure 73: Plot of Mid-point Pressure-time and Displacement-time for MS-C7

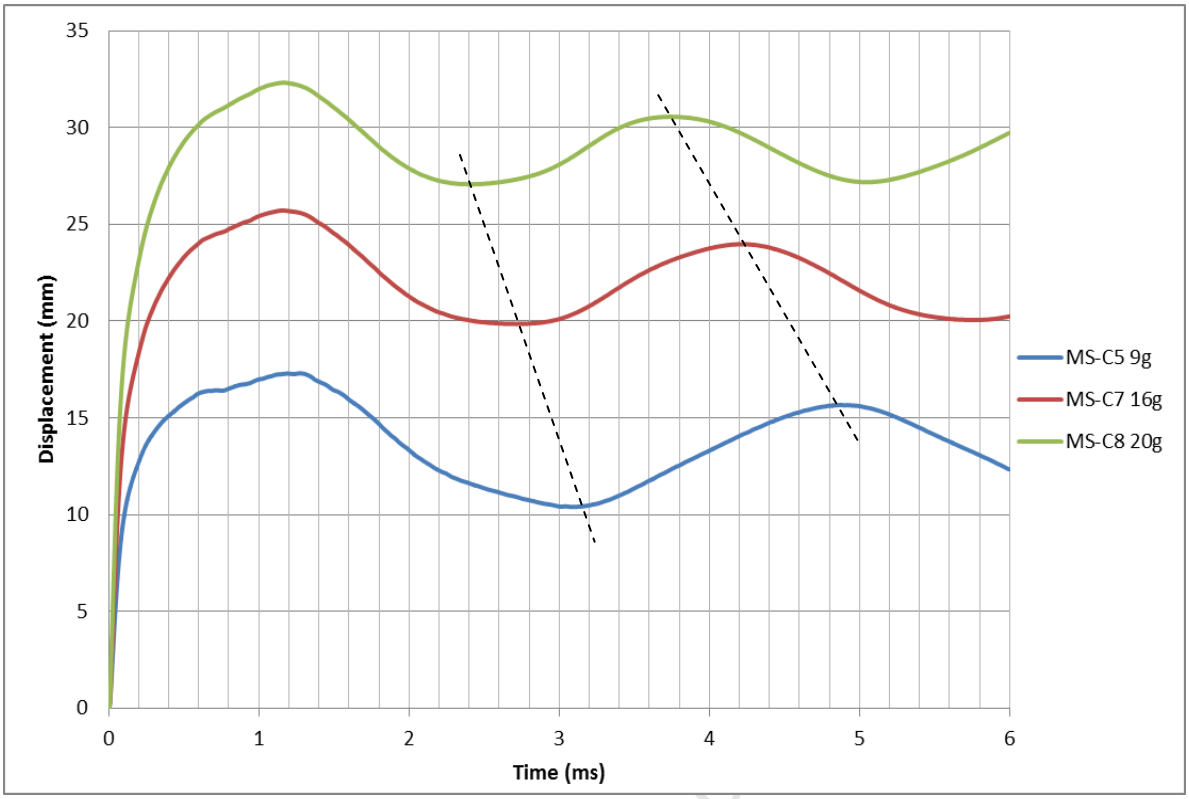

Figure 74: Displacement-time histories of mild steel subjected to 9g, 16g and 20g charge masses

The simulated displacement-time histories for mild steel subjected to blast loads of 9g, 16g and 20g are shown in Figure 74. As expected, the displacements increase with increasing charge mass. It was also observed that the period from the second peak onwards also shortens as the charge mass is increased. The period between oscillations decreases by approximately half a millisecond between each increase in charge mass. This was most likely due to the increased plasticity and the shape of the deformed plate changing, making the period of elastic vibration change.

6. EXPERIMENTAL RESULTS: 400 X 400 PLATES

The results of blast tests on mild steel, aluminium, Twintex GFPP and Dyneema UHMWPE plates with a side length of 400mm are presented in this chapter. Once clamped, these plates have an exposed are of 300mm x 300mm. The results are reported by material type in the following sections.

6.1. Mild Steel

The response of the smaller mild steel plates was similar to the larger ones with regards to the deformation profiles and the back face displacement. Three plates exhibited varying stages of failure, namely: MS400-11 (Mode IIIp), MS400-12 (Mode Itc) and MS400-15 (Mode II*c). MS400-12, subjected to a 24g charge at a stand-off distance of 25mm, showed preliminary signs of failure with signs of capping and thinning clearly distinguishable in Figure 75 and Figure 76. The next stage of failure was tearing and partial capping of the central region of the blast loaded plate shown by MS400-15, loaded with a 33g charge at a stand-off distance of 38mm, in Figure 77,Figure 78 and Figure 79. A summary of the test parameters and results for all the mild steel plates are shown in Table 9.

Table 9: Table of blast testing parameters and results for 3mm thick mild steel

Plate Number	Charge Mass (g)	SOD (mm)	Charge Diameter (mm)	Permanent Mid-Point Displacement (mm)	Impulse (Ns)	Dimensionless Impulse	d/H
MS400-4	7	25	50	10.32	13.02	8.31	3.44
MS400-5	9	25	50	17.18	19.10	12.18	5.73
MS400-6	12	25	50	25.15	25.42	16.21	8.38
MS400-7	16	25	50	36.02	33.02	21.06	12.01
MS400-8	20	25	50	42.33	44.85	28.61	14.11
MS400-12	24	25	50	48.51	46.41	29.60	16.17
MS400-11	28	25	50	torn	54.00	34.45	N/A
MS400-1	12	25	75	15.38	20.27	10.76	5.13
MS400-2	17	25	75	29.38	36.07	19.14	9.79
MS400-3	21	25	75	39.46	46.84	24.85	13.15
MS400-9	9	38	50	16.24	18.88	8.49	5.41
MS400-10	12	38	50	22.25	26.61	11.96	7.42
MS400-16	16	38	50	25.88	28.16	12.66	8.63
MS400-14	20	38	50	37.26	37.01	16.64	12.42
MS400-17	24	38	50	40.56	44.50	20.01	13.52
MS400-13	28	38	50	43.89	52.77	23.73	14.63
MS400-15	33	38	50	62.84	62.85	28.26	20.95

The subsequent stages of the formation of petalling behaviour are shown in Figure 75-Figure 82. With increasing blast loads, the energy from the blast must be dissipated by the plate in the form of capping and petalling. Initially necking occurs in a circular region in the centre of the plate, shown in Figure 75 and Figure 76, followed by tensile fracture of the necked region shown in Figure 77-Figure 79. The most severe of the observed failures was the petalling and rupture exhibited by MS400-11 shown in Figure 80, Figure 81 and Figure 82 (loaded with a 28g charge at a stand-off distance of 25mm). According to Wierzbicki [60], once capping has occurred, a further

increase in the amount of explosive results in radial cracks which run outward from the capped hole and a set of six to seven petals develop. Wierzbicki [60] reported that the process of necking, capping and subsequent petalling are ways in which energy from the blast load is dissipated. During the petalling process, the propagation of the radial cracks and the curling of the petals act to dissipate the energy from the blast [60].

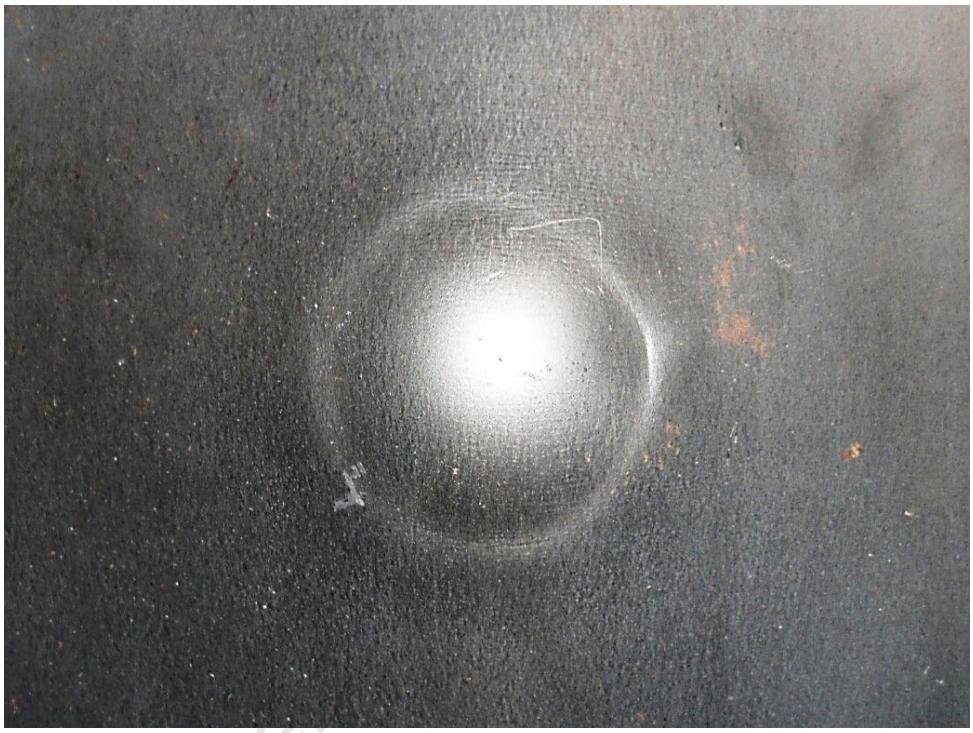

Figure 75: Photograph of ring at centre of plate showing signs of necking and capping on MS400-12, subjected to a blast load of 24g at 25sod

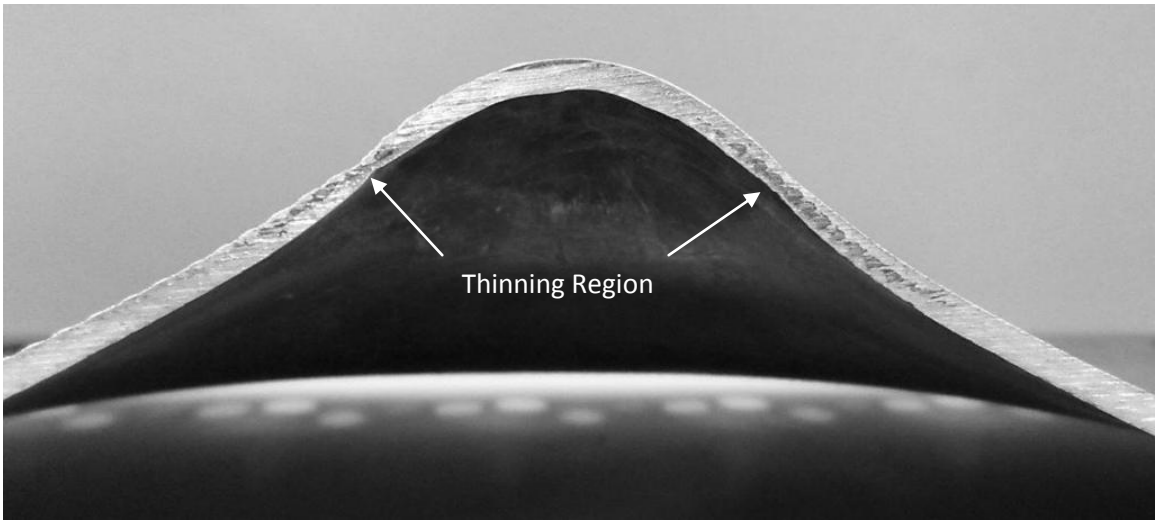

Figure 76: Photograph of cross-section of plate showing deformation profile and thinning on MS400-12, subjected to a blast load of 24g at 25sod

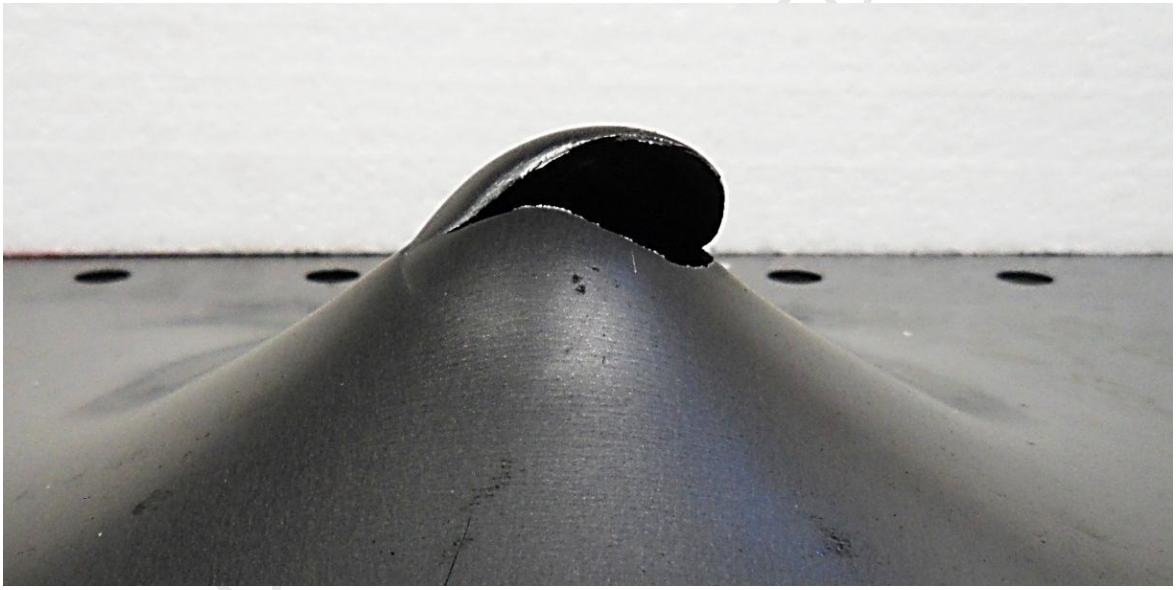

Figure 77: Photograph showing partial capping on MS400-15, subjected to a blast load of 33g at 38sod

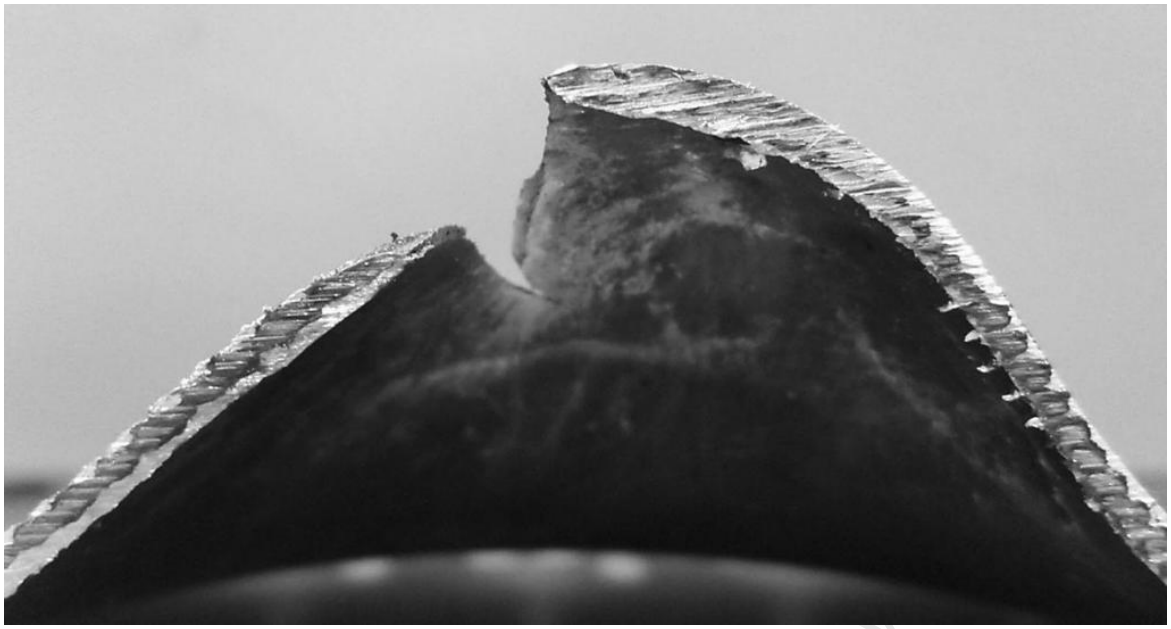

Figure 78: Photograph of cross-section showing deformation profile of partially capped MS400-15, subjected to a blast load of 33g at 38sod

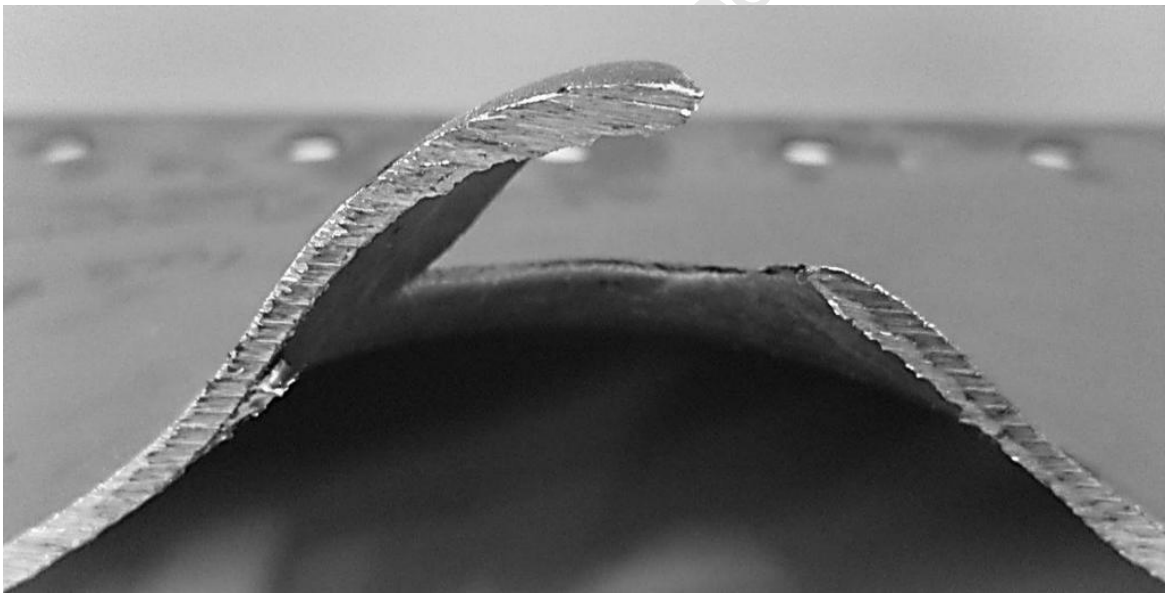

Figure 79: Photograph showing opposite cross-section deformation profile of MS400-15, subjected to a blast load of 33g at 38sod

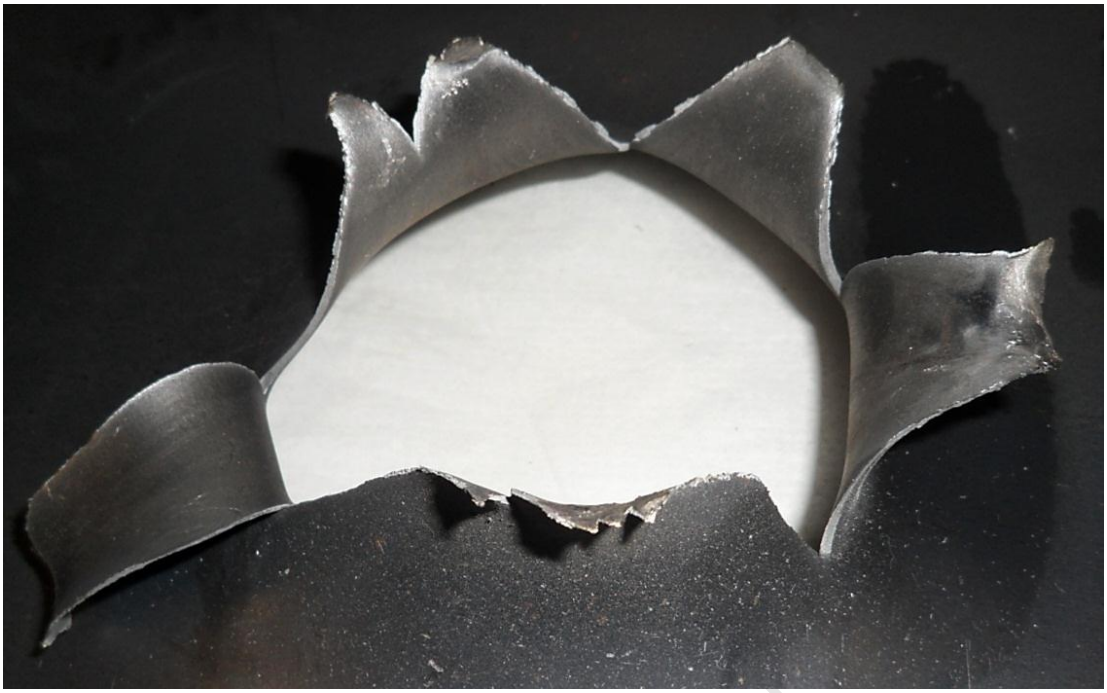

Figure 80: Photograph showing ruptured MS400-11, blast loaded with 28g charge at 25sod

Figure 81: Photograph of failure surface of ruptured MS400-11 showing thinning and ductile fracture surface

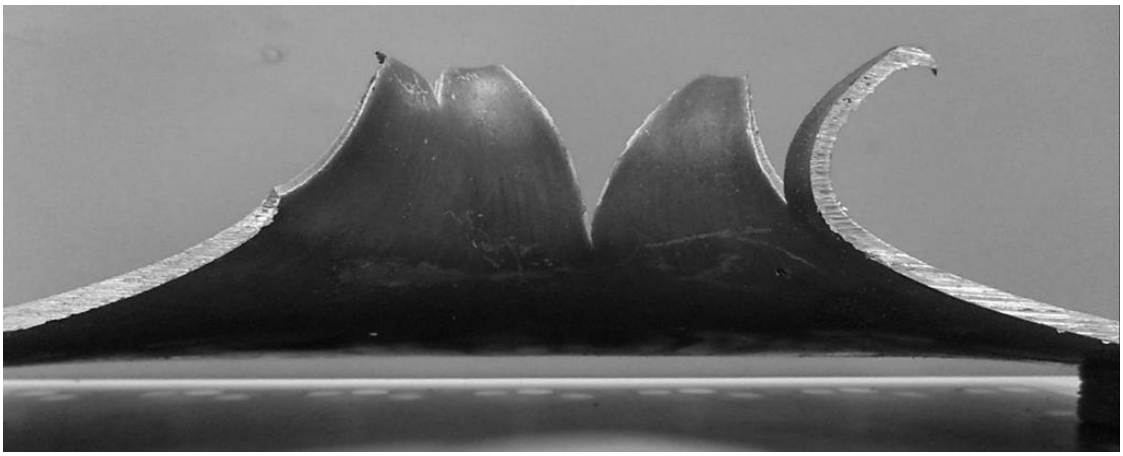

Figure 82: Photograph of cross-section of MS400-11 showing profile of petalled plate

The full range of deformation profiles is shown in Figure 83-Figure 85 arranged in ascending order from lowest displacement to highest (bottom to top). The plate profiles were also separated into 25mm stand-off and 38mm stand-off charge configuration profile photographs shown in Figure 83 and Figure 84 respectively.

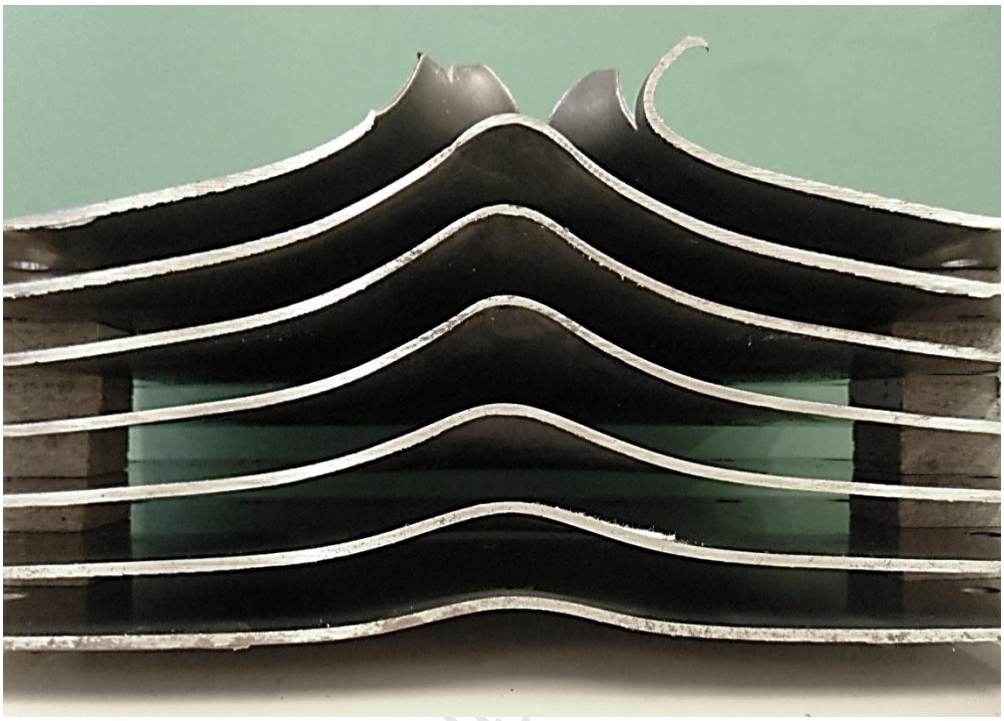

- MS400-11: Torn
- MS400-12: 48.51mm
- MS400- 8: 42.33mm
- MS400- 7: 36.02mm
- MS400- 6: 25.15mm
- MS400- 5: 17.18mm
- MS400- 4: 10.32mm

Figure 83: Photograph of deformation profiles of 3mm Mild steel plates subjected to 50mm diameter blasts at 25mm sod

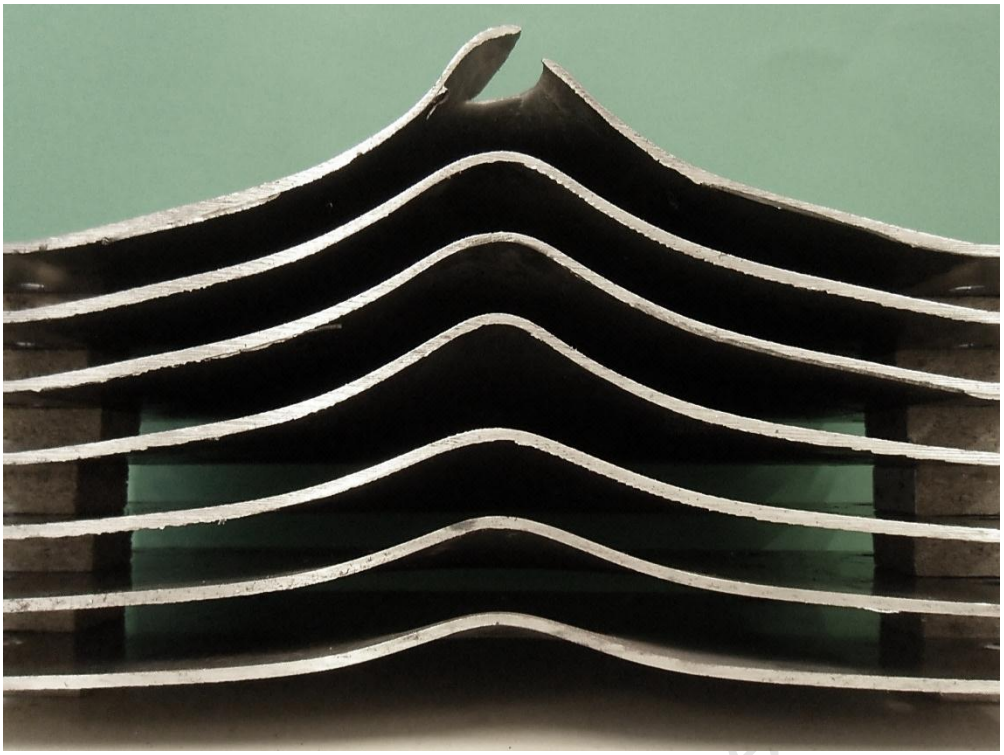

- MS400-15: Capped
- MS400-13: 43.89mm
- MS400-17: 40.56mm
- MS400-14: 37.26mm
- MS400-16: 25.88mm
- MS400-10: 22.25mm
- MS400- 9: 16.24mm

Figure 84: Photograph of deformation profiles of 3mm Mild steel plats subjected to 50mm diameter blasts at 38mm sod

A small number of tests were also performed using a 75mm diameter charge mass and a stand-off distance of 25mm. Figure 85 shows the photograph of the displacement profiles.

Figure 85: Photograph of deformation profiles for 75mm diameter charge mass at 25mm sod

A graph of displacement versus impulse is shown in Figure 86. A relationship of linear increase of displacement with increasing impulse is observed for a given charge diameter/stand-off combination.

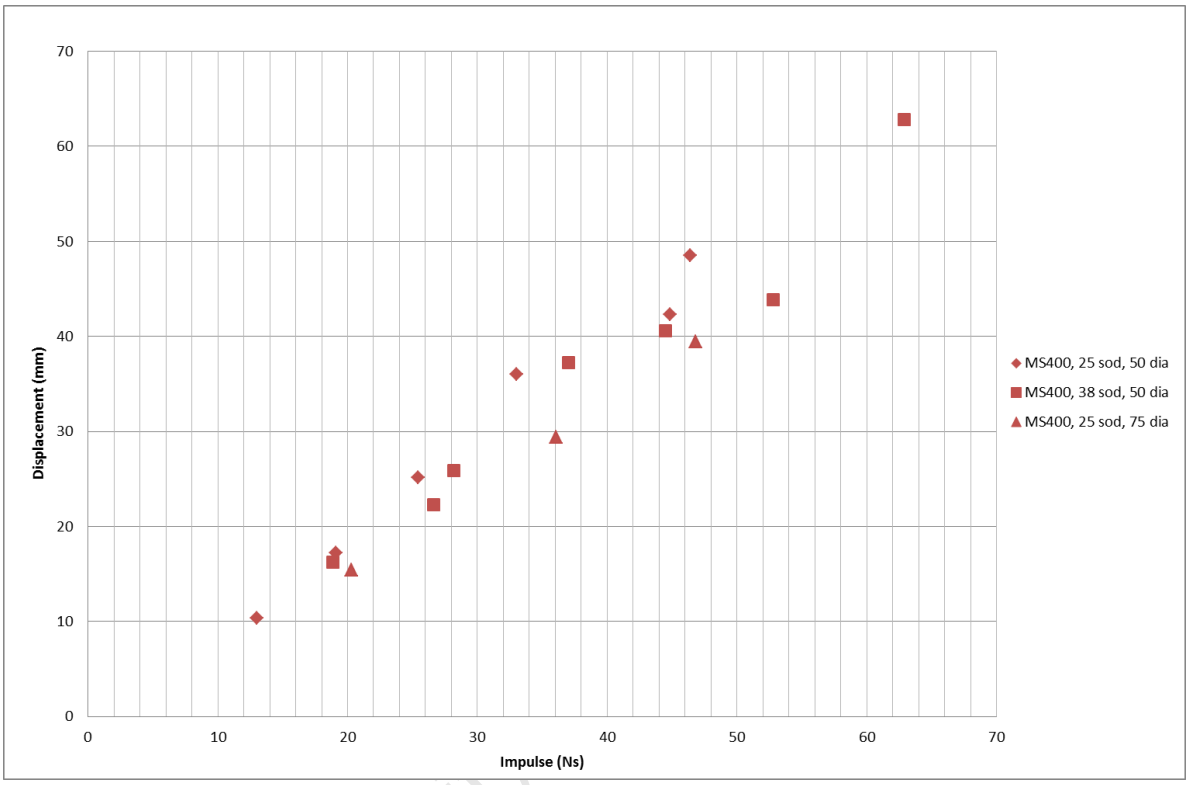

Figure 86: Graph showing displacement versus impulses for all MS400 Tests

6.2. Aluminium Plates

Aluminium plates of 10.5mm nominal thickness were tested as equivalent mass comparison specimens to mild steel, with a nominal mass of 3.8 kg per plate. The aluminium alloy was 5083-H116 (marine grade) obtained from a local manufacturer. The material properties are given in Table 4 and the blast test results are given in Table 10.

Table 10: Table of blast testing parameters and results for Al 5083-H116 aluminium

Plate Number	Charge Mass (g)	SOD (mm)	Charge Diameter (mm)	Permanent Mid-Point Displacement (mm)	Impulse (Ns)	Dimensionless Impulse	d/H
AL-9	12	25	50	9.08	22.15	2.14	0.86
AL-7	16	25	50	14.45	31.88	3.08	1.36
AL-2	20	25	50	20.66	39.01	3.77	1.95
AL-4	28	25	50	26.18	56.68	5.47	2.47
AL-5	33	25	50	torn	63.84	6.16	N/A
AL-8	16	38	50	11.41	31.25	2.13	1.08
AL-1	20	38	50	17.42	39.90	2.72	1.64
AL-3	28	38	50	23.12	56.05	3.81	2.18
AL-6	33	38	50	29.05	62.85	4.28	2.74

Large inelastic deformation was again observed. A change in the plate thickness over the central region of the plate was observed at higher charge masses (28g-33g), due to the damage on the front surface of the aluminium plates. The surface damage observed on the front faces of selected plates are shown in Figure 87 and Figure 88. The deformation profiles of the blast tested plates are shown in Figure 99-Figure 101.

The front face of all the aluminium plates shows a distinct melt region, shown in the photographs in Figure 87 and Figure 88. A pitted region that was slightly larger than the charge radius was evident. Also evident in Figure 87 and Figure 88 is a large area of aluminium spray which coated the plate surface around the periphery of the central melt region. The spray was approximately two to three times the diameter of the melted region in each case. The proximity of the explosive charge and the high temperature of the explosion appear to result in the melt and outward spray of the aluminium during the blast.

The reduced thickness of the plate in the centre supports the idea that the explosion caused localised melting of the aluminium and the blast pressure caused the molten aluminium to spray radially outwards. The spray of the melted aluminium is categorized into two separate categories, namely: the burn diameter; and the spray diameter. The burn diameter is defined as the maximum diameter of an area of visible surface damage such as pitting as well as removal of material. The spray diameter is defined as the maximum visible diameter of the outward spray of melted material due to the blast. The burn and spray diameters of each of the aluminium test plates are given in Table 11.

Figure 87: Photograph showing a distinct melted region in the centre of AL-6 plate subjected to 33g charge at 38mm SOD

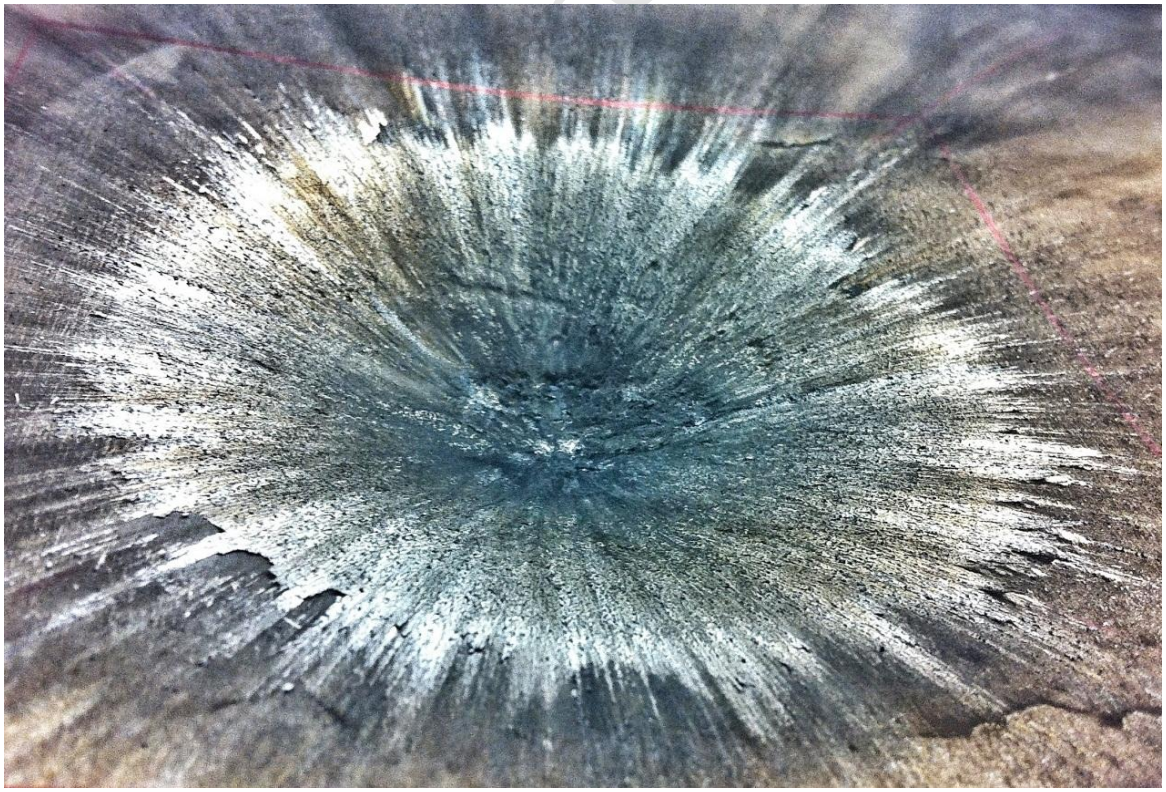

Figure 88: Photograph showing the melted region as well as a circular spray of melted material in AL-3 subjected to 28g charge at 38mm SOD

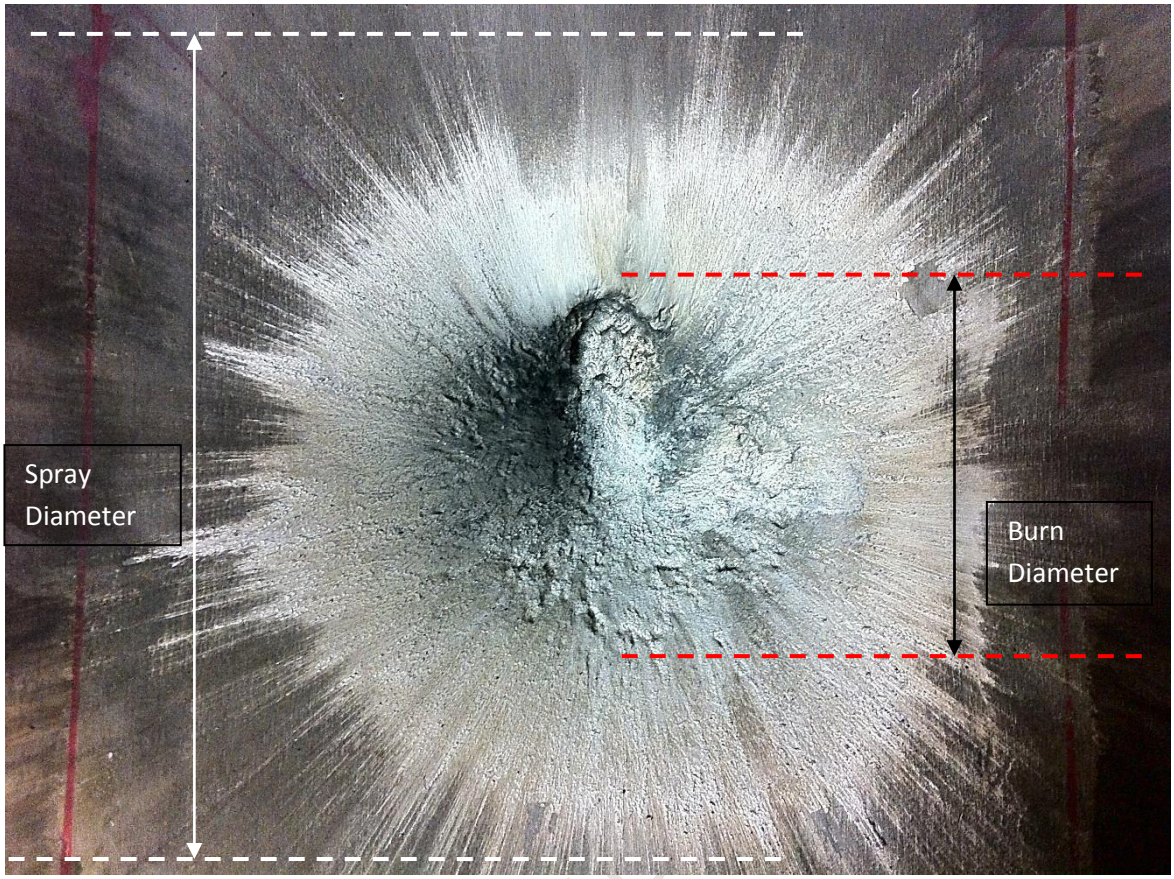

Figure 89: Diagram showing the burn and spray diameters measured from the AL plates

Table 11: Table of Burn Diameters and Spray Diameter of Aluminium Test Plates

Plate	Charge Mass (g)	Stand-Off Distance (mm)	Mid-point Displacement (mm)	Plate Thickness (mm)	Mid Point Thickness (mm)	Thickness Reduction %	Burn Diameter (mm)	Spray Diameter (mm)
AL-9	12	25	9.08	10.52	9.92	5.70	50	98
AL-7	16	25	14.45	10.54	9.44	10.44	50	110
AL-2	20	25	20.66	10.52	8.48	19.39	53	128
AL-4	28	25	26.18	10.54	7.86	25.43	53	137
AL-5	33	25	Failed	10.54	N/A	N/A	55	178
AL-8	16	38	11.41	10.54	9.84	6.64	51	110
AL-1	20	38	17.42	10.54	9.14	13.28	53	116
AL-3	28	38	23.12	10.54	8.62	18.22	54	131
AL-6	33	38	28.98	10.56	7.48	29.17	56	162

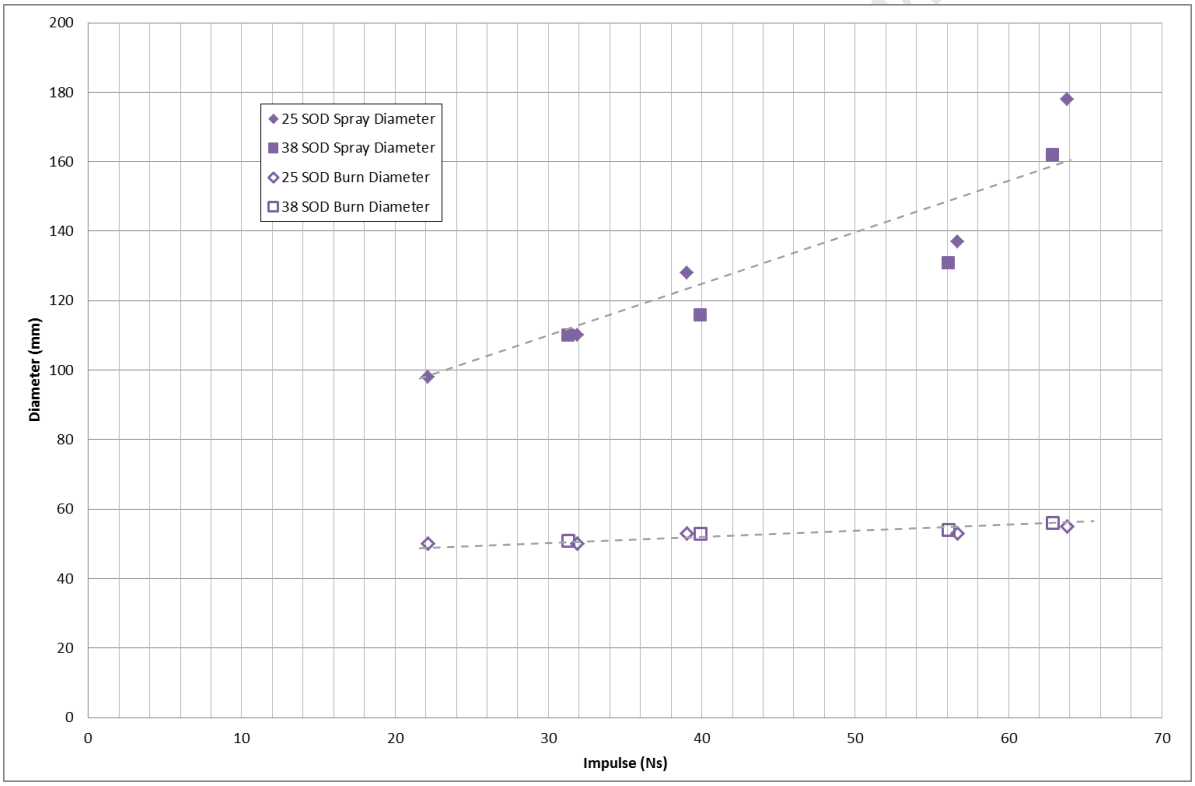

Figure 90: Graph showing spray and melt diameters of melted aluminium versus impulses

A graph of spray diameter versus impulse is shown in Figure 90. From Figure 90, the spray diameter appears to increase linearly with increasing impulse. This suggests that the higher the charge masses and impulses are the more material is melted during the blast and sprayed outwards, which is consistent with the percentage reductions in thickness exhibited by the

plates. Also, the higher intensity of the blast load caused the melted material to spray further. Both of these scenarios would fit the trend suggested by the graph.

At higher impulses (from 33g charge), cracking is observed, a mode of brittle fracture as evidenced by the jagged, planar fracture surface shown in Figure 92-Figure 96. The tensile test specimens also exhibited a moderate ductile to brittle failure, as shown by the fracture surface as well as the 45 degree fracture angle on all of the specimens in Figure 97-Figure 98.

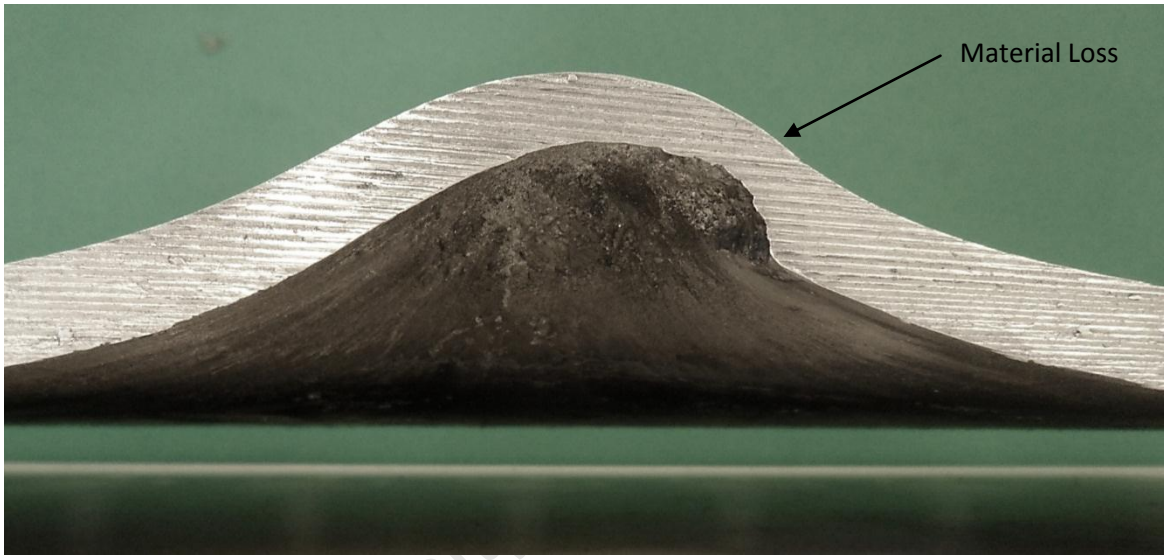

Figure 91: Close-up photograph of cross-section of AL-6 showing thinning and material loss due to melting

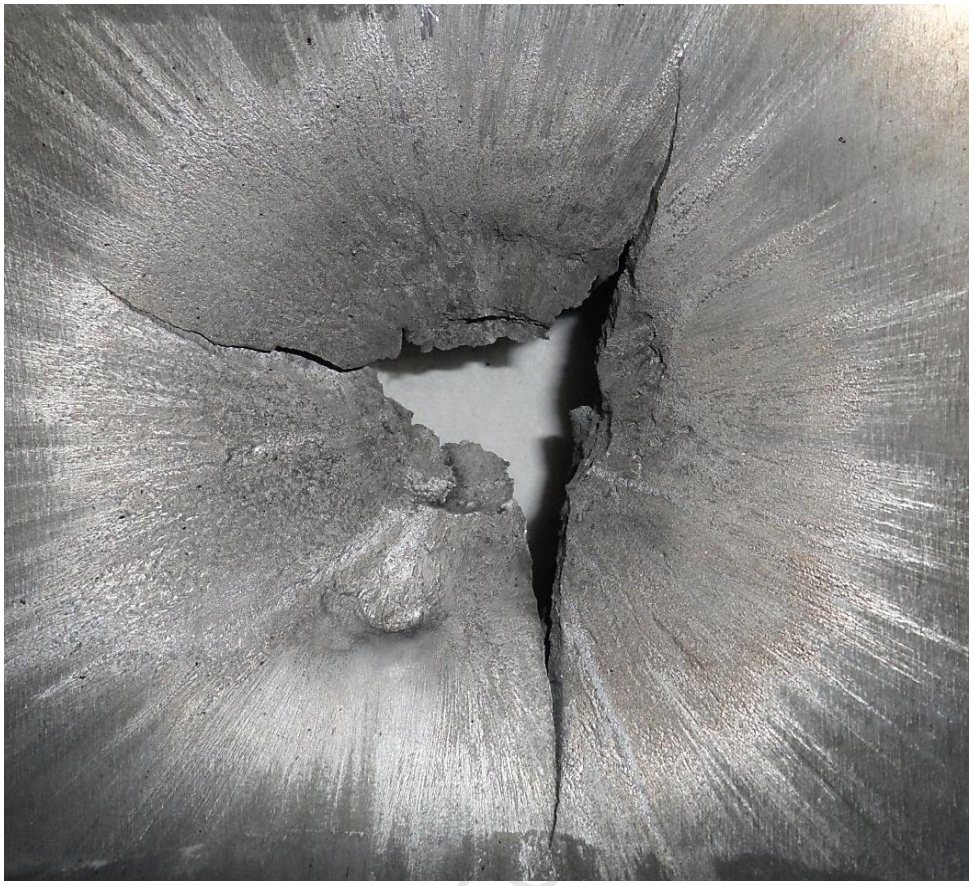

Figure 92: Photograph showing the front face fracture surface of AL-5

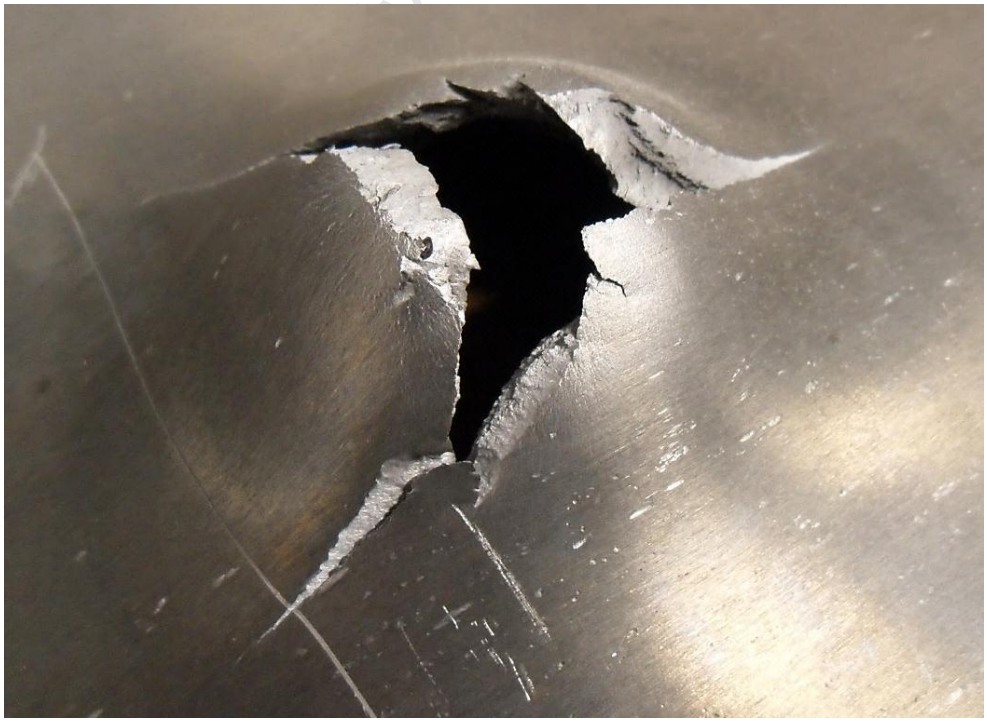

Figure 93: Photograph showing the back face of the fracture surface of AL-5

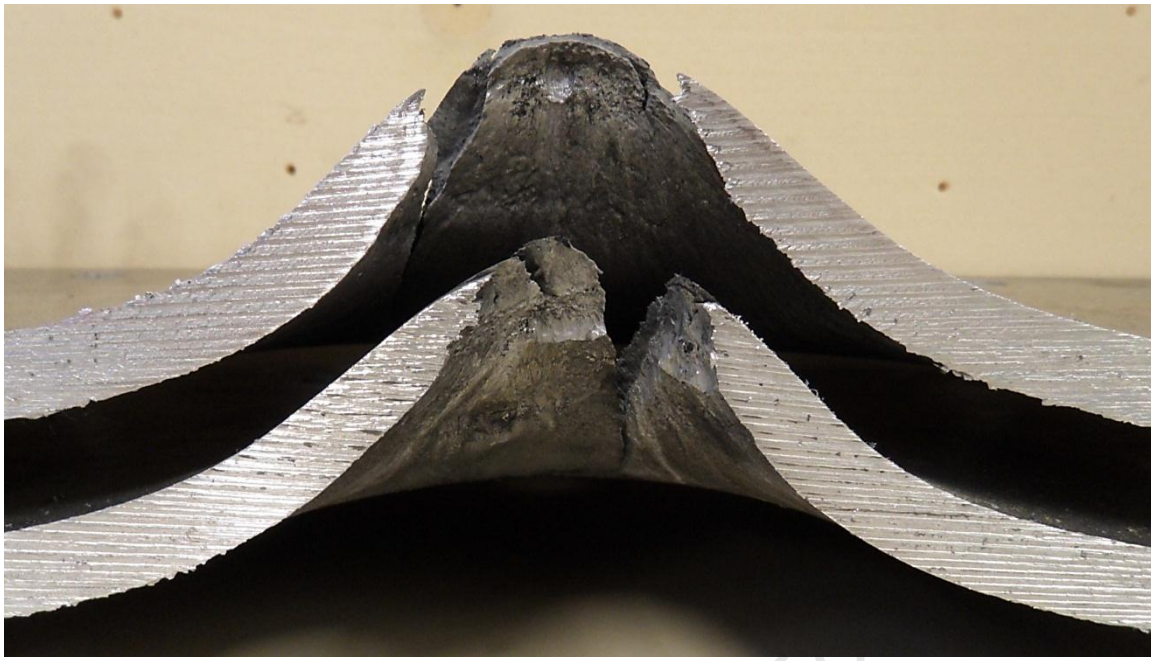

Figure 94: Cross-Section photograph of AL-5 showing fracture surfaces and displacement profiles

Figure 95: Close-up photograph showing brittle fracture surface and signs of melting

Figure 96: Close-up photograph of AL-5 showing mid-point fracture surface with pitting and melting visible

Figure 97: Photograph showing 45 degree shear in the aluminium tensile specimens

Figure 98: Photograph of 45 degree shear surface of aluminium tensile test specimens

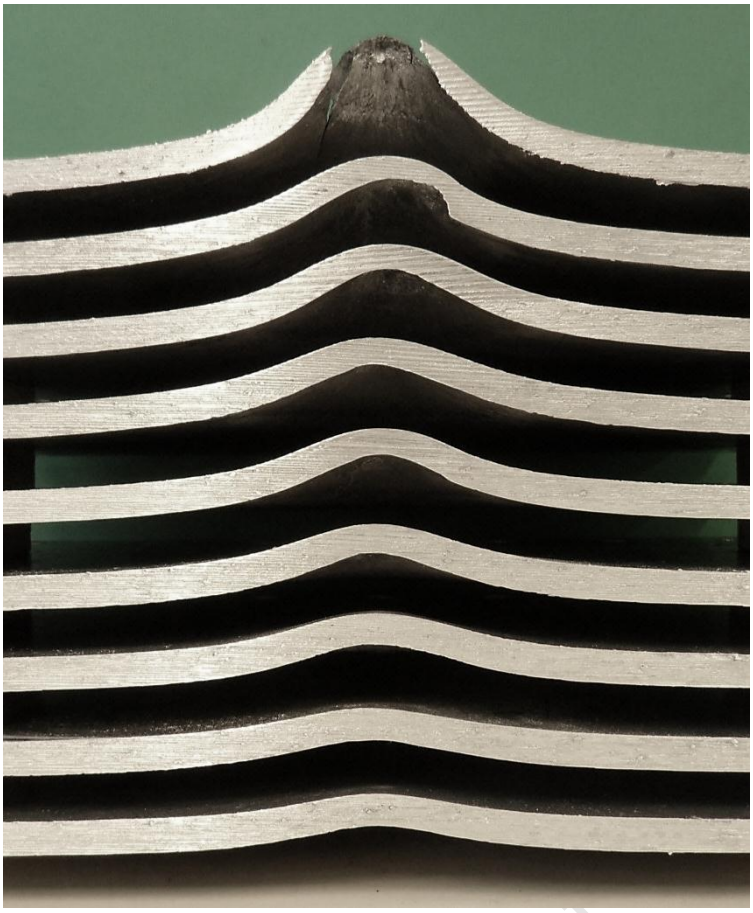

- AL-5: 46.14mm, Dia: 50mm, sod:25mm
- AL-6: 29.05mm, DIa: 50mm, sod: 38mm
- AL-4: 26.18mm, Dia: 50mm, sod: 25mm
- AL-3: 23.12mm, DIa: 50mm, sod: 38mm
- AL-2: 20.66mm, Dia: 50mm, sod: 25mm
- AL-1: 17.42mm, Dia: 50mm, sod: 38mm
- AL-7: 14.45mm, Dia: 50mm, sod: 25mm
- AL-8: 11.41mm, Dia: 50mm, sod: 38mm
- AL-9: 9.08mm, Dia: 50mm, sod: 25mm

Figure 99: Photograph of cross-section of displacements arranged in descending order

- AL-5: 46.14mm
- AL-4: 26.18mm
- AL-2: 20.66mm
- AL-7: 14.45mm
- AL-9: 9.08mm

Figure 100: Photograph of cross-section of plates subjected to50mm diameter blast load at 25mm stand-off distance

- AL-6: 29.98mm
- AL-3: 23.12mm
- AL-1: 17.42mm
- AL-8: 11.41mm

Figure 101: Photograph of cross-section of plates subjected to 50mm diameter blast load at 38mm stand-off distance

Certain aspects of the behaviour and response of the aluminium were unexpected. The melting effect and spray of aluminium were unexpected: the final permanent displacements of the aluminium were lower than that of equivalent mass mild steel, and the failure threshold impulse higher.

From Table 11, it is observed that there was a significant reduction in thickness in the central region of the aluminium plates as charge masses increased for both stand-off distances of up to 29% (33g test performed at a 38mm stand-off). The ductile nature of the aluminium combined with the thickness of the plates allowed them to dissipate some of the blast load by thinning significantly while also deforming. The displacement versus impulse graph in Figure 102 shows a linear correlation for both stand-off distances with the 38mm stand-off tests having lower displacements at similar impulses.

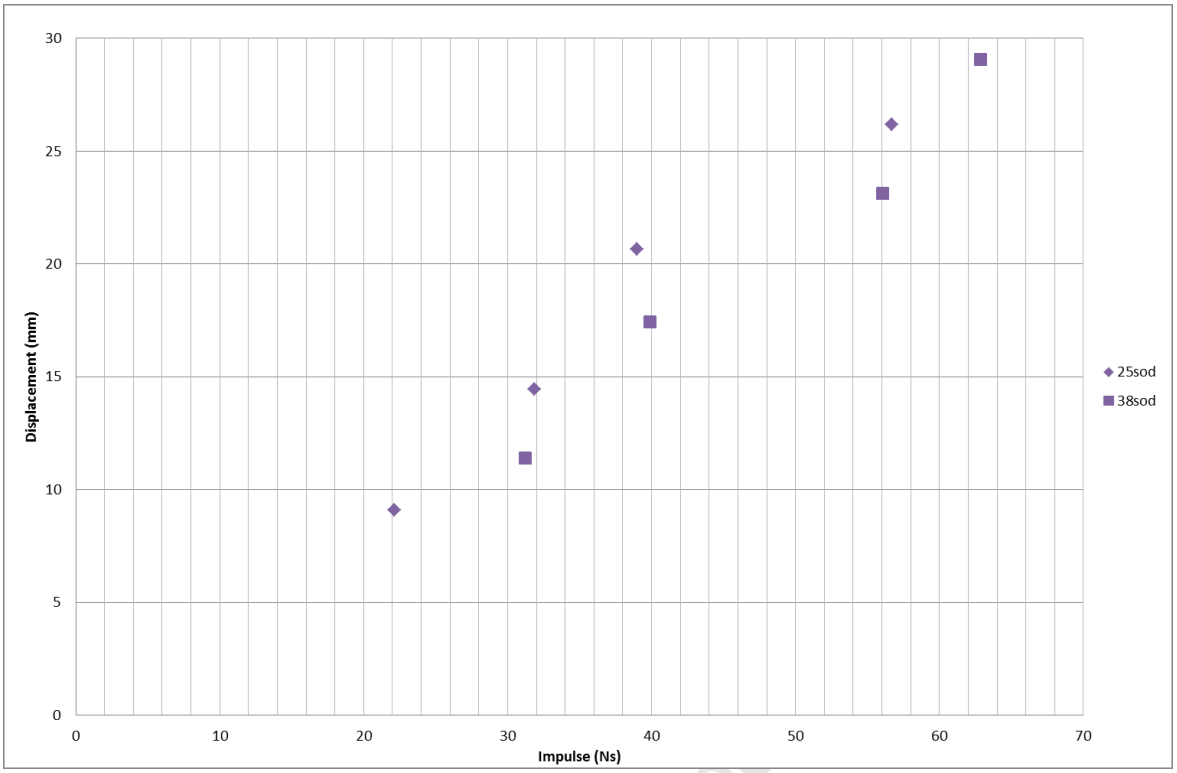

Figure 102: Displacement versus Impulse for blast test on aluminium plates at 25mm and 38mm stand-off distances

6.3. Twintex Plates

Twintex panels of 11.4mm nominal thickness were tested as equivalent mass panels to the 3mm thick mild steel panels. The loading configurations of the explosive charges used were similar to those used on the mild steel plates. The Twintex panels used were manufactured at the BISRU laboratory at the University of Cape Town.

6.3.1. Plate Damage Analysis

The results from the seven blast tests performed on the Twintex panels are summarised in Table 12. The Twintex panels showed minimal damage at the lower charge masses (up to 20g) but exhibited failure and fibre fracture at the higher charge masses and closer stand-off distances. All the panels sustained burn damage and failure of the outer layers on the front face of the panels, shown in Figure 103-Figure 105. Some delamination of the outer back face layers was also evident in the plates subjected to higher blast loads as can be seen on TW-1 in Figure 107.

Table 12: Table of blast testing parameters and results for Twintex composite panels

Plate Number	Charge Mass (g)	SOD (mm)	Charge Diameter (mm)	Permanent Mid-Point Displacement (mm)	Impulse (Ns)	Dimensionless Impulse	d/H
TW-7	12	25	50	3.32	21.80	2.13	0.30
TW-6	16	25	50	4.88	29.70	2.74	0.43
TW-4	20	25	50	torn	36.72	3.42	N/A
TW-5	12	38	50	2.54	21.80	1.39	0.22
TW-2	16	38	50	3.75	29.70	1.91	0.33
TW-1	20	38	50	4.38	37.65	2.49	0.39
TW-3	24	38	50	torn	46.07	3.07	N/A

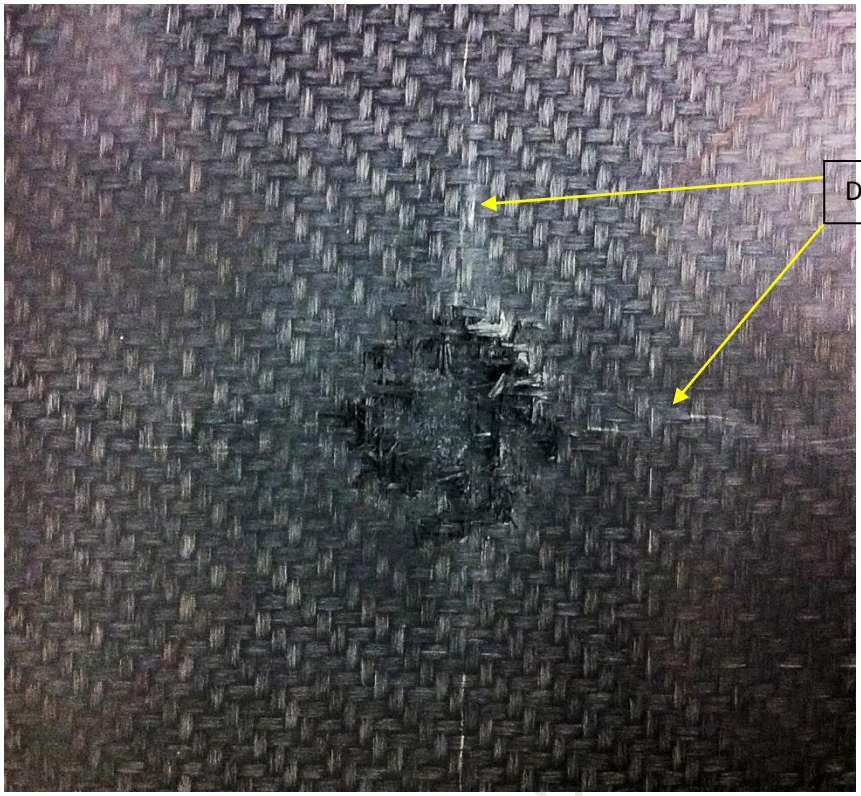

Figure 103: Photograph of front face damage on TW-1 showing fibre fracture as well as delamination lines

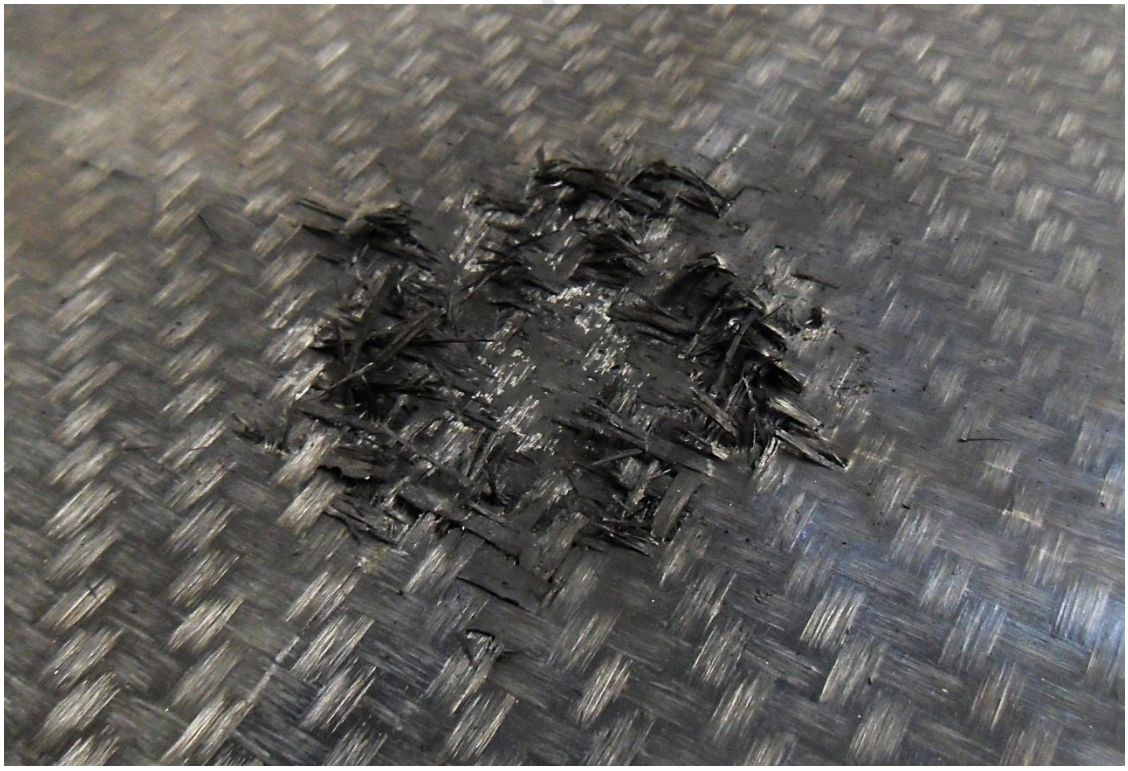

Figure 104: Close-up photograph showing the damage on the front face of TW-1

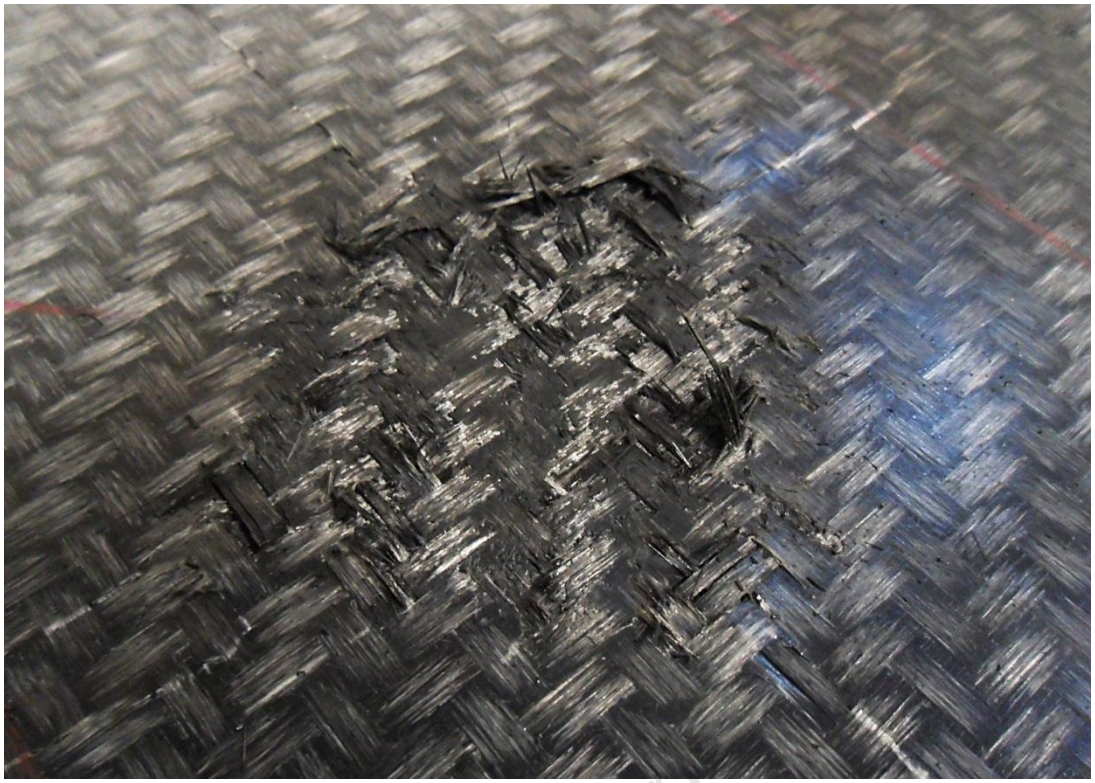

Figure 105: Photograph of the front face damage sustained by TW-7

As the charge mass increased and the stand-off distance decreased, the back face started to exhibit some cracking within the polypropylene matrix in the central area of the plate. At higher impulses fibre fracture and complete failure of the panel occurred. Figure 106-Figure 109 show the various stages of failure as the intensity of the blast load increased.

Twintex panel TW-6, shown in Figure 106, exhibited inelastic deformation of the back face and cracking of the polypropylene matrix under a blast load of 16g at a 25mm stand-off. Figure 107 shows TW-1, which exhibited minimal back face fibre rupture and matrix failure, subjected to a blast load of 20g at a 38mm stand-off. TW-3 exhibited extensive back face fibre rupture and matrix failure under a blast load of 24g at a 38mm stand-off (Figure 108). Finally, complete fibre rupture can be seen in Figure 109, where TW-4 was subjected to a blast load of 20g at a 25mm stand-off.

Figure 106: Photograph showing the back face of TW-6 where matrix cracking is visible as well as minimal fibre fracture

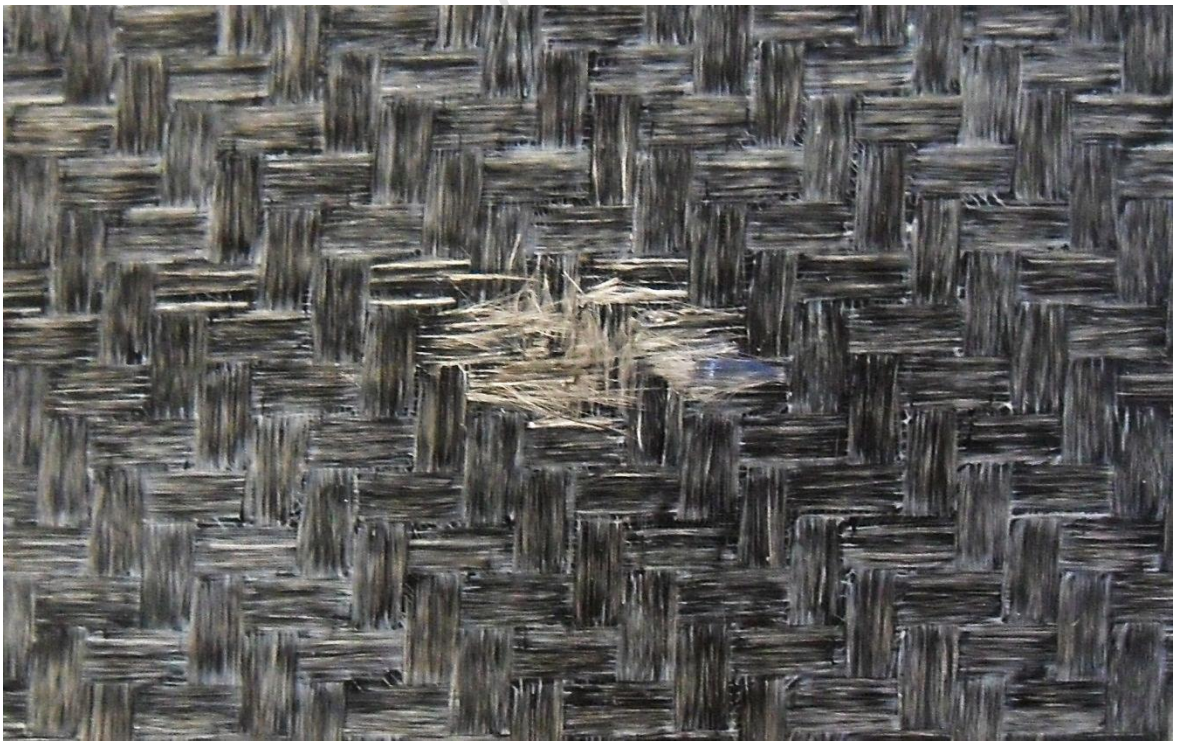

Figure 107: Photograph showing the small area of fibre fracture and matrix cracking on the back face of panel TW-1

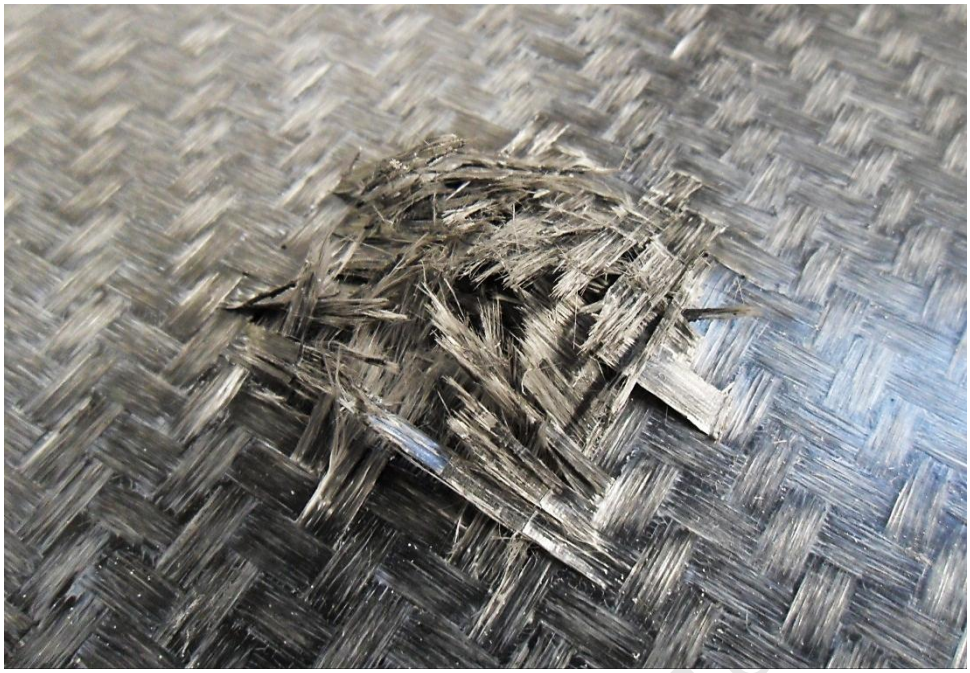

Figure 108: Photograph of TW-3 showing more extensive back-face fibre fracture as the charge mass is increased

Figure 109: Photograph of TW-4 showing complete failure as a result of decreasing the stand-off distance

Although the permanent back face displacements for the Twintex panels are relatively low, there is still a discernable difference between the displacements of the 25mm and 38mm stand-off distances, as shown in Figure 110.

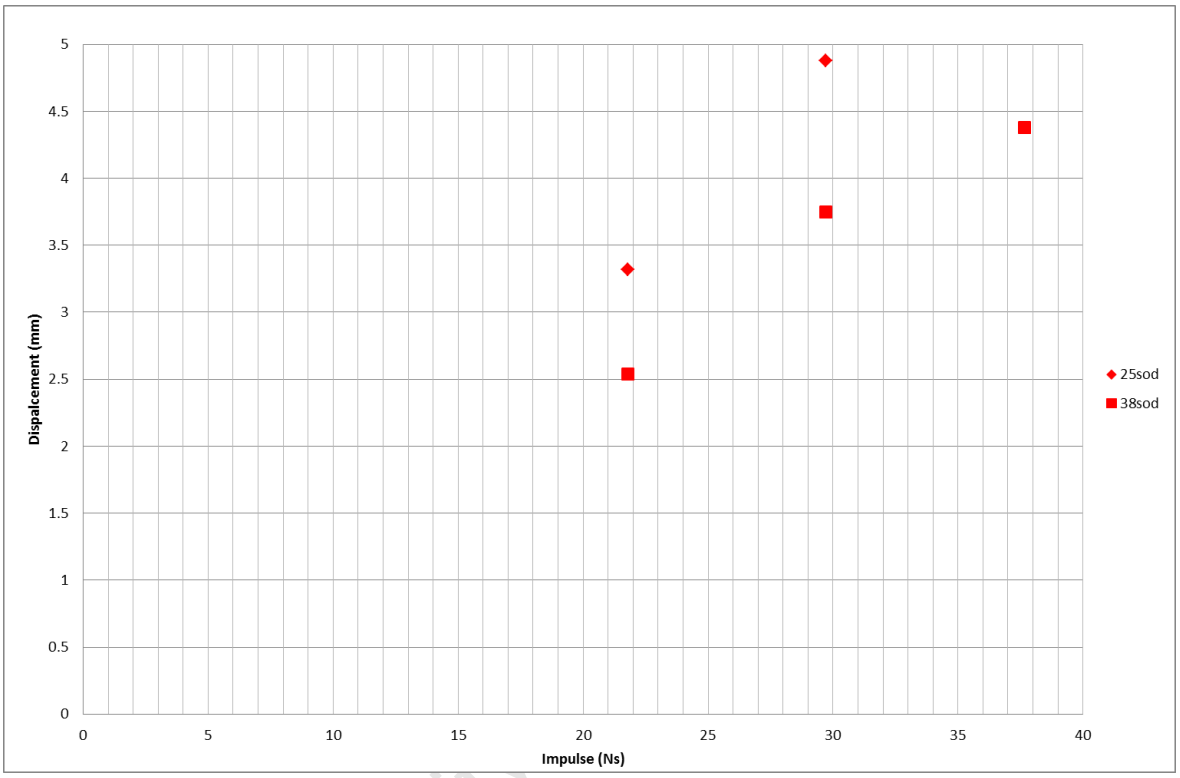

Figure 110: Displacement versus impulse for Twintex composite panels

6.4. Dyneema Plates

The Dyneema panels showed large plastic deformation, but none had failed catastrophically up to an impulse of 114.40Ns (60g). Post-test analysis of the panels showed that the mid-point thickness for all the panels increased, despite the fact that several front-face layers had been destroyed during the blast as shown in Figure 111. This is likely due to delamination of the layers which causes an increase in overall thickness of the panels.

Table 13: Table of Results for Dyneema Blast Tests

Plate Number	Charge Mass (g)	SOD (mm)	Charge Diameter (mm)	Permanent Mid-Point Displacement (mm)	Impulse (Ns)	Pre-Test Thickness (mm)	Pre-Test Mass (kg)	Post-Test Thickness (mm)	Post-Test Mass (kg)
DYN-6	15	50	50	10.52	28.48	24.16	3.52	25.48	3.52
DYN-5	23	50	50	16.34	43.94	24.14	3.56	24.64	3.56
DYN-2	28	50	50	19.80	53.74	24.14	3.54	24.71	3.54
DYN-3	36	50	50	28.08	68.86	24.16	3.54	24.60	3.54
DYN-7	44	50	50	33.40	85.19	24.14	3.54	25.74	3.54
DYN-4	53	50	50	39.31	98.54	24.12	3.54	27.30	3.54
DYN-8	60	50	50	43.21	114.40	24.12	3.56	28.12	3.56

6.4.1. Plate Damage Analysis

Due to the semi-rigid boundary conditions, the plates exhibited large pull-in behaviour on the sides shown in Figure 111, Figure 112 and Figure 115. The layers within the panel were able to slide across each other due to the low in-plane shear resistance. Plates subjected to higher blast loads showed more significant pull-in behaviour as well as sustaining greater front face damage in the form of the destruction and melting of some of the front-face layers. The quadrangular shape of the damaged front face region was due to the weave pattern of the UHMWPE.

The graph of displacement versus impulse for the Dyneema tests, in Figure 117, shows that there is a consistent linear correlation of increasing displacement with increasing impulse.

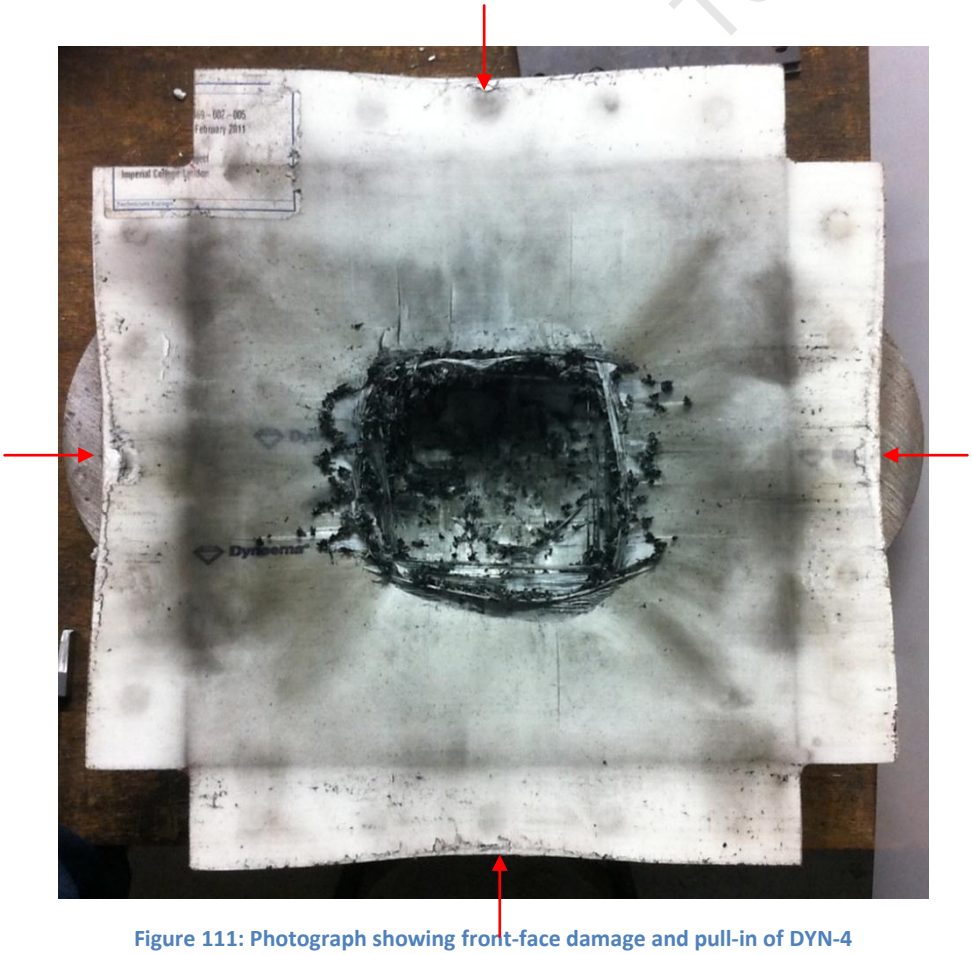

Figure 111: Photograph showing front-face damage and pull-in of DYN-4

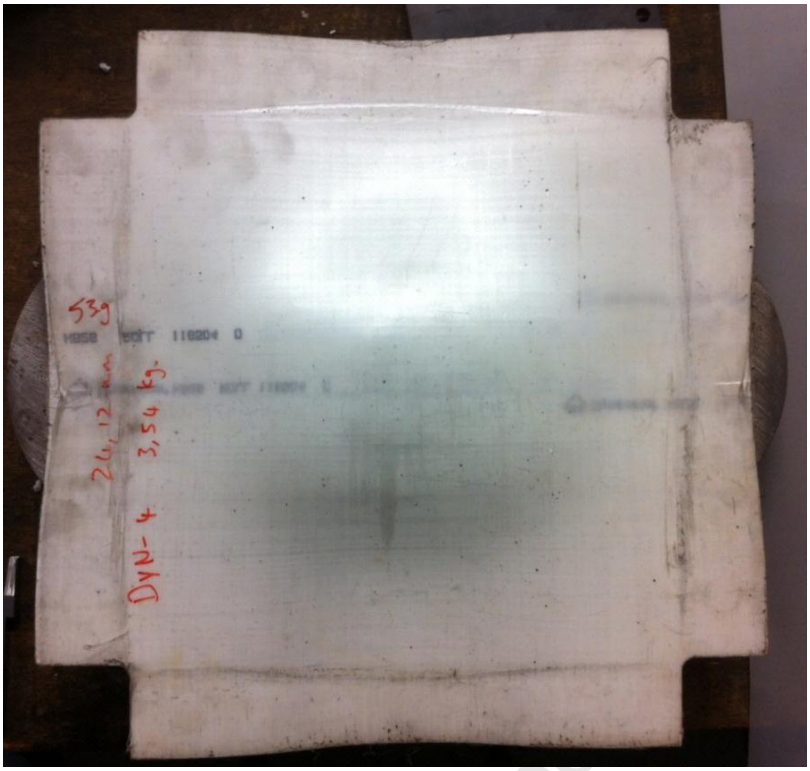

Figure 112: Photograph showing back-face deformation and Pull-in of DYN-4, subjected to a blast load of 53g at 50mm sod

Figure 113: Photograph showing close-up of front-face of DYN-4, with melting and destroyed layers clearly visible

Figure 114: Photograph showing area of damage on front-face of DYN-4

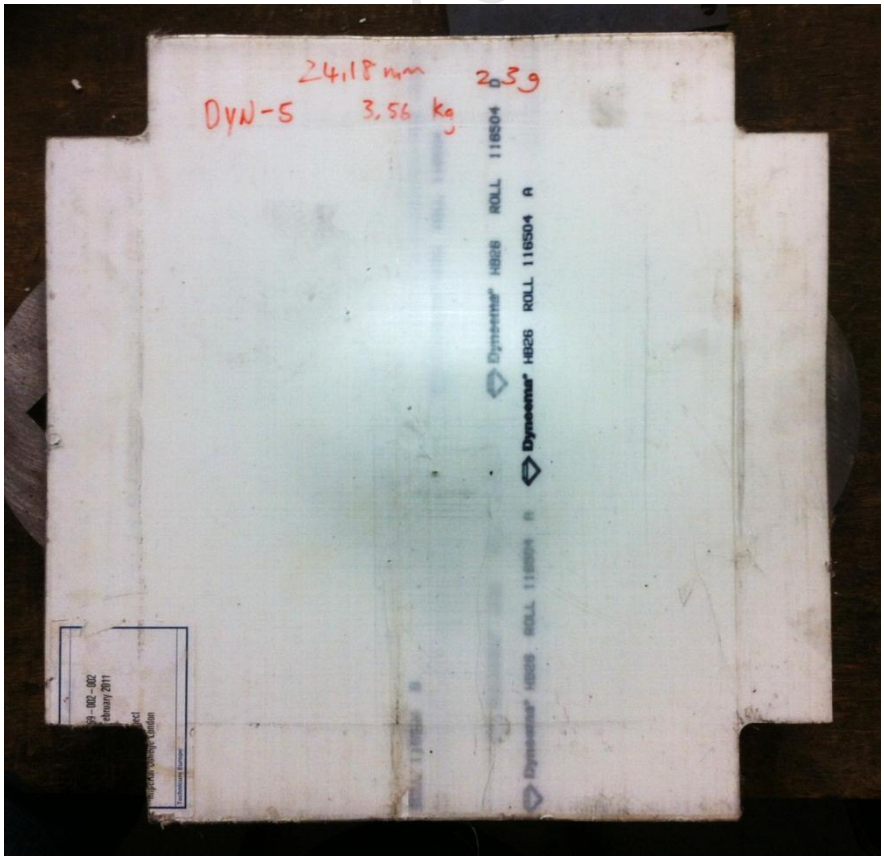

Figure 115: Photograph of DYN-5 subjected to blast load of 23g at 50mm sod, showing significantly less pull-in

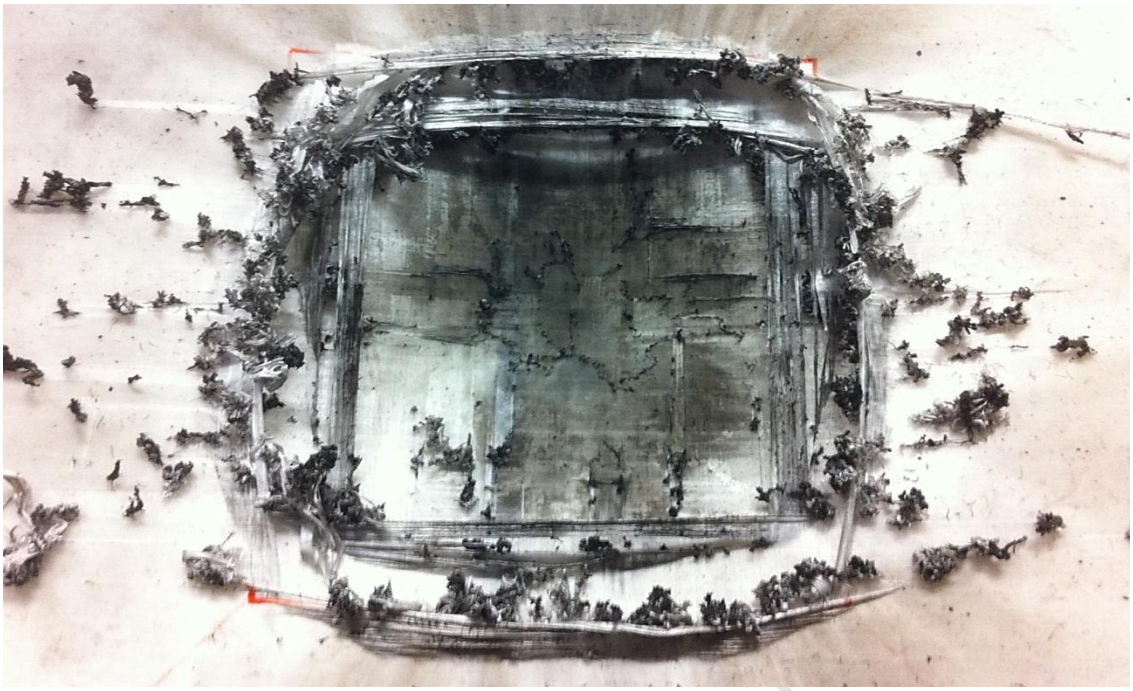

Figure 116: Photograph showing front-face damage on DYN-5, subjected to blast load of 23g at 50mm sod

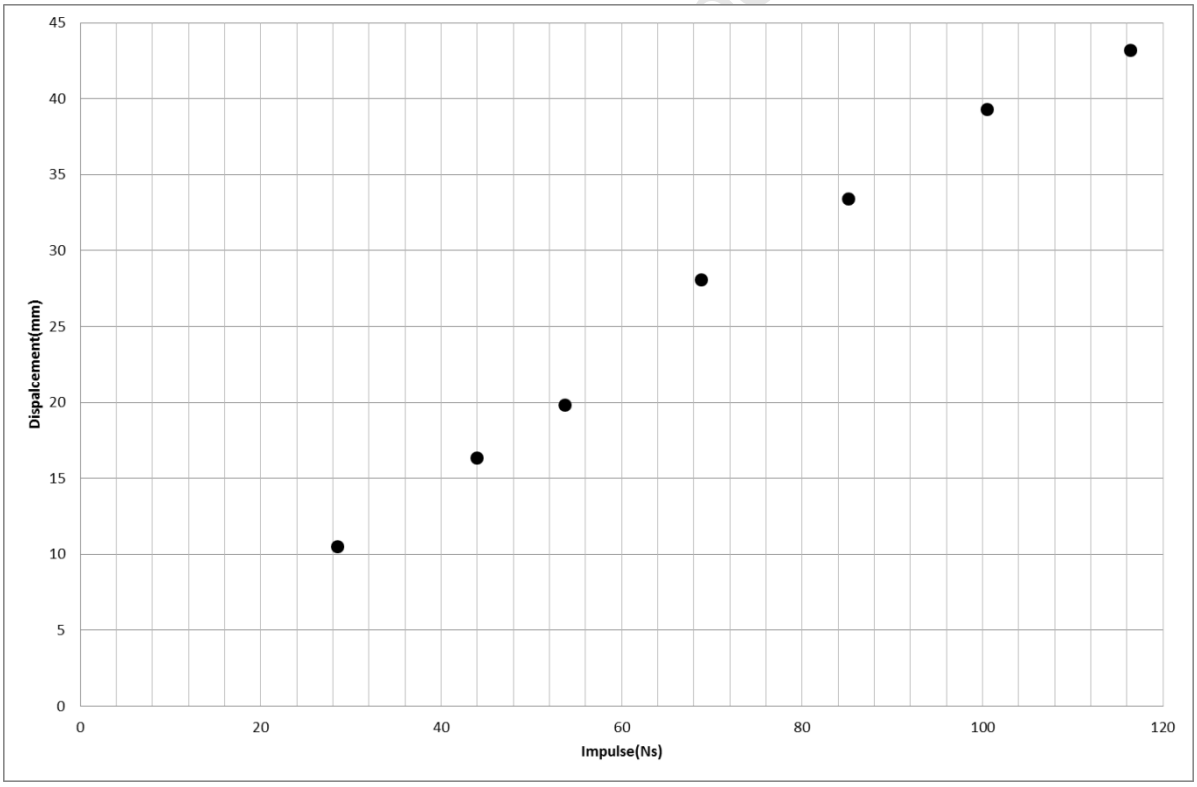

Figure 117: Graph of Displacement versus Impulse for Dyneema Panels

7. DISCUSSION

7.1. Comparison of 500 x 500 Equivalent Mass Plates

The Armox 370T plates were tested and compared to the mild steel plates.

7.1.1. Permanent Displacement Profiles

As expected, the Armox 370T armour steel performed better than the mild steel with lower permanent mid-point displacements for each of the various blast load configurations in Mode I. However it is noted that both steels fractured for the same loading condition (charge mass of 40g, 50mm diameter at a stand-off distance of 25mm). This shows that although the armour steel is stronger than the mild steel, the two steels have similar failure threshold impulses. Figure 118 shows photographs of the cross-sections of various Armox 370T and mild steel plates for three different charge mass configurations. The Armox 370T clearly exhibits significantly lower displacements than the mild steel. The armour steel sustained a brittle type of fracture as evident from the photograph shown in Figure 52, whereas the mild steel plate sustained a more ductile fracture with evidence of thinning as shown in Figure 44.

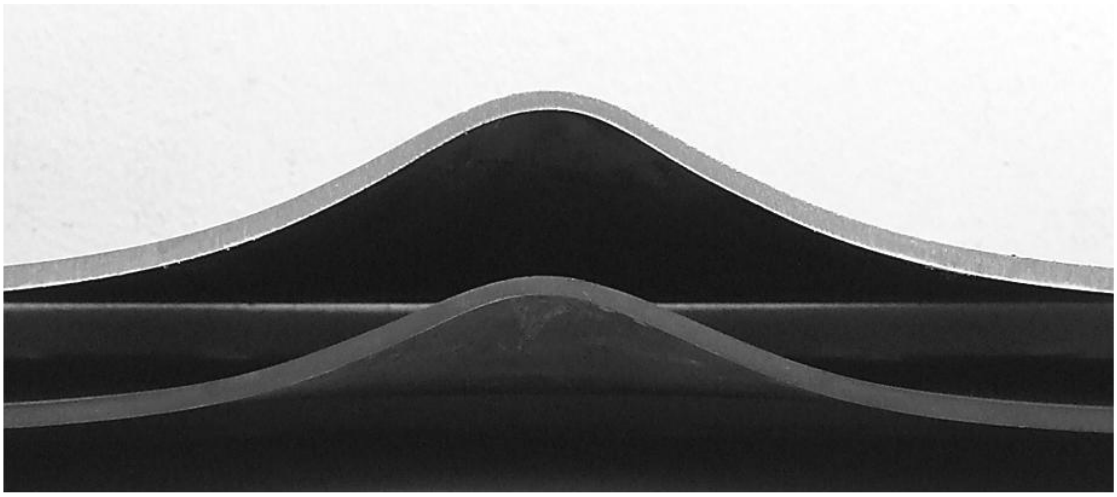

(a) Charge Mass : 33g, Diameter : 50, SOD : 25mm; MS-P8 (top) vs AS-P2 (bottom)

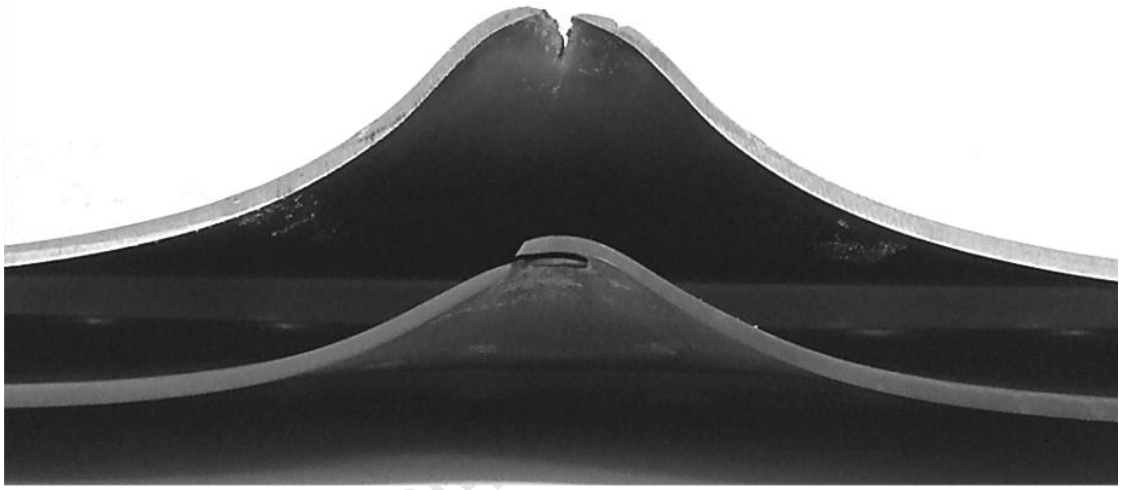

(b) Charge Mass : 40g, Diameter : 50, SOD : 25mm; MS-P6 (top) vs AS-P1 (bottom)

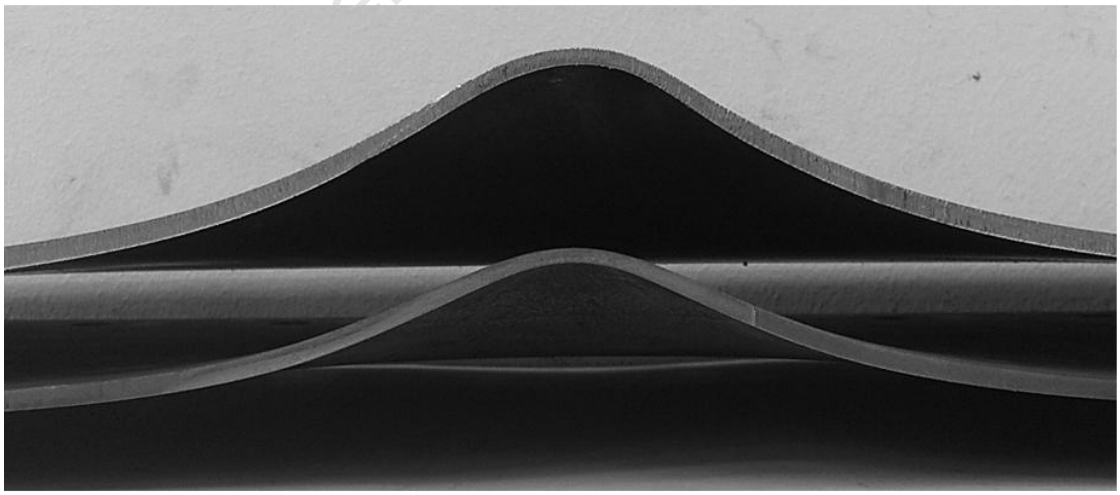

(c) Charge Mass : 50g, Diameter : 50, SOD : 38mm; MS-P10 (top) vs AS-P6 (bottom)

Figure 118: Photographs showing the cross-section profiles for three different charge mass configurations between mild steel(TOP) and Armox 370T (BOTTOM)

7.1.2. Comparison of the Transient Responses

The light interference equipment described in Section 3 was used to record transient displacement measurements. Displacement-time measurements were recorded for some of the 500mm x 500mm plates blast tested, with satisfactory results relating to the maximum and final transient displacements. Unfortunately, the displacements in the lower displacement range have some uncertainty as the equipment could not accurately detect movement in the 7mm to 20mm range. The displacement-time histories for the selected tests are shown in Figure 119-Figure 121.

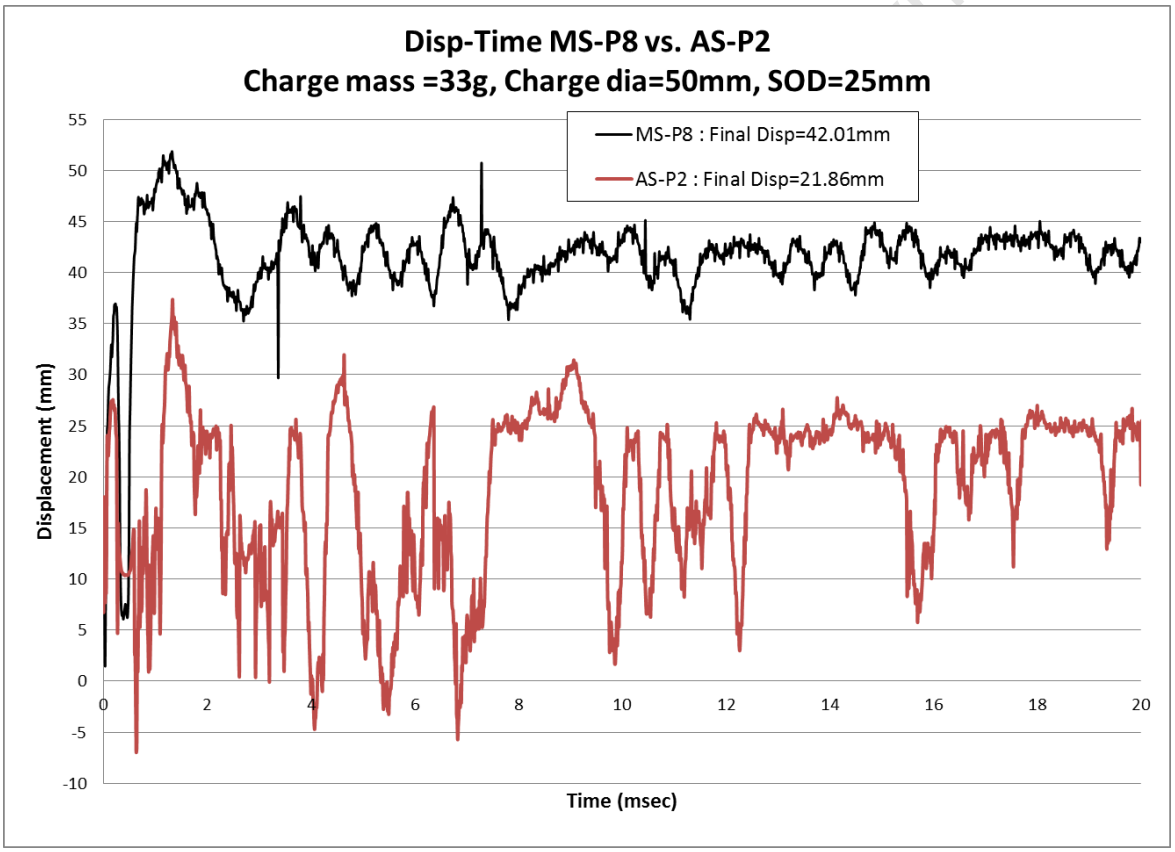

Figure 119: Displacement-time histories of mild steel and Armox 370T

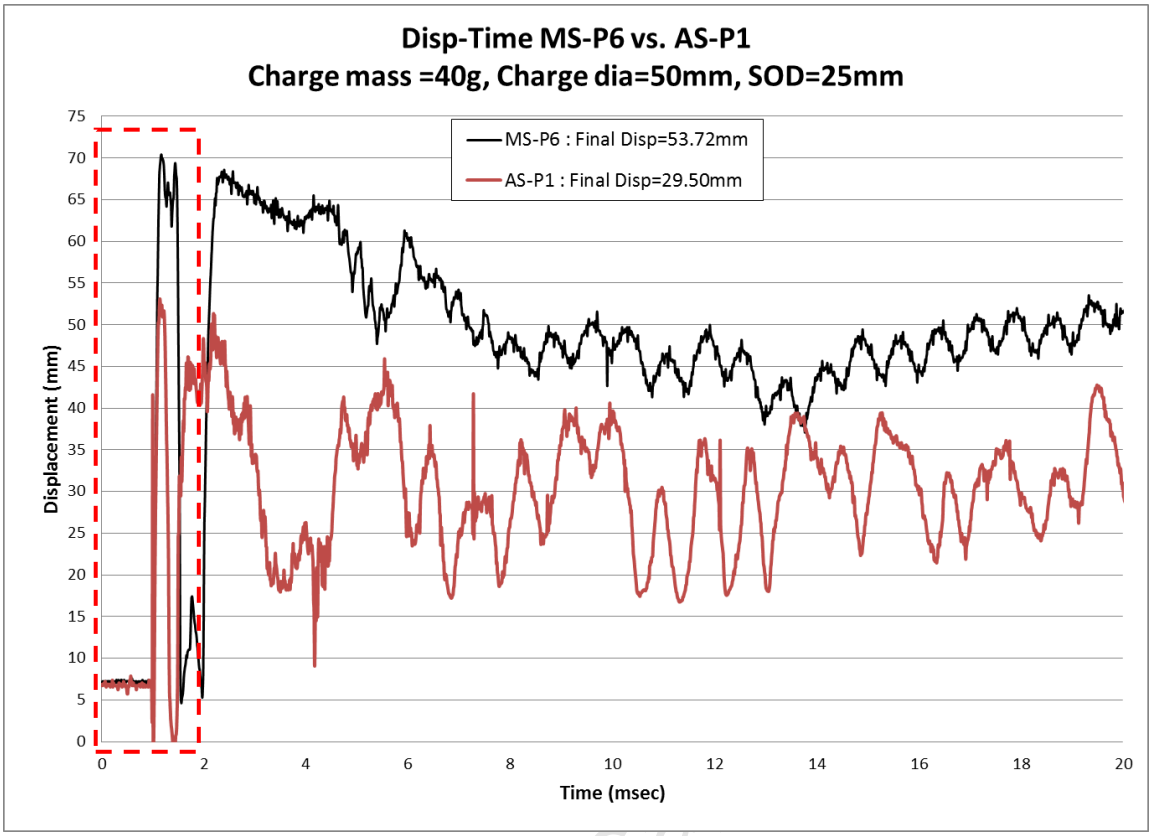

Figure 120: Displacement-time histories of steel and Armox 370T

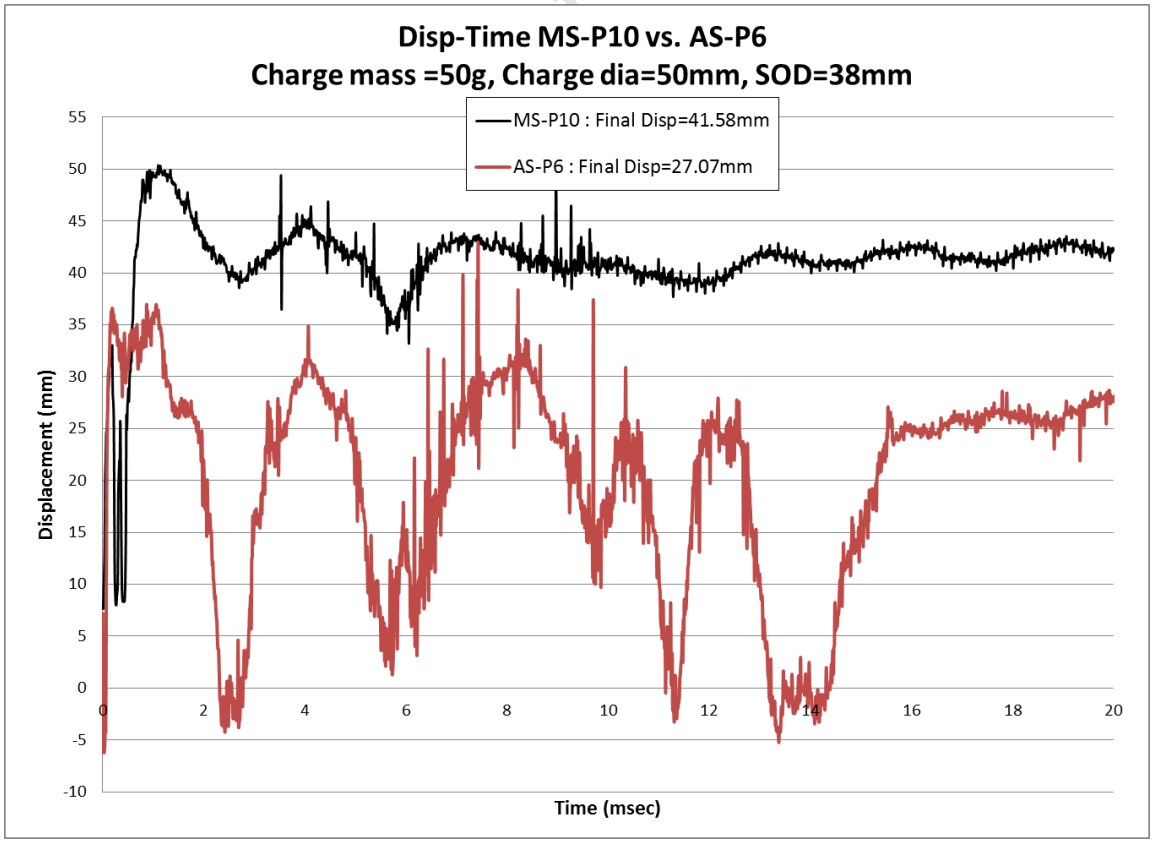

Figure 121: Displacement-time histories of steel and Armox 370T

The Armox 370T shows significant elastic responses in each of the three cases, shown by the large peak to trough amplitudes in the later response. The elastic recovery of the Armox steel is largely due to its significantly higher tensile strength.

There is an initial displacement spike visible in each of the displacement-time histories, indicated by the red rectangle in Figure 120, which is probably caused by the electronic detonator which is connected to the same electrical circuit which also powers the LIE. The significant drop immediately after the detonation spike is thus ignored and the graph is considered to be continuous. The numerical simulations do not show the spike attributed to detonation.

The mean of elastic oscillations recorded by the LIE correlates well with the permanent displacement measured post-test, with the deviations within one plate thickness.

The small vibrations in each of the displacement-time histories are attributed to the vibration on the clamping frame exerted by the blast load.

7.1.3. Comparison of Numerical and Experimental Results

Numerical simulations were performed to ascertain a greater insight into the loading and response of the plates. The displacement-time history comparisons of selected tests are discussed here.

7.1.3.1. Mild Steel

The simulated displacement-time histories are shown in Figure 122-Figure 126. Good correlation between the numerical results, in terms of their maximum and permanent displacements, is observed.

The vibration period, shown in the post-peak response, corresponded well with its experimental counterpart in all the tests. The experimental results, however, exhibit a higher elastic response from the material than the simulated results. The simulated final displacements predicted by AUTODYN were slightly higher than the measured final displacements in each test, but are all within a one plate thickness tolerance for the Mode I responses.

The displacement-time histories in Figure 125 show significant differences between the simulated and measured responses. However, in the experimental case, the MS-P6 plate ruptured. As the damage progression in the steel has not been included in the numerical models, poor agreement was expected as the plate response approaches rupture failure.

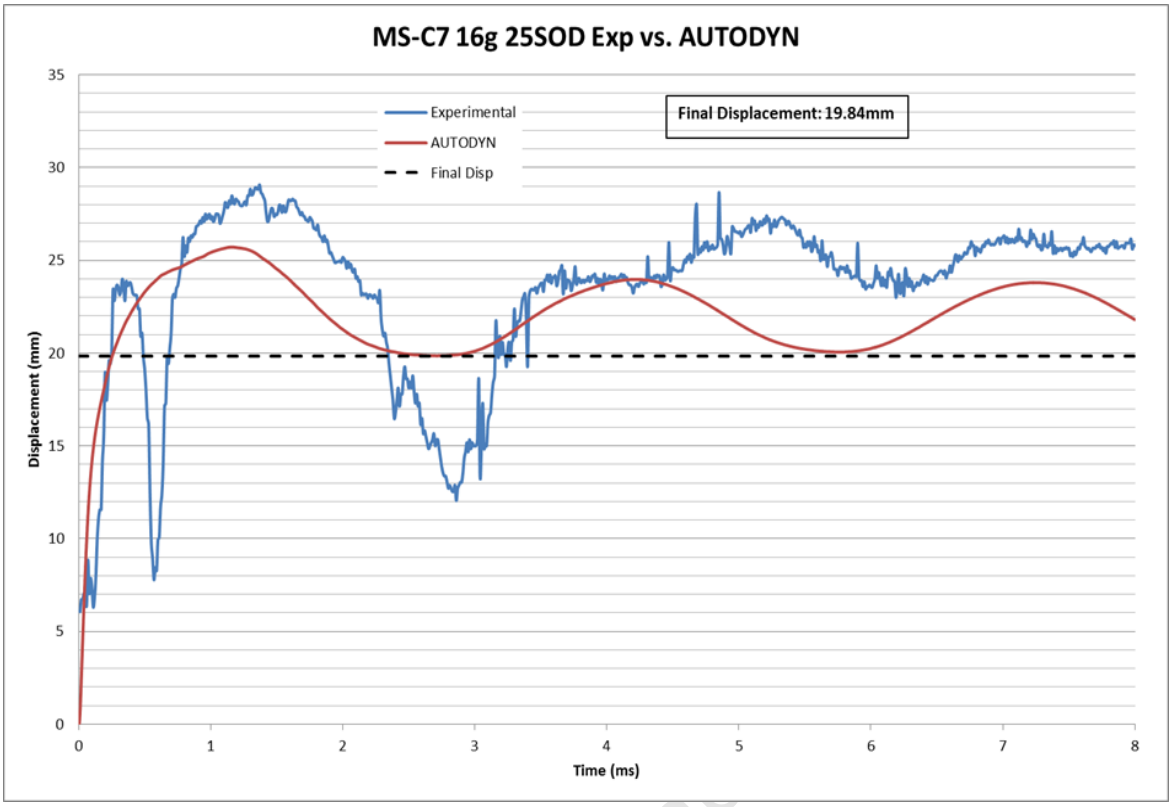

Figure 122: Graph to show the measured and simulated disp-time histories for mild steel (16g charge, 50mm diameter, 25mm sod)

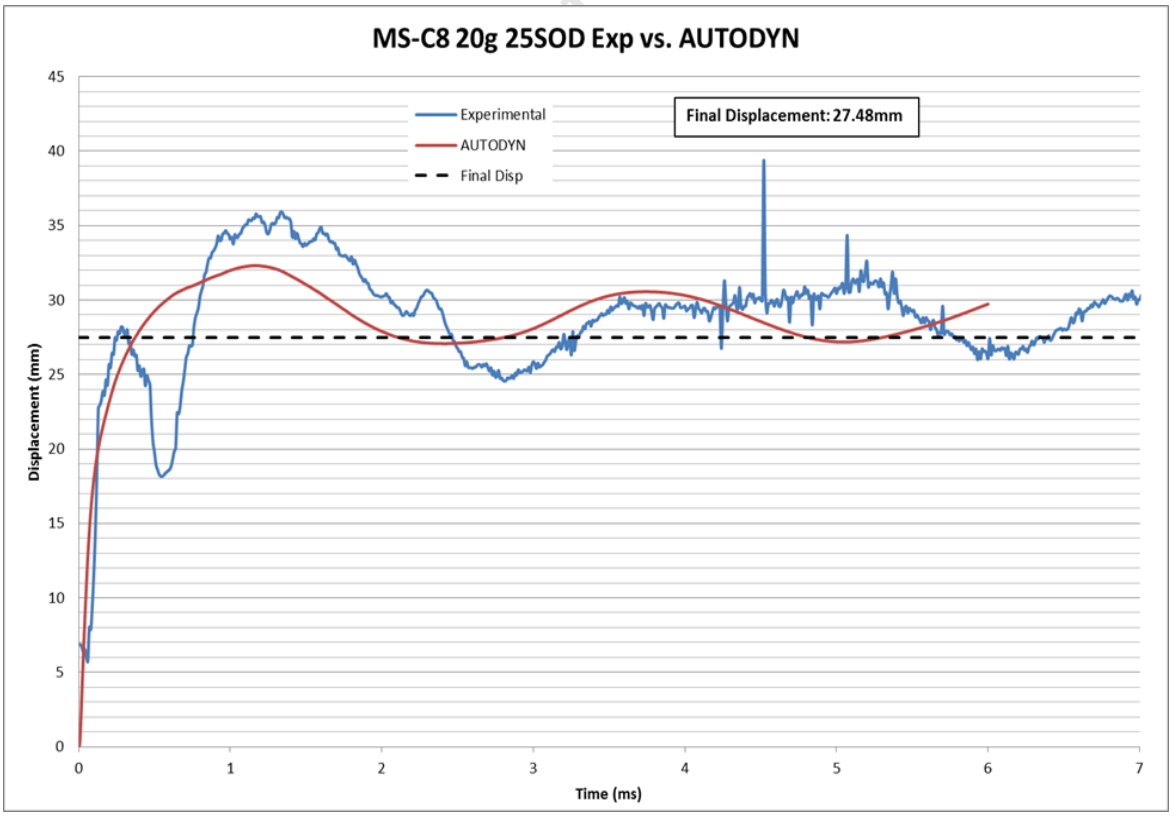

Figure 123: Graph to show the measured and simulated disp-time histories for mild steel (20g charge, 50mm diameter, 25mm sod)

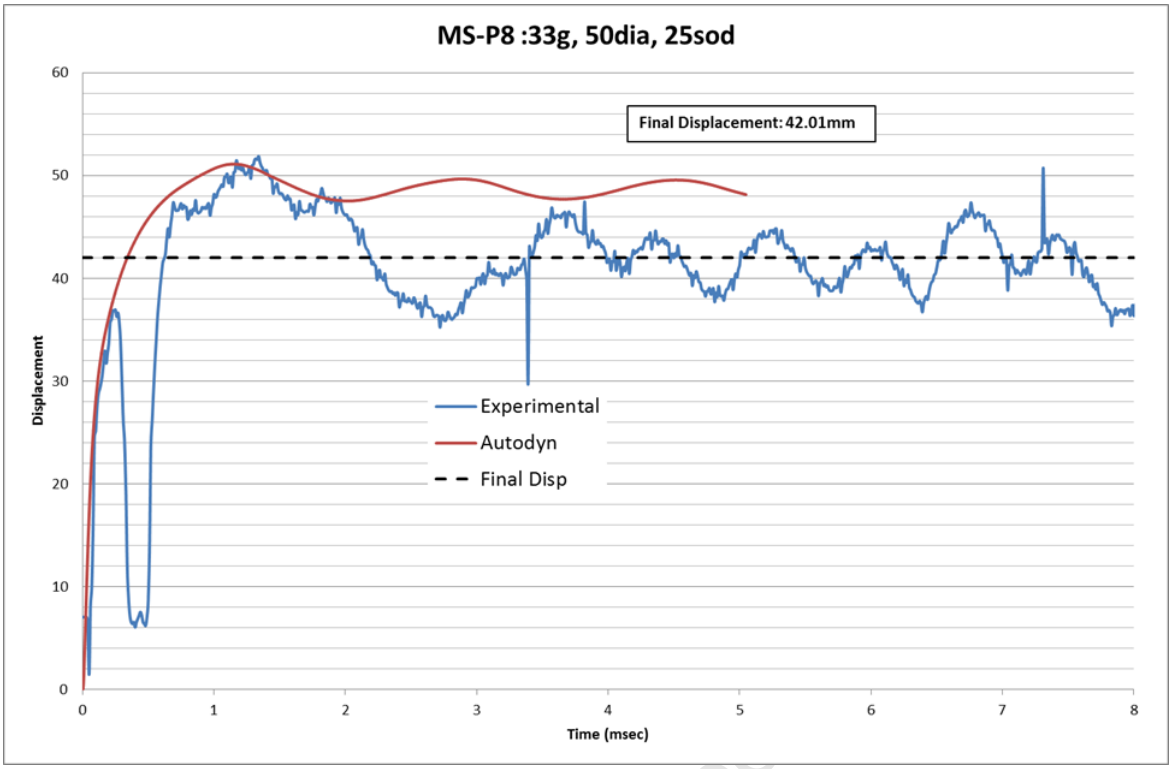

Figure 124: Graph to show the measured and simulated disp-time histories for mild steel (33g charge, 50mm diameter, 25mm sod)

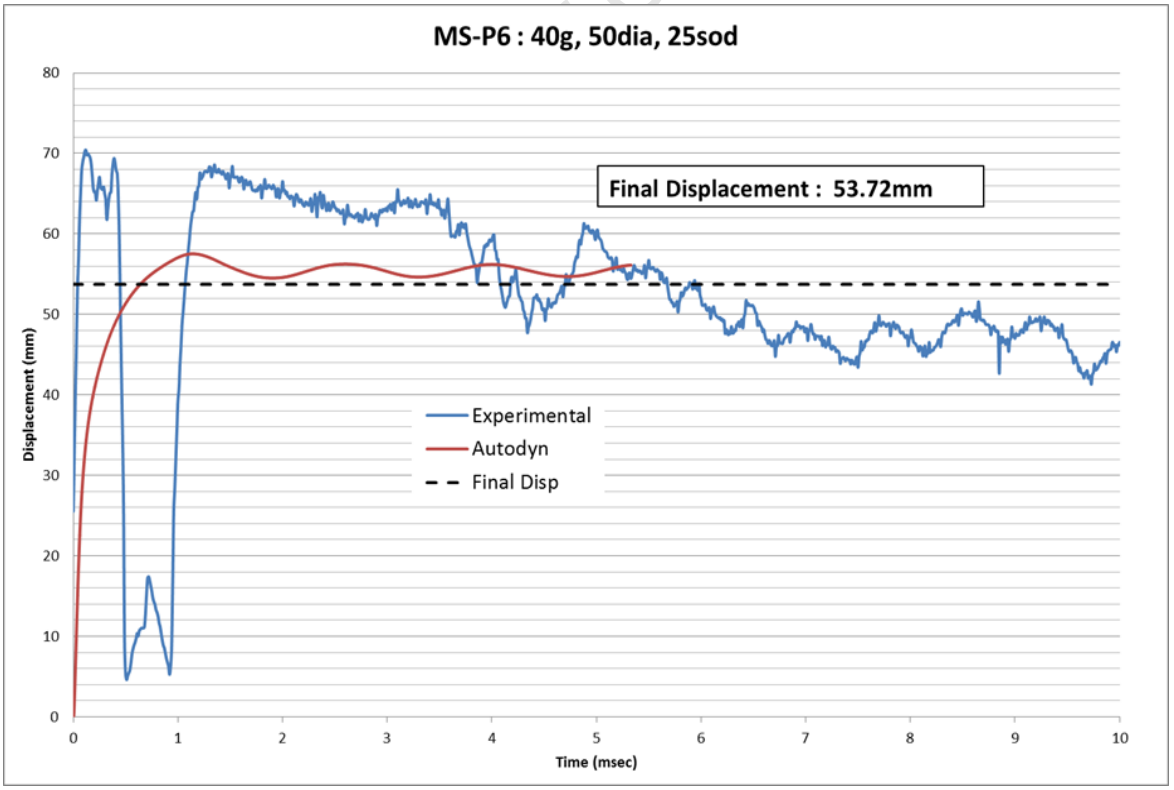

Figure 125: Graph to show the measured and simulated disp-time histories for mild steel (40g charge, 50mm diameter, 25mm sod)

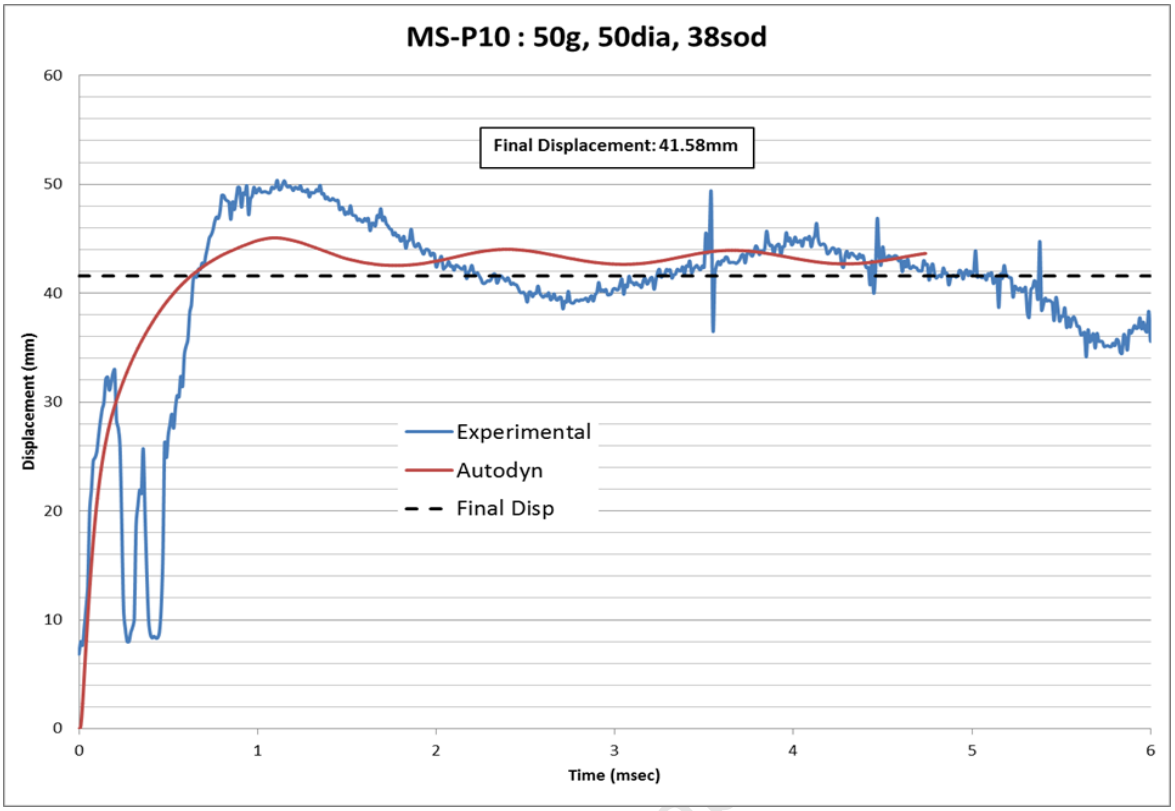

Figure 126: Graph to show the measured and simulated disp-time histories for mild steel (50g charge, 50mm diameter, 38mm sod)

7.1.3.2. Armox 370T

The displacement-time histories for the Armox 370T plates are shown in Figure 127-Figure 129. From the comparisons of the numerical and experimental displacement-time histories in Figure 127-Figure 129 it was observed that the simulations under-predict the peak displacement and the final displacement.

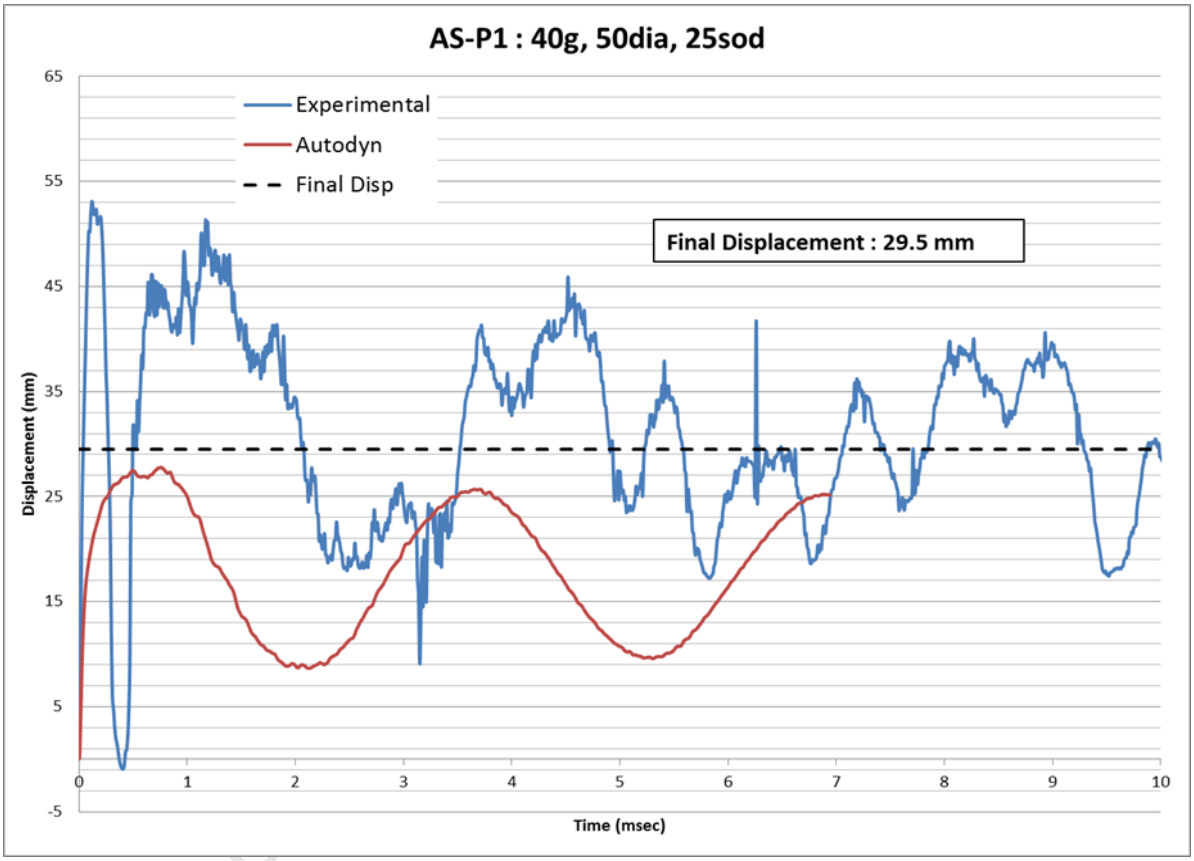

Figure 127: Graph to show the measured and simulated disp-time histories for Armox 370T (40g charge, 500m diameter, 25mm sod)

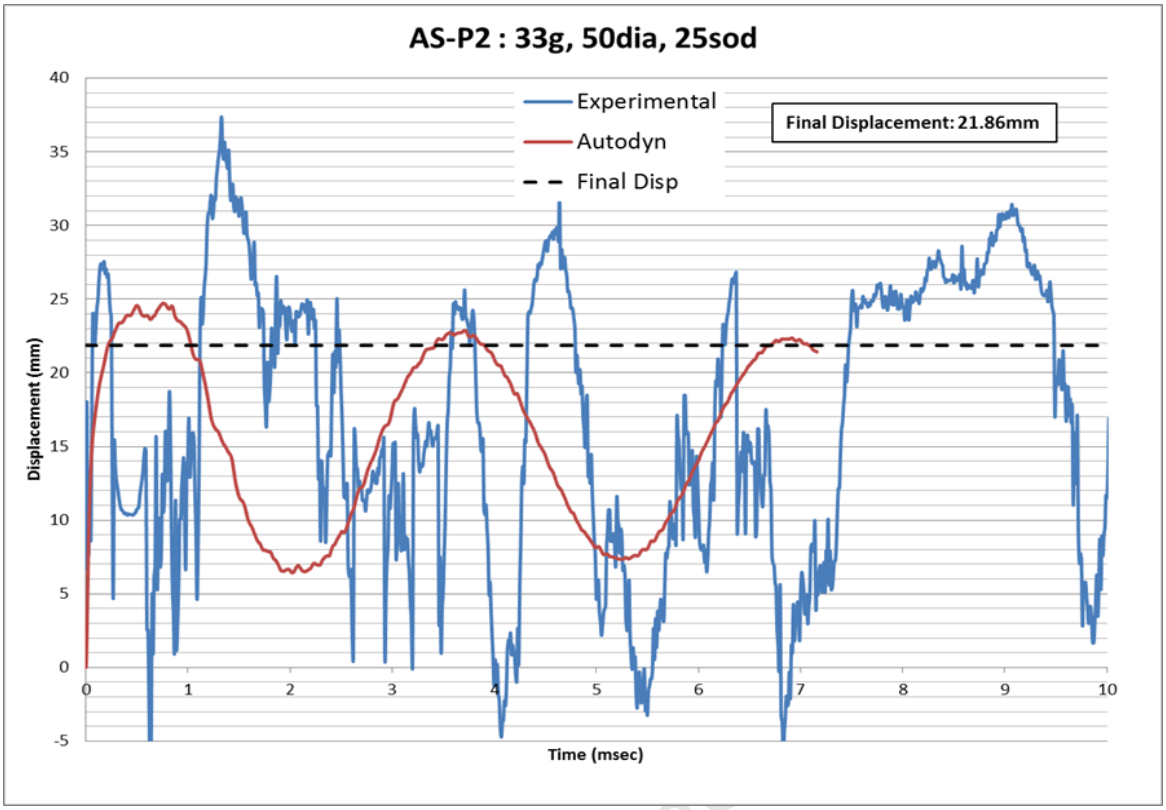

Figure 128: Graph to show the measured and simulated disp-time histories for Armox 370T (33g charge, 50mm diameter, 25mm sod)

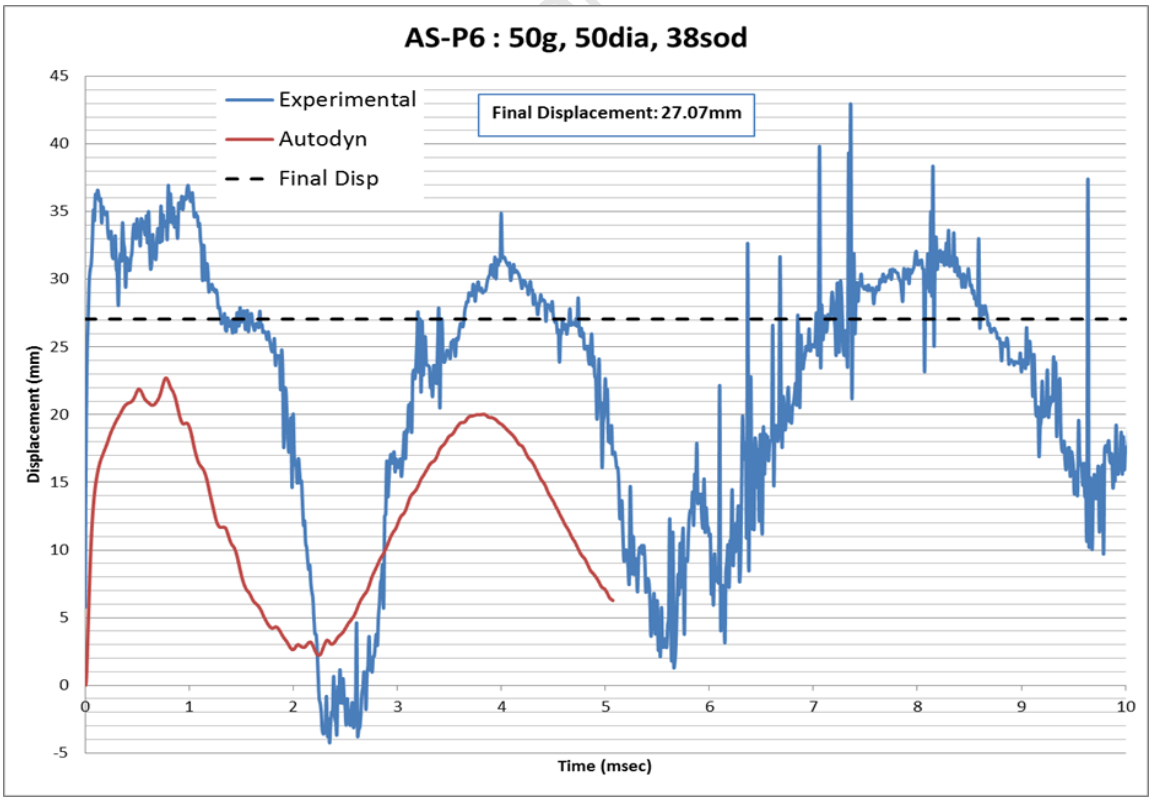

Figure 129: Graph to show the measured and simulated disp-time histories for Armox 370T (50g charge, 50mm diameter, 38mm sod)

Although the quantitative comparisons are poor, the qualitative comparisons of the simulated and measured transient response are reasonable, that is the oscillation period and highly elastic behaviour of the Armox 370T. However, the experimental exhibit noise and irregular amplitudes in the rebound phases, features not present in the simulation predictions.

7.1.3.3. Summary of Numerical Results

The majority of the mild steel simulations show good correlation, with permanent and maximum displacements within one plate thickness, shown in Figure 130 and Figure 131. The armour steel correlation is unsatisfactory, as the displacements did not fall within the one plate thickness experimental variation. The under prediction in the Armox 370T simulations was not due the choice of air mesh size as the same air mesh was used for the mild steel simulations. The impulses measured from the pressure-time simulations all show acceptable correlation with the experimentally measured impulses, as shown in Figure 132.

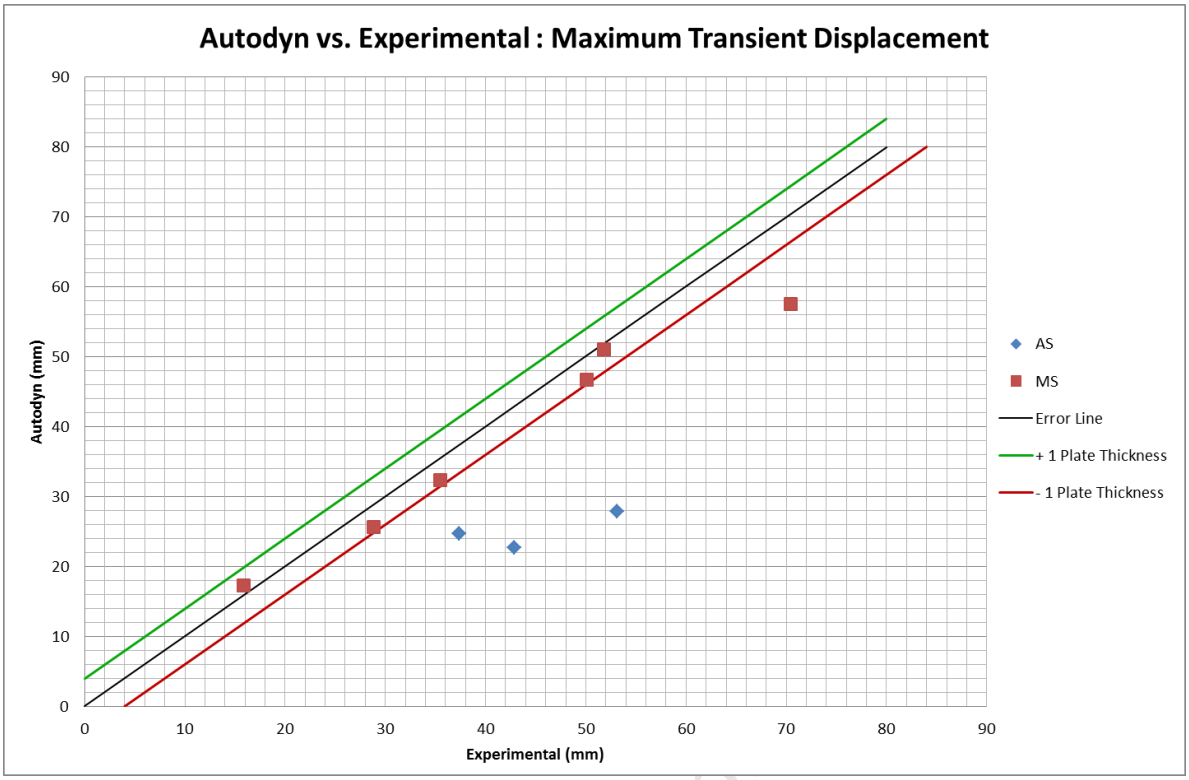

Figure 130: Plot of Maximum transient displacement of AUTODYN vs. Experimental Results

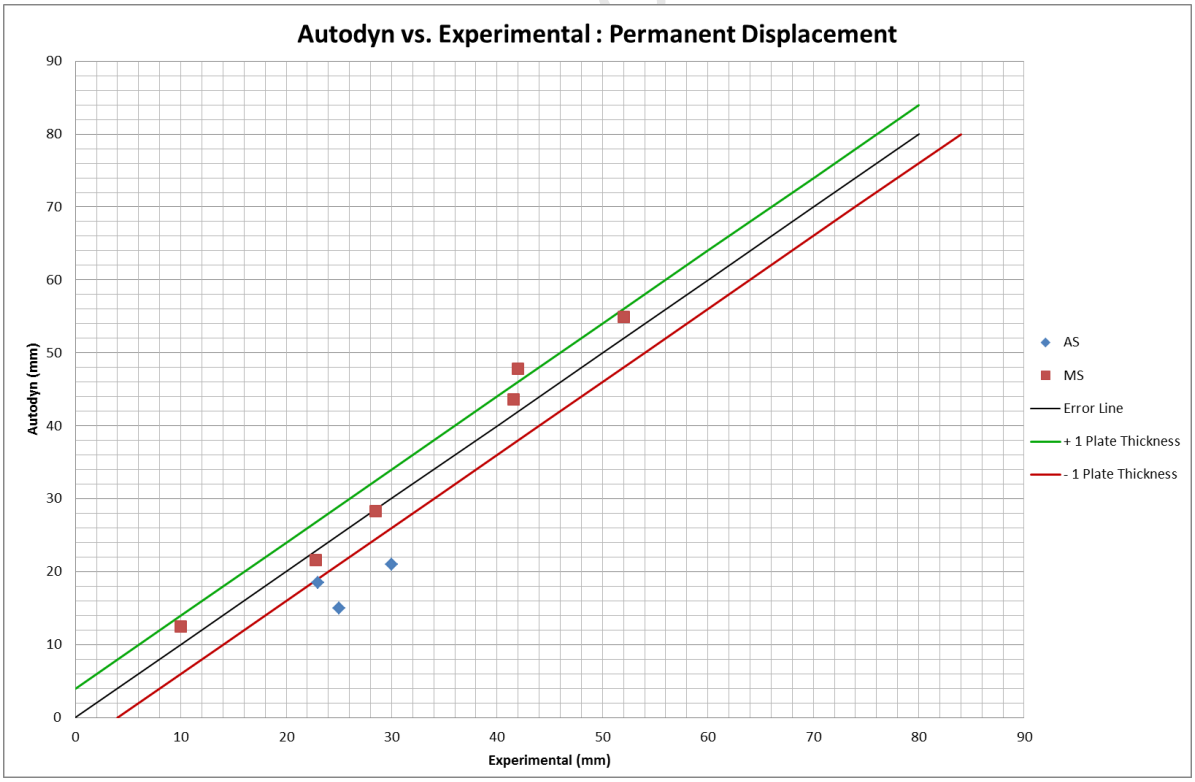

Figure 131: Plot of Permanent transient displacement of AUTODYN vs. Experimental Results

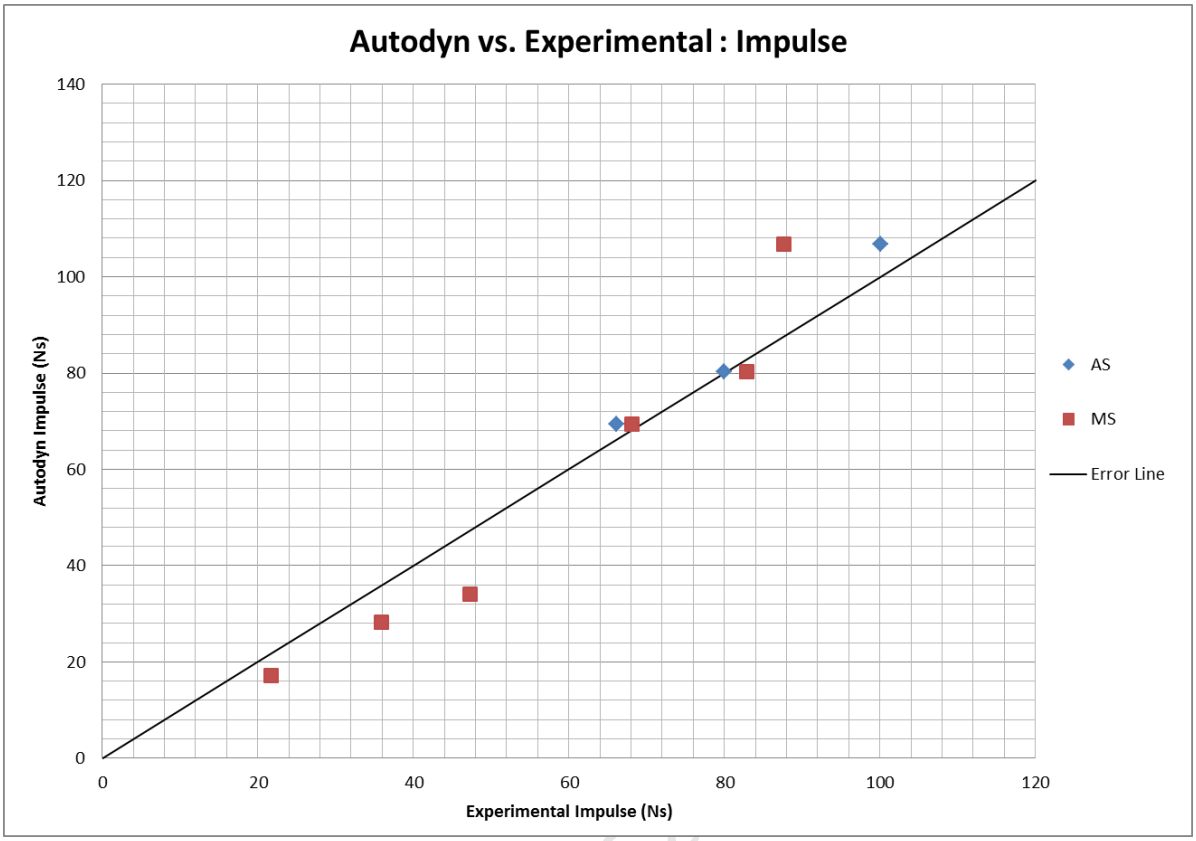

Figure 132: Plot of Impulse for AUTODYN vs. Experimental tests

7.1.4. Effect of Grade on Armour Steel: Armox 370T vs. 440T

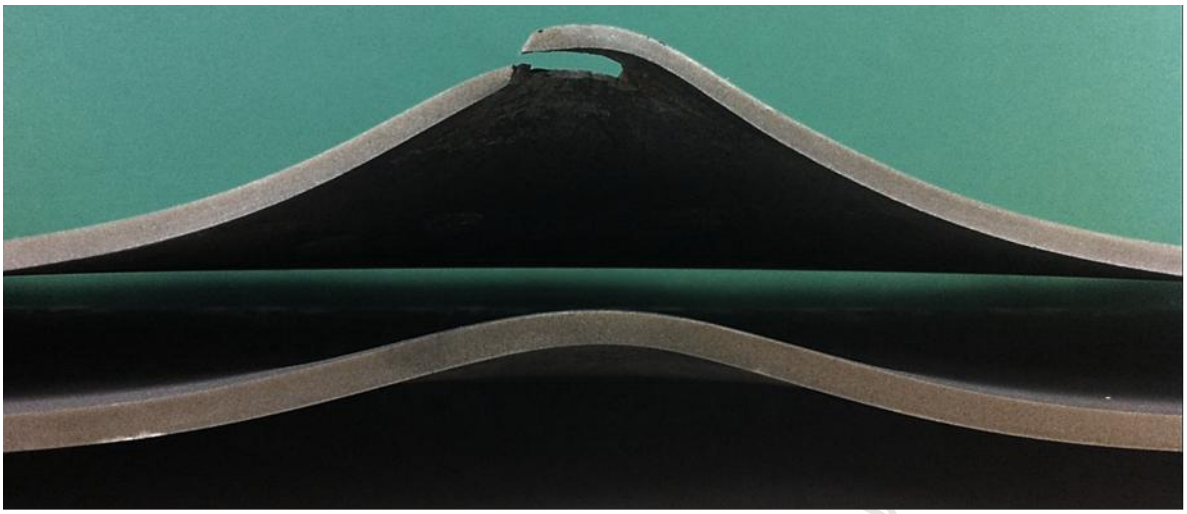

(a) Charge Mass : 40g, Diameter : 50, SOD : 25mm

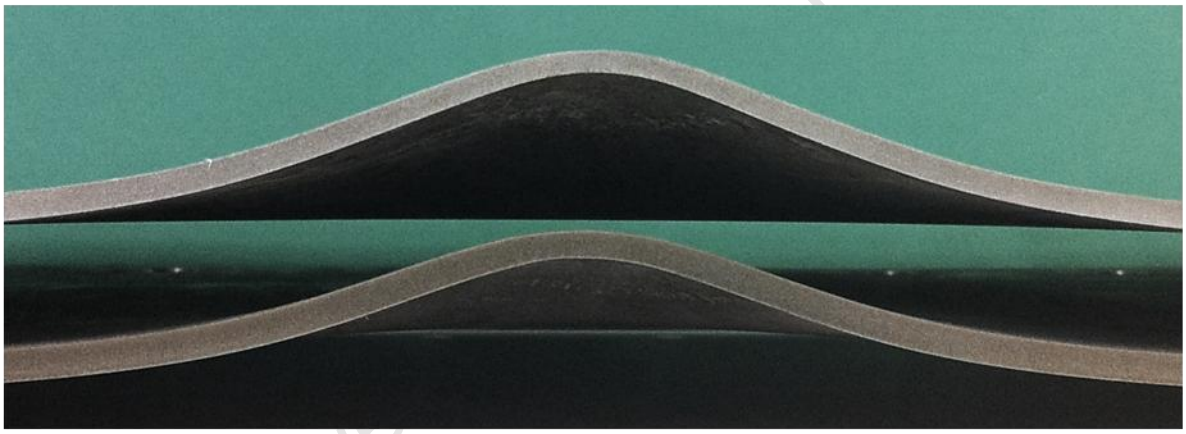

(b) Charge Mass : 33g, Diameter : 50, SOD : 25mm

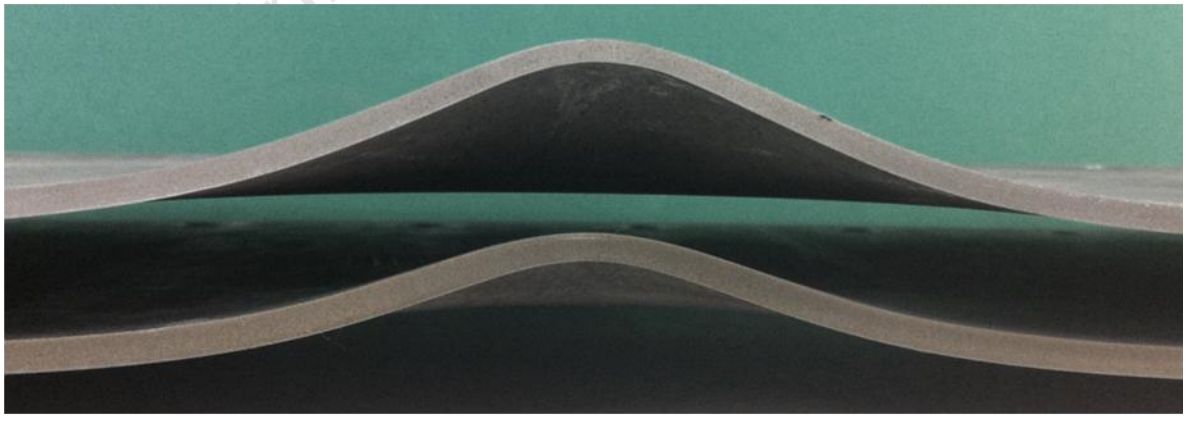

(c) Charge Mass : 40g, Diameter : 50, SOD : 38mm

Figure 133: Photographs showing the deformation profiles for three different charge mass configurations for Armox370T (TOP) and Armox 440T (BOTTOM)

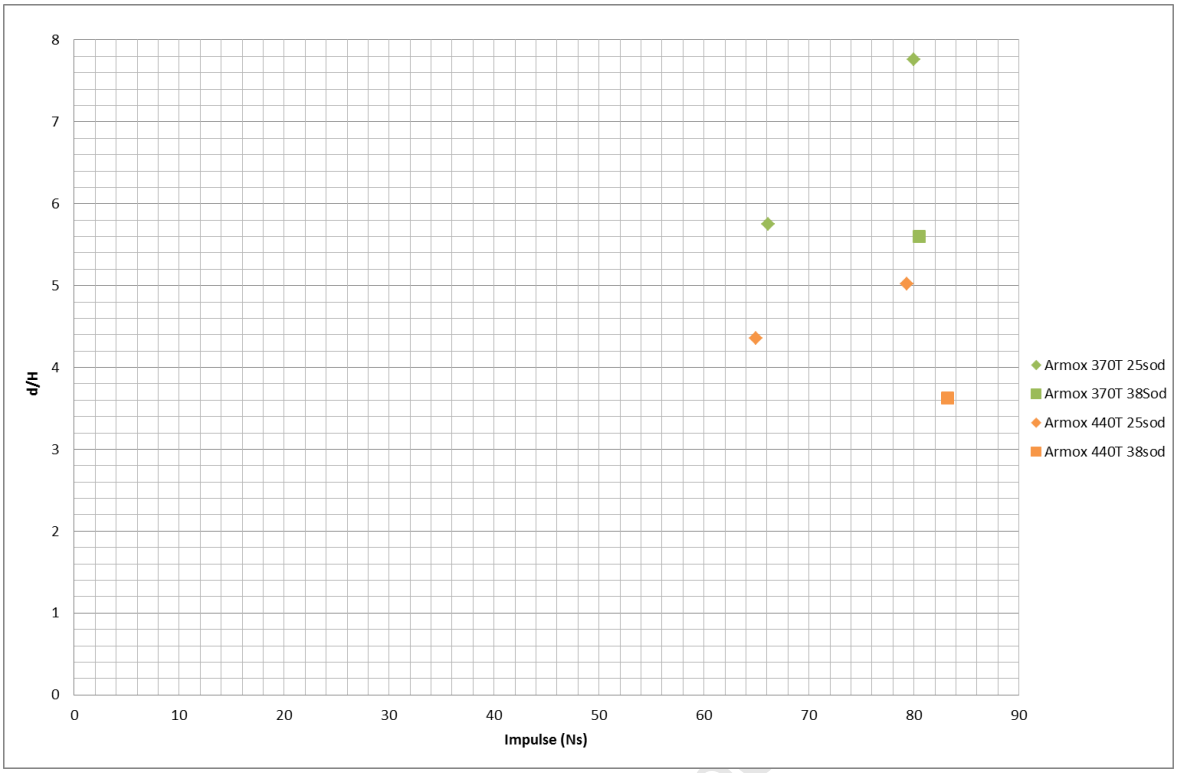

Figure 134: Graph of displacement/thickness ratio versus impulse for Armox 370T and 440T

Due to the Armox 440T plates being 0.6mm thicker than the Armox 370T plates, a graph of displacement/thickness ratio versus impulse was plotted in order compare the two materials quantitatively, shown in Figure 134. The Armox 440T plates performed better than the Armox 370T which shows that the grade of the steel has a significant effect on the response of the plates.

Table 14: Table of test results for Armox 370T vs. Armox 440T listed in same order as photographs

Plate Number	Charge Mass (g)	SOD (mm)	Charge Diameter (mm)	Permanent Mid-Point Displacement (mm)	Impulse (Ns)	Dimensionless Impulse	d/H	Grade
AS-P1	40	25	50	29.50	80.02	12.45	7.76	370T
AS-P14	40	25	50	19.07	79.31	9.01	5.02	440T
AS-P2	33	25	50	21.86	66.15	10.29	5.75	370T
AS-P10	33	25	50	16.57	64.94	7.38	4.36	440T
AS-P5	40	38	50	21.27	80.47	8.82	5.60	370T
AS-P13	40	38	50	13.78	83.20	6.65	3.63	440T

7.2. Comparison of 400 x 400 Plates

7.2.1. Mild Steel vs. Aluminium

Aluminium 5083-H116 was blast tested and compared to the 3mm thick mild steel plates on an equivalent mass basis. Blast tests were performed with charge masses ranging between 12g to 33g and stand-off distance of 25mm and 38mm. The photographs from Figure 135-Figure 139 show the cross-section profiles of the mild steel plates and aluminium plates.

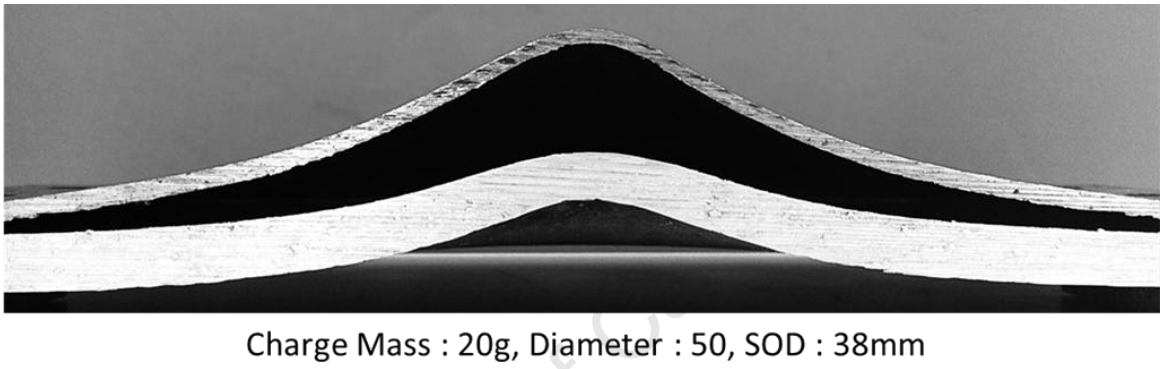

Figure 135: Photograph showing deformation profiles for AL-1 (BOTTOM) vs. MS400-14(TOP)

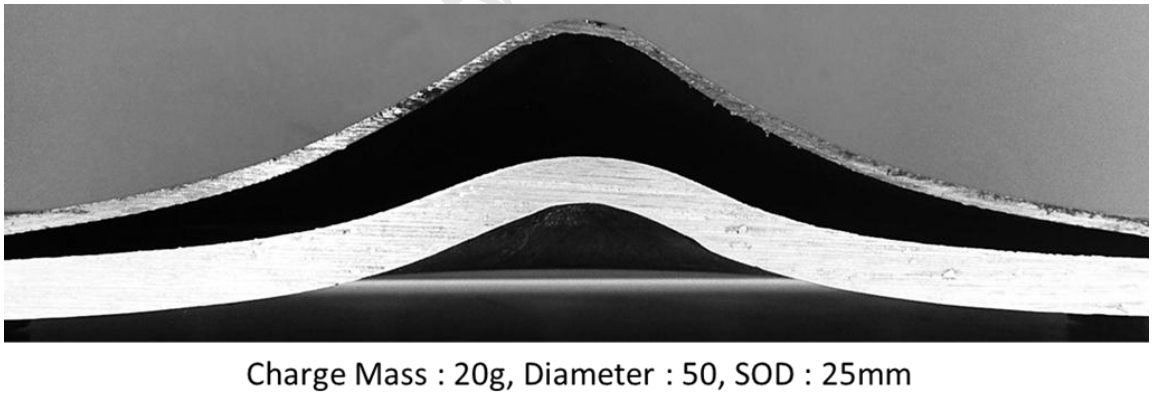

Figure 136: Photograph showing deformation profiles for AL-2 (BOTTOM) vs. MS400-8(TOP)

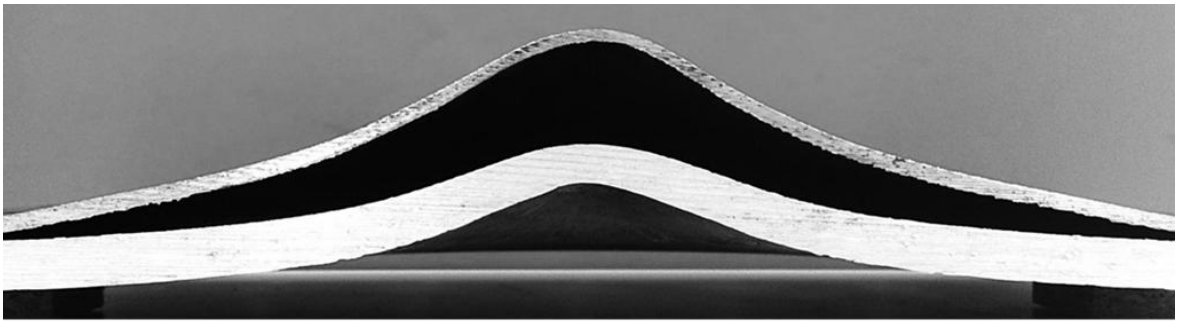

Charge Mass : 28g, Diameter : 50, SOD : 38mm

Figure 137: Photograph showing deformation profiles for AL-3 (BOTTOM) vs. MS400-13(TOP)

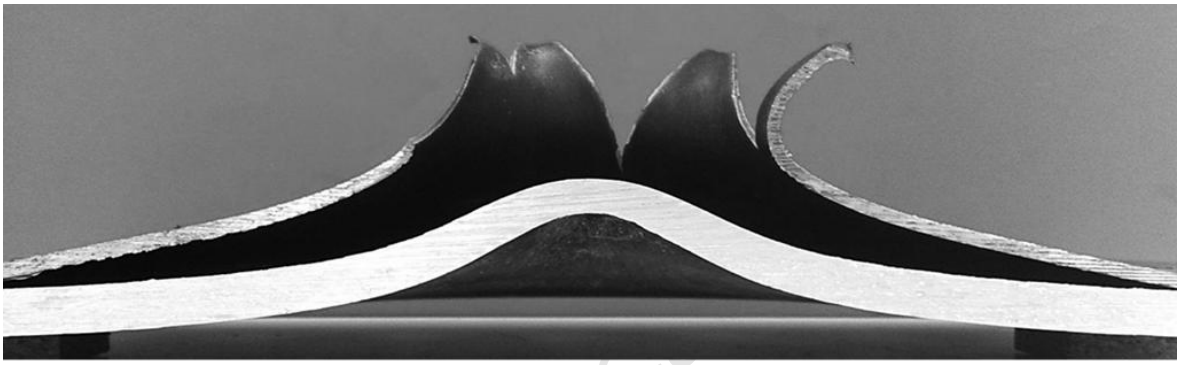

Charge Mass : 28g, Diameter : 50, SOD : 25mm

Figure 138: Photograph showing deformation profiles for AL-4 (BOTTOM) vs. MS400-11(TOP)

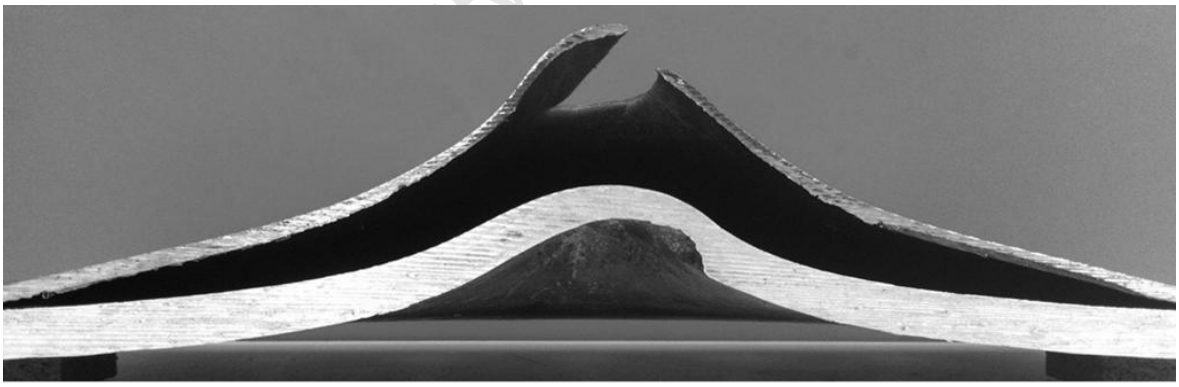

Charge Mass : 33g, Diameter : 50, SOD : 38mm

Figure 139: Photograph showing deformation profiles for AL-6 (BOTTOM) vs. MS400-15(TOP)

It is observed from Figure 135-Figure 139 that the aluminium was able to sustain higher blast loads than the mild steel without failure. This is evident in Figure 138 and Figure 139, where the mild steel plates both failed while the aluminium did not rupture under the same blast loading conditions. The thickness of the aluminium plates may have been a factor in its lower displacements. The aluminium plates exhibited significant thinning at higher blast loads, together with the lower melting temperature of the aluminium, which resulted in the melt and spray during blasting, allowed the aluminium plates to dissipate the blast load more effectively than mild steel.

From the graph of permanent mid-point displacement versus Impulse in Figure 140, it is observed that the aluminium plates sustained significantly lower displacements than the 3mm thick mild steel plates at similar impulses. Although the aluminium had lower displacements, the displacements of each material increased linearly with increasing impulse.

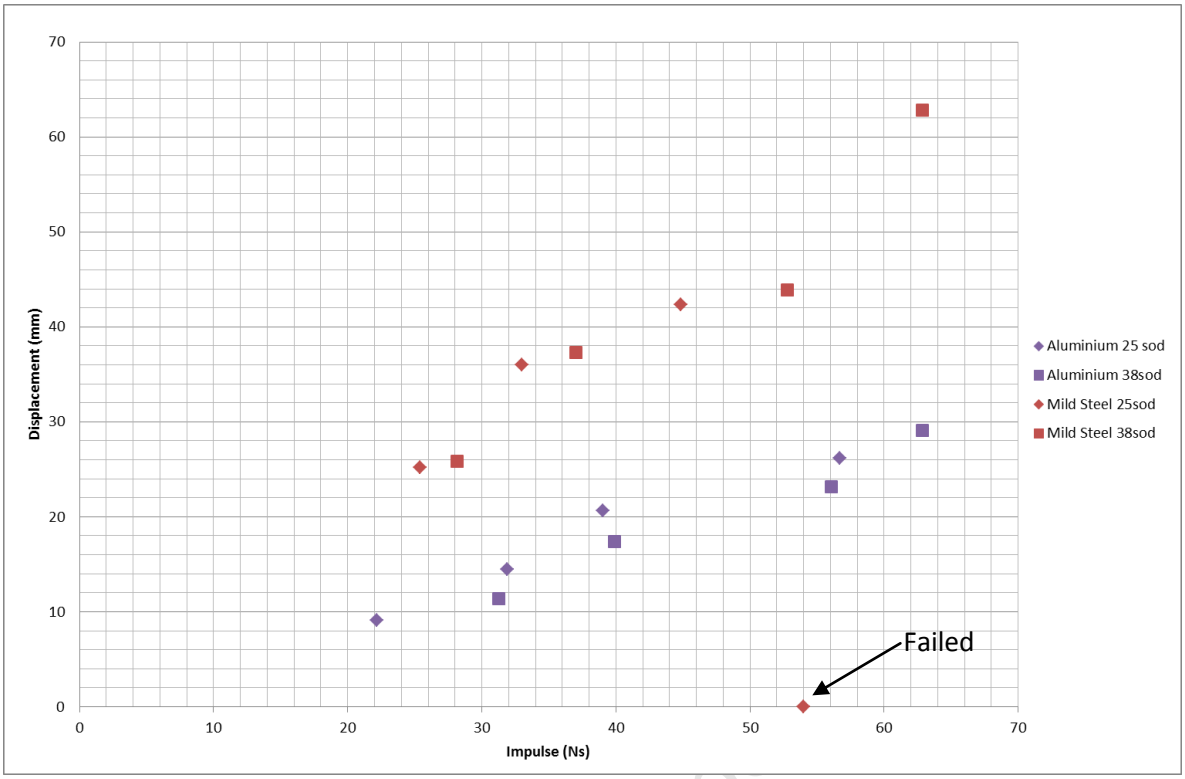

Figure 140: Graph of Displacement versus Impulse for aluminium and Mild Steel

Table 15: Table of test results for 3mm thick Mild Steel vs. Aluminium

Plate Number	Charge Mass (g)	SOD (mm)	Charge Diameter (mm)	Permanent Mid-Point Displacement (mm)	Impulse (Ns)	Dimensionless Impulse	d/H
MS400-6	12	25	50	25.15	25.42	16.21	8.38
AL-9	12	25	50	9.08	22.15	2.14	0.86
MS400-16	16	38	50	25.88	28.16	12.66	8.63
AL-8	16	38	50	11.41	31.25	2.13	1.08
MS400-7	16	25	50	36.02	33.02	21.06	12.01
AL-7	16	25	50	14.45	31.88	3.08	1.36
MS400-15	33	38	50	62.84	62.85	28.26	20.95
AL-6	33	38	50	29.05	62.85	4.28	2.74
MS400-11	28	25	50	torn	54.00	34.45	N/A
AL-4	28	25	50	26.18	56.68	5.47	2.47
MS400-13	28	38	50	43.89	52.77	23.73	14.63
AL-3	28	38	50	23.12	56.05	3.81	2.18
MS400-8	20	25	50	42.33	44.85	28.61	14.11
AL-2	20	25	50	20.66	39.01	3.77	1.95
MS400-14	20	38	50	37.26	37.01	16.64	12.42
AL-1	20	38	50	17.42	39.90	2.72	1.64

7.2.2. Composite Panels

The difference in boundary conditions between the Twintex and Dyneema panels means that a quantitative comparison cannot be made. However, observations can be made regarding their methods of failure.

The stiffer inelastic Twintex panels exhibited brittle failure, as evident through matrix cracking, relatively small deformations and fibre fracture. The stiffness of the Twintex panels allows it to withstand lower impulse blast relatively well, exhibiting small displacements and slight matrix cracking. Once the impulse is increased and the panels can no longer deform, fibre fracture occurs and increases with increasing impulse until complete rupture of the panel.

The highly elastic Dyneema panels were able to withstand significantly higher impulses (up to 114Ns) compared to the Twintex panels. However, the Dyneema panels had different boundary conditions which may have allowed the panels to sustain higher impulses. The large displacements of the panels suggest that Dyneema is more ductile than Twintex and would be able to withstand higher impulses before failure. The virtually unrestrained clamping conditions and low in plane shear resistance allowed the Dyneema panels to buckle slightly and dissipate the blast load.

7.3. Summary of Impulse Versus Charge Mass for all Blasts

A graph of impulses versus charge mass is shown in Figure 141. It is observed from Figure 141 that impulse increased linearly with increasing charge mass, with all the data points corresponding with the expected trend [1], [13] , [53]. These results show that the tests were performed in a repeatable fashion, similarly to previous work. The material type does not alter the impulse imparted to the plates in any discernable way.

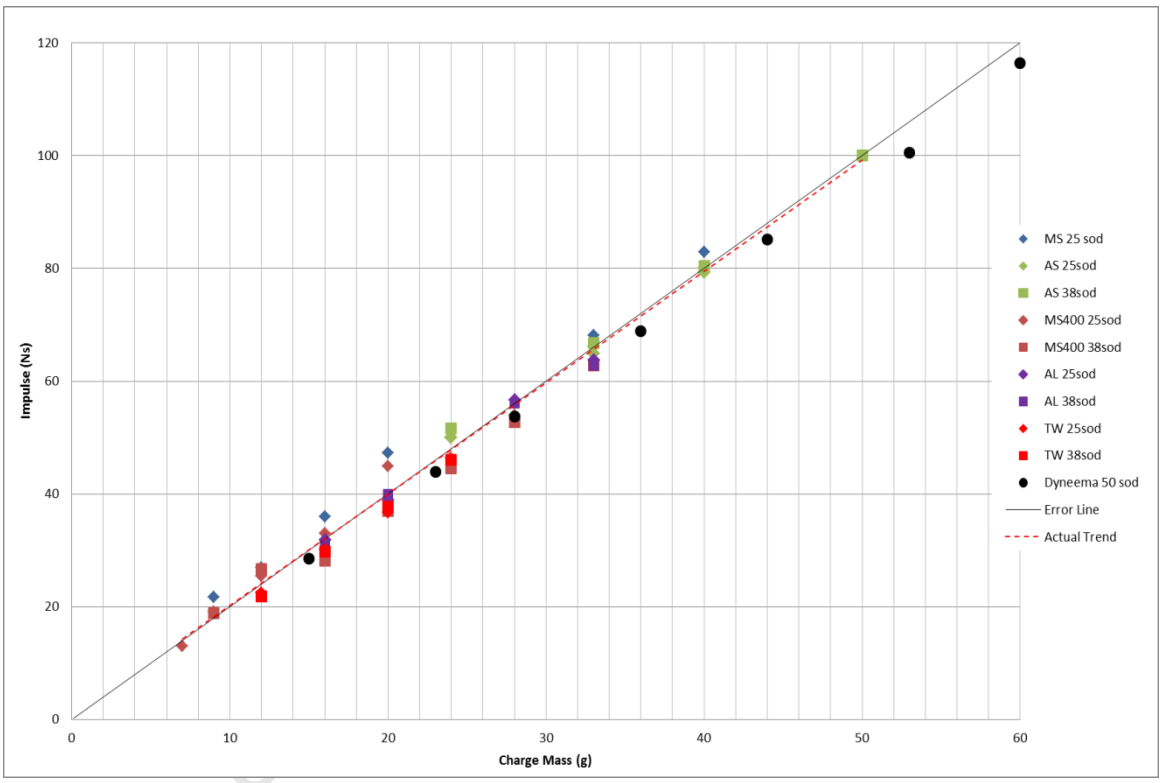

Figure 141: Plot of Impulse versus charge mass for all blast tests performed

7.4. Dimensionless Analysis

Dimensionless analysis was performed to enable comparisons between plates of different materials and sizes tested at different stand-off distances and for different configurations. The calculations performed were as described in Section 3 using the modified dimensionless impulse parameter used by Jacob *et al* [7], who introduced a scaling factor to account for stand-off distance from the dimensionless impulse number first developed by Nurick and Martin [52]. The factor was developed for experiments where the stand-off distance was created using a rigid tube between the explosive and the test plate [8].

$$\phi_{ql} = \frac{I\left(1+ln\left(\frac{lb}{\pi R_0^2}\right)\right)}{2H^2(bl\rho\sigma_0)^{\frac{1}{2}}} \times \frac{1}{\zeta_s} \qquad \text{(Recall eq. 25)}$$

In cases where the charge radius is greater than stand-off distance (R_o > S), (eq. 25) is used without the stand-off distance parameter. The stand-off distance parameter ζs is only incorporated into (eq. 23) in cases where the charge radius is less than the stand-off distance (R_o < S).

$$\phi_{ql} = \frac{I\left(1+ln\left(\frac{lb}{\pi R_0^2}\right)\right)}{2H^2(bl\rho\sigma_0)^{\frac{1}{2}}} \qquad \text{(Recall eq. 23)}$$

Figure 142 shows a graph of displacement/thickness ratios versus dimensionless impulses for all the tests. Unexpectedly, the 38mm stand-off tests have unusually low dimensionless impulse values when compared to the 25mm stand-off tests. It can also be observed that the 75mm diameter 25mm stand-off tests show good correlation with the 50mm diameter 25mm stand-off tests in terms of the displacement/thickness ratios. It can be assumed that the 75mm diameter

charge may not impart the same amount of impulse onto the test plate as its larger diameter results in a greater amount of the blast pressure flowing past the test plate. The larger diameter also means that the 75mm diameter charge will impart a more uniform load distribution than the 50mm diameter charge.

The empirical relationship proposed by Nurick and Martin [52] in order to predict the mid-point deflection/thickness ratios is represented by the solid line shown in Figure 142.

$$\frac{\delta}{H} = 0.48\phi_q \qquad \text{(Recall eq. 27)}$$

Most of the data points were above the empirical line, with a combined linear trend of $0.58\phi_q$ which is slightly higher (20%) than the predicted trend. The only exceptions are the Twintex data points which are all below the empirical line for both stand-off distances. The experimental data deviated further from the predicted trend as the dimensionless impulse increased.

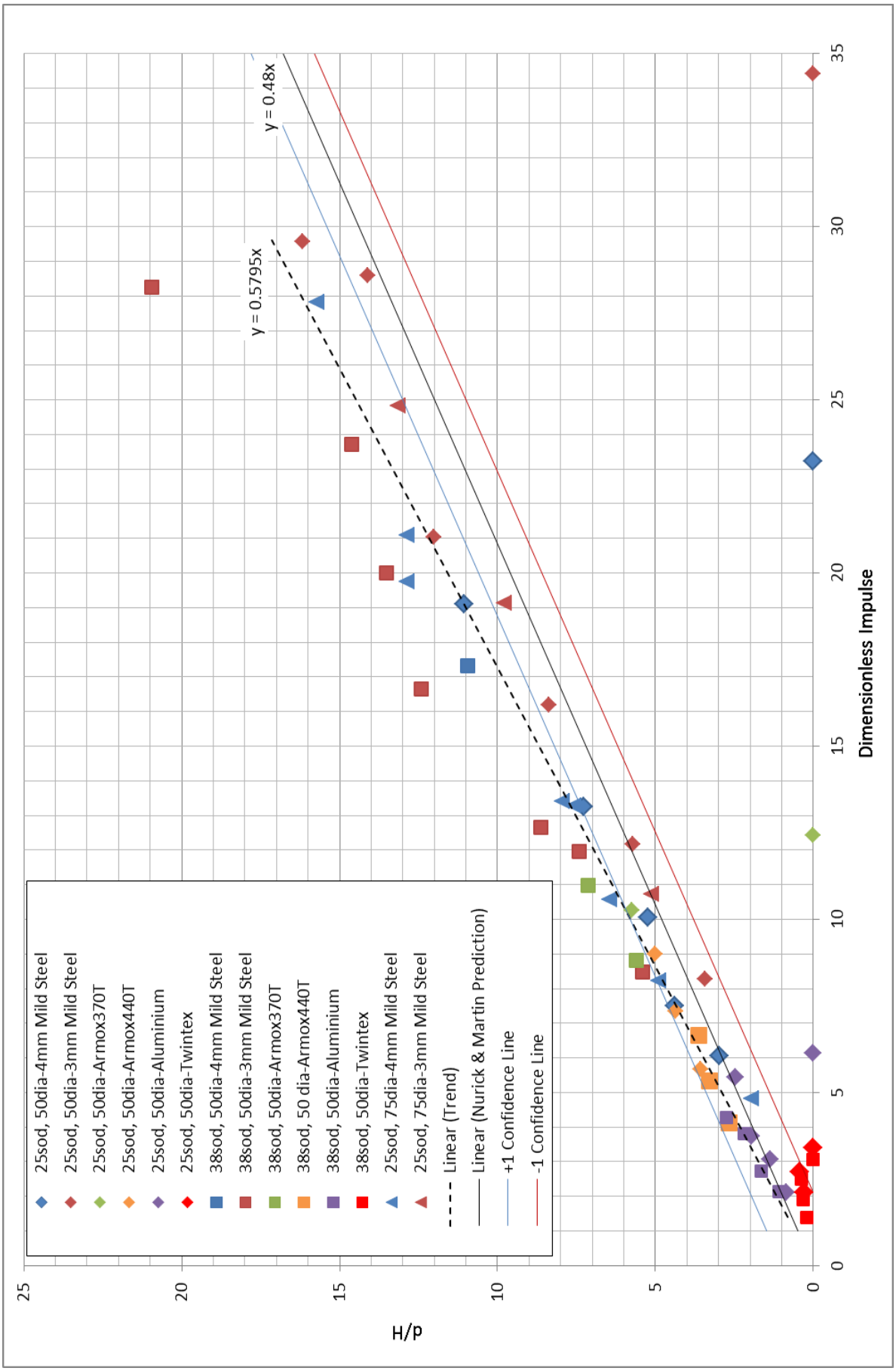

Figure 142: Graph of Displacement/thickness Ratios versus Dimensionless Impulse for all Tests

It can be observed from Figure 142 that most of the 25mm stand-off tests show a closer correlation than the 38mm stand-off tests have a larger deviation from the 90% confidence lines of $\pm 1 \frac{d}{t}$, which originated from test work performed by Nurick and Martin [52]. The stand-off distance reduction factor which was included in the modified Nurick and Martin dimensionless impulse calculations [7], for stand-off distances greater than the charge radius, contributed to the deviation seen in Figure 142.

One purpose of using dimensionless impulse is to correct for the effects of charge diameter and stand-off distance. The stand-off distance scaling factor is responsible for the significant deviation from the trend line shown in Figure 142.

The experimental arrangement used by Jacob [7] employed a tube, shown in Figure 143, for localised blast loading which created confinement of the blast load. The tube confinement may cause the blast wave to be reflected and impart additional impulse, accounted for in the scaling factor. However, the experimental arrangement used herein does not employ a blast tube. The blasts are considered to be free-air blasts. Thus, the application of the scaling factor (which in this case would be multiplying by 0.704) results in a 30 percent reduction in the dimensionless impulse of the 38mm stand-off tests.

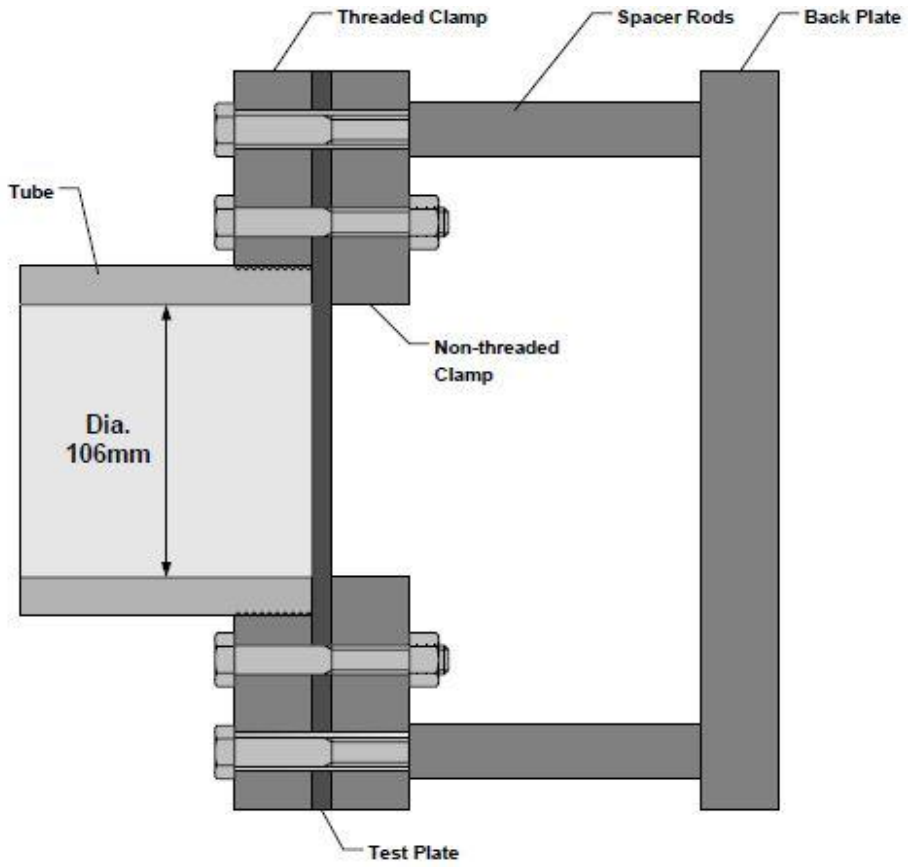

Figure 144: Schematic of set-up used by Jacob showing the tube used [7]

Figure 145 shows a schematic illustrating the effects that the tube confinement has on the resulting impulse due to the blast waves reflecting off the tube walls and in effect, recycling the pressure and creating additional impulse. The direction of the blast wave is dictated by the effective charge height investigated by Kennedy [5]. The reason that the additional impulse is accounted for in the case of the tube is due to the fact that this additional impulse is not the true impulse loading the test plate. Thus the stand-off distance scaling parameter ζ_s used by Jacob [7], may not be valid in this instance (case without blast tube).

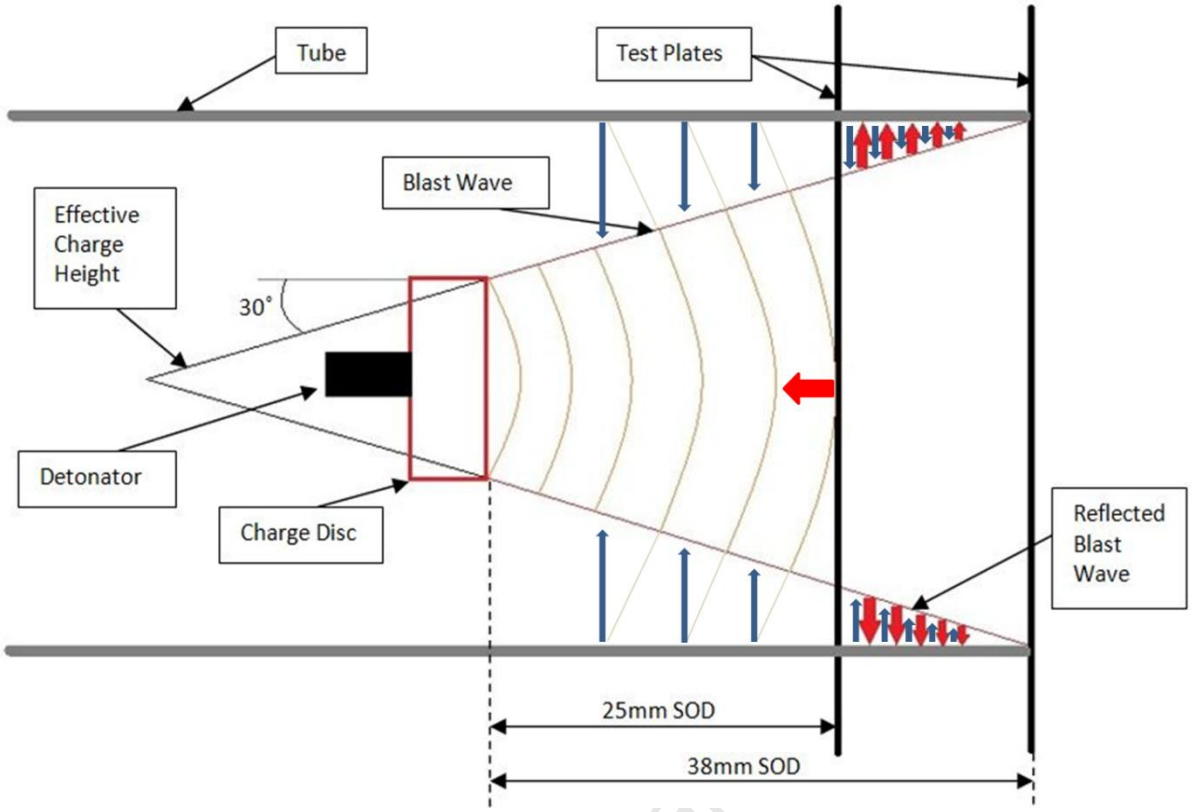

Figure 145: Highly Simplified Illustration Showing Blast Propagation in a Tube

Due to the stand-off distance parameter used in equation 25 resulting in values for the 38mm stand-off dimensionless impulse falling outside the 90% confidence lines, the graph shown in Figure 142 was re-plotted with the stand-off distance parameter removed (using equation 23). The new dimensionless impulse values are shown in Table 16. The displacement/thickness versus dimensionless impulse values are re-plotted in Figure 146 and Figure 147. Figure 146 shows complete range of data and the 38mm stand –off distance tests are now within the confidence lines. The lower displacement portion of Figure 146 is plotted in Figure 147. The overall gradient of the linear regression fit is now 0.5132, which is much closer to the predicted Nurick and Martin [52] trend of 0.48.

The low displacement/thickness values for Twintex can be attributed to its high thickness (value) and linear elastic brittle material characteristics.

The data points for the aluminium blast tests show a good linear correlation with the empirical predictions, particularly for the 25mm stand-off tests. The aluminium plates were thicker than the mild steel and armour steel plates as well as having a lower melting temperature. This correlation is surprising given the different failure mechanisms present in the aluminium response (thinning, material melting and spray). The greater thickness of the aluminium plates resulted in significantly lower displacement/thickness values, which could be matching the variation.

It can be seen from Figure 147 that the aluminium and Armox 440T 38mm stand-off data points are now slightly below the predicted trend although still within the 90% confidence interval. All of the points in the highlighted section, with the exception of Twintex, are now within the confidence lines.

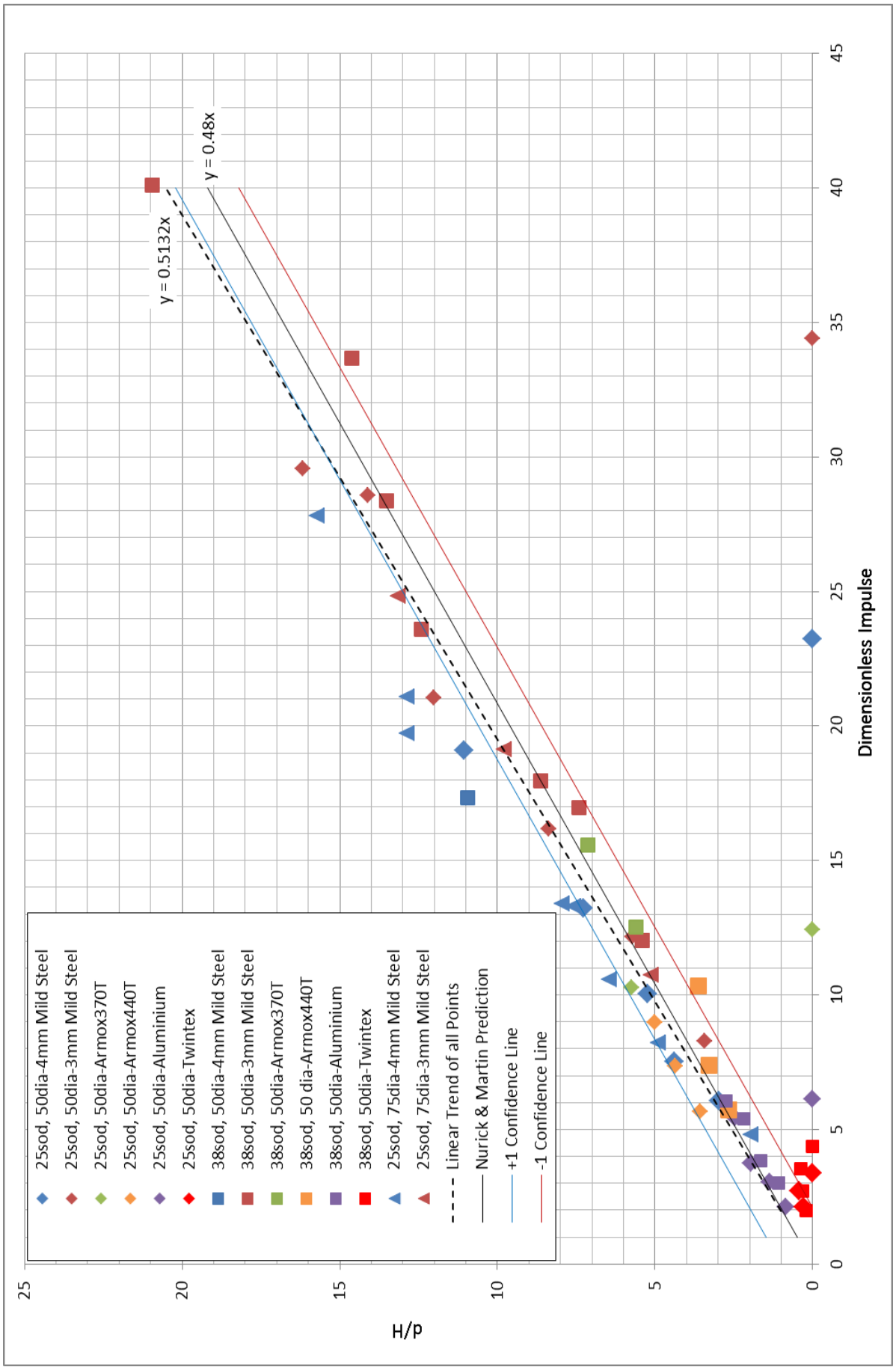

Figure 146: Displacement/Thickness ratio versus Dimensionless Impulse Plots with corrected 38mm stand-off

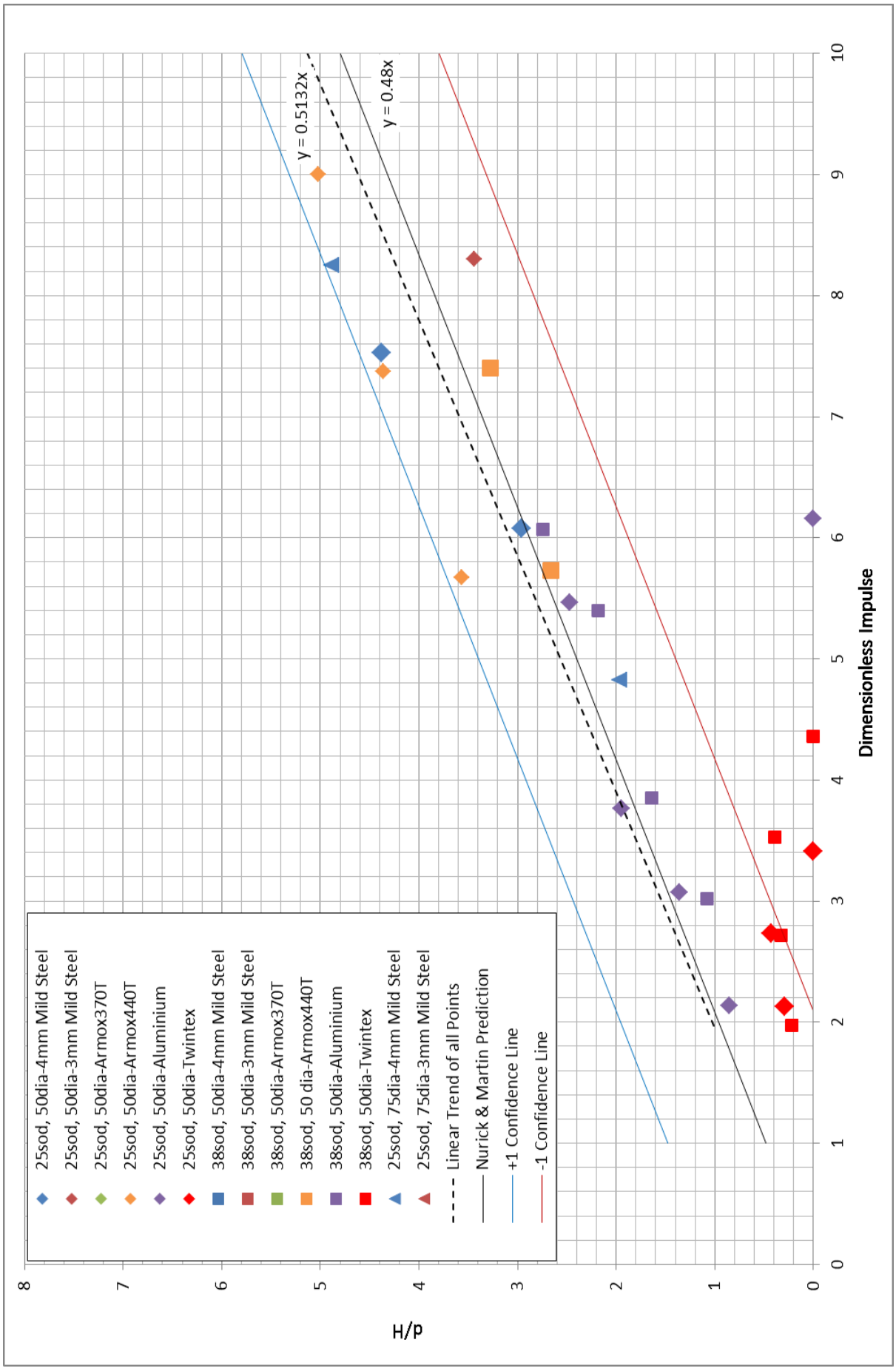

Figure 147: Graph of Displacement/thickness ratio versus Dimensionless impulse of highlighted section from Figure 146

Table 16: Table of Test Results with updated Dimensionless Impulse for 38mm SOD

Plate Number	Charge Mass (g)	SOD (mm)	Charge Diameter (mm)	Permanent Mid-Point Displacement (mm)	Impulse (Ns)	Dimensionless Impulse	d/H
AS-P5	40	38	50	21.27	80.47	12.52	5.60
AS-P7	40	38	40	17.62	82.20	13.85	4.64
AS-P6	50	38	50	27.07	100.06	15.57	7.12
AS-P8	50	38	40	18.62	91.01	15.33	4.90
AS-P11	24	38	50	10.10	51.61	5.73	2.66
AS-P9	33	38	50	12.44	66.71	7.40	3.27
AS-P13	40	38	50	13.78	83.20	10.32	3.63
MS-P10	50	38	50	41.58	87.66	17.33	10.94
MS400-9	9	38	50	16.24	18.88	12.04	5.41
MS400-10	12	38	50	22.25	26.61	16.97	7.42
MS400-16	16	38	50	25.88	28.16	17.96	8.63
MS400-14	20	38	50	37.26	37.01	23.61	12.42
MS400-17	24	38	50	40.56	44.50	28.38	13.52
MS400-13	28	38	50	43.89	52.77	33.66	14.63
MS400-15	33	38	50	62.84	62.85	40.09	20.95
AL-8	16	38	50	11.41	31.25	3.02	1.08
AL-1	20	38	50	17.42	39.90	3.85	1.64
AL-3	28	38	50	23.12	56.05	5.40	2.18
AL-6	33	38	50	29.05	62.85	6.07	2.74
TW-5	12	38	50	2.54	21.80	1.97	0.22
TW-2	16	38	50	3.75	29.70	2.72	0.33
TW-1	20	38	50	4.38	37.65	3.53	0.39
TW-3	24	38	50	torn	46.07	4.36	N/A

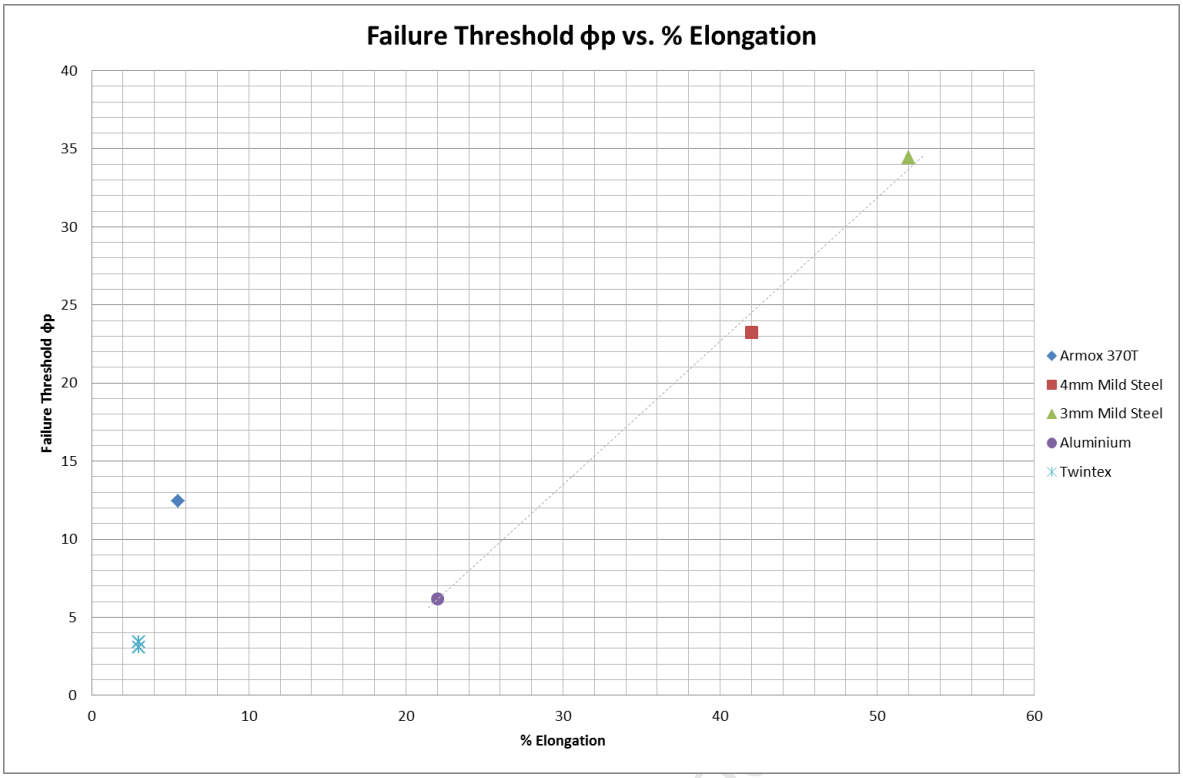

Figure 148: Graph of Failure Thresholds for each Material plotted against % Elongation

The failed test plates are highlighted in Figure 142, with the lower dimensionless impulse values for each material type assumed to be the dimensionless failure threshold value for each material. These data points are plotted in Figure 148 against their respective elongation percentage values. A graph of dimensionless impulse at rupture versus percentage elongation is shown in Figure 148 for the steels aluminium and Twintex materials. Dyneema is excluded because none of the Dyneema panels failed in fracture. From Figure 148 it is clear that the failure threshold dimensionless impulse values for the Armox 370T and Twintex plates show a different trend to the mild steel and aluminium plates. Both the Armox 370T and Twintex plates are relatively brittle in nature, as evident in both of their failure methods as well as in the amount of elongation experienced before failure. Both of these materials thus deform significantly less than either the mild steel or aluminium before failing under blast loading. The more ductile mild steel and aluminium plates appear to form a linear trend of increasing failure threshold with increasing percentage elongation at failure.

8. CONCLUSIONS

The project aimed to investigate the response of different materials to blast loading. The study was mainly conducted through experimental investigation by blast loading square plates, varying different parameters, namely: material type, test plate dimensions, the mass of the explosive and the stand-off distance. A combination of the experimental and numerical modelling was used to investigate the transient response of the 500mm square plates (using light interference equipment and ANYSYS AUTODYN respectively). Dimensionless analysis was performed on all of the materials with the exception of the Dyneema composites.

8.1. Sensitivity of the Experimental Setup

The light interference equipment used for the 500mm square plate tests exhibited reasonable results and repeatability for most of the higher charge masses but due to the required calibration, was not suitable for accurately recording displacements below 10mm. Due to the relatively fragile nature of the LIE, it was often damaged during the blast and had to be replaced. There was also some noise experienced by the sensors which was attributed to the vibration in the clamp frame caused by the blast. Thus the LIE was not as reliable as initially expected. The ballistic pendulum used to record the experimental impulses showed good repeatability and recorded impulses which were all within the acceptable range.

8.2. Effect of Varying Loading Parameters on Plate Response

The variation of stand-off distance had a significant effect on the permanent displacement even with small differences at such close proximities. Plates loaded using the same charge mass exhibit noticeably lower permanent displacement and more uniform deformation profiles (attributed to more uniform loading conditions) when the stand-of distance is increased.

The impulses showed minimal difference between the different charge configurations, unlike the results obtained by Jacob *et al* [7] where much greater variation in stand-off distances were used.

8.3. The Influence of Material Type

The majority of the steel plates exhibited large inelastic deformation with some degree of thinning in the central region (Mode Itc). Two of the 400mm square plates exhibited petalling failure, namely aluminium at a charge mass of 33g and stand-off of 25mm and mild steel at a charge mass of 28g at the same stand-off distance (Mode IIIp). The 500mm Armox 370T and mild steel plates both exhibited large inelastic deformation and partial tearing in the central region under the same loading condition of 40g charge mass at a stand-off of 25mm (Mode II*c).

The composite materials exhibited inelastic deformation of the back face, tearing of the front and back face and complete catastrophic failure with increasing impulse. The Twintex panels exhibited all three modes of failure with increasing charge mass or decreasing stand-off distances with complete failure at a charge mass of 20g at a stand-off of 25mm as well as at a charge mass of 24g at a stand-off of 38mm. The Dyneema panels exhibited front face damage in the form of burnt fibre with large inelastic deformation for all of the tests. There was also an increase in thickness of the panels with increasing impulse, as a result of delamination in the central region of the panels.

8.3.1. Comparison of Different Materials

Comparisons were drawn between most of the materials, namely mild steel with Armox 370T, mild steel with aluminium and Twintex and Armox 370T with 440T.

8.3.1.1. Mild Steel vs. Armox 370T

In drawing comparisons between the mild steel and Armox 370T plates the behaviour of both materials in terms of permanent displacement was as expected, with the weaker and more ductile mild steel sustaining higher displacements for the same loading conditions as the Armox 370T. The one unexpected result was that both of the materials failed when subjected to the same blast loading conditions, rupturing when subjected to a blast load of 40g at a 25mm stand-off distance. The significance of this result is that it implies that under blast loading conditions, armour steel of a lower grade may not necessarily be better than cheaper mild steel. While it is undisputed that armour steel is more suited to withstanding projectile penetration due to its high strength and hardness, it can be argued that for single blast loading at close proximity mild steel may perform equally well, if displacement is not limited by operational requirements.

8.3.1.2. Mild Steel vs. Aluminium

Under blast loading the weaker but thicker aluminium plates performed significantly better than the mild steel plates. The thickness and lower melting temperature of the aluminium were contributing factors to its lower permanent displacements and greater failure threshold. The lower melting temperature of the aluminium allowed the material to melt and flow under blast loading and thus dissipate the blast pressure more effectively. Thus the aluminium plates were able to sustain higher blast loads than the mild steel, rupturing under blast load of 33g at 25mm stand-off distance compared to 28g for mild steel. Aluminium, on an equivalent mass basis,

appears to perform better than mild steel, although the significantly higher cost would offset the advantage of using aluminium.

8.3.1.3. Armox 370T vs. Armox 440T

Under similar loading conditions the Armox 440T performed better than the 370T grade in terms of the permanent displacements sustained. Although the 440T grade of Armox was slightly stronger and thicker than the 370T grade, it still performed better when displacement/thickness ratios were compared. The results were thus as expected, with Armox 440T performing better than Armox 370T due to its higher strength.

8.3.1.4. Twintex and Dyneema

Although both Twintex and Dyneema are classified as composites, they possess different material properties as evident in their failure modes. The Twintex exhibited brittle fibre fracture whereas the Dyneema panels only exhibited large inelastic deformation. The brittle nature of the Twintex panels is attributed to the brittle glass fibre and polypropylene matrix. The Dyneema is comprised of ductile polyethylene fibres which are more elastic and the layers are able to slide across each other. The different clamping conditions of the Dyneema panels may have been more favourable than the Twintex panels and allowed for greater dissipation of energy through deformation.

8.4. Validity of Numerical Results

The numerical models for mild steel produced very accurate results with respect to the permanent mid-point displacements and peak transient displacements. The numerical models for the armour steel did not correlate with the experimental data however as all of the models in this range of simulations under-predicted the responses of the plate. The discrepancies could be due to the unavailability of material properties for the Armox grade under investigation.

8.5. Significance of Applying Dimensionless Analysis

The aim of investigating the response of the various plates through dimensionless analysis was to obtain a quantitative comparison of the different materials and their geometries and loading conditions. Unlike the results obtained by Jacob *et al* [7], the dimensionless analysis performed in this specific investigation proved to be inaccurate in terms of the application of the stand-off distance scaling factor.

The scaling factor was intended to account for variations in stand-off distances of the explosive for the 38mm stand-off tests but was formulated with a particular experimental setup in mind, namely the tube used to set different stand-off distances [7]. It was thus decided that due to the different loading nature of this investigation, it was not necessary to apply the stand-off distance scaling factor due to the fact that the blast performed were unconfined as well as at close proximity. Once the scaling factor was removed it can be seen that the dimensionless impulse values for the 38mm stand-off tests conformed to the predicted Nurick and Martin [52] trend.

9. RECOMMENDATIONS

- Future attempts to record transient structural response during blast tests, should consider implementing high speed photography and Digital Image Correlation, which can provide finer resolution data and can capture strain fields of a surface (such as the back face, or at least a portion of it), not just one point of interest.
- The effect of varying more charge diameters should be investigated in order to determine its significance on the response of materials as compared to varying stand-off distances.
- More stand-off distances should be investigated to obtain a wider range of data and to fully understand its effect on the impulse and displacement experienced by the blast loaded plates.
- Other materials should be compared to Armox in order to determine whether Armox is in fact the most suitable material for blast protection at close proximities.
- Dynamic material characterisation of the materials under investigation is required, particularly for modelling purposes.
- Other hydrocodes should be evaluated for the modelling of steel behaviour (such as LS-DYNA) which may allow for refined meshes with reasonable computational run-times.
- Further investigation into the effect of stand-off distance and confinement on the dimensionless impulse should be investigated in order to determine an appropriate scaling factor, if any.

REFERENCES

1 Nurick G.N. Large Deformations of Thin Plates Subjected to Impulsive Loading. PhD Thesis. University of Cape Town; 1987.

2 Jones N, Baeder R.A. An Experimental Study of the Dynamic Plastic Behaviour of Rectangular Plates. In: Symposium on Plastic Analysis of Structures; 1972; Rumania.

3 Baker W.E. Explosions in Air. Austin: University of Texas; 1973.

4 Weckert S, Anderson C. A Preliminary Comparison Between TNT and PE4 Landmines. Technical Report. Weapons Systems Division, Defence Science and Technology Organisation, Department of Defence, Australian Government; 2006.

5 Kennedy J.E. Explosive Output for Driving Metal. In: Behavior and Utilization of Explosives Symposium (12th); 1979; Albuquerque.

6 Nurick, G.N.; Martin, J.B. Deformation of Thin Plates Subjected to Impulsive Loading - A Review. International Journal of Impact Engineering. 1989;Vol. 8:p159-170.

7 Jacob N, Chung Kim Yuen S, Nurick G.N, Desai S.A, Tait D. Scaling aspects of quadrangular plates subjected to localised blast loads—experiments and predictions. International Journal of Impact Engineering. 2004;Vol. 30:p1179-1208.

8 Jacob N, Nurick G.N, Langdon G.S. The effect of stand-off distance on the failure of fully clamped circular mild steel plates subjected to blast loads. Engineering Structures. 2007;Vol. 29:p2723-2736.

9 Langdon G.S, Chi Y, Nurick G.N, Haupt P. Response of GLARE Panels to Blast Loading. Engineering Structures. 2009;Vol. 31:p3116-3120.

10 Langdon G.S, Nurick G.N, Cantwell W.J. The response of fibre metal laminate panels subjected to uniformly distributed blast loading. European Journal of Mechanics A/Solids, Vol.27. 2008 107-115.

11 Marchand K.A, Alfawakhiri F. Blast and Progressive Collapse - Facts for Steel Buildings, No. 2. Technical Report. American Institute of Steel Construction, Inc.; 2004.

12 Langdon G.S, Lemanski S.L, Nurick G.N, Simmons M.C, Cantwell W.J, Schleyer G.K. Behaviour of Fibre–Metal Laminates Subjected to Localised Blast. International Journal of Impact Engineering. 2007;Vol. 34:p1202-1222.

13 Nurick G.N, Radford A. Deformation and Tearing of Clamped Circular Plates Subjected to Localised Central Blast Loads. In: Recent developments in computational and applied mechanics: a volume in honour of John B. Martin. Barcelona: International centre for numerical methods in engineering (CIMNE); 1997. p. p276-301.

14 Langdon G.S, Karagiozova D, von Klemperer C.J, Nurick G.N, Ozinsky A, Pickering E.G. The Air-Blast Response of Sandwich Panels with Composite Face Sheets and Polymer Foam Cores: Experiments and Predictions. International Journal of Impact Engineering. 2013;Vol. 54:p64-82.

15 Bonorchis D, Nurick G.N. The Influence of Boundary Conditions on the Loading of Rectangular Plates Subjected to Localised Blast Loading - Importance in Numerical Simulations. International Journal of Impact Engineering. 2009;Vol. 36:p40-52.

16 Langdon G.S, Rossiter I.B, Balden V.H, Nurick G.N. Performance of Mild Steel Perforated Plates as a Blast Wave Mitigation Technique: Experimental and Numerical Investigation. International Journal of Impact Engineering. 2010;Vol. 37:p1021-1036.

17 Langdon G.S, Nurick G.N, du Plessis N.J. The Influence of Separation Distance on the Performance of Perforated Plates as a Blast Wave Shielding Technique. Engineering Structures. 2011;Vol. 33:p3537-3545.

18 SSAB. SSAB (Swedish Steel Corporation). [Internet]. 2012 [cited 2012 September]. Available from: http://www.ssab.com/Global/ARMOX/Datasheets/en.

19 Aluminum 5083-H116; 5083-H321. [Internet]. 2012 [cited 2012 September]. Available from: http://www.matweb.com/search/DataSheet.aspx?MatGUID=1efe7441a72f4a22a53c0dc1bd9c87ec.

20 Kauffman J.G. Properties of Aluminum Alloys: Fatigue Data and the Effects of Temperature, Product Form, and Processing. ASM International.

21 Børvik T, Forrestal M.J, Warren T.L. Perforation of 5083-H116 Aluminum Armor Plates with Ogive-Nose Rods and 7.62mm APM2 Bullets. In: SEM Annual Conference; 2009; Albuquerque.

22 Rowe L. The Response of Steel-Based Fibre-Metal Laminates to Localised Blast Loading. Undergraduate Thesis. Cape Town: University of Cape Town; 2008.

23 TWINTEX Technical Data. [Internet]. [cited 2012 February]. Available from: http://fiberglassindustries.com/glasspolyprotechdata.htm.

24 Applications of Dyneema. [Internet]. 2012 [cited 2012 September]. Available from: http://www.dyneema.com/emea/applications/life-protection/vehicle-protection.aspx.

25 Stein H.L. Engineered Materials Handbook. 1998. p. p167-171.

26 vd Werff H, Heisserer U, Phoenix S.L. Modelling of Ballistic Impact on Fiber Composites. Technical Report. 2010.

27 Taylor G.I. The Distortion Under Pressure of a Diaphragm which is Clamped Along its Edge and Stressed Beyond its Elastic Limit. Underwater Explosion Research. 1950;Vol. 3 : The Damage Processes:p107-121.

28 Johnson W, Poynton A, Singh H, Travis F.W. Experiments in the Underwater Stretch Forming of Clamped Circular Blanks. International Journal of Mechanical Science. 1966;Vol. 8:p237-270.

29 Travis F.W, Johnson W. Experiments in the Dynamic Deformation of Clamped Circular Sheets of Various Metals Subject to an Underwater Explosive Charge. In: Sheet Metal Industries, Vol. 39. 1961. p. p456-474.

30 Witmer E.A, Balmer N.A, Leech J.W, Pian T.N.N. Large Dynamic Deformations of Beams , Rings, Plates and Shells. AIAA. 1963;Vol. 1:p1848-1857.

31 Humphreys J.S. Plastic Deformation of Impulsively Loaded Straight Clamped Beams. Journal of Applied Mechanics. 1965;Vol. 32:p7-10.

32 Jones N, Uran T, Tekin S.A. The Dynamic Plastic Behaviour of Fully Clamped Rectangular Plates. International Journal of Solid Structures. 1970;Vol. 6:p1499-1512.

33 Nurick G.N, Martin J.B. Deformation of Thin Plates Subjected to Impulsive Loading - A Review Part 1: Theoretical considerations. International Journal of Impact Engineering. 1989;Vol. 2:p159-169.

34 Nurick G.N, Shave G.C. The Deformation and Tearing of Thin Square Plates Subjected To Impulsive Loads - An Experimental Study. International Journal of Impact Engineering. 1996;Vol. 18:p99-116.

35 Nurick G.N, Gelman M.E, Marshall N.S. Tearing of Blast Loaded Plates with Clamped Boundary Conditions. International Journal of Impact Engineering. 1996;Vol. 18:p803-827.

36 Neuberger A, Peles S, Rittel D. Springback of Circular Clamped Armor Steel Plates Subjected to Spherical Air-Blast Loading. International Journal of Impact Engineering. 2009;Vol. 36:P53-60.

37 Veldman R.L, Ari-Gur J, Clum C, DeYoung A, Folkert J. Effects of Pre-Pressurization on Blast Response of Clamped Aluminum Plates. International Journal of Impact Engineering. 2006;Vol. 32:p1678-1695.

38 Tekalur S.A, Shivakumar K, Shukla A. Mechanical Behaviour and Damage Evolution in E-Glass Vinyl Ester and Carbon Composites Subjected to Static and Blast loads. Composites: Part B. 2008;Vol. 39:p57-65.

39 Batra R.C, Hassan N.M. Blast Resistance of Unidirectional Fiber Reinforced Composites. Composites: Part B. 2008;Vol. 39:p513-536.

40 Yahya M.Y, Cantwell W.J, Langdon G.S, Nurick G.N. The blast resistance of a woven carbon fiber-reinforced epoxy composite. Journal of Composite Materials. 2011;Vol. 45.

41 Langdon G.S, Rowe L.A. Blast Loading of Fibre-Metal Laminates: Preliminary Tests. Engineering and Computational Mechanics. 2011;Vol. 164:p139-146.

42 Menkes S.B, Opat H.J. Tearing and Shear Failures in Explosively Loaded Broken Beams. Experimental Mechanics. 1973;Vol. 13:p480-486.

43 Langdon G.S, Cantwell W.J. The Blast Response of Novel Thermoplastic Based Fibre Metal Laminates - Some Preliminary Results and Observations. Composite Science Technology. 2005;Vol. 65:p861-872.

44 Thomas B, Nurick G.N. The Effect of Boundary Conditions on Thin Plates Subjected to Impulsive Loads. In: Plasticity 95- Dynamic Plasticity and Structural Behaviours. 1995. p. p85-88.

45 Nurick G.N. A New Technique to Measure The Deflection-Time History of a Structure Subjected to High Strain Rates. International Journal of Impact Engineering. 1985;Vol. 3:p17-26.

46 Nurick G.N. Using Photo Voltaic Diodes to Measure the Deformation Response of a Structure Subjected to an Explosive Load. In: SPIE Vol. 674, High Speed Photography; 1986; Pretoria. p. p215-225.

47 Nurick G.N. The Measurement of The Deformation Response of a Structure Subjected to an Explosive Load Using a Light Interference Technique. In: SEM Spring Conference on Experimental Mechanics; 1986.

48 Geretto C. The Effects of Different Degrees of Confinement on the Deformation of Square Plates Subjected to Blast Loading. PhD Thesis. Cape Town 2012.

49 Tiwari V, Sutton M.A, McNeill S.R, Xu S, Deng X, Fourney W.L, Bretall D. Application of 3D Image Correlation for Full-Field Transient Plate deformation Measurements During Blast Loading. International Journal of Impact Engineering. 2009;Vol. 36:p862-874.

50 Tay C.J, Quan C, Huang Y.H, Fu Y. Digital Image Correlation for Whole Field Out-of-Plane Displacement Measurement Using a Single Camera. Optics Communications. 2005 p23-36.

51 Jones N. Structural Impact. Cambridge: Cambridge University Press; 1989.

52 Nurick G.N, Martin J.B. Deformation of Thin Plates Subjected to Impulsive Loading - A Review, Part II : Experimental Studies. International Journal of Impact Engineering. 1989;Vol.8:p171-186.

53 Ozinsky A. A Numerical Investigation into the Behaviour of Perforated Plates as Blast Wave Mitigation Devices. Cape Town: University of Cape Town; 2011.

54 Rossiter I.B. Performance of Mild Steel Plates as a Blast Wave Mitigation Technique. MSc Thesis. Cape Town 2008.

55 Pickering E.G. The Response of Quadrangular Plates to Buried Charges. Undergraduate Thesis. Cape Town: University of Cape Town; 2011.

56 Tekalur S.A, Shivakumar K, Shukla A. Mechanical Behavior and Damage Evolution in E-glass Vinyl Ester and Carbon Composites Subjected to Static and Blast Loads. Composites: Part B. 2008;Vol. 39:p57-65.

57 Micallef K. Private Communication. Imperial College London 2012.

58 Nurick G.N, Olson M.D, Fagnan, J.R. Deformation and Rupture of Blast Loaded Square Plates - Predictions and Experiments. International Journal of Impact Engineering. 1993;Vol. 13:p279-291.

59 Ansys. AUTODYN User's Manual R13.

60 Wierzbicki T. Petalling of Plates Under Explosive and Impact Loading. International Journal of Impact Engineering. 1999;Vol. 22:p935-954.

61 ASTM. ASTM Standard EM8-04. 2004.

62 AISI 1005 low carbon steel. [Internet]. [cited 2012 February]. Available from: http://matweb.com/search/DataSheet.aspx?MatGUID=1e1bb328dc144aa3b50d3eb9c39f8b8b.

63 Vlot A, Gunnink J. Fibre Metal Laminates: An Introduction. Netherlands: Kulwer Academic Publications; 2001.

64 Tagarielli V.I, Deshpande V.S, Fleck N.A. Prediction of the dynamic response of composite sandwich beams under shock loading. Int. J. Impact Eng. Vol. 37. 2010 854-864.

65 Baumert E, Johnson W, Cano R, Jensen B, Wesier E. Mechanical Evaluation of New Fiber Metal Laminates Made By The VARTM Process. 2008.

66 Villaneuva G.R, Cantwell W.J. The mechanical properties of fiber-metal laminates based on glass fibre reinforced polypropylene. Composite Sci. Tech. Vol 60. 2000 1085-94.

67 Tekalur S.A, Bogdanovich A.E, Shukla A. Shock loading response of sandwich panels with 3-D woven E-glass composite skins and stiched foam core. Composites Science and Technology, Vol. 69. 2009 736-753.

68 Ozinsky A. Design, Build and Testing of Polymeric Sandwich Panels. Undergraduate Thesis. Cape Town: University of Cape Town; 2010.

69 Tekalur S.A, Shukla A, Shivakumar K. Blast Resistance of Polyurea Based Layered Composite Materials. Composite Structures. 2008;Vol. 84:p271-281.

70 Mouritz AP. Ballistic Impact and Explosive Blast Resistance of Stitched Composites. Composites: Part B. 2001;Vol. 32:p431-439.

71 Park S.Y, Choi W.J, Choi H.S, Kwon H. Effects of Surface Pre-Treatment and Void Content on GLARE Laminate Process Characteristics. Journal of Materials Processing Technology. 2010;Vol. 8:p1008-1016.

APPENDIX A: Material Characterisation

The material properties of the mild steel, Armox 440T and aluminium were obtained from uni-axial tensile tests performed on the Zwick tensile testing machine at the Centre for Materials Engineering at the University of Cape Town. ASTM Standard EM8-04 [61] was used for the sizing of the tensile test specimens, shown in Figure A. 1, with the geometry listed in Table A. 1.

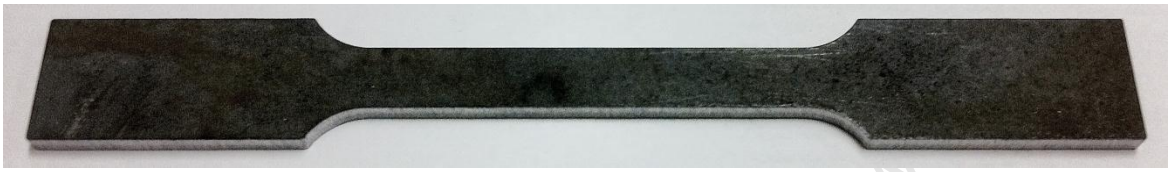

Figure A. 1: Photograph of typical tensile test specimen

Table A. 1: Tensile test specimen geometry

Nominal Width	12.5mm
Gauge Length	50mm
Total Length	200mm
Fillet Radius	12.5mm

The force and displacement values obtained from the Zwick test machine were converted to engineering stress and strain and plotted as an engineering stress versus strain curve. The engineering stress versus strain curves obtained for the materials tested at various crosshead speeds are shown in Figures A. 2 – 5.

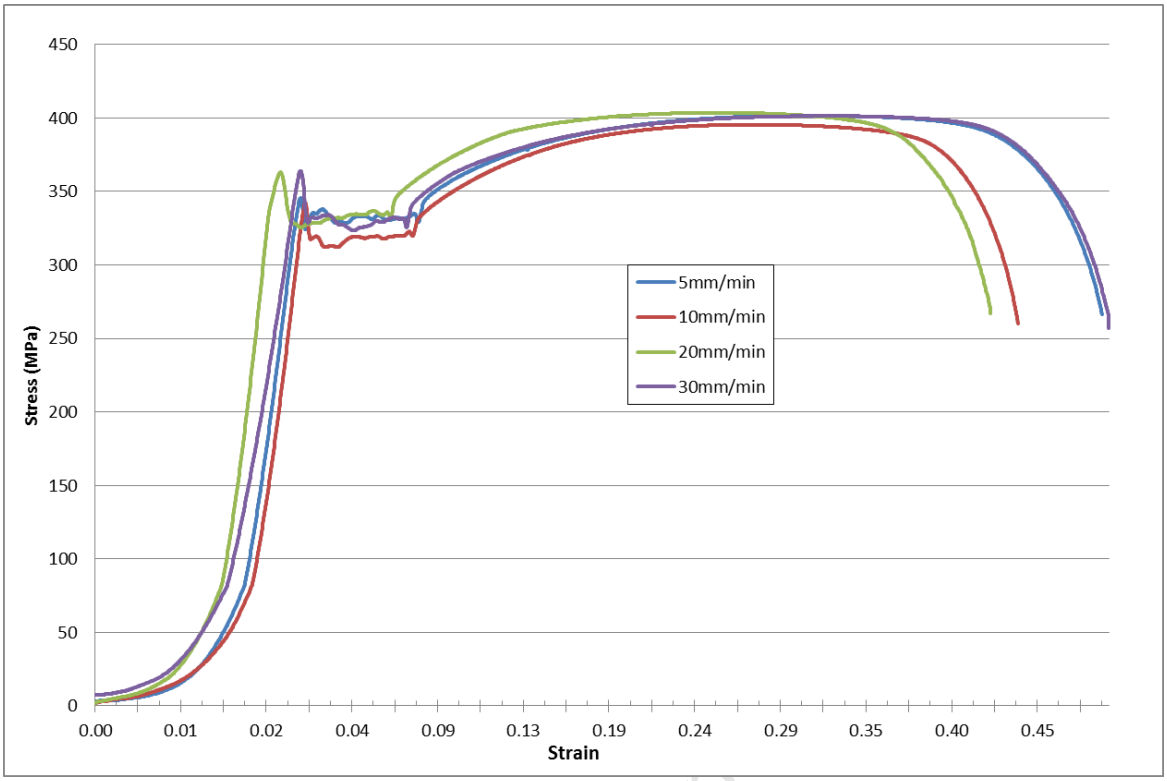

Figure A. 2: Engineering Stress-Strain curves at varying crosshead speeds for 4mm thick Mild Steel

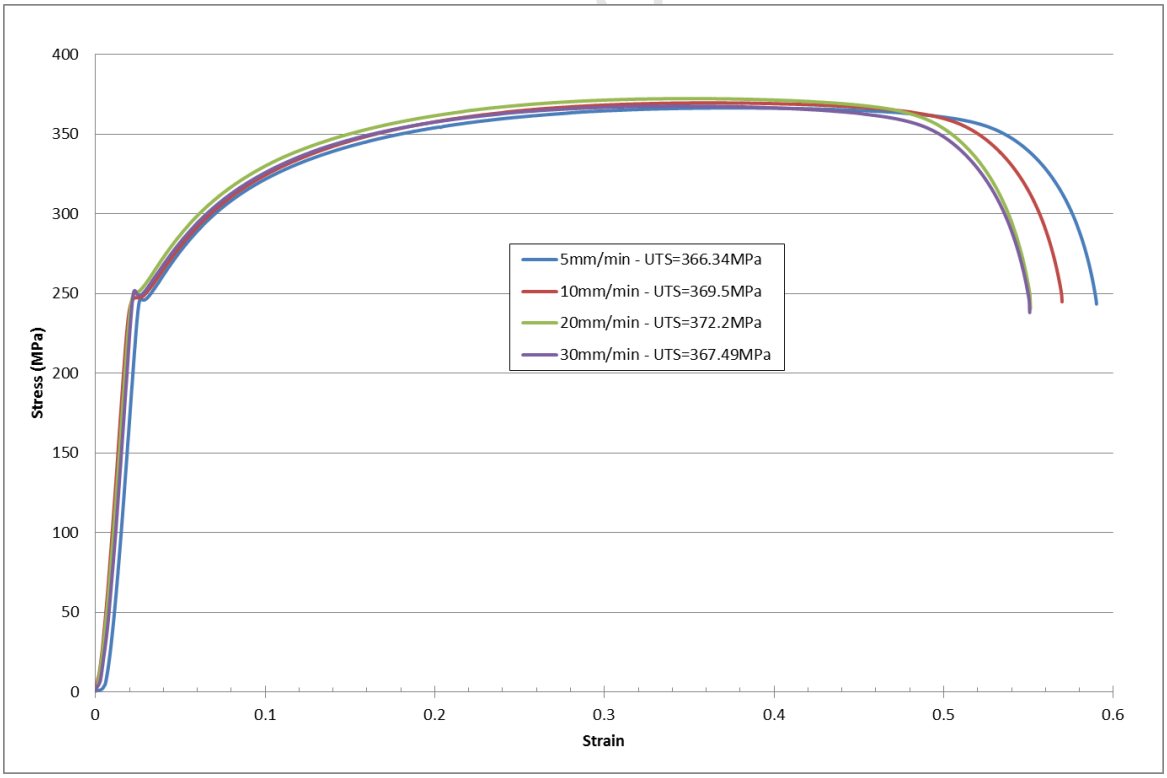

Figure A. 3: Engineering Stress-Strain curves at varying crosshead speeds for 3mm thick Mild Steel

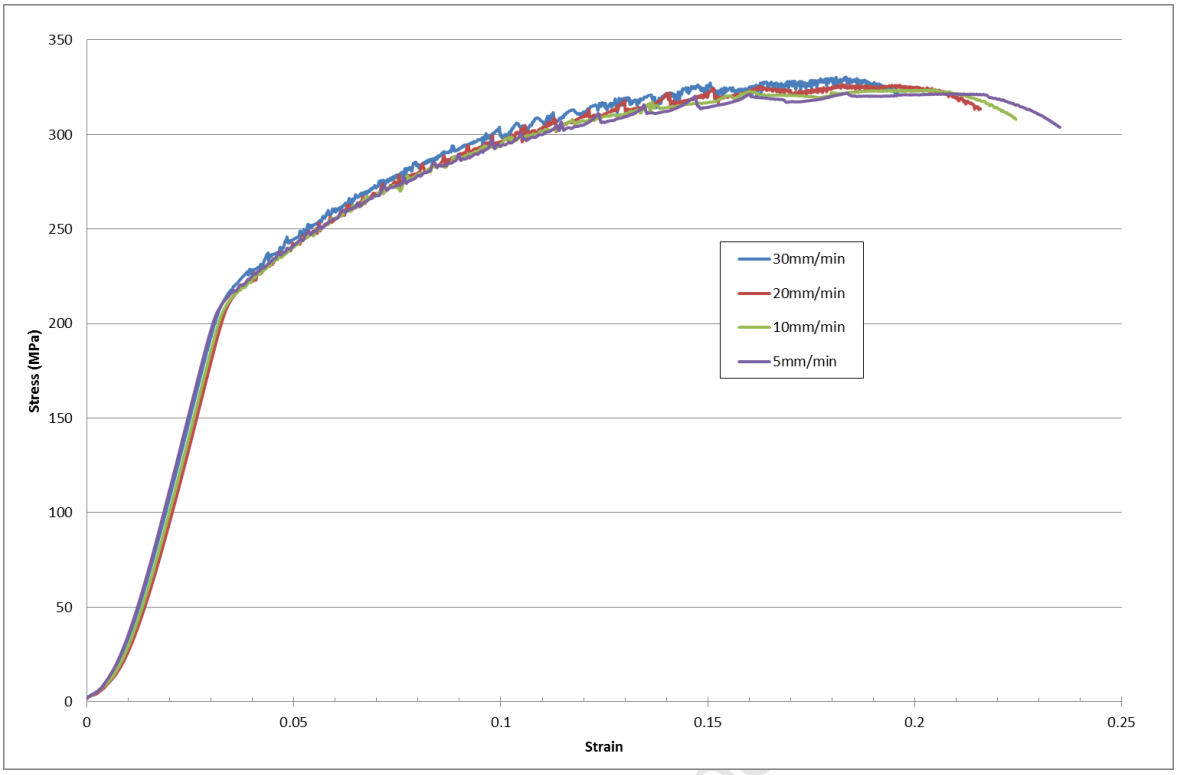

Figure A. 4: Engineering Stress-Strain curves at varying crosshead speeds for Aluminium 5083-H116

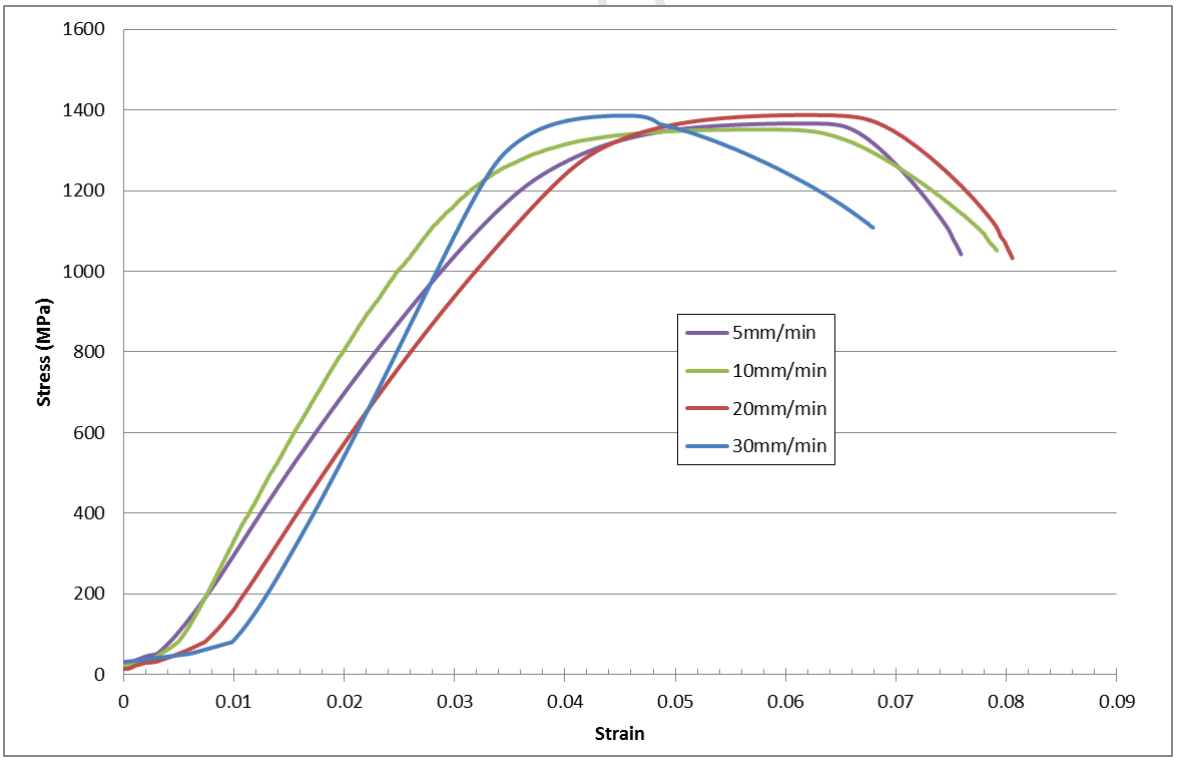

Figure A. 5: Engineering Stress-Strain curves at varying crosshead speeds for Armox 440T

In order to obtain the A, B and n values used in the Cowper-Symonds strength model in AUTODYN the true stress versus true strain were calculated and plotted. A best fit between the true stress-strain curve up until the point of necking, and power law hardening equation was used to obtain the required A, B and n values. The following equations were used to calculate the true stress and true strain values:

$$\sigma_T = \sigma_E \times (\varepsilon_E + 1) \quad \text{(eq. A1)}$$

$$\varepsilon_T = \ln(\varepsilon_E + 1) \quad \text{(eq. A2)}$$

Where σ_E - engineering stress and ε_E - engineering strain

The true stress-strain curve is used because it provides a more accurate indication of deformation characteristics of the material in the plastic region as it takes into account the reduction in cross-sectional area. A graph showing the best fit between the true stress-strain and power law hardening curves for 4mm thick mild steel is shown in Figure A. 6.

The Young's Modulus of elasticity used for mild steel specimens was obtained from literature to be 200GPa [62]. Due to the specimen attachment grips of the tensile testing machine being faulty (resulting in slippage under low strains), Young's Modulus could not be accurately measured. Young's Modulus for the Armox 370T was obtained by tests performed externally to be 192GPa [57].

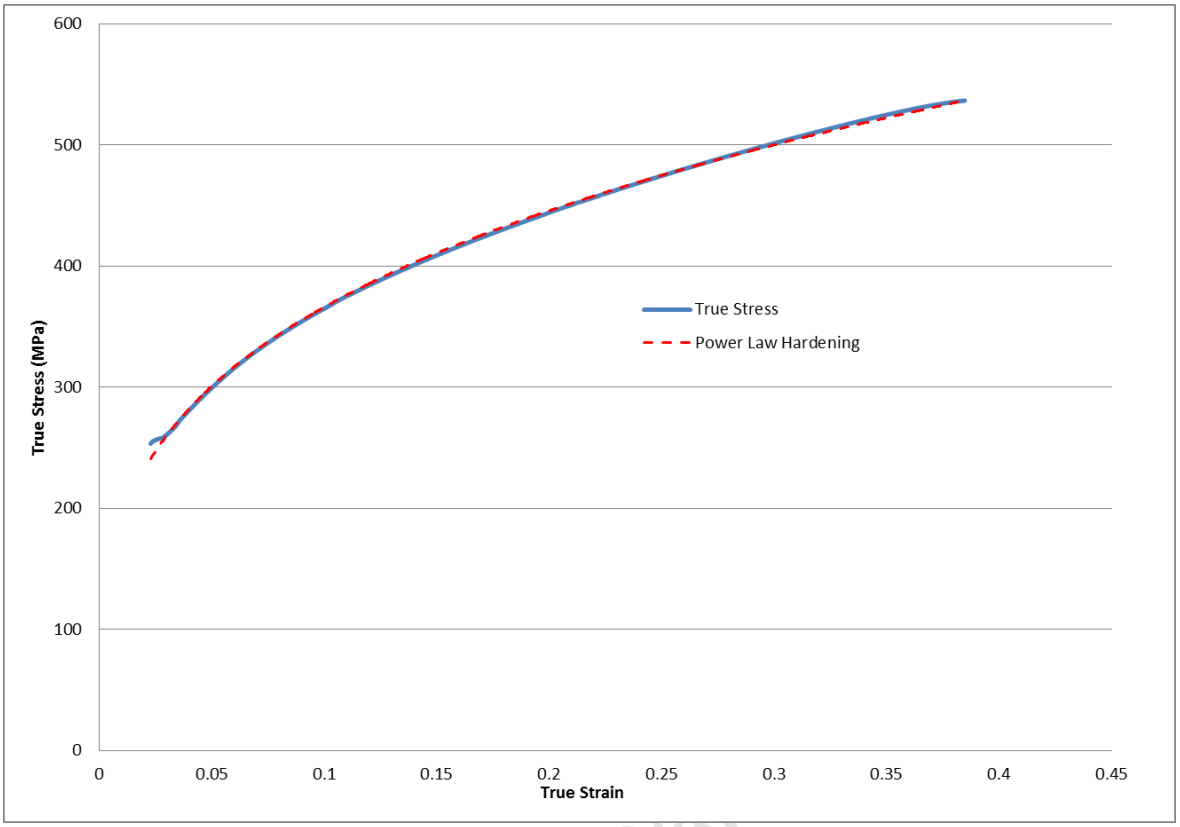

Figure A. 6: Graph showing best fit between true stress strain and power law hardening curves for 4mm mild steel

APPENDIX B: Additional Numerical Simulation Details

B.1. Investigating the Effect of De-activating the Air Mesh

The air mesh was de-activated at 0.1ms for all of the simulations performed as the blast pressure had already sufficiently subsided. In order to determine whether this had any effect on the transient displacement of the plate, selected models were run with the air mesh de-activated at 0.1ms and the same model was then run without de-activating the air mesh. The two displacement-time histories were then plotted on the same graph in order to determine if there was any significant difference between them. The displacement-time history comparisons are shown in Figure B. 1 – 3. It is observed that there is minimal difference between the two displacement-time histories. It was thus justifiable to de-activate the air mesh at 0.1ms as this did not have a significant effect on the displacement response of the plates.

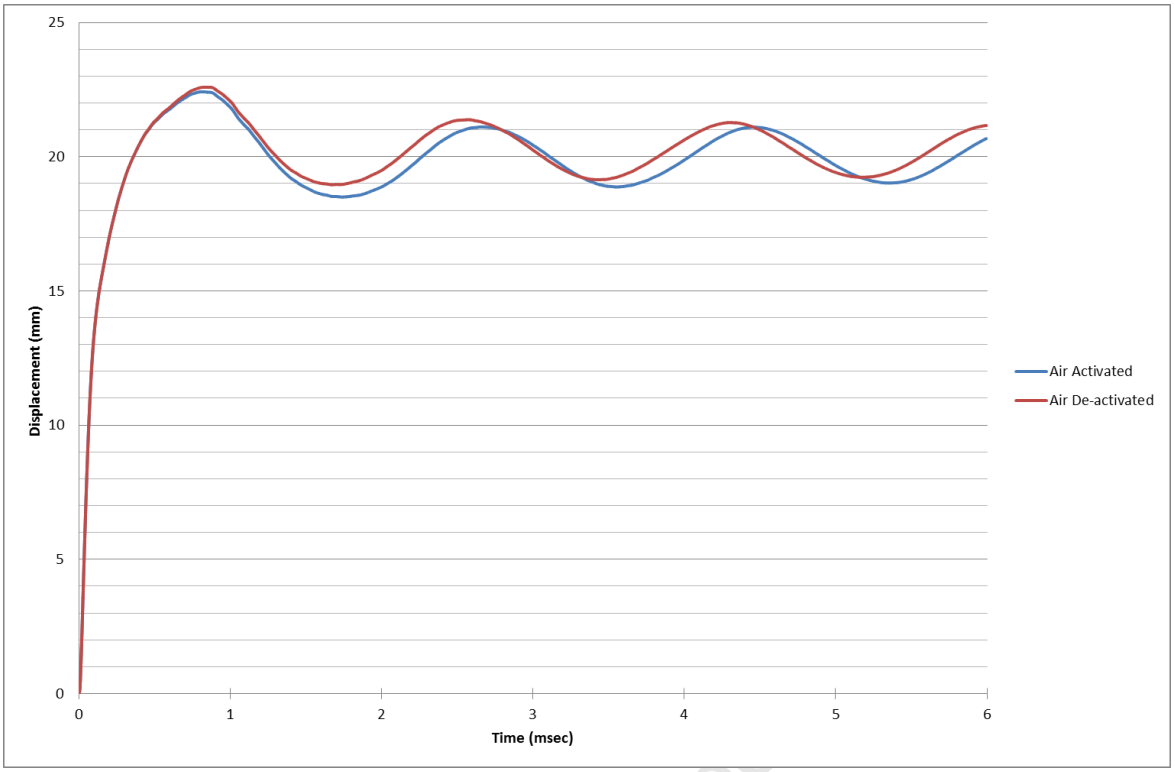

Figure B. 1: Displacement-time history for 16g charge at 25mm sod

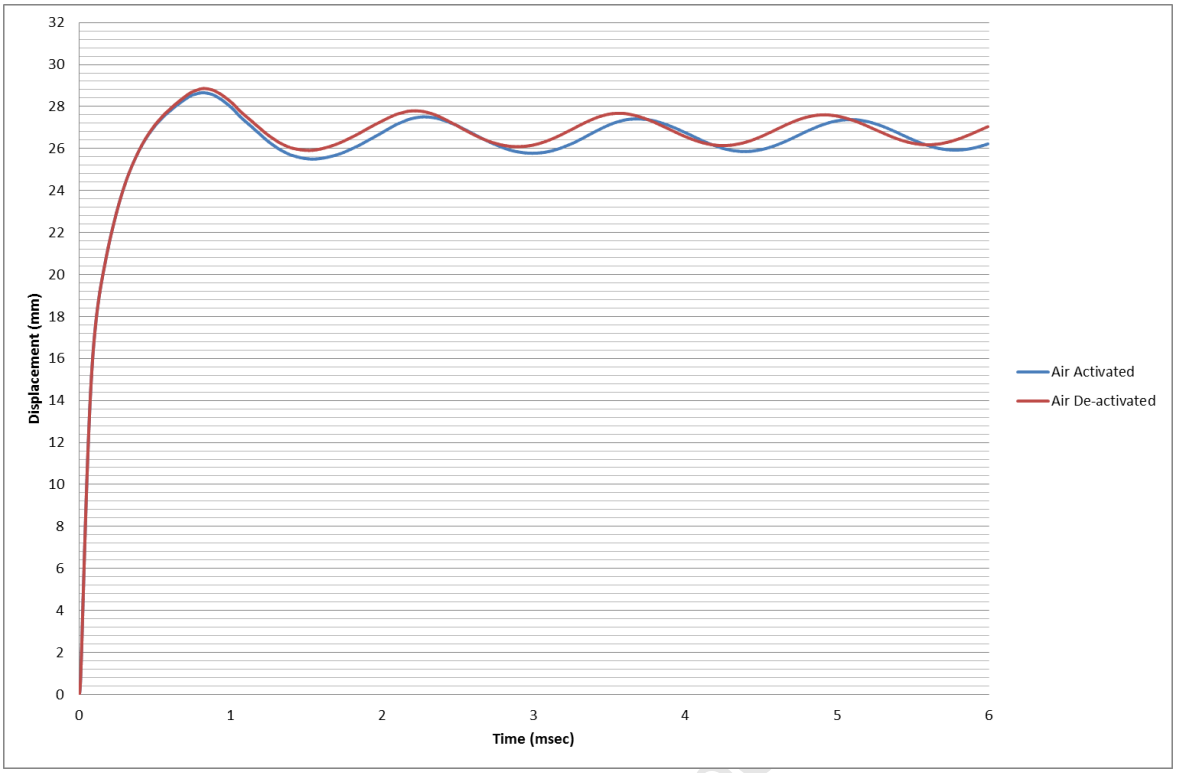

Figure B. 2: Displacement-time history for 20g charge at 25mm sod

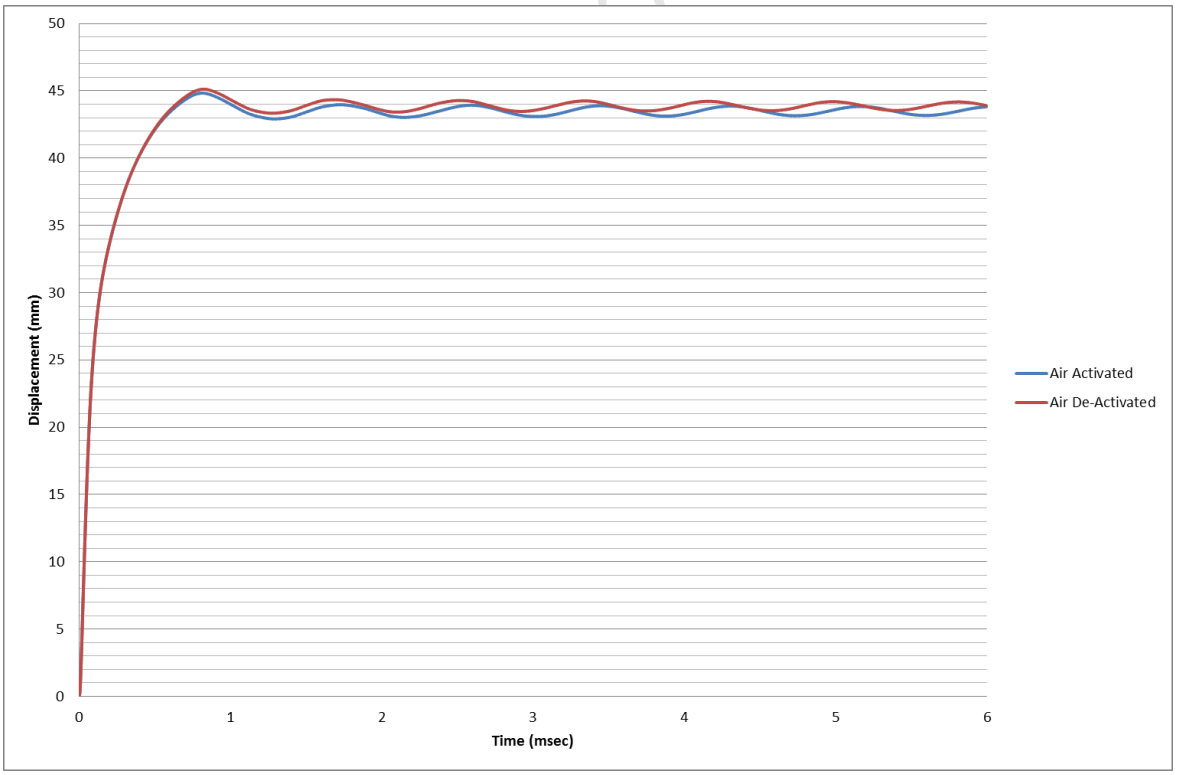

Figure B. 3: Displacement-time history for 33g charge at 25mm sod

B.2. Effect of a Leader Charge on Profile of Blast Wave

Ozinsky [53] investigated the effect of using an explosive leader in the detonation model and reported that presence of a leader influences the direction of the blast wave. Thus two different charge configurations were investigated to determine the effect of the blast wave, namely: a charge configuration with a 1g leader and another one without the leader. In the charge configuration with a 1 g leader, the mass of the leader is included in the total charge mass, i.e. a 20g blast consists of a 19g disc of explosive and a 1g leader. The geometry of the charge without a leader is shown in Figure B. 4 with the red line indicating the point of detonation.

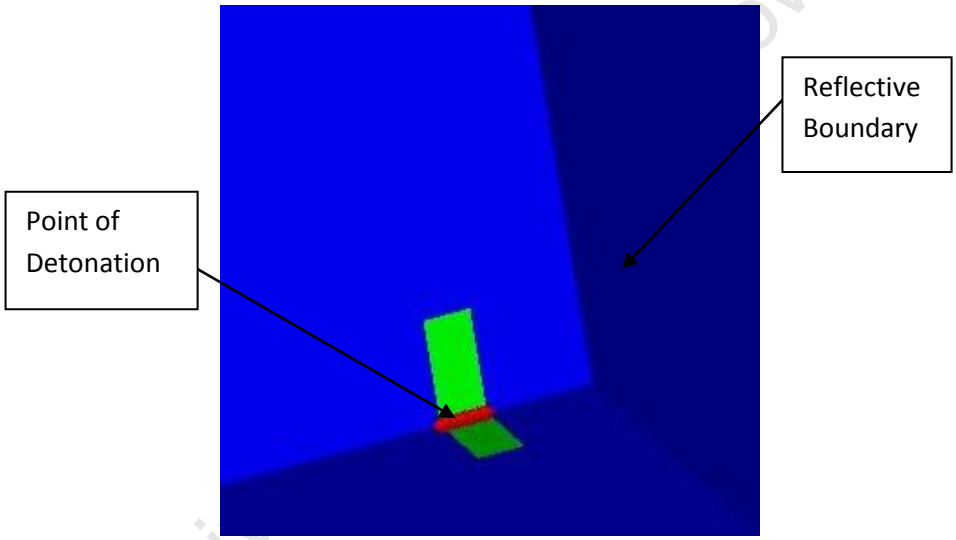

Figure B. 4: Explosive charge without leader showing point of detonation as red line

The pressure contours for the two different charge configurations at specific times are shown in Figure B. 5. From the initially detonation it can be seen that the blast wave from the charge without a leader is more spherical and less biased towards to direction of the leader, as is the case with the leader detonation. The pressure-time histories from the two different 33g charge configurations are shown in Figure B. 6. There is a discernable difference between the two configurations with the 1 g leader exhibiting a lower peak pressure but longer peak loading duration. This is attributed to the biased detonation direction created by the leader.

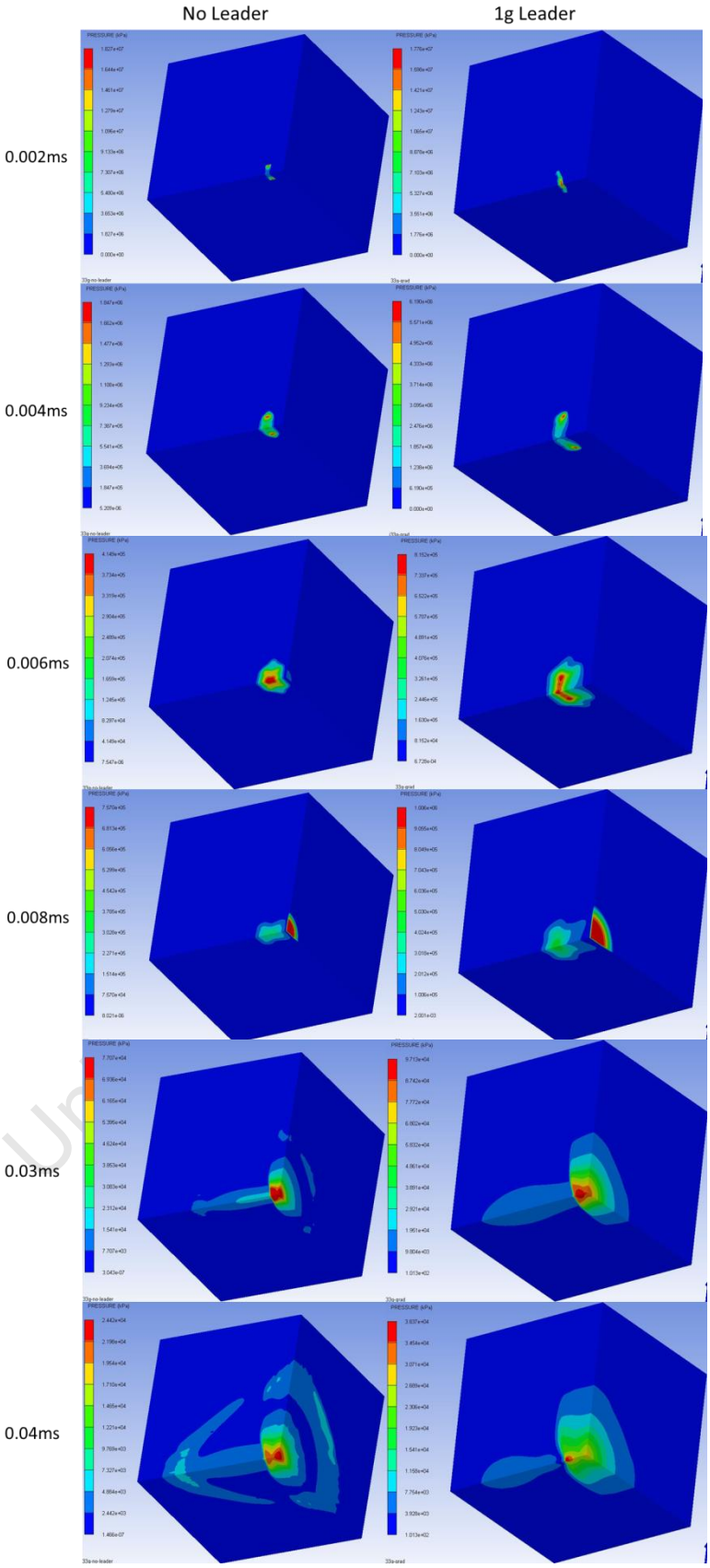

Figure B. 5: Pressure contours showing the difference between blast wave propagation at various times

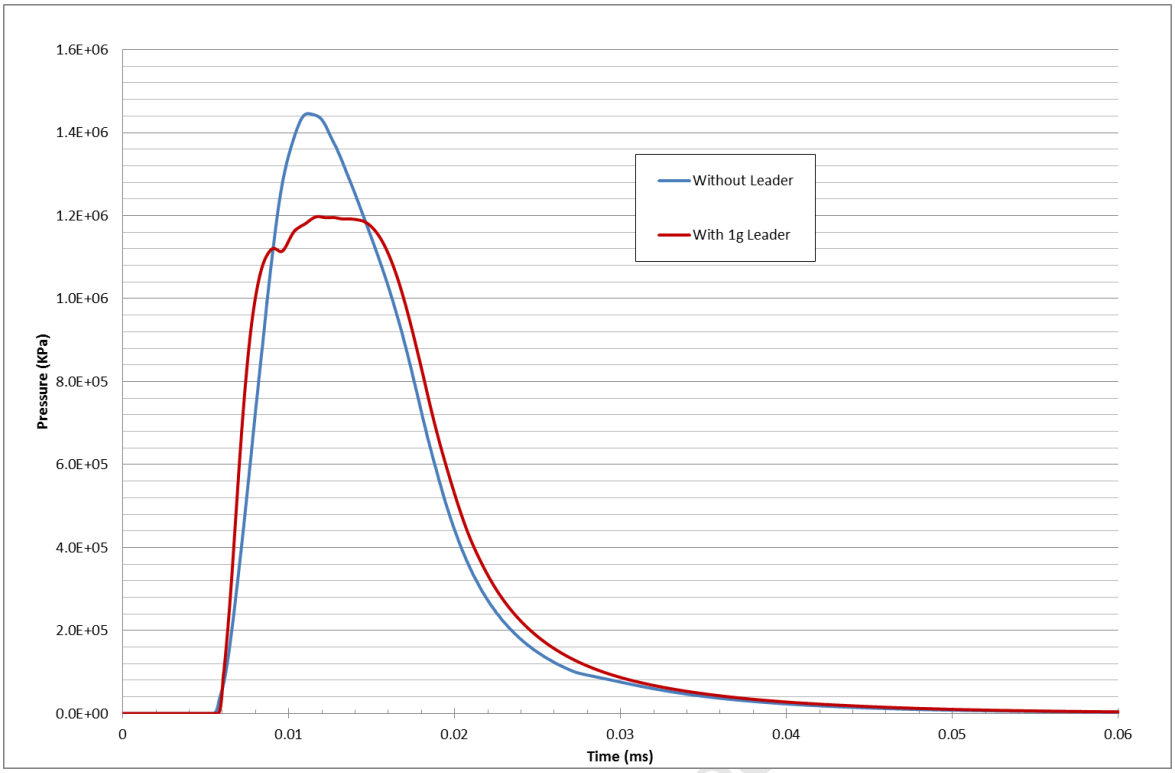

Figure B. 6: Graph of Pressure-time histories of a 33g detonation with a 1g leader and without the leader

B.3. Impulse Calculations from Simulations

In order to determine the impulse generated in an AUTODYN simulation, pressure histories are required. Impulse can be calculated as the sum of all the integrals of pressure acting over a specific area of the plate. The air pressures on the surface of the plate are recorded from the initial rise until it has subsided back down to ambient pressure. The pressure model consists of a reflective boundary in place of the test plate, the same configuration discussed in Section 5.

Gauges are placed at 5mm intervals from the mid-point of the plate to the outer edge. The pressure recorded by each of the gauges is integrated and multiplied by the area of the plate in which it is located. The sum of all of the pressure integrals gives the impulse experienced by the plate.

APPENDIX C: Pendulum Impulse Derivation

This appendix describes the method and equations used to calculate the impulse of a blast load using pendulum theory. Provided that the pendulum is balanced, it will maintain its orientation throughout its swing and will move according to simple pendulum motion.

The required measurements are shown as variables in Figure C.1 are pen displacements ΔL and ΔR (measured from the recordings on the tracing paper), cable length L_c, pendulum height above the pen tip a_1, and pen length Z. Other requirements include the natural frequency T of the pendulum and the total pendulum mass M_p.

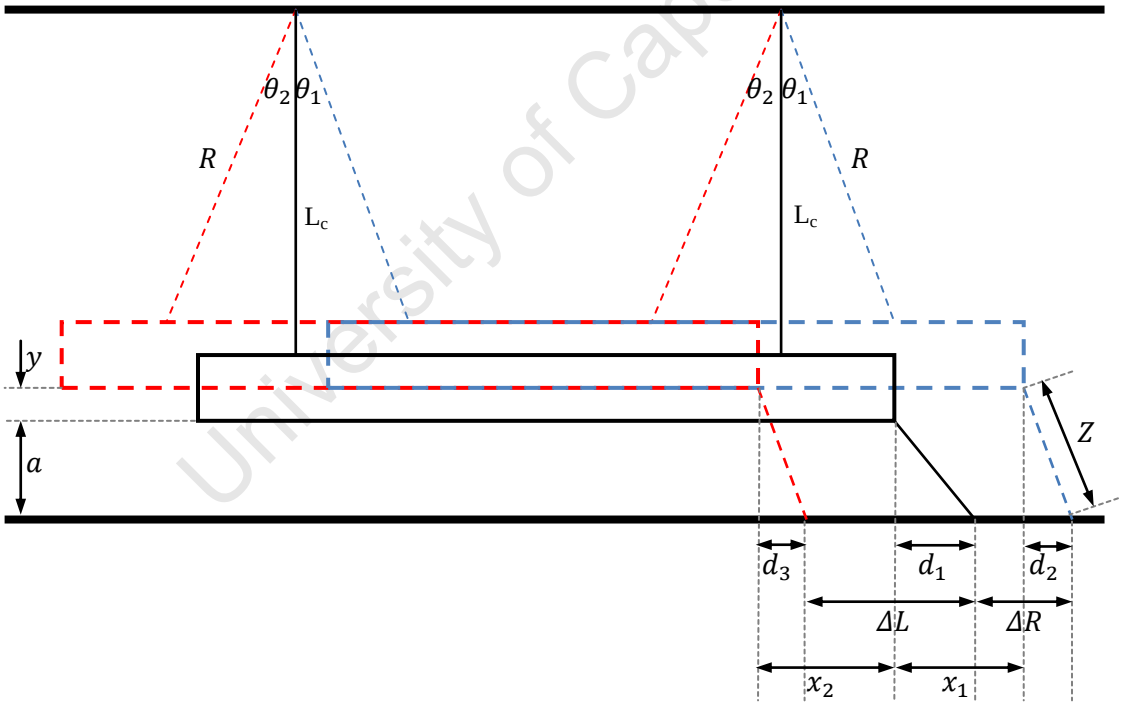

Figure C. 1: Schematic of ballistic pendulum showing required variables

The horizontal distance from the initial back position of the pendulum and the tip of the pen is

$$d_1 = \sqrt{Z^2 - a_1^2} \tag{C.1}$$

The horizontal distance from the backward swing of the pendulum (to the right of Figure) and the backward displacement of the pen is

$$d_2 = \sqrt{Z^2 - a_2^2} \tag{C.2}$$

Where,

$$\begin{aligned} a_2 &= L_c(1 - \cos\theta_1) + a_1 \\ &= y + a_1 \end{aligned} \tag{C.3}$$

and $y = f(\theta_1)$

Similarly, the horizontal distance from the forward swing of the pendulum and the forward displacement of the pen is

$$d_3 = \sqrt{Z^2 - a_3^2} \tag{C.4}$$

Where,

$$\begin{aligned} a_3 &= L_c(1 - \cos\theta_2) + a_1 \\ &= y + a_1 \end{aligned} \tag{C.5}$$

and $y = f(\theta_2)$

If x_1 and x_2 are defined as the backward and forward displacements of the pendulum respectively, then x_1 and x_2 are given by

$$x_1 = L_c \sin\theta_1 \tag{C.6}$$

and

$$x_2 = L_c \sin\theta_2 \tag{C.7}$$

The measured displacements ΔL and ΔR can then be defined as:

$$\begin{aligned}\Delta R &= x_1 - d_1 + d_2 \\ &= L_c \sin\theta_1 - \sqrt{Z^2 - a_1^{\,2}} + \sqrt{Z^2 - (L_c(1-\cos\theta_1) + a_1)^2}\end{aligned} \tag{C.8}$$

and

$$\begin{aligned}\Delta L &= x_2 + d_1 - d_3 \\ &= L_c \sin\theta_2 + \sqrt{Z^2 - a_1^{\,2}} - \sqrt{Z^2 - (L_c(1-\cos\theta_2) + a_1)^2}\end{aligned} \tag{C.9}$$

All the variables in equations (D.8) and (D.9) above are measured and calculated from these measurements, except for θ_1 and θ_2. For small angles it is assumed that $\sin\theta \approx \theta$ and $\cos\theta \approx 1$. Therefore,

$$x_1 = R\theta \tag{C.10}$$

and

$$y = \frac{R\theta^2}{2} \tag{C.11}$$

Substituting equation (D.10) into (D.11) gives:

$$y = \frac{x_1^{\,2}}{2R} \tag{C.12}$$

Substituting equation (C.12) into (C.2), (C.3), (C.8) and (C.9), and rearranging results in:

$$x_1 = \Delta R + \sqrt{Z^2 - a_1^{\,2}} - \sqrt{Z^2 - \left(\frac{x_1^{\,2}}{2R} + a_1\right)^2} \qquad \text{(C.13)}$$

and

$$x_2 = \Delta L - \sqrt{Z^2 - a_1^{\,2}} + \sqrt{Z^2 - \left(\frac{x_1^{\,2}}{2R} + a_1\right)^2} \qquad \text{(C.14)}$$

x_1 and x_2 are then calculated using iterations in Microsoft Office Excel.

The motion of a pendulum is assumed to have viscous damping described by the differential equation:

$$\ddot{x} + 2\beta\dot{x} + \omega_n^{\,2} x = 0 \qquad \text{(C.15)}$$

Where,

$$\beta = \frac{C}{2m\omega_n} \qquad \text{(C.16)}$$

and

$$\omega_n = \frac{2\pi}{T} \qquad \text{(C.17)}$$

where β - viscous damping factor, m - mass of the pendulum (including the blast rig, test panel and counterweights), ω_n - natural frequency of the pendulum and T - natural period of the

pendulum. The period was calculated by measuring the pendulum's free swing and the time taken for 10 oscillations, using:

$$T = \frac{total\ time}{number\ of\ oscillations} \tag{C.18}$$

The solution to differential equation (D.15) is given by:

$$x(t) = \frac{(e^{-\beta t})\dot{x}_0 \sin \omega_d t}{\omega_d} \tag{C.19}$$

where $\dot{x}_0$ - initial velocity of the pendulum and ω_d - damped natural frequency, given by:

$$\omega_d = \omega_n{}^2 \sqrt{1-\beta^2} = \frac{2\pi}{T_d} \tag{C.20}$$

T_d is the damped period. x_1 and x_2 can now be defined from equation (D.19) at times $t = \frac{T_d}{4}$ and $t = \frac{3T_d}{4}$,respectively. Therefore,

$$x_1 = \frac{\dot{x}_0 T_d}{2\pi} e^{-\beta T_d / 4} \tag{C.21}$$

and

$$x_2 = -\frac{\dot{x}_0 T_d}{2\pi} e^{-3\beta T_d / 4} \tag{C.22}$$

The ratio of the successive amplitudes x_1 and x_2 is:

$$\frac{x_1}{x_2} = e^{\beta T_d / 2} \tag{C.23}$$

Solving for β in terms of x_1 and x_2 by rearranging equation (D.18) gives:

$$\beta = \frac{2}{T_d} \ln \frac{x_1}{x_2} \tag{C.24}$$

The initial velocity is then:

$$\dot{x}_0 = \frac{2\pi}{T} x_1 e^{-\beta T / 4} \tag{C.25}$$

Impulse (I) is then calculated using:

$$I = m \dot{x}_0 \tag{C.26}$$

APPENDIX D: Engineering Drawings

This section contains the engineering drawings for parts designed and manufactured for the current work.

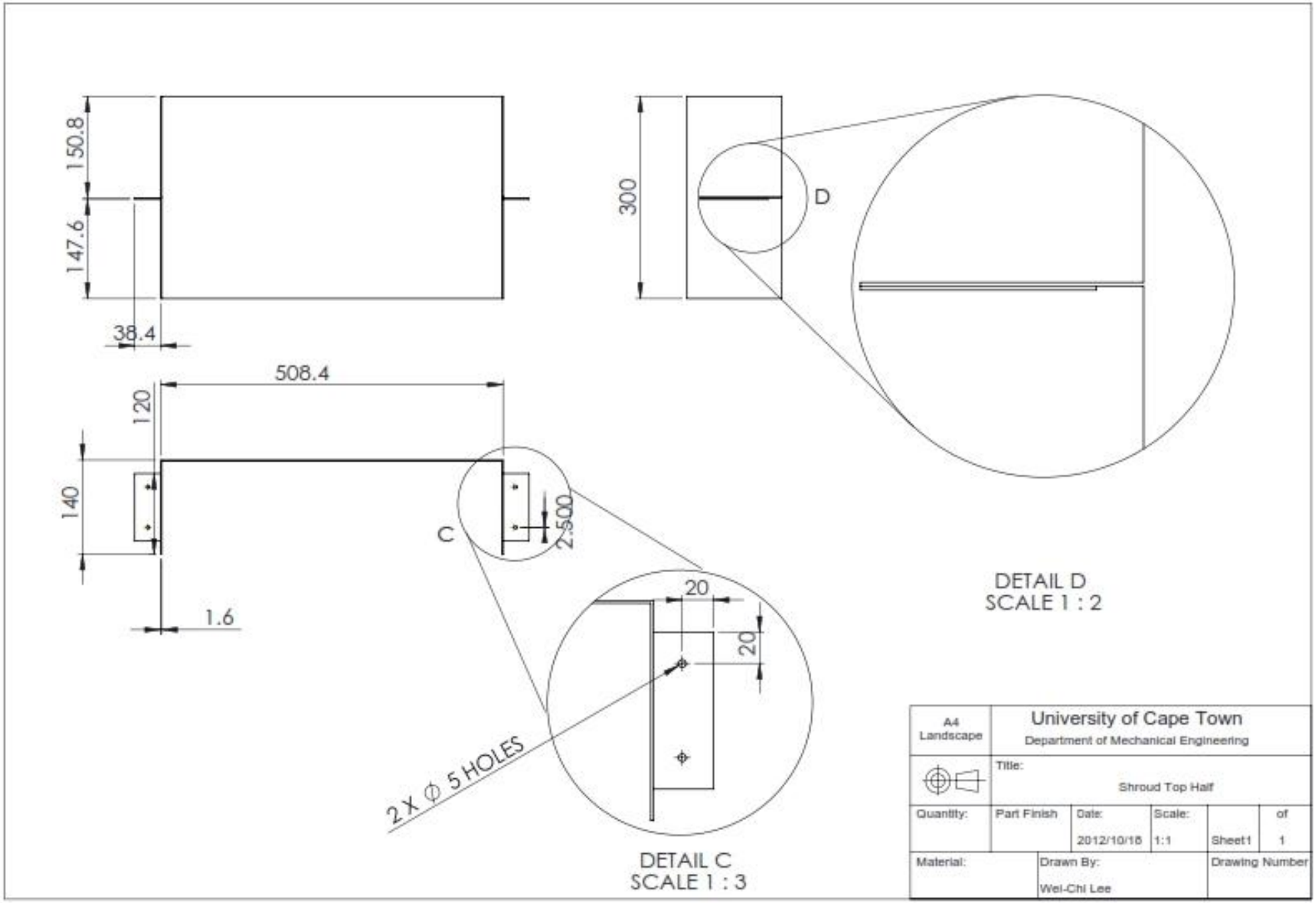
150.8
147.6
38.4
508.4
120
140
1.6
C
2.500
2 X ⌀ 5 HOLES
20
20
DETAIL C
SCALE 1 : 3
300
D
DETAIL D
SCALE 1 : 2
A4
Landscape
University of Cape Town
Department of Mechanical Engineering
Title:
Shroud Top Half
Quantity:
Part Finish
Date:
2012/10/16
Scale:
1:1
Sheet1
of
1
Material:
Drawn By:
Wei-Chi Lee
Drawing Number

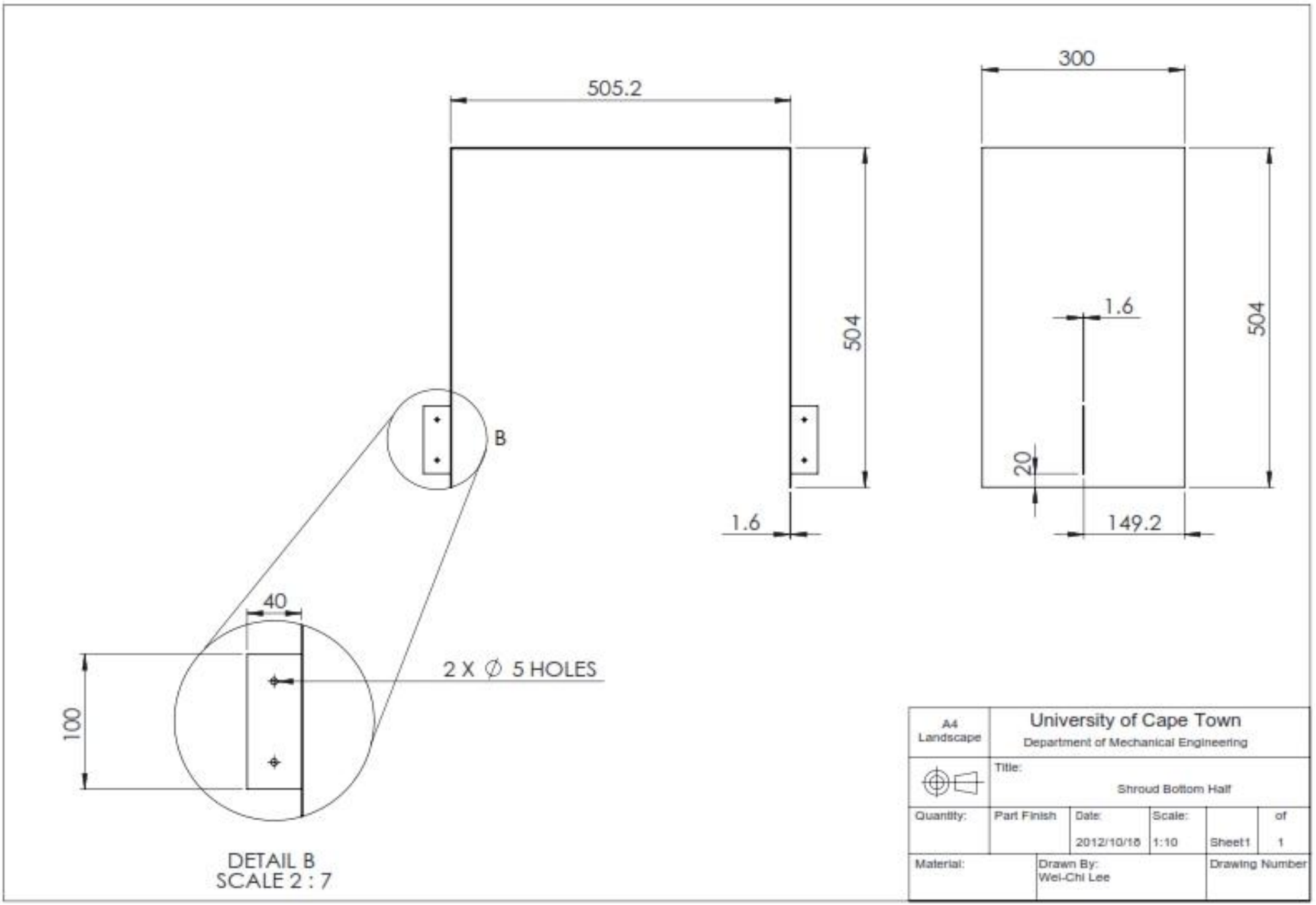
505.2
300
504
1.6
504
1.6
20
149.2
B
40
2 X ∅ 5 HOLES
100
DETAIL B
SCALE 2 : 7
A4
Landscape
University of Cape Town
Department of Mechanical Engineering
Title:
Shroud Bottom Half
Quantity:
Part Finish
Date:
2012/10/18
Scale:
1:10
Sheet1
of
1
Material:
Drawn By:
Wei-Chi Lee
Drawing Number

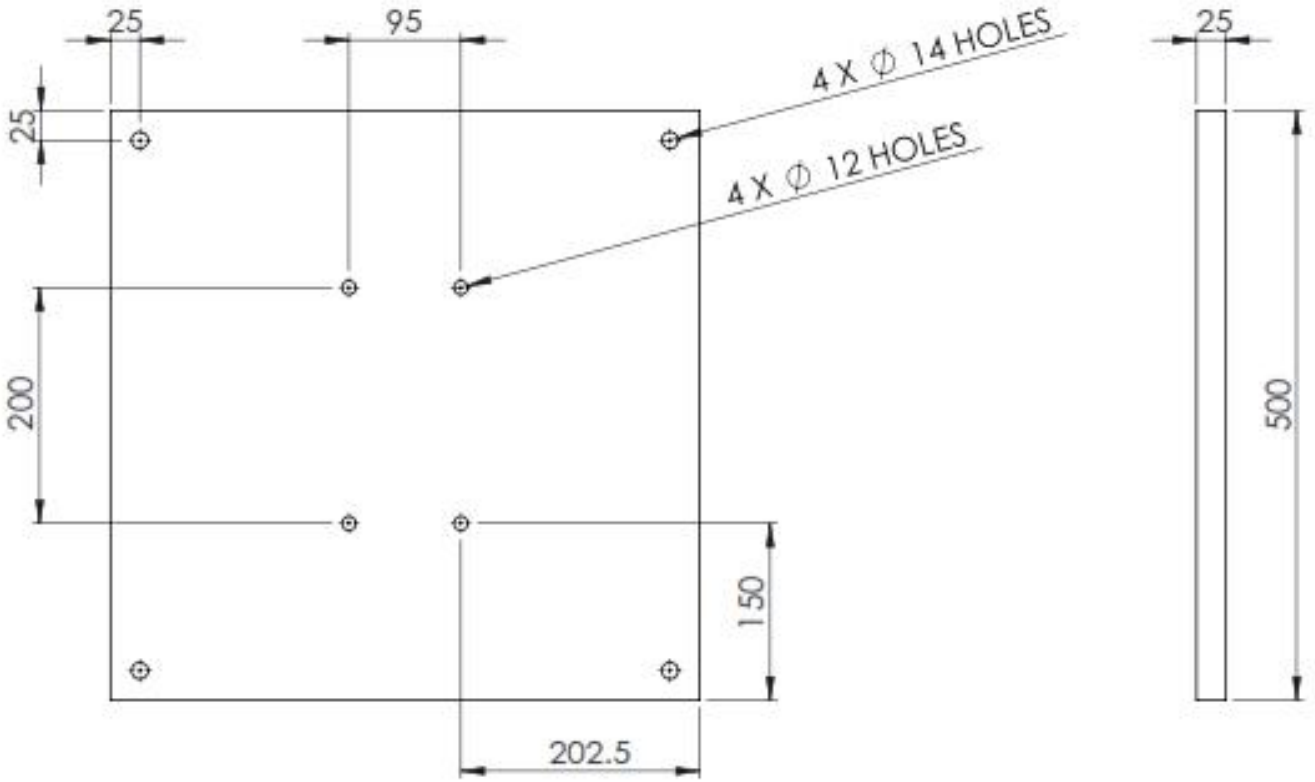

A4 Landscape	University of Cape Town Department of Mechanical Engineering				
	Title: Clamp Frame Mount Plate				
Quantity:	Part Finish	Date: 2012/10/16	Scale: 1:1	Sheet1	of 1
Material: Plain Carbon Steel	Drawn By: Wei-Chi Lee			Drawing Number	

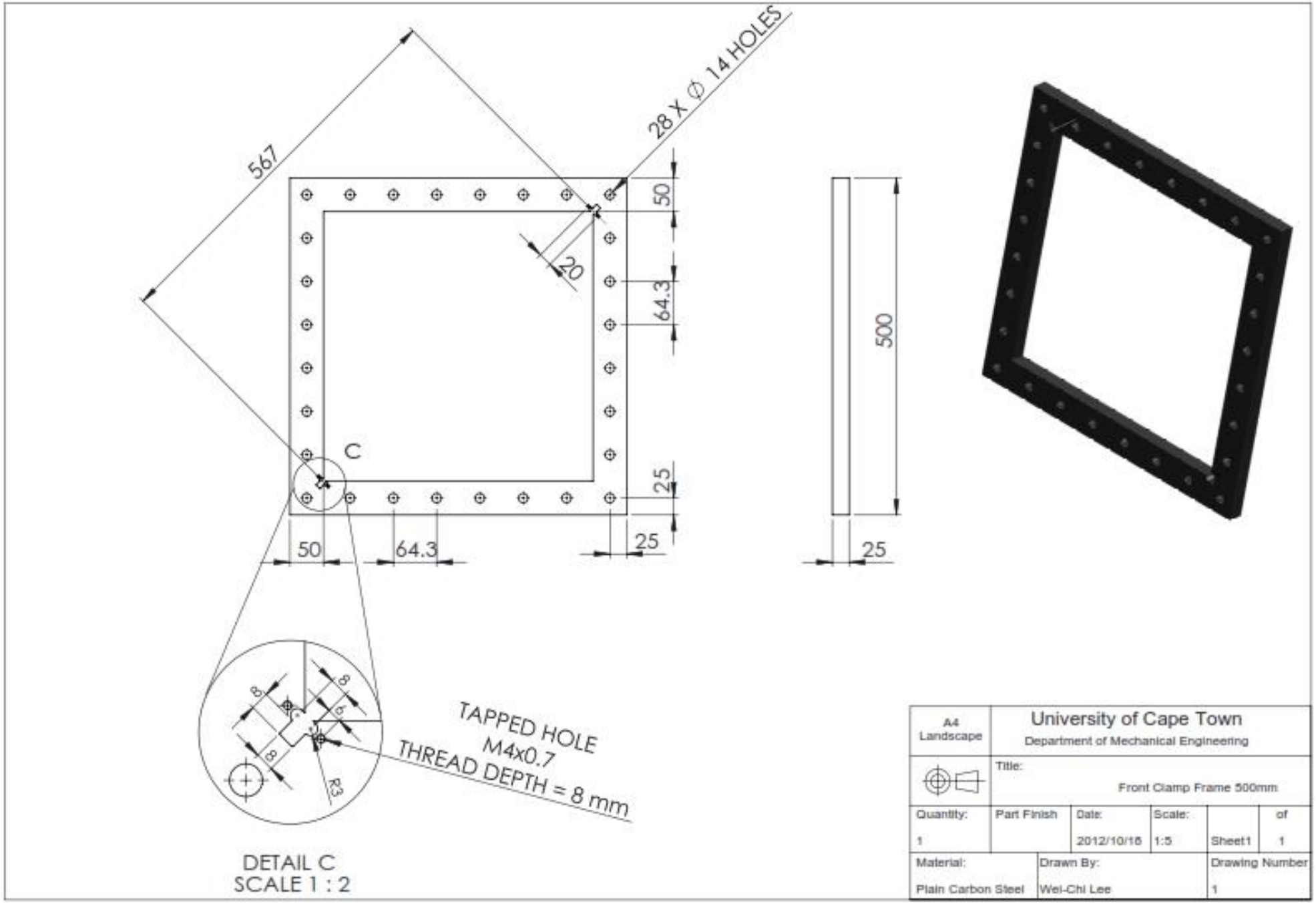
28 X ∅ 14 HOLES
567
50
20
64.3
500
25
C
50
64.3
25
25
8
8
8
8
R3
TAPPED HOLE
M4x0.7
THREAD DEPTH = 8 mm
DETAIL C
SCALE 1 : 2
A4
Landscape
University of Cape Town
Department of Mechanical Engineering
Title:
Front Clamp Frame 500mm
Quantity:
1
Part Finish
Date:
2012/10/16
Scale:
1:5
Sheet1
of
1
Material:
Plain Carbon Steel
Drawn By:
Wei-Chi Lee
Drawing Number
1

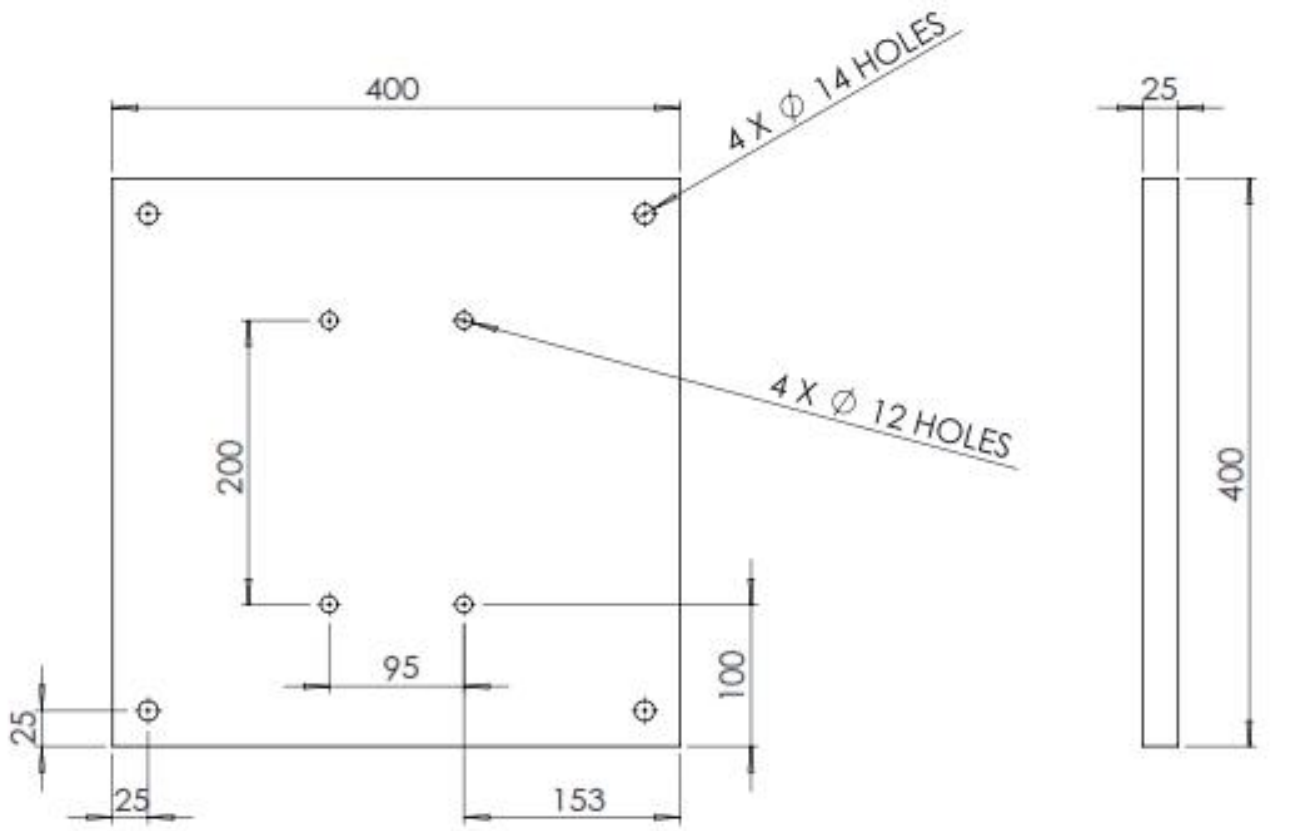

A4 Landscape	University of Cape Town Department of Mechanical Engineering				
	Title: Mount Plate Back 400mm				
Quantity:	Part Finish	Date: 2012/10/16	Scale: 1:5	Sheet1	of 1
Material: Plain Carbon Steel	Drawn By: Wei-Chi Lee			Drawing Number	

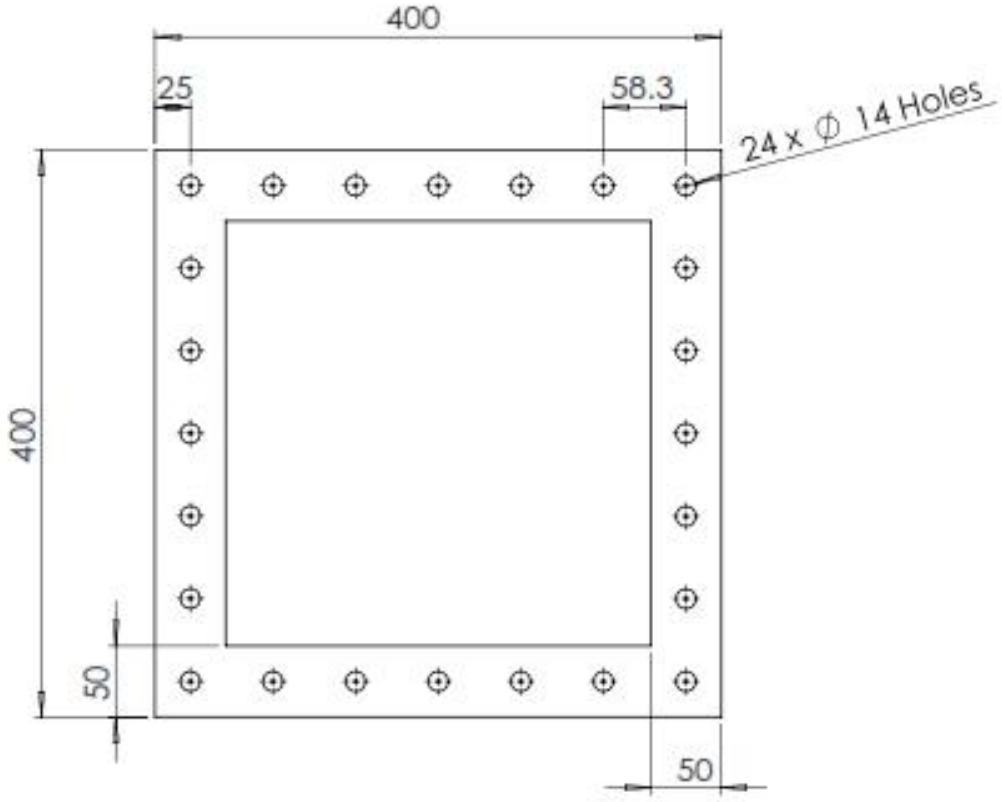

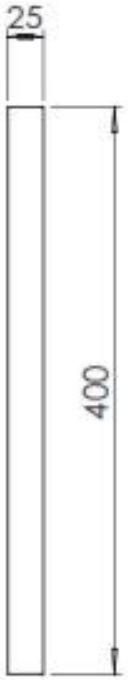

A4 Landscape	University of Cape Town Department of Mechanical Engineering				
	Title: Clamp_frame_400mm				
Quantity:	Part Finish	Date: 2012/10/16	Scale: 1:5	Sheet1	of 1
Material: Plain Carbon Steel	Drawn By: Wei-Chi Lee			Drawing Number	

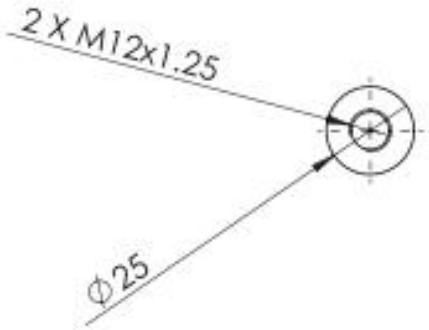

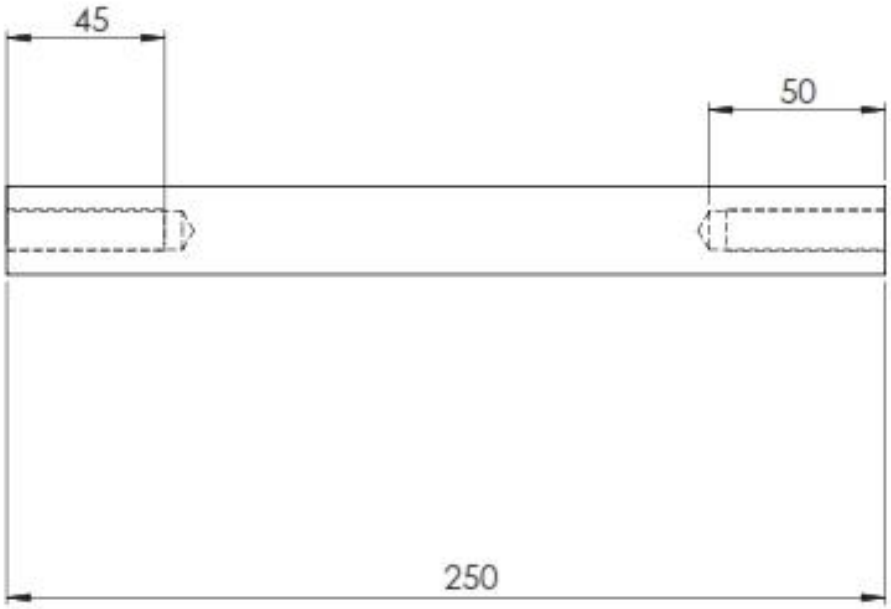

A4 Landscape	University of Cape Town Department of Mechanical Engineering				
	Title: Spacer Rod				
Quantity:	Part Finish	Date: 2012/10/16	Scale: 1:5	Sheet1	of 1
Material: Plain Carbon Steel	Drawn By: Wei-Chi Lee			Drawing Number	

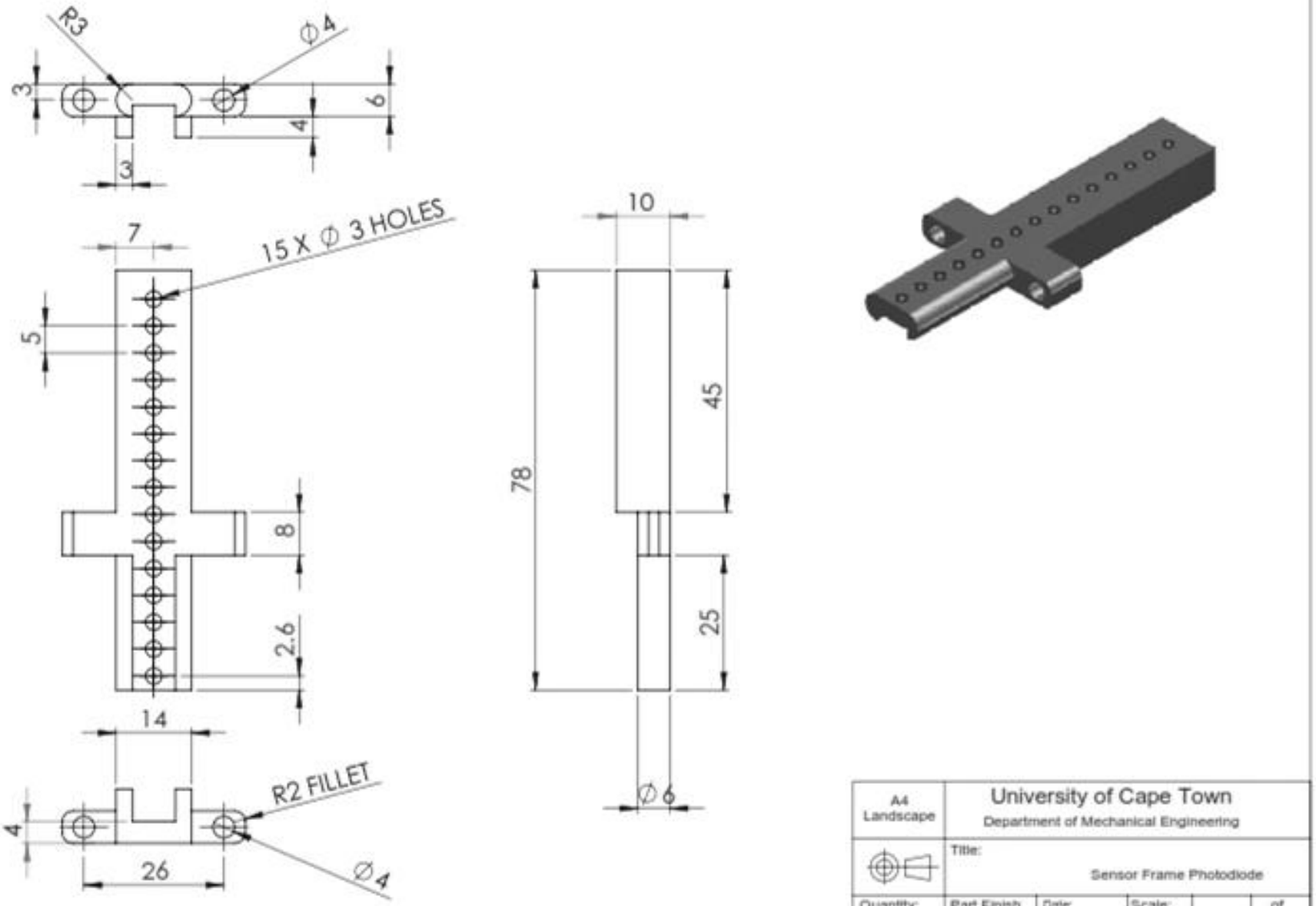
R3
Ø4
3
6
4
3
7
15 X Ø 3 HOLES
5
8
2.6
14
R2 FILLET
4
26
Ø4
10
78
45
25
Ø6
A4 Landscape
University of Cape Town
Department of Mechanical Engineering
Title:
Sensor Frame Photodiode
Quantity:
Part Finish
Date:
2012/10/16
Scale:
1:1
Sheet1
of
1
Material:
Aluminium
Drawn By:
Wei-Chi Lee
Drawing Number

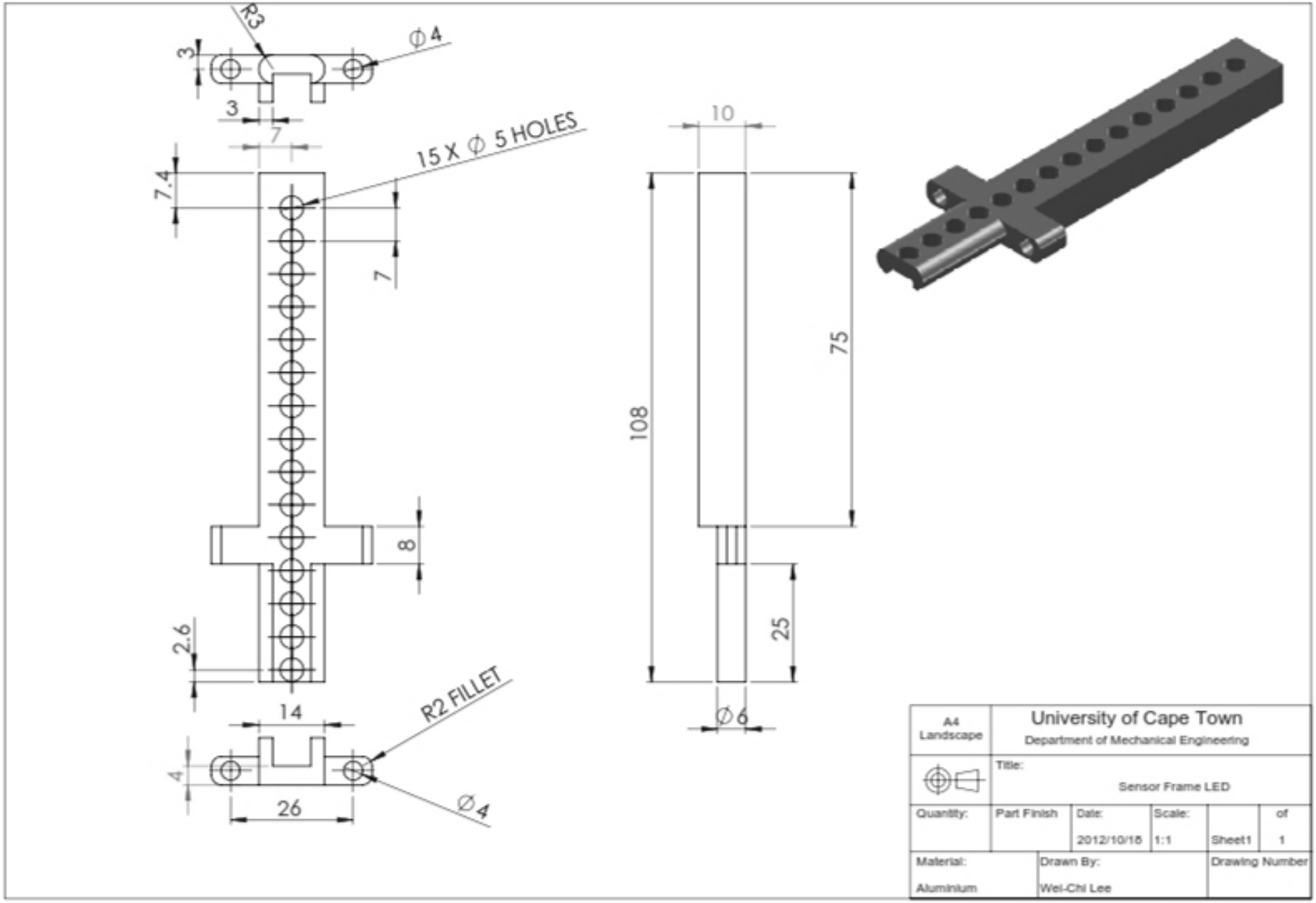
R3
Ø4
3
3
7
15 X Ø 5 HOLES
7.4
7
8
2.6
14
R2 FILLET
4
26
Ø4
10
108
75
25
Ø6
A4
Landscape
University of Cape Town
Department of Mechanical Engineering
Title:
Sensor Frame LED
Quantity:
Part Finish
Date:
2012/10/18
Scale:
1:1
Sheet1
of
1
Material:
Aluminium
Drawn By:
Wei-Chi Lee
Drawing Number

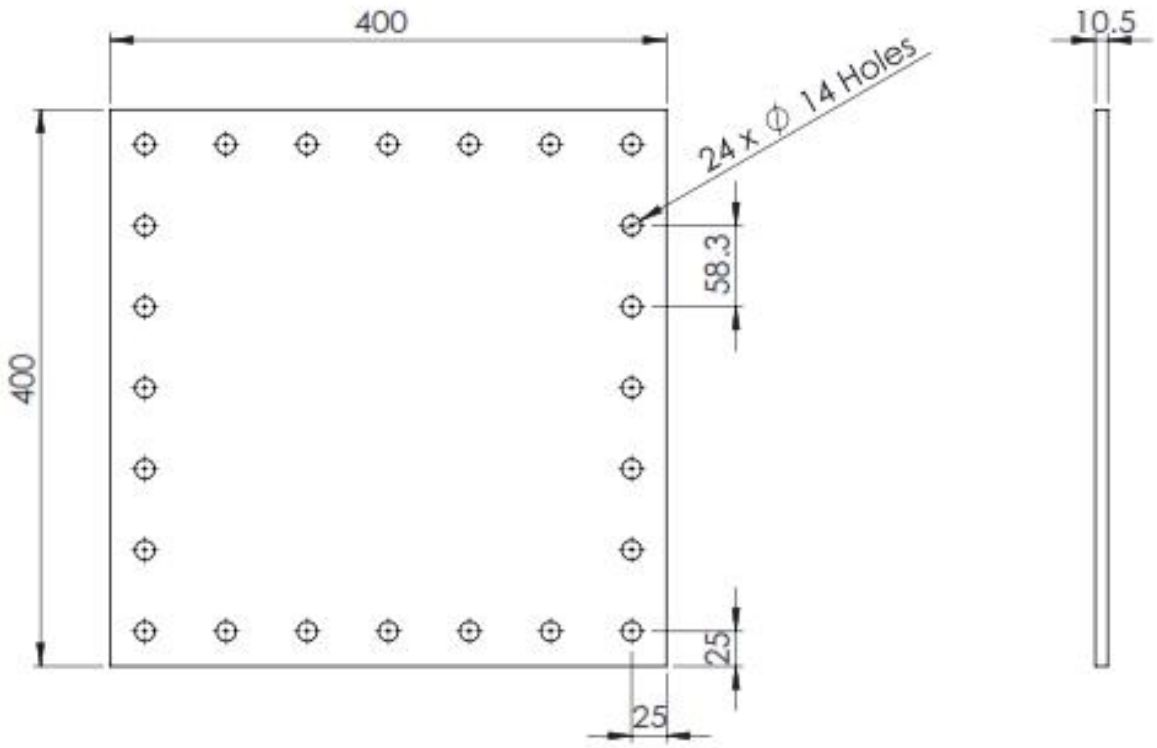

A4 Landscape	University of Cape Town Department of Mechanical Engineering				
	Title: Test Plate 400 Aluminium				
Quantity:	Part Finish	Date: 2012/10/18	Scale: 1:10	Sheet1	of 1
Material: AL 5083-H116	Drawn By: Wei-Chi Lee			Drawing Number	

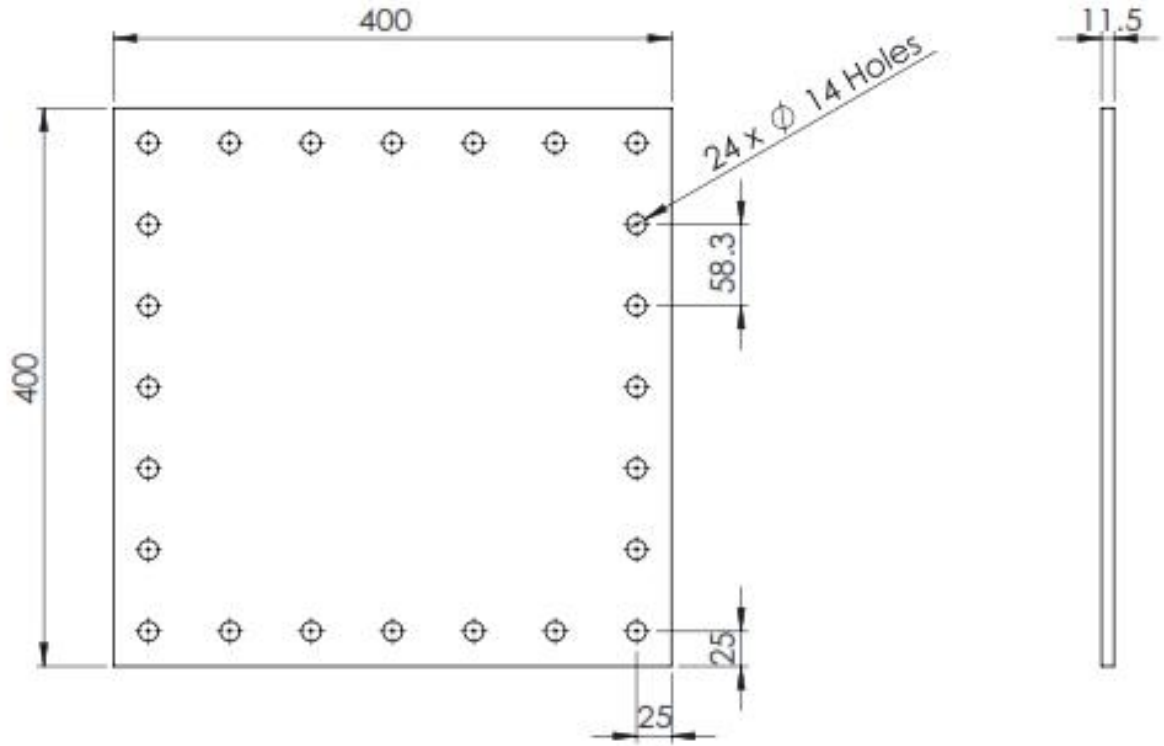

A4 Landscape	University of Cape Town Department of Mechanical Engineering				
	Title: Test PLate 400mm Twintex				
Quantity:	Part Finish	Date: 2012/10/16	Scale: 1:10	Sheet1	of 1
Material: Twintex	Drawn By: Wei-Chi Lee			Drawing Number	

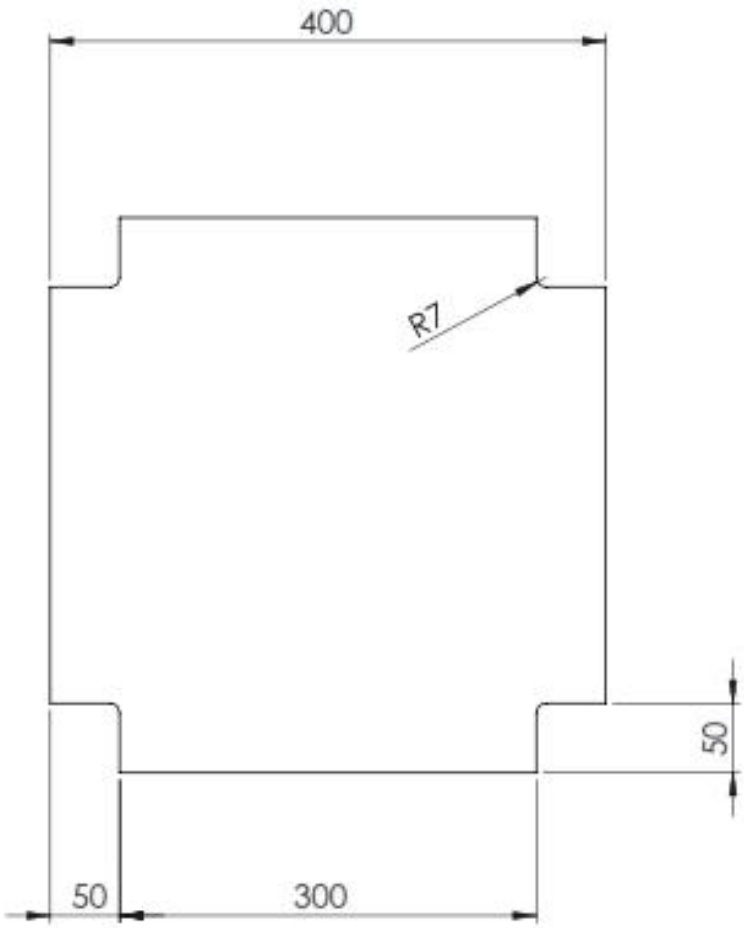

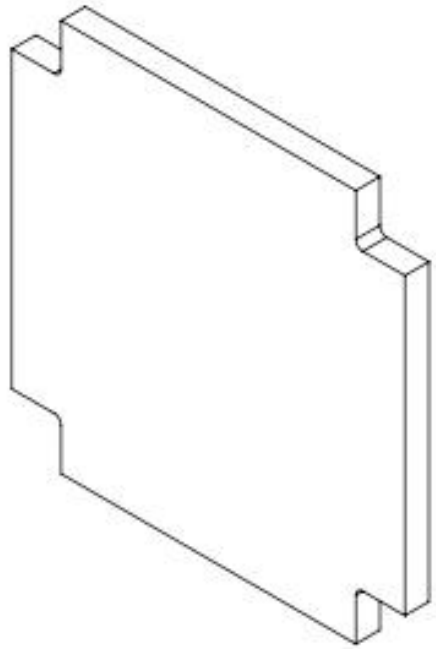

A4 Landscape	University of Cape Town Department of Mechanical Engineering				
	Title: Dyneema Plate				
Quantity:	Part Finish	Date: 2012/10/16	Scale: 1:5	Sheet1	of 1
Material:	Drawn By: Wei-Chi Lee			Drawing Number	

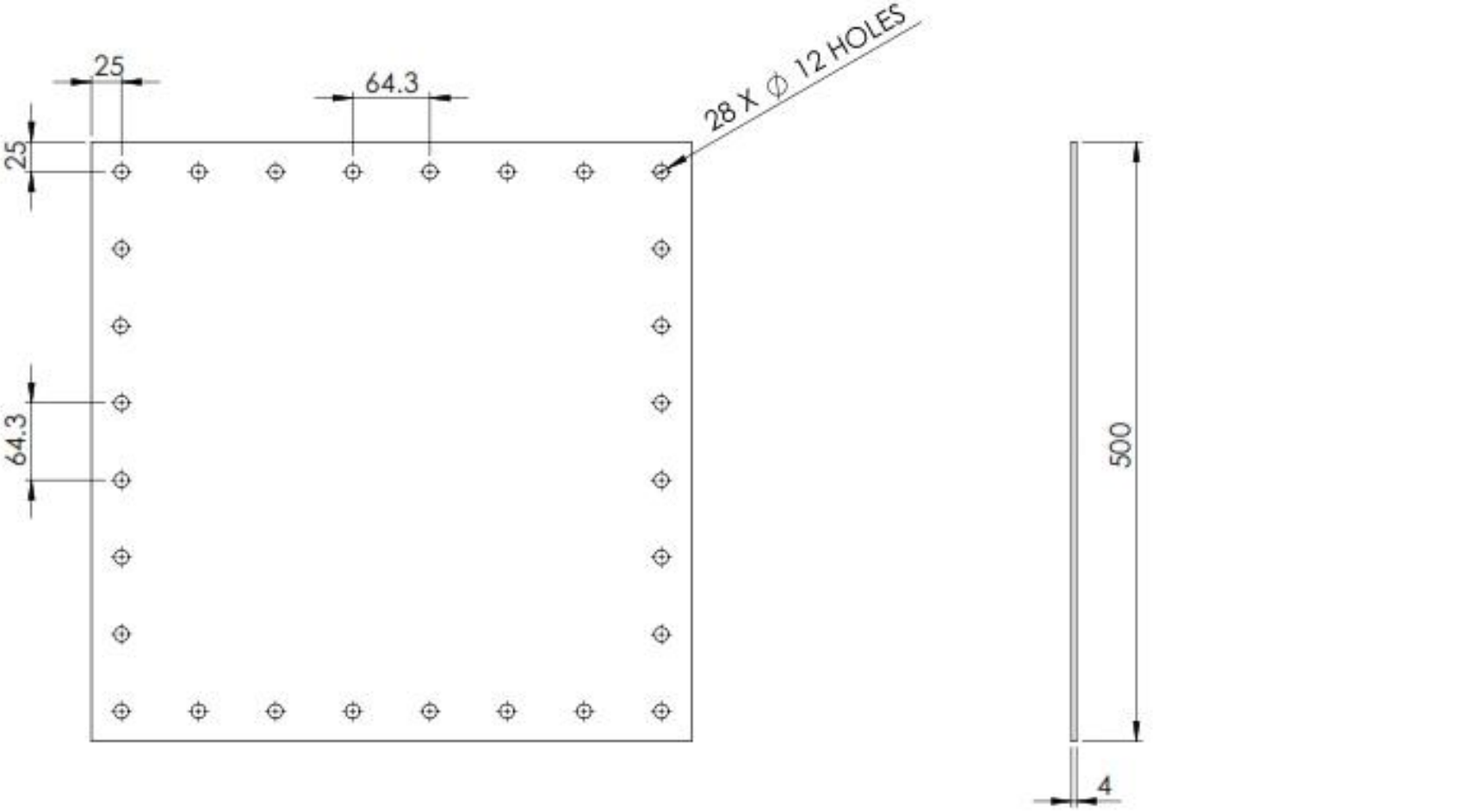

A4 Landscape	University of Cape Town Department of Mechanical Engineering				
	Title: Test plate 500mm				
Quantity:	Part Finish	Date: 2011/03/18	Scale: 1:5	Sheet1	1
Material:	Drawn By:			Drawing Number	

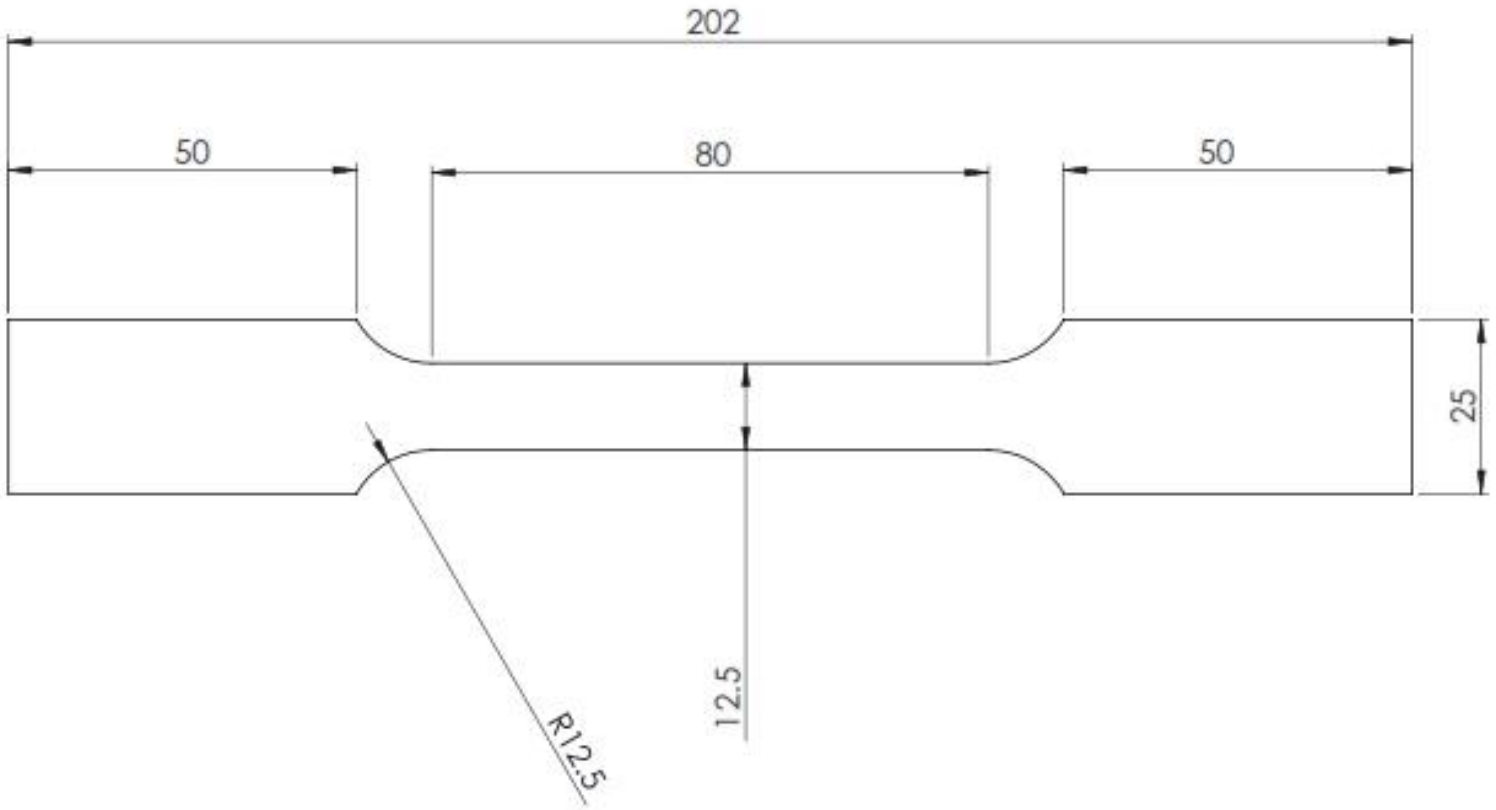

A4 Landscape	University of Cape Town Department of Mechanical Engineering				
	Title: Tensile Test Specimen				
Quantity:	Part Finish	Date: 2012/10/16	Scale: 1:1	Sheet1	of 1
Material:	Drawn By: Wei-Chi Lee			Drawing Number	

APPENDIX E: Light Interference Example

The example in this section demonstrates the method for calculating the light intensity percentage transmitted onto the receivers. The intensity is calculated according to the conditions for equation 28 and 29 in Chapter 3, based on a plate displacement of 34mm. Table E 1 lists the height position of each LED on the transmitter and their relative light intensity.

Table E 1: Table of light intensity for each LED based on plate displacement of 34mm

Height Of Emitter (mm)	Percentage of Light Transmitted to Receiver	Disp (mm)	Height of Receiver (mm)	Exposed area of Plate	Distance Between sensors
0	2.86	34	70	400	565.69
7	12.86				
14	22.86				
21	32.86				
28	42.86				
35	52.86				
42	62.86				
49	72.86				
56	82.86				
63	92.86				
70	100.00				
77	100.00				
84	100.00				
91	100.00				
98	100.00				

Total Percentage of Light Transmitted to Receiver:	**65.24 %**

For the LED at the 28mm high position, equation 28 will be used to calculate its intensity as it is less than the height of the plate displacement as follows:

$$LI = \left\{\frac{[70 - 34 - (34 - 28)]}{70}\right\} \times 100 = 42.86\%$$

If the height of the LED is at 42mm, which is higher than the plate displacement, then equation 29 will be used to calculate its relative light intensity:

$$LI = \left\{\frac{[70 - 34 + (42 - 34)]}{70}\right\} \times 100 = 62.86\%$$

The light intensities for the rest of the LEDs are calculated according to either equation 28 or 29 and the total light intensity will be the average of the sum of all the light intensity percentages.

APPENDIX F: Ethics Declaration